

Interaction between Water Vapor, Radiation and Convection in the Tropics

by

Tom Beucler

B.E., Ecole Polytechnique (2013)

S.M. Mechanics, Ecole Polytechnique (2014)

Submitted to the Department of Earth, Atmospheric, and Planetary
Sciences

in partial fulfillment of the requirements for the degree of

Doctor of Philosophy

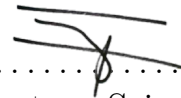
at the

MASSACHUSETTS INSTITUTE OF TECHNOLOGY

February 2019

© Massachusetts Institute of Technology 2019. All rights reserved.

Author



Department of Earth, Atmospheric, and Planetary Sciences

Dec 7, 2018

Certified by

Timothy Cronin

Kerr-Mcgee Career Development Assistant Professor

Thesis Supervisor

Certified by

Kerry Emanuel

Cecil & Ida Green Professor of Atmospheric Science

Thesis Supervisor

Accepted by

Robert van der Hilst

Schlumberger Professor of Earth Sciences

Head of Department of Earth, Atmospheric and Planetary Science

Interaction between Water Vapor, Radiation and Convection in the Tropics

by

Tom Beucler

Submitted to the Department of Earth, Atmospheric, and Planetary Sciences
on Dec 7, 2018, in partial fulfillment of the
requirements for the degree of
Doctor of Philosophy

Abstract

The spatiotemporal variability of water vapor near the Equator remains poorly understood because convective organization simultaneously spans the cloud scale ($\sim 10\text{km}$) and the planetary scale ($\sim 10,000\text{km}$). Spatiotemporal variability of tropical water vapor may result from internal instabilities of the atmosphere, arising from the interaction between water vapor, radiation and convection. The present work leverages the instability of radiative-convective equilibrium, the most fundamental state of the tropical atmosphere, to connect convective organization in cloud-permitting models with the observed variability of water vapor through common physical mechanisms. First, we propose a simple theory that explains when instability of radiative-convective equilibrium may occur: If the total atmospheric cooling decreases with column water vapor, then radiative-convective equilibrium may be unstable to the growth of moist and dry perturbations. Secondly, we combine a linear response framework with the weak temperature gradient approximation to analyze the interaction between convection, radiation and water vapor at each level of the atmosphere. We find that convection may interact with radiation to trigger the growth of mid-tropospheric water vapor anomalies by transporting water vapor to the upper troposphere, where it can prevent lower-tropospheric water vapor from radiatively cooling to space. Thirdly, we turn to the spatial organization of water vapor anomalies and relate the evolution of the size of moist and dry regions to diabatic fluxes in twenty cloud-permitting simulations on large domains. Longwave radiation from ice clouds aggregates convection at larger scales, shortwave radiation aggregates convection at smaller scales, and surface enthalpy fluxes smooth out water vapor anomalies through their enthalpy disequilibrium component. Finally, we relate the transient zonal variability of precipitable water to convective-aggregation mechanisms in realistic models and observations of the atmosphere. Radiative fluxes generate transient water vapor structures of planetary scales, while surface enthalpy fluxes and horizontal energy transport act to smooth out these structures, suggesting parallels between observations and idealized simulations of aggregated convection.

Thesis Supervisor: Timothy Cronin
Title: Kerr-Mcgee Career Development Assistant Professor

Thesis Supervisor: Kerry Emanuel
Title: Cecil & Ida Green Professor of Atmospheric Science

Acknowledgments

Written on the 17th floor of the Green Building during a cold Thanksgiving night, with a -10°C low and gusts of 30km/h .

First, I thank my thesis co-advisors: I thank Kerry for taking me in as a graduate student almost five years ago, for his humanity, wisdom, patience, support, for the invaluable independence he gave me as a researcher, and for his “Radiative-convective Instability” paper which inspired my thesis topic. I thank Tim for taking me in as his first student while he was still a postdoctoral fellow at Harvard, for his understanding, flexibility, for teaching me the rudiments of scientific writing and computational science, and for unsuccessfully trying to help me work more reasonable hours. I also thank the rest of my thesis committee for their guidance throughout the thesis process: Paul O’Gorman for his constant support and advice, Chris Bretherton for encouraging me to progress towards the real atmosphere, and Zhiming Kuang for providing data and detailed advice that helped me overcome a particularly challenging chapter of this thesis. I would also like to thank Caroline Muller, Allison Wing, Raffaele Ferrari and Glenn Flierl for advice and help with my research at various stages of my PhD, as well as Marat Khairoutdinov for letting me use the SAM cloud-permitting model which made this thesis possible.

I am grateful for the close friends that I have made in America, who helped me make the most of the first half of my twenties. David, Jean, Bart, Bryan, Cael, Gabrielle, Diami and many others during the first two years; life changed a lot during my last two years as I started working unreasonably long hours, and I am very grateful that I could make new friends during that time mostly spent at MIT, including (but not restricted to): Derek, Cam, Stephane, Guillaume, Rene, Michael, my labmates Rohini, Sydney, Jonathan, Raphael, Tristan, Nick and Daniel. I thank the EAPS community for providing a relaxed yet stimulating environment, and Faith for her

outstanding administrative support. Last but not least, I would like to thank my loving and chaotic family on the other side of the Atlantic, Sara, Nathan, Marguerite, Marc and Jeremie: Some of them for communicating regularly and being constant sources of support, others for occasionally picking up their phones to debate abstract philosophical topics.

The research in this thesis benefited from high-performance computing support from the Engaging cluster at MIT, and I am grateful for support from the Neil and Anna Rasmussen Foudation Fund, SERDP grant RC-2336, NSF grants AGS-1136480, AGS-1418508, AGS-1520683 and the Houghton fund.

Contents

1	Introduction	27
1.1	Background and motivation	27
1.1.1	Water vapor, radiation and convection in the troposphere . . .	27
1.1.2	Spatiotemporal variability of water vapor	31
1.1.3	Moist radiative-convective instability	35
1.2	Outline	37
2	Moisture-Radiative Cooling Instability	43
2.1	Introduction	44
2.2	Theory	46
2.2.1	Moisture-radiative cooling instability	46
2.2.2	Clear-sky longwave radiation	49
2.2.3	Clear-sky shortwave radiation	56
2.2.4	Cloud longwave radiative effects	58
2.3	Real-gas radiative transfer	60
2.4	Observations	63
2.4.1	Method	63
2.4.2	A case study: Chuuk Lagoon	65
2.4.3	MRCI growth rates in the Tropics	66
2.5	Conclusion	68
2.6	Appendix A: Analytical form of the longwave radiative fluxes	72
2.7	Appendix B: Dependence of MRCI on surface temperature	72
2.8	Appendix C: Cloudy radiative fluxes	73

2.9	Appendix D: Growth rates of MRCI	76
2.10	Appendix E: Two-band longwave radiative transfer	78
3	A Linear Response Framework for Radiative-Convective Instability	81
3.1	Introduction	82
3.2	Linear response framework	84
3.2.1	Linear response function	84
3.2.2	Linear response matrix	87
3.3	Linear response of convection	91
3.3.1	Convection in cloud-permitting models	91
3.3.2	Betts-Miller scheme	96
3.3.3	Bulk plume equations	99
3.4	Linear response of radiation	106
3.4.1	Two-stream model of longwave radiation	106
3.4.2	One-stream model of shortwave radiation	109
3.4.3	Real-gas radiative transfer	112
3.5	Linear evolution of small water vapor perturbations	114
3.6	Conclusion	118
3.7	Appendix A: Linear response of the bulk-plume equations	121
3.7.1	A.1. Basic state	121
3.7.2	A.2. Linear response	122
3.7.3	A.3. Leading eigenvalue of the convective response matrices	124
3.8	Appendix B: Linear response of the Schwarzschild equations	125
3.8.1	B.1. Two-stream model of longwave radiation	125
3.8.2	B.2. One-stream model of shortwave radiation	128
3.8.3	B.3. Choice of the optical thickness	129
3.9	Appendix C: Sensitivity to convective model parameters	130
4	A Budget for the Size of Convective Self-aggregation	133
4.1	Introduction	133
4.2	Method	136

4.2.1	Definitions	136
4.2.2	Budgets	139
4.2.3	Simulation design	143
4.2.4	Calculation of the budget terms	144
4.2.5	Interpretation of the expansion tendency	147
4.3	Results	148
4.3.1	Convective aggregation length scales	148
4.3.2	Evolution of the length scale diabatic tendencies	151
4.3.3	Radiative rates	157
4.3.4	Surface flux rates	159
4.4	Conclusion	162
4.5	Appendix A: Alternative definitions of L	165
4.5.1	A.1. Comparison of spectrally-defined scales to the auto-correlation length scale	165
4.5.2	A.2. Budget for the integral moist static energy scale	168
4.6	Appendix B: Equivalence of the moist static energy variance and power spectrum budgets	170
4.7	Appendix C: Summary table for all experiments	174
4.8	Appendix D: Spectral moist static energy tendencies and cloud water coherence	175
5	Are Convective-Aggregation Mechanisms Relevant for the Transient Zonal Variability of Precipitable Water in the Tropics?	179
5.1	Introduction	180
5.2	Methods	182
5.2.1	Data characteristics	182
5.2.2	Transient precipitable water variance budgets	185
5.2.3	Statistical and spectral analyses	186
5.3	Preliminary results	188
5.3.1	Interaction between water vapor, radiation and convection	188

5.3.2	Zonal Spectra of Convective-Aggregation Feedbacks	192
5.4	Discussion	195
5.5	Appendix A: Comparison between DYAMOND and observations . . .	197
5.6	Appendix B: Relation between total diabatic fluxes and precipitable water	197
6	Conclusion	199
6.1	Introduction	199
6.2	Key results	200
6.3	Directions for future research	203
6.3.1	Organization of convection over an interactive surface	203
6.3.2	Role of radiation and convection during extreme events	203
A	Impact of cloud radiation on the organization of non-rotating con- vection	207
A.1	Experimental design	207
A.2	Results	209
B	Linear Response of a Full-physics Column Model	215
B.1	Introduction	215
B.2	Experimental design	215
B.3	Results	218
B.3.1	Radiative-convective equilibrium	218
B.3.2	Convective response	219
B.3.3	Radiative response	222
B.3.4	Full linear response	224

List of Figures

1-1	Molecular structure of water (from Hardinger [2018]). 1) Median absorption coefficient of water vapor in the shortwave domain (using intervals of 50cm^{-1} , Figure 5.13 from Pierrehumbert [2009]). 2) Median absorption coefficient of water vapor in the longwave domain (full black line, Figure 4.19 from Pierrehumbert [2009]). 3) Schematic phase diagram of water substance (adapted from Emanuel [1994]). 4) Median absorption coefficient of liquid water (full line, Figure 4.28 of Pierrehumbert [2009]). The electromagnetic wavenumber (in units cm^{-1}) is defined as the inverse wavelength.	28
1-2	Observations of precipitable water on October 17th, October 20th and October 23rd 2017 at 00GMT (ERA5 reanalysis).	32
1-3	Temporal (horizontal axis) and spatial (vertical axis) scales of tropical water vapor variability; black boxes indicate the scales of: clouds, mesoscale convective complexes (MCC), local radiative-convective equilibrium (RCE), tropical depressions (TD), tropical cyclones (TC), and the Madden-Julian Oscillation (MJO). We indicate the typical scales covered by atmospheric models: CPM (light blue box), operational meteorological models (purple box) and global climate models (orange box). The long-channel RCE framework (blue box) is at the intersection of these scales.	34

1-4	Simultaneous snapshots of two different regions of the same long-channel simulation at fixed sea surface temperature (LCCAM300 in Chapter 4). Despite homogeneous boundary conditions, a dry anomaly has formed and deep convection is suppressed in the region located at $x \in [600, 780]$ km, resulting in high values of the net atmospheric long-wave cooling to space. In contrast, a moist anomaly has formed and deep convection is active in the region located at $x \in [9600, 9780]$ km, resulting in lower values of longwave cooling to space.	36
1-5	Temporal (horizontal axis) and spatial (vertical axis) scales of tropical water vapor variability addressed in each chapter and appendix of the thesis (blue boxes). Black boxes indicate the scales of: clouds, mesoscale convective complexes (MCC), tropical depressions (TD), tropical cyclones (TC), and the Madden-Julian Oscillation (MJO). . .	38
2-1	Mechanism of MRCI: A moist perturbation decreases the radiative cooling, leading to an amplification of this moist perturbation. . . .	49
2-2	a) Temperature profile $T(p)$ and b), c) water vapor mixing ratio profile $r(p)$ in January at Chuuk Lagoon. The average observational profiles are shown in solid black lines and the idealized fits are shown in blue dashed lines; b) and c) are identical but b) has a linear scale for $r(p)$ and c) has a logarithmic scale.	51
2-3	Two methods of varying column water vapor used in this chapter; a) varied mixing ratio (r_s) and fixed shape; b) varied shape ($n = 1.7, 2.2, 3.0, 4.3, 7.0$) and fixed surface mixing ratio. The reference profile is gray and the different colors represent equal increments of total column water vapor.	54

2-4	Outgoing longwave radiation (OLR), surface net longwave radiation (SLW), and longwave clear-sky radiative cooling \hat{Q}_L as a function of column water vapor \hat{r} , a) varying the surface mixing ratio at fixed shape, and b) varying the water vapor profile shape at constant surface mixing ratio. Crosses show maxima of radiative cooling, and green axis labels indicate surface optical thickness, τ_s . The surface temperature is 300K. Note the similarity to figure 4 of Takahashi [2009].	55
2-5	Longwave \hat{Q}_L and total \hat{Q} clear-sky radiative cooling as a function of column water vapor, a) varying the surface mixing ratio at fixed shape, and b) varying the water vapor profile shape at constant surface mixing ratio. Crosses show maxima of radiative cooling. The surface temperature is 300K.	57
2-6	Optical thickness profile for a cloud at $p_c = 850\text{hPa}$ with cloud optical thickness $\Delta\tau = 2.5$	58
2-7	Total radiative cooling in the presence of a low ($p_c = 900\text{hPa} \Leftrightarrow T_c = 295\text{K}$), high ($p_c = 200\text{hPa} \Leftrightarrow T_c = 234\text{K}$), thick ($\Delta\tau = 5$) or thin ($\Delta\tau = 0.5$) cloud with a) varied surface mixing ratio, and b) varied shape. Crosses show maxima of radiative cooling. The surface temperature is 300K.	60
2-8	As in Figures 2-4 and 2-5, but using the RRTMG model instead of gray-gas radiative transfer. Outgoing longwave radiation (OLR), surface net longwave radiation (SLW), longwave \hat{Q}_L and total \hat{Q} clear-sky radiative cooling as a function of column water vapor, a) varying the surface mixing ratio at fixed shape, and b) varying the water vapor profile shape at constant surface mixing ratio. Crosses show maxima of radiative cooling. The surface temperature is 300K.	62

2-9	Dependence of total radiative cooling \hat{Q} on column water vapor \hat{r} in RRTMG calculations that include cloud layers, for a) varied surface mixing ratio and b) varied water vapor profile shape. The four different types of clouds correspond to those described in section 2.2.4 and Figure 2-7. The surface temperature is 300K.	63
2-10	For Chuuk Lagoon station, profiles for average (gray line), $+1\sigma$ (blue line) and -1σ (orange line) conditions: (a) Computed mixing ratio profiles used for the RRTMG input (b) Relative humidity profiles (c) Net upwards longwave radiative flux (d) Net downwards shortwave radiative flux. Longwave radiative cooling values \hat{Q}_L are respectively 241 (dry: $< -1\sigma$), 233 (average), and 227 (moist: $> +1\sigma$) W m^{-2} . The shortwave radiative heating values $-\hat{Q}_S$ are respectively 76 (dry: $< -1\sigma$), 84 (average), and 89 (moist: $> +1\sigma$) W m^{-2}	67
2-11	Observed MRCI growth rates based on a) slope of clear-sky longwave cooling vs. column water vapor and b) slope of clear-sky longwave plus shortwave cooling vs. column water vapor, for the Caribbean stations (blue squares with red borders) West Pacific stations (blue stars) and Amazonian stations (green circles with yellow borders)	68
2-12	Total \hat{Q} clear-sky radiative cooling as a function of column water vapor, a) varying the surface mixing ratio at fixed shape, and b) varying the water vapor profile shape at constant surface mixing ratio, for three different choices of surface temperature. Crosses show maxima of radiative cooling.	74
2-13	RCE column water vapor (black line) and critical column water vapor threshold \hat{r}_{crit} , as a function of the surface temperature. On the left of the intersection point, RCE is stable. On the right of the intersection point, MRCI is satisfied. We obtain approximate surface temperature thresholds of 21 °C for varied shape, and 24 °C for varied surface mixing ratio. These values should be taken as illustrative rather than exact, and are sensitive to model assumptions.	74

2-14	Two-band outgoing longwave radiation (OLR), surface net longwave radiation (SLW), and longwave clear-sky radiative cooling \hat{Q}_L as a function of column water vapor \hat{r} , a) varying the surface mixing ratio at fixed shape, and b) varying the water vapor profile shape at constant surface mixing ratio. Crosses show maxima of radiative cooling.	79
3-1	The interaction of a water vapor perturbation with atmospheric radiation and convection leads to a water vapor tendency that can amplify, damp, or move the perturbation.	83
3-2	Guide to reading the linear response matrix M : The horizontal axis is the pressure at which water vapor is perturbed (p_j , in hPa), while the vertical axis is the pressure of the water vapor response (p_i , in hPa). In the example depicted above, water vapor is perturbed at $p_j = 400$ hPa, and the water vapor tendency response can be read in the green column. At the local perturbation level $p_i = 400$ hPa, a negative matrix element indicates that a perturbation would decay in time; below the perturbation level at $p_i = 600$ hPa, a positive matrix element indicates that a perturbation would amplify in time. In this simple case, a water vapor perturbation at 400 hPa would be moved to 600 hPa at a unit rate.	89
3-3	Linear convective matrix from the linear response matrices of Kuang [2012], where the HAM has been evaluated from the mean state of the simulation. The top of the boundary layer, identified as the relative humidity maximum in the lower troposphere, is indicated with dashed black lines. (Bottom panel) Vertically-integrated growth rate (\widehat{M}_j in day^{-1}). (Right panel) Eigenvector corresponding to the leading eigenvalue real part λ , normalized to have a maximum of 1.	92
3-4	Vertical profiles of (a) specific humidity (in g/kg), (b) temperature (in K), (c) HAM and (d) log 10 of the ozone volume concentration (in ppmv) in the SAM simulations ran by Tristan Abbott.	94

3-5	Betts-Miller linear convective matrix for $\tau_{\text{BM}} = 3\text{hours}$, where the HAM has been evaluated from the reference SAM RCE profile. (Bottom panel) Vertically-integrated growth rate (\widehat{M}_j in day^{-1}). (Right panel) Eigenvector corresponding to the leading eigenvalue real part λ , normalized to have a maximum of 1.	98
3-6	Entrainment and detrainment rate profiles (in hour^{-1}) and condensation rate profile (in month^{-1}) in RCE, as diagnosed from the reference SAM RCE temperature and moisture profiles.	102
3-7	The moist perturbation at level p_j is entrained in the cloudy updraft, where it detrains and releases latent heat through condensation at level $p_{i>j}$ above the perturbed level. The moist perturbation is also advected downwards to level p_{j-1} by the subsidence mass flux.	103
3-8	Bulk-plume linear convective matrix ($M_{\text{LH}} + M_{\text{DSE}}$) for $\widehat{Q}_{\text{BP}} = 150 \text{ W m}^{-2}$. (Bottom panel) Vertically-integrated growth rate (\widehat{M}_j in day^{-1}). (Right panel) Eigenvector corresponding to the leading eigenvalue real part λ , normalized to have a maximum of 1 (note that the leading eigenvalue here is negative, so it represents the slowest-decaying mode).	105
3-9	(a) Longwave linear response matrix (in month^{-1}) and vertically integrated longwave growth rate (in day^{-1}) plotted against perturbation level (in hPa). (b) Shortwave linear response and vertically integrated shortwave growth rate. The total optical thickness of the free troposphere is 6 in the longwave and 0.5 in the shortwave. It corresponds to a net free-tropospheric cooling of 215 W m^{-2} . The analytical matrices, with leading real eigenvalues λ , have both been tested against a numerical version of the two-stream Schwarzschild model.	111

3-10	(a) Longwave linear response matrix (in month ⁻¹) and vertically integrated longwave growth rate (in day ⁻¹) plotted against perturbation level (in hPa). (b) Shortwave linear response and vertically integrated shortwave growth rate. The HAM has been evaluated from the reference SAM RCE profile. The leading real eigenvalue λ of each matrix is indicated in the corresponding bottom panel.	113
3-11	(a) Leading eigenvalue real part (in day ⁻¹) as a function of the RCE surface temperature (in K). (b) Corresponding eigenvectors for the 300K reference case: Radiative response alone (RRTM), Betts-Miller response alone (BM, $\tau_{\text{BM}} = 3\text{hours}$), bulk-plume response alone (BP, $\widehat{Q}_{\text{BP}} = 150 \text{ W m}^{-2}$), and their sums (RRTM+BP) & (RRTM+BM). The lines for (BM) and (RRTM+BM) are indistinguishable. The eigenvectors have been normalized to have the same pressure-average. . .	115
3-12	(a) Convective moistening (M_{LH}) and (b) Convective heating (M_{DSE}) linear response matrices, in units day ⁻¹	123
3-13	(a) Free-tropospheric longwave cooling (red line) and shortwave heating (blue line) and total net radiative cooling (black line) in Wm^{-2} , versus surface optical thickness. The net radiative cooling in SAM is denoted with a dotted black line, and intersects the total radiative cooling of the gray model for two values of the surface optical thickness (denoted with green and orange vertical dotted lines). (b) Logarithm 10 of optical thickness profile in pressure space when the absorption coefficient is $\kappa = 0.022\text{m}^2.\text{kg}^{-1}$ (green line) and $\kappa = 0.17\text{m}^2.\text{kg}^{-1}$ (orange line). . .	130
3-14	Leading eigenvalue real part of the 300K linear response (in day ⁻¹) as a function of $\log_{10} \tau_{\text{BM}}$ (in hours, for the RRTM+BM and BM cases) and \widehat{Q}_{BP} (in W m^{-2} , for the RRTM+BP and BP cases). The scale for τ_{BM} and the scale for \widehat{Q}_{BP} are aligned so that the responses depicted on figure 3-5 (BM, $\tau_{\text{BM}} = 3\text{hours}$) and 3-7 (BP, $\widehat{Q}_{\text{BP}} = 150 \text{ W m}^{-2}$) fall on the same vertical line (central vertical gray line). The two other vertical gray lines indicate the range of realistic convective parameters.	131

- 4-1 Hovmöller diagram of the frozen moist static energy spatial anomaly H' (in MJ m⁻²) for the three MD experiments and the control LC300 CAM experiment. The vertical axis is time (in days) and the horizontal axis is x (in 1000km). The anomaly has been spatially-averaged in the y -direction. The distance between the left vertical axis and the thick, black line represents the one-dimensional time-varying convective aggregation length scale $L(t)$ (in 1000km, defined in equation 4.2). 145
- 4-2 Snapshots of the frozen moist static energy spatial anomaly H' , averaged in time over periods of five days (in MJ m⁻²) for the two SQ experiments and the BSQ experiment. For each snapshot of the doubly-periodic square domain, the horizontal axis is x (in 1000km) and the vertical axis is y (in 1000km). The radius of each black circle represents the two-dimensional time-varying convective aggregation length scale $L(t)$ (in 1000km, defined in equation 4.2). 146
- 4-3 We use the time-averaged data from the first 30 days of the LC300 simulation as an example.
- (Black line)** Time-averaged convective aggregation length scale L (in day⁻¹).
- (Blue line)** Length scale \mathcal{L}_{lw} of the longwave tendency $\dot{\varphi}_{\text{lw}}$.
- (1-Arrows)** Longwave radiation tries to “stretch” the convective aggregation length scale L to its preferred length scale \mathcal{L}_{lw} , because $\langle \dot{\varphi}_{\text{lw}} \rangle > 0$ and $\mathcal{L}_{\text{lw}} > L$.
- (2-Dots)** Normalized longwave spectral rates $\dot{\varphi}_{\text{lw}} / \langle \varphi \rangle$ (in day⁻¹) for each wavelength λ (in 1000 km). The spectral-average of the spectral rates equals the longwave aggregation rate $\langle \dot{\varphi}_{\text{lw}} \rangle / \langle \varphi \rangle$ (in day⁻¹).
- (3-expansion tendency)** The combination of the positive longwave aggregation rate $\langle \dot{\varphi}_{\text{lw}} \rangle / \langle \varphi \rangle > 0$ with the growth from L to $\mathcal{L}_{\text{lw}} > L$ leads to a positive longwave expansion tendency $\dot{L}_{\text{lw}} > 0$ 149

4-4	<p>Evolution of (a) the convective aggregation length scale L (in 1000 km, defined in equation 4.2) and (b) the spatial standard deviation of MSE (in MJ.m⁻²) during the 75 days of each experiment. The solid lines represent the experiments using the CAM radiation schemes, and are identified using the acronyms defined in table 4.1 and the value of the fixed surface temperature. The dotted lines represent the experiments using the RRTM radiation scheme. We indicate the time-averaged value in the mature phase using parentheses, and use a time-moving-average of 1 week before plotting each variable.</p>	152
4-5	<p>(a) Evolution of the expansion tendency \dot{L}_i (in ms⁻¹, on the right-hand side of equation 4.13) during the 75 days of experiment LC300 CAM. (b) Evolution of the aggregation rate $\langle \dot{\varphi}_i \rangle / \langle \varphi \rangle$ (in day⁻¹) in LC300 CAM. Lines in both subplots are smoothed using a time-moving-average of 1 week.</p>	153
4-6	<p>Representation of the twenty experiments in $(\dot{L}_i/L, \langle \dot{\varphi}_i \rangle / \langle \varphi \rangle)$ space. The aggregation and expansion rates have been time-averaged over the first month (Growth phase, depicted with dotted lines and empty circles) or later months (Mature phase, depicted with full lines and filled circles) of each experiment. Colors indicate different MSE fluxes: Longwave (blue), Shortwave (orange), Surface enthalpy flux (green) and advective flux (pink). All subplots use the same scale for both axis.</p>	156
4-7	<p>Representation of five characteristic experiments in $(\mathcal{L}_i, \langle \dot{\varphi}_i \rangle / \langle \varphi \rangle)$ space. The longwave and shortwave rates have been time-averaged over the growth phases ((a) and (c) respectively) and mature phases ((b) and (d) respectively) of each simulation. The arrows go from the time-averaged convective length scale L (represented with a circle) to the radiative length scale \mathcal{L}_i, and represent the length scale growth of each experiment (an arrow to the right corresponds to $\dot{L}_i > 0$). The color code is that of Figure 4-4.</p>	157

4-8 Decomposition of the surface flux aggregation rate (a), difference between diabatic length scale and MSE anomaly scale (b) and expansion tendency (c) for the LC300 CAM experiment. Panels (a) and (c) use a running time-average of 1 week while panel (b) shows length scale differences computed using 15 day time-averages. According to equation 4.15, the expansion rate (c) can be obtained by multiplying the aggregation rate (a) by the length scale difference (b). 160

4-9 Expansion rate (in 1/day) versus sea surface temperature for the long-channel experiments using the (a) CAM and (b) RRTM radiation schemes. The rates are time-averaged during the first month (Growth phase, empty circles) and later months (Mature phase, filled circles) of each simulation; we use error bars to indicate three standard deviations normalized by the sample size's square root. Each color corresponds to a MSE flux: Longwave (blue), Shortwave (orange), Surface enthalpy flux (green) and Advective flux (pink). 164

4-10 (Black line) $L(t)$, (Red line) $L_\varphi(t)$, (Blue line) $\sqrt{LK^{-1}}(t)$ and (Sky blue line) $K^{-1}(t)$ (in 1000 km) versus time (in days) for the reference LC300CAM simulation. 167

4-11 (a) Normalized power spectral tendencies (in day/m) of the longwave (blue), shortwave (orange), surface enthalpy (green) and advective (pink) fluxes of MSE during the growth (first month of simulation) and mature (last months of simulation) phases of the reference LC300CAM simulation. (b) Normalized spectral coherence (unitless) between MSE and cloud water concentration: Total cloud water (gray), liquid (orange) and ice (blue) water. (c) Normalized power spectral tendencies (in day/m) of the total surface enthalpy flux (green), enthalpy disequilibrium component (blue), surface wind speed component (orange) and eddy term (pink). The total normalization factor used in all three panels is equal to $\left(\lambda \langle \varphi \rangle \int_{k_0}^{k_N} dk\right)^{-1}$. All spectra are octave-averaged (dots) and plotted versus wavelength (in m) on a logarithmic scale. The diabatic length scale \mathcal{L}_i (in m) corresponding to each flux is indicated with a dotted vertical line (growth phase) and a full line (mature phase). For reference, the convective aggregation length scale L (in m) is depicted with a dotted black line (growth phase) and a full black line (mature phase). 176

5-1 Time-mean PW (a) and moist static energy fluxes (c,e), time-mean transient variance of PW (b) and twice the time-mean covariance between transient PW and transient surface enthalpy fluxes (d,f) versus longitude for ERA, CERES and GFDL for the five years 2010-2014. 188

5-2	(a) Probability density function of transient PW and (b-c) Expected value of diurnally-averaged transient diabatic fluxes conditioned on PW for all datasets. For ERA, we indicate the inter-quartile range of the fluxes conditioned on PW with vertical green lines. The right panels show the anomalous fluxes conditioned on anomalous PW after applying a rectangular window-filter to only keep the zonal variability at scales below one thousand kilometers, with black double-arrows indicating the inter-quartile range of filtered transient PW anomalies for different datasets.	191
5-3	(a) PW transient power spectrum versus wavelengths for all datasets. For LC and NG, we additionally plot mechanism denial experiments with uniform radiation using dashed lines, and with uniform surface fluxes using dotted lines, respectively. (b-d) Moist static energy flux spectral cross-spectral densities, multiplied by 2.	193
5-4	Time-mean PW (a) and diabatic fluxes (c,e), time-mean transient variance of PW (b) and twice the time-mean covariance between transient PW and transient surface diabatic fluxes (d,f) versus longitude for ERA, CERES and DYAMOND for the time period: Aug 8th 2016 - Sep 10th 2016.	197
5-5	(a) Probability density function of PW, with black double-arrows indicating the inter-quartile range of PW over specific regions and (b-c) Expected value of diurnally-averaged diabatic fluxes conditioned on PW for all datasets. For ERA, we indicate the inter-quartile range of the fluxes conditioned on PW with vertical green lines. The right panels show the anomalous fluxes conditioned on anomalous PW after applying a rectangular window-filter to only keep the zonal variability at scales below one thousand kilometers, with black double-arrows indicating the inter-quartile range of filtered PW anomalies for different datasets.	198

A-1	Hovmoller plots of anomalous moist static energy. The anomaly was taken from the spatial mean moist static energy at each time step, and normalized by the latent heat of vaporization to yield units of kg m^{-2} . The average column water vapor during the last week of each simulation is indicated in the subplot's titles using square brackets.	210
A-2	Normalized variance input from each term of equation A.1 over the 75 days of each simulation. The total variance tendency is obtained by integrating each curve over the logarithmic wavelength scale.	212
B-1	(a) Specific humidity (in g/kg), (b) HAM (c) temperature (in K) and (d) flux convergence (in $\text{W.m}^{-2}.\text{hPa}^{-1}$) profiles. In panel (d), the longwave radiative heating is red, the shortwave radiative heating blue, the convective heating orange, and the total convergence flux is represented with a dotted black line. The profiles are ensemble averages of the 10-members chosen to represent radiative-convective equilibrium. The surface temperature is fixed to 300K and cloud-radiation interactions are deactivated.	219
B-2	(Top) Convective component of the linear response matrix ($M_{\text{LH}} + M_{\text{DSE}}$), in units month^{-1} . (Bottom) Vertically-integrated growth rates (in units day^{-1}) versus perturbation level (in hPa).	220
B-3	(a) Convective moistening (M_{LH}) and (b) Convective heating (M_{DSE}) linear response matrices, in units month^{-1}	220
B-4	(Top) Radiative component of the linear response matrix ($M_{\text{LW}} + M_{\text{SW}}$), in units month^{-1} . (Bottom) Column-integrated growth rates (in units day^{-1}) versus perturbation level (in hPa). Letters indicate effects that are described in the text.	223
B-5	(a) Longwave (M_{LW}) and (b) Shortwave (M_{SW}) linear response functions, in units month^{-1}	223

B-6	(Top) Full linear response matrix (M), in units month^{-1} . (Bottom) Column-integrated growth rates (in units day^{-1}) versus perturbation level (in hPa).	225
B-7	Growth rate of a uniform water vapor perturbation (in day^{-1}) versus sea surface temperature (in K) for +1% (blue) and -1% (red) perturbations. The total growth rate (square) is decomposed into its radiative (star) and convective (triangle) components.	226

List of Tables

2.1	Locations of the stations used in sounding analysis. Number of soundings used for each season indicated in the rightmost columns.	64
4.1	Characteristics of the twenty cloud-permitting experiments used in this chapter. From top to bottom: Acronym given to the series of simulations (LC: Long-channel domain, MD: Mechanism-denial experiments, SQ: Square domain, BSQ: Big square domain), number of simulations in each series, fixed surface temperature T_s , domain size and radiation scheme.	144
4.2	Guide for interpreting equation 4.15 which relates the expansion tendencies \dot{L}_i to the aggregation rates $\langle \dot{\varphi}_i \rangle / \langle \dot{\varphi} \rangle$ and the diabatic scales \mathcal{L}_i	148
4.3	Guide for interpreting equation 4.29, which relates the integral scale tendencies $(K^{-1})_i$ to the aggregation tendencies $\langle \dot{\varphi}_i \rangle / \langle \dot{\varphi} \rangle$ and the diabatic integral scales \mathcal{K}_i^{-1}	169

4.4	For each experiment (Exp), variables (Var) from top to bottom are: Time-averaged convective aggregation scale L (in 1000 km) during the growth phase (subscript G) and the mature phase (subscript M), time-averaged aggregation rate during the growth phase $(\langle \dot{\varphi}_i \rangle / \langle \varphi \rangle)_G$ (in day^{-1}), time-averaged aggregation rate during the mature phase $(\langle \dot{\varphi}_i \rangle / \langle \varphi \rangle)_M$ (in day^{-1}), 10 times the time-averaged expansion rate during the growth phase $(\dot{L}_i/L)_G$ (in day^{-1}), 10 times the time-averaged expansion rate during the mature phase $(\dot{L}_i/L)_M$ (in day^{-1}), time-averaged diabatic length scale during the growth phase $(\mathcal{L}_i)_G$ (in 1000 km), and time-averaged diabatic length scale during the mature phase $(\mathcal{L}_i)_M$ (in 1000 km). i represents a generic flux in the legend; in practice, fluxes are listed in the following order: Longwave Shortwave Surface enthalpy flux Advection flux.	174
5.1	Dataset acronym, type, time period, model zonal resolution and temporal resolution of the data used in this study.	183
A.1	List of long-channel experiments available on the MIT Engaging cluster. From left to right: Category, number, characteristics of experiments and useful references when applicable.	208
B.1	Parameters used in the MIT single-column model	218

Chapter 1

Introduction

“Double is my account: for at one time it grew to be one alone from many, at another in turn it grew apart to be many from one, fire and water and earth and the immense height of air and destructive strife apart from them, equally balanced in all ways”

Empedocles, Frag. B17 (Simplicius, *Physics*, 157–159)

1.1 Background and motivation

1.1.1 Water vapor, radiation and convection in the troposphere

The interaction between atmospheric water, heating and winds lies at the heart of Earth’s climate (e.g. Trepanier [2000], Stevens and Bony [2013]). The mere presence of water in the atmosphere approximately doubles the equator-to-pole energy transport for given winds (e.g. Pierrehumbert [2002]) and not resolving the spatial distribution of atmospheric water can lead to errors as large as 25% in the local outgoing radiation from Earth to space (e.g. Pierrehumbert et al. [2007]). About 99.5% of atmospheric water is in the form of water vapor (e.g. Schneider et al. [2010], Trenberth and Smith [2005]), a multi-faceted gas with four notable characteristics that we highlight in Figure 1-1.

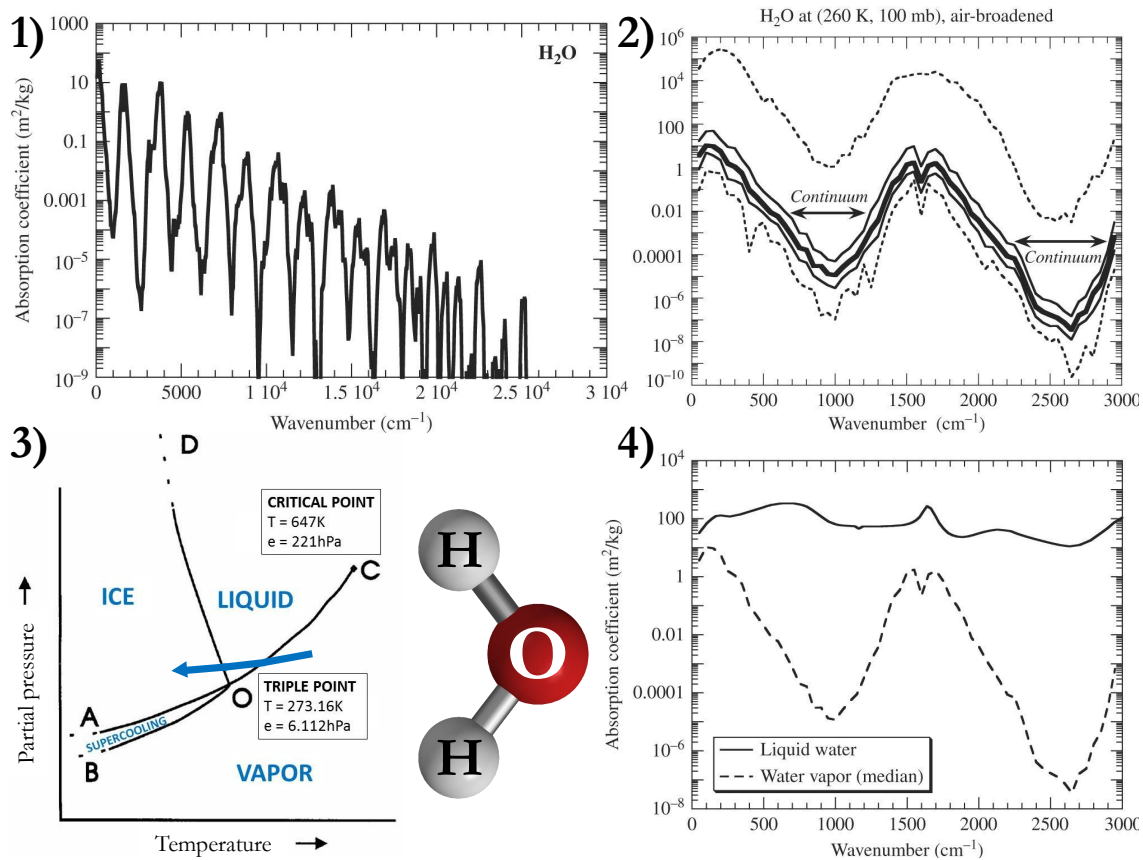


Figure 1-1: Molecular structure of water (from Hardinger [2018]). 1) Median absorption coefficient of water vapor in the shortwave domain (using intervals of 50cm^{-1} , Figure 5.13 from Pierrehumbert [2009]). 2) Median absorption coefficient of water vapor in the longwave domain (full black line, Figure 4.19 from Pierrehumbert [2009]). 3) Schematic phase diagram of water substance (adapted from Emanuel [1994]). 4) Median absorption coefficient of liquid water (full line, Figure 4.28 of Pierrehumbert [2009]). The electromagnetic wavenumber (in units cm^{-1}) is defined as the inverse wavelength.

1) **Water vapor is the main absorber of solar radiation in the troposphere¹.** Water vapor has strong absorption features in the near-infrared and visible radiation frequencies, depicted in Figure 1-1.1) for standard atmospheric conditions

¹The troposphere is the lowest layer of Earth’s atmosphere, where most of the “weather” occurs. It typically extends upward to about 8-20 km, with the highest extent near the Equator and the lowest extent at the Poles.

(260K,100hPa). As the sun emits radiation between 4.10^3cm^{-1} and 4.10^4cm^{-1} , water vapor efficiently absorbs radiation in the $(10^4 - 4.10^4)\text{cm}^{-1}$ wavenumber range, especially in the lower troposphere where its partial pressure is high.

2) Water vapor is the most abundant greenhouse gas in the atmosphere.

The asymmetry of the water molecule creates a dipole moment from the Oxygen to the Hydrogen atoms, which generates a large absorption band at $1.6.10^3\text{cm}^{-1}$ associated with the bending of the H_2O molecule, as well as two other rotational-vibrational features at 10^2cm^{-1} and $3.7.10^3\text{cm}^{-1}$. Between rotational-vibrational absorption features, the collision of water molecules leads to absorption continua that become prominent at large temperatures. As the Earth's surface emits most radiation between 150cm^{-1} and 1500cm^{-1} at its typical temperature of $280 - 300\text{K}$, the absorption features of the large water vapor mass can "trap" a large portion of this radiation below it, making water vapor the primary greenhouse gas in the atmosphere.

3) Water vapor is tightly related to atmospheric convection. In the atmosphere, convection usually refers to small-scale (less than 10km) thermally-direct (from hot to cold) circulations resulting from the action of gravity upon an unstable distribution of mass (lighter air parcels below heavier air parcels, e.g. Emanuel 1994). Convective currents lift moist air parcels upwards from the surface, expanding and cooling them. The typical trajectory of water as it cools and expands is represented with a blue arrow in the phase diagram of water (Figure 1-1.3), and results in the condensation of water vapor into liquid and solid water (i.e. clouds). The energy that water loses by transitioning from the vapor to the liquid phase is released into the surrounding atmosphere and warms it, referred to as "latent heating". Latent heating can reduce the vertical gradients of temperature by a factor that can be as large as two in the tropical atmosphere, because of the unusually large latent heat of vaporization of water. In contrast, precipitating liquid and ice water can re-evaporate into relatively dry layers of the atmosphere, thereby cooling the environment and regulating the amount of atmospheric convection.

4) Water vapor condenses to form clouds, which have strong radiative effects. As can be seen in Figure 1-1.4), water in the liquid phase is a far better absorber than water vapor per unit mass. To a good approximation, liquid and solid water are gray (i.e. their absorption features do not depend on the electromagnetic frequency) with an effective absorption coefficient as high as $100\text{m}^2 \text{kg}^{-1}$! Therefore, clouds have a powerful greenhouse effect as longer electromagnetic waves are preferentially absorbed, and clouds are the dominant reflector of sunlight, as shorter electromagnetic waves are preferentially scattered by cloud particles (e.g. droplets, snowflakes, graupel, hail).

These four characteristics of water vapor make it an active tracer (e.g. Schneider et al. [2010]): changes of its concentration in space and time modify atmospheric heating through radiation and convection, which in turn affects the atmospheric circulation. The active role of water vapor is most visible in the Tropics: First, as the warmest region of Earth, the Tropics hold 64% of Earth's atmospheric water vapor (defined as the region between 30°S and 30°N , calculated from ERA5 analysis with hourly data between 2000 and 2018, Hennermann and Guillory [2018]). Second, because the vertical component of Earth's rotation vector is small in the Tropics, the Coriolis force cannot sustain large-scale pressure gradients like it does in the mid-latitudes (e.g. Hoskins and James [2014]). Hence, large-scale temperature gradients cannot be sustained in the tropical atmosphere, so that anomalous atmospheric heating is balanced by large-scale vertical motion (e.g. Sobel and Bretherton [2000]): Anomalous warming causes large-scale ascent, while anomalous cooling causes large-scale descent. Therefore, changes in tropical water vapor cause anomalous radiative and convective heating, which is balanced by large-scale vertical motion. Large-scale vertical motion may affect evaporation or precipitation, and thus feed back on water vapor.

The potential of water vapor anomalies to reinforce themselves through their dynamical effect is the starting idea of this thesis: *Water vapor variability may result*

from internal instabilities of the tropical atmosphere, arising from the interaction between water, radiation and convection in the Tropics. The total variability of water vapor near the Equator remains poorly understood despite its importance for tropical weather (e.g. LeMone et al. [1998]) and the planetary climate (e.g. Trenberth et al. [2002]): If a large portion of this variability were internal, it could facilitate the modeling of disturbances in the Tropics (e.g. tropical precipitation events), and change our understanding of long-term variations in the Earth’s energy balance.

1.1.2 Spatiotemporal variability of water vapor

The variability of water vapor in space and time, referred to as spatiotemporal variability, can be observed using various techniques (e.g. Sherwood et al. [2010]):

- Meteorological stations observe water vapor at the ground using wet-bulb thermometers and profile water vapor in the troposphere with radiosondes, usually launched twice a day using weather balloons.
- Satellites deploy various instruments that can measure water vapor: High-resolution infrared sounders with multiple channels measure the upper-tropospheric water vapor to the extent that it can be distinguished from clouds (e.g. Divakarla et al. [2006]), microwave sounders are less affected by clouds and observe column water vapor at low-opacity wavenumbers (e.g. Bauer and Schuessel [1993], Fu et al. [1994]) or upper-tropospheric water vapor using several microwave absorption features (e.g. Waters et al. [2006], Grody et al. [2001]), and the global positioning system observe column water vapor at high temporal resolution above well-equipped surfaces, to the extent that the temperature is known (e.g. Bevis et al. [1992], Wang and Zhang [2008]).
- Research and commercial aircraft routinely measure water vapor in the troposphere and lower stratosphere with hygrometers and scattering instruments (e.g. Marengo et al. [1998], Daniels et al. [2002]), providing an alternative to weather balloons, e.g. over oceans where they are harder to launch.

- Finally, active sensing devices such as the water vapor Raman Laser Detection and Ranging (LIDAR, e.g. Whiteman et al. [1992]) observe water vapor to good accuracy in the lower to mid-troposphere if deployed on ground, with the caveat that they are neither standardized nor commercialized in 2018.

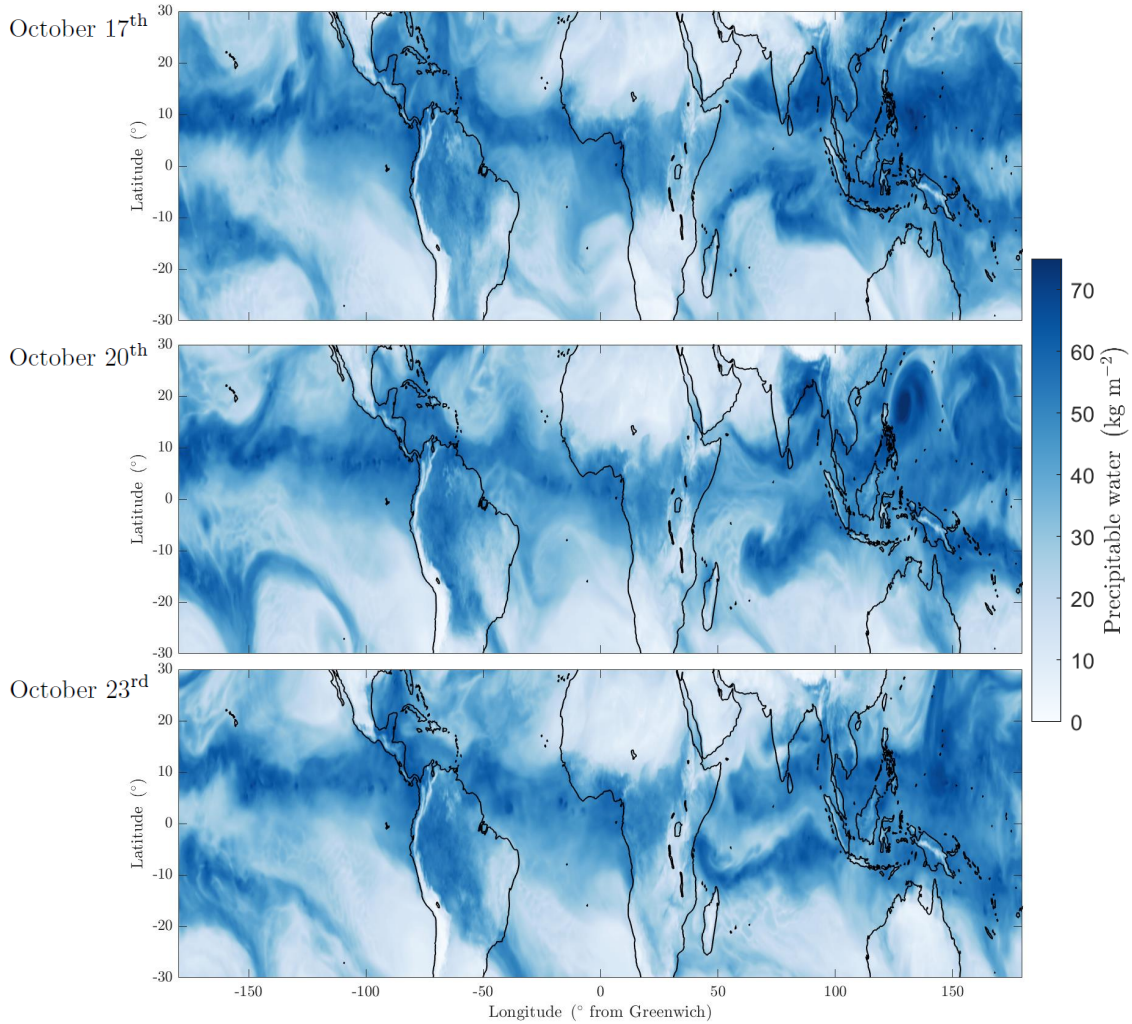


Figure 1-2: Observations of precipitable water on October 17th, October 20th and October 23rd 2017 at 00GMT (ERA5 reanalysis).

A blend of these observations can be assimilated into operational meteorological models (e.g. Dee et al. [2011]) to reconstruct the historical variability of water vapor. In Figure 1-2, we use the latest reanalysis of the European Centre for Medium-Range Weather Forecasts, ERA5 (Hennermann and Guillory [2018]), to visualize the vari-

ability of column water vapor ² in the Tropics during the week of October 17th to October 23rd, 2017.

Figure 1-2 shows patterns of water vapor variability at different scales, which are integral components of “Tropical weather”: In the Western Pacific, typhoon Lan intensifies from a tropical storm on October 17th to a tropical cyclone (TC) on October 20th as it moves northwards. Simultaneously, the Madden-Julian Oscillation (MJO), defined as the main mode of intra-seasonal variability in the Tropics (e.g. reviews by Madden and Julian [1994], Zhang [2005]), is in its active phase. During that week, it propagates eastward from the Maritime Continent to the Western Pacific, according to the RMM1 and RMM2 indices used for operational monitoring (e.g. Wheeler and Hendon [2004]).

To forecast extreme precipitation events associated with intra-seasonal disturbances such as TCs or the MJO, meteorological models are typically run every six hours to simulate the weather with a forward horizon of two weeks (purple box in Figure 1-3). Because weather forecast centers need to run large ensembles of simulations to characterize the chaotic weather system (e.g. Molteni et al. [1996]), computational resources in 2018 limit the typical horizontal resolution of global weather simulations to a few dozen kilometers, although high-resolution forecasts with meshes as fine as 2.8km are appearing (e.g. Giorgetta et al. [2018], Crueger et al. [2018]). For long-term societal planning (e.g. Masson-Delmotte et al. [2018]), global climate models need to be run on time periods as long as several centuries (orange box in Figure 1-3) to simulate the effect of long-term forcings, such as the anthropogenic emission of greenhouse gases, on the climate system. In that case, it would be prohibitive to run simulations at the cloud-scale and convective processes are represented using empirically-derived models, referred to as parametrizations and limited by the human interpretation of physical processes and observations. As a consequence, global climate models cannot faithfully represent the patterns of water vapor variability (black boxes in Figure 1-3), motivating the use of high-resolution full-physics models to bolster our under-

²The mass of water vapor in an atmospheric column, in units kg m^{-2} , interchangeably referred to as precipitable water.

standing of atmospheric physics. We use numerical models that explicitly represent non-hydrostatic atmospheric flows and the evolution of different water species (e.g. vapor, liquid, snow, graupel, etc.) below the 10km scale of individual convective systems. These models are commonly referred to as cloud-permitting models (CPM, light blue box in Figure 1-3) because they permit (although do not resolve) individual cloud elements (e.g. Randall et al. [2003], Bryan et al. [2002]).

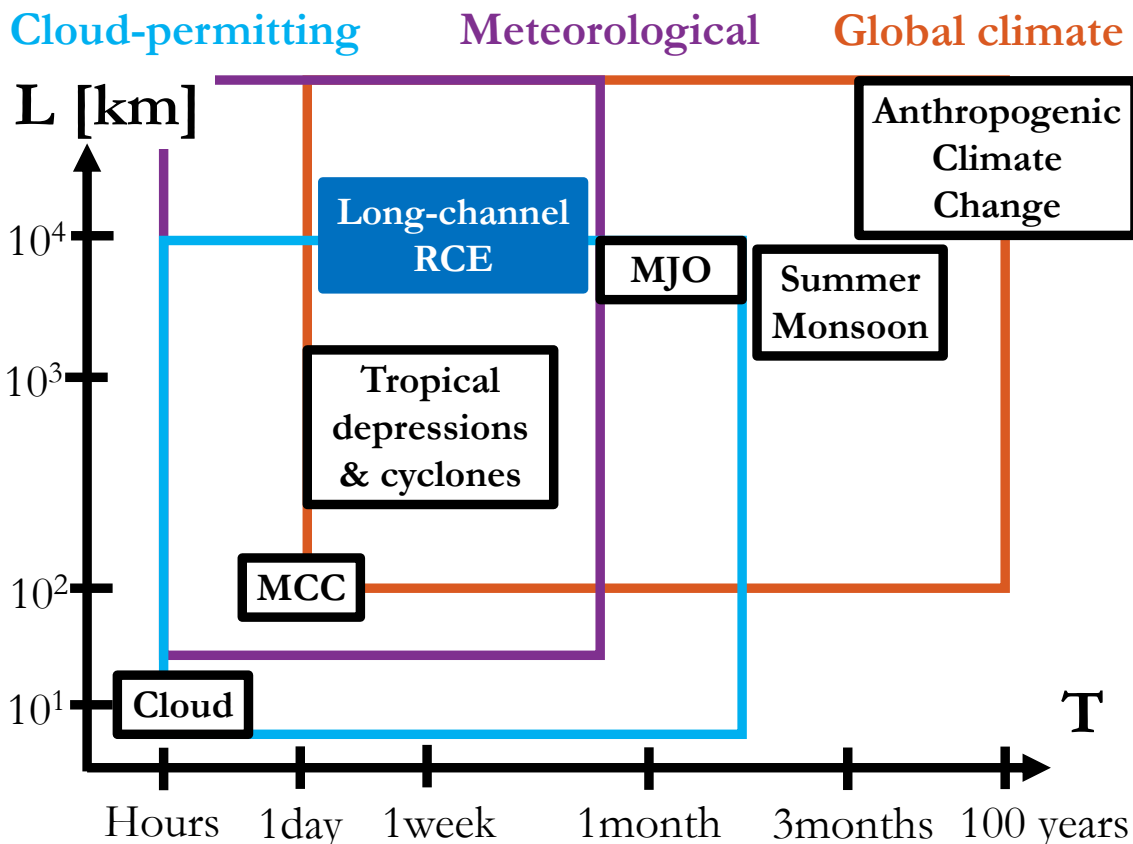


Figure 1-3: Temporal (horizontal axis) and spatial (vertical axis) scales of tropical water vapor variability; black boxes indicate the scales of: clouds, mesoscale convective complexes (MCC), local radiative-convective equilibrium (RCE), tropical depressions (TD), tropical cyclones (TC), and the Madden-Julian Oscillation (MJO). We indicate the typical scales covered by atmospheric models: CPM (light blue box), operational meteorological models (purple box) and global climate models (orange box). The long-channel RCE framework (blue box) is at the intersection of these scales.

Cloud-permitting models are a central tool of this thesis, as they *connect the spatiotemporal variability of water vapor to the explicitly-simulated physics of atmospheric convection*. To explain the internal variability of water vapor, we need to simulate an unforced base state of the tropical atmosphere: Radiative-Convective Equilibrium (RCE).

1.1.3 Moist radiative-convective instability

RCE is arguably the simplest paradigm for the tropical atmosphere, in which convective heating balances radiative cooling without horizontal transport of water vapor or energy (e.g. Ramanathan and Coakley [1978]). RCE is uniquely defined at the cloud-scale (10 km) if greenhouse gases (including water vapor), clouds, insolation and surface temperatures are held fixed (e.g. Emanuel [1994]). However, as long as water is allowed to be a variable, a large-scale circulation spontaneously develops when using CPM to simulate RCE on horizontal domains larger than a few hundred kilometers, even if homogeneous boundary conditions and forcings are applied. This large-scale circulation amplifies water vapor anomalies to form a dry subsiding region and a moist ascending region, where deep convection aggregates. This moist instability of RCE, referred to as “convective self-aggregation” (e.g. reviews by Wing et al. [2017], Holloway et al. [2017]), has been widely documented in the context of two-dimensional (e.g. Held et al. [1993], Grabowski and Moncrieff [2001]) and three-dimensional (e.g. Bretherton et al. [2005], Jeevanjee and Romps [2013], Wing and Emanuel [2014]) CPM, as well as in global climate models with explicit convection (e.g. Satoh et al. [2016]). If the horizontal domain is too small (e.g. less than 4000km long with a fixed surface temperature of 300K), convection aggregates in a single moist “blob”, whose size depends on the domain’s characteristics (e.g. Muller and Held [2012]), giving self-aggregation the appearance of a numerical artifact. However, simulating RCE in CPM on large horizontal domains shows the emergence of multiple moist and dry regions of finite size (e.g. Khairoutdinov and Emanuel [2018], Wing and Cronin [2016]). Accordingly, the long-channel RCE configuration used throughout this thesis (small blue box in Figure 1-3) simultaneously contains dry regions, where convection

is shallow and the average radiative cooling is high, and moist regions, with active deep convection and lower radiative cooling (see Figure 1-4).

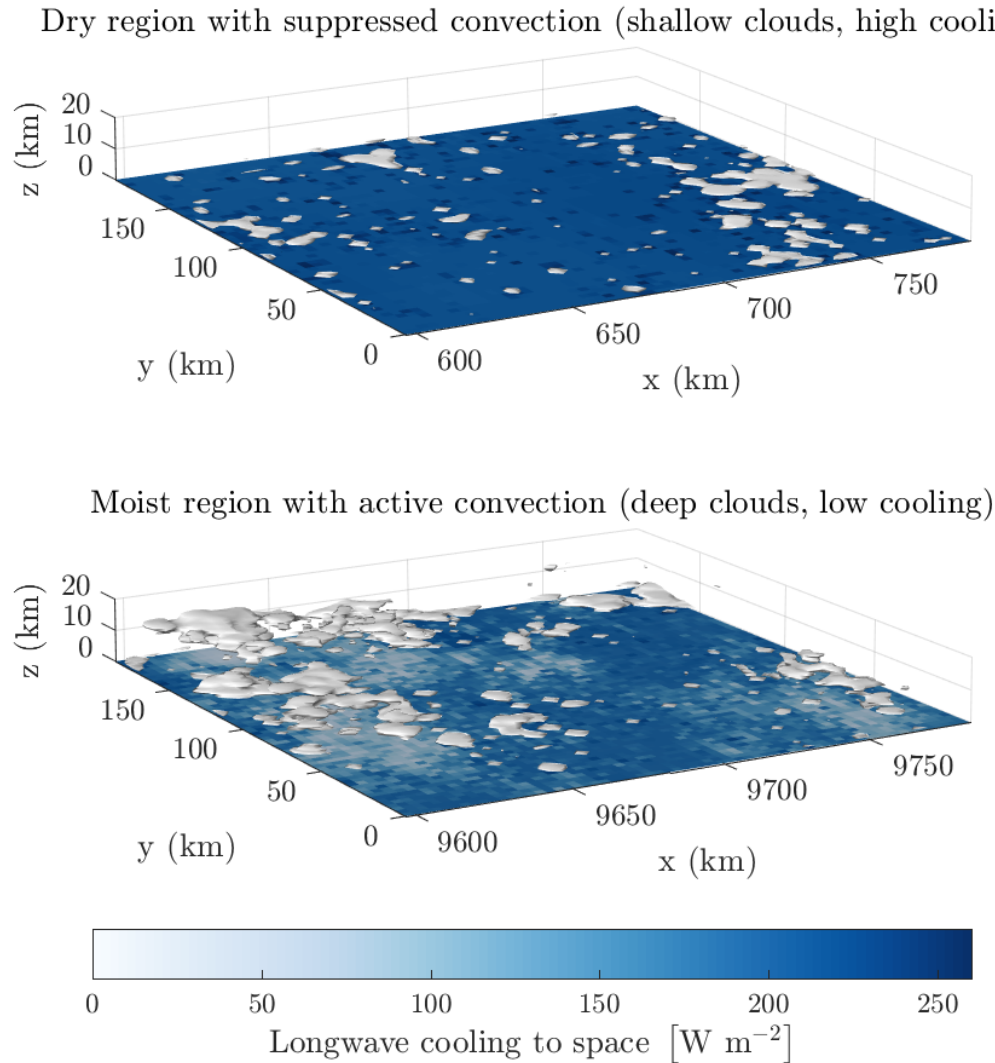


Figure 1-4: Simultaneous snapshots of two different regions of the same long-channel simulation at fixed sea surface temperature (LCCAM300 in Chapter 4). Despite homogeneous boundary conditions, a dry anomaly has formed and deep convection is suppressed in the region located at $x \in [600, 780]$ km, resulting in high values of the net atmospheric longwave cooling to space. In contrast, a moist anomaly has formed and deep convection is active in the region located at $x \in [9600, 9780]$ km, resulting in lower values of longwave cooling to space.

Because the water vapor profile, radiative cooling and large-scale vertical motion in this configuration compare well with observations (e.g. Wing et al. [2017], Cronin and Wing [2017]), we see high-resolution CPM as a bridge between fundamental atmospheric physics and the hydrological cycle of the observed tropical atmosphere. In that spirit, the present work aims at *leveraging the physical mechanisms of radiative-convective instability to connect convective self-aggregation with the observed spatiotemporal variability of water vapor*. To achieve this goal, we formulate intermediate, directed questions:

- (Chapter 2) What is the simplest theory that can explain the moist instability of RCE using variables that can be observed in the real atmosphere?
- (Chapter 3) What physical mechanisms govern the interactions between water vapor, convection and radiation, and how do these interactions affect the evolution of a water vapor perturbation?
- (Chapter 4) How do radiation, surface enthalpy fluxes and advection contribute to the emergence and evolution of a dominant length scale for convective self-aggregation?
- (Chapter 5) How can we quantify convective-aggregation mechanisms across scales in the real atmosphere?

1.2 Outline

We address these questions with a wide variety of methods and datasets:

- Observations, including local meteorological soundings (Chapter 2), satellite observations and meteorological reanalysis (Chapter 5),
- Time-evolving high-resolution three-dimensional models of the atmosphere, including square CPM (Chapters 3 and 4), elongated-domain CPM (Chapters 4, 5 and Appendix A), global climate CPM and general circulation models (Chapter 5).

- Column models of the atmosphere, including operational radiative transfer models (Chapters 2 and 3) and a full-physics column model (Appendix B).
- Theoretical models, including analytical models of radiative transfer (Chapters 2 and 3), convection (Chapter 3) and scale-dependent enthalpy fluxes (Chapter 4).

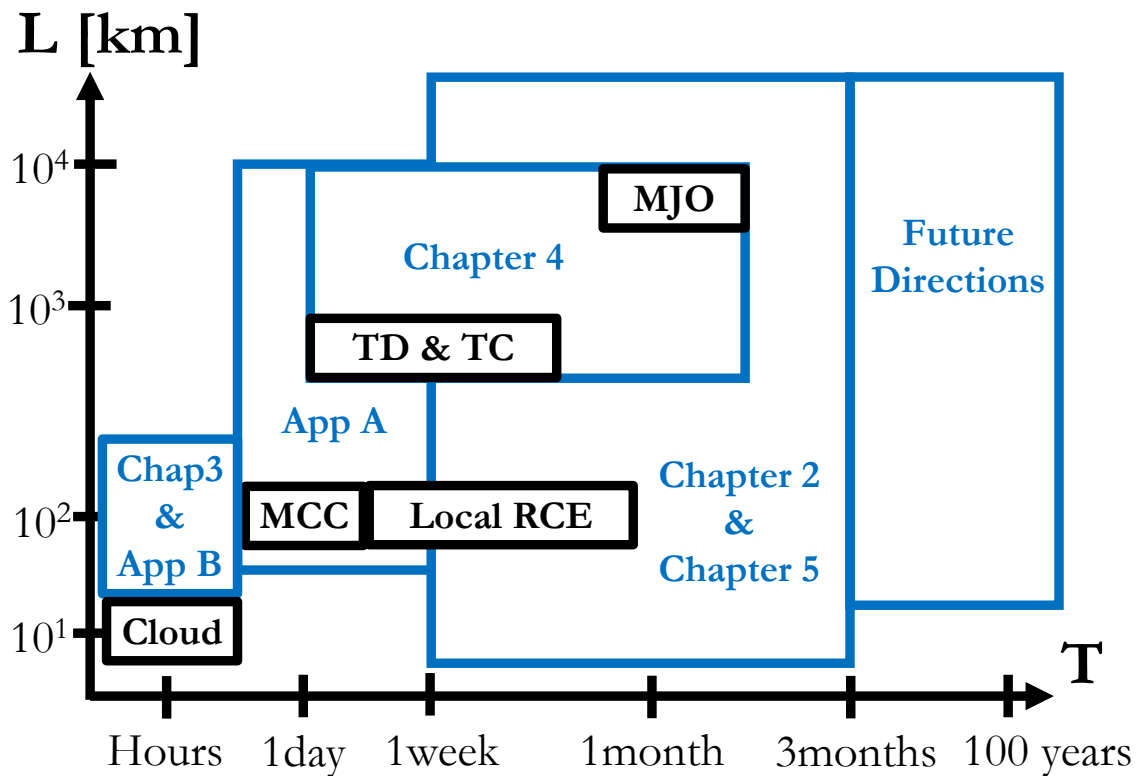


Figure 1-5: Temporal (horizontal axis) and spatial (vertical axis) scales of tropical water vapor variability addressed in each chapter and appendix of the thesis (blue boxes). Black boxes indicate the scales of: clouds, mesoscale convective complexes (MCC), tropical depressions (TD), tropical cyclones (TC), and the Madden-Julian Oscillation (MJO).

Each chapter covers different spatiotemporal scales of tropical water vapor variability, depicted in Figure 1-5. The thesis progresses from the instability of RCE, the most

fundamental state of the tropical atmosphere, to the physical mechanisms of water vapor variability in realistic datasets of the tropical atmosphere.

Chapter 2 proposes a simple theory that explains when instability of RCE may occur: If the total atmospheric radiative cooling decreases with column water vapor, then RCE may be unstable to the growth of moist or dry perturbations, referred to as moisture-radiative cooling instability (MRCI). We build physical understanding by starting with the clear-sky longwave cooling of a gray atmosphere and progressively adding clear-sky shortwave heating, cloud-radiation interactions, before relaxing the gray approximation using an operational radiative transfer model (RRTMG Iacono et al. [2000]). We find that MRCI is satisfied when column water vapor exceeds a critical threshold, with a linear growth rate proportional to the sensitivity of radiative cooling to column water vapor. Observational soundings of the tropical atmosphere confirm that clear-sky MRCI is satisfied across a wide range of regions and seasons, with approximate growth rates of 1 month^{-1} . Both the threshold and linear growth rate of MRCI are very sensitive to the vertical structure of water vapor, which is modulated by atmospheric convection on time scales as short as 1 hour!

The sensitivity of MRCI to the vertical structure of water vapor motivates Chapter 3, which analyzes the stability of RCE to level-by-level perturbations of water vapor. We pose radiative-convective instability (RCI) as a rigorous linear stability problem for the water vapor profile by combining a linear response framework (e.g. Kuang [2010, 2018]) with the weak temperature gradient approximation (e.g. Sobel and Bretherton [2000], Sobel et al. [2001]), which introduces a key parameter: the heating-to-advection-of-moisture conversion rate (HAM). We separate the linear response of RCE to water vapor perturbations into a convective response and a clear-sky radiative response. Combining these responses, we calculate the structure of the most unstable water vapor perturbation and its corresponding growth rate. Despite consistent radiative feedbacks, the characteristics of moist convection dominate this structure: For Betts-Miller convection (e.g. Betts and Miller [1993]), warmer atmospheres with higher HAM exhibit more instability. In contrast, bulk-plume convection (e.g. Yanai et al. [1973], Romps [2014]) is stable across temperatures, but becomes

unstable once combined with radiation, with approximate growth rates of 10 days. Because the system behavior after the initial instability is implicit in a column framework, the linear response framework does not inform us on the horizontal scale of moist and dry regions that appear as a result of RCI.

To address this question, Chapter 4 uses twenty large-domain simulations of RCE, and introduces a diagnostic framework to relate the evolution of the size of moist and dry regions to radiative heating, surface enthalpy fluxes, and horizontal energy transport. We find that both longwave and shortwave fluxes contribute to convective aggregation, but that the net longwave flux operates at large scales (1000-5000 km) and stretches the size of moist and dry regions, while the net shortwave flux operates at smaller scales (500-2000 km) and shrinks it. The surface flux effect on the scale of convective aggregation is dominated by convective gustiness, which acts to aggregate convective activity at smaller scales (500-3000 km). We suggest that these physical mechanisms may apply to the observed convective activity near the Equator: While inhomogeneous boundary forcing, large-scale shear and interaction with the land and ocean surfaces may contribute to the constantly-evolving size of moist and dry regions in the real Tropics, our scale-resolving diagnostic framework is general enough to apply to more realistic datasets of the atmosphere.

Therefore, Chapter 5 generalizes the framework of Chapter 4 to relate the transient zonal variability of precipitable water to convective-aggregation mechanisms in realistic models and observations of the tropical atmosphere. We find that the interaction between radiative cooling and water vapor can reinforce planetary-scale transients of water vapor near the Equator. Surface enthalpy fluxes weaken precipitable water structures across scales in realistic datasets of the atmosphere, similarly to idealized simulations that exhibit aggregated convection. Our preliminary results confirm the relevance of RCI to real-world convective organization, while providing a framework to understand thermodynamic discrepancies between high-resolution observations and models.

We summarize the key results of the four research chapters in Chapter 6 and propose directions for future research. Appendix A uses the long-channel framework of

Chapter 4 to test the effect of cloud radiation and the microphysical parametrization on the organization of non-rotating convection. Appendix B applies the linear response framework of Chapter 3 to a full-physics column model (e.g. Renno et al. [1994], Emanuel and Zivkovic-Rothman [1999]) which includes unsaturated downdrafts in its convective scheme, a physical mechanisms largely overlooked in Chapter 3.

Chapters 2 to 5 are in varying stages of publication or preparation for publication in peer-reviewed journals. Chapters 2 and 3 are published in the journal *Journal of Advances in Modeling Earth Systems*³. Revisions to chapter 4 are in review at *Quarterly Journal of the Royal Meteorological Society* and Chapter 5 is work in progress. The material presented in Appendix A could be included in future publications, while the material presented in Appendix B will most likely not be published.

³Material in these Chapters are edited versions of:

Chapter 2: Beucler, Tom, and Timothy W. Cronin. "Moisture-radiative cooling instability." *Journal of Advances in Modeling Earth Systems* 8.4 (2016): 1620-1640.

Chapter 3: Beucler, Tom, Timothy Cronin, and Kerry Emanuel. "A Linear Response Framework for Radiative-Convective Instability." *Journal of Advances in Modeling Earth Systems* 10.8 (2018): 1924-1951.

(C)2016,2018. American Geophysical Union. All Rights Reserved.

Chapter 2

Moisture-Radiative Cooling Instability

Abstract

Radiative-convective equilibrium (RCE) – the statistical equilibrium state of the atmosphere where convection and radiation interact in the absence of lateral transport – is widely used as a basic-state model of the tropical atmosphere. The possibility that RCE may be unstable to development of large-scale circulation has been raised by recent modeling, theoretical, and observational studies, and could have profound consequences for our understanding of tropical meteorology and climate. Here, we study the interaction between moisture and radiative cooling as a contributor to instability of RCE. We focus on whether the total atmospheric radiative cooling decreases with column water vapor; this condition, which we call moisture-radiative cooling instability (MRCI), provides the potential for unstable growth of moist or dry perturbations. Analytic solutions to the gray-gas radiative transfer equations show that MRCI is satisfied when the total column optical depth – linked to column water vapor – exceeds a critical threshold. Both the threshold and the growth rate of the instability depend strongly on the shape of the water vapor perturbation. Calculations with a realistic radiative transfer model confirm the existence of MRCI for typical tropical values of column water vapor, but show even stronger dependence on the vertical structure of water vapor perturbation. Finally, we analyze the sensitivity of atmospheric radiative cooling to variability in column water vapor in observed tropical soundings. We find that clear-sky MRCI is satisfied across a range of locations and seasons in the real tropical atmosphere, with a partial growth rate of $\sim 1 \text{ month}^{-1}$.

2.1 Introduction

Spatial and temporal variability of water vapor in the tropical atmosphere play a large role in Earth's energy balance – due not only to the direct effects of water vapor as a greenhouse gas, but also to the role of humidity in modulating clouds. This variability is usually understood as a result from heterogeneous external forcing – including spatial variability in incident sunlight, sea surface temperature and ocean heat uptake, the distribution of land, and transport of air from higher latitudes. However, moisture variability may also result from internal instabilities of the tropical atmosphere to moist or dry perturbations, which can grow from a homogeneous basic state. If internal instability leads to much of the variability of humidity in the tropics, it could have significant consequences for our understanding of intraseasonal disturbances in the tropical atmosphere (e.g., the Madden-Julian oscillations and tropical cyclones), as well as longer-term variations in Earth's energy balance (e.g., climate change). This chapter is centered on the idea that radiative-convective equilibrium (RCE), a classical basic state for the tropical atmosphere, may allow for unstable interaction between water vapor and radiative cooling. If unchecked by other influences, these interactions lead to the growth of dry and moist perturbations.

The starting point for this idea is the existence of a basic state for the tropical atmosphere: radiative-convective equilibrium (RCE). RCE is the hypothetical equilibrium (in a statistical sense) of the atmosphere when radiation, convection, and water phase changes are taken into account, and in the absence of lateral transport. RCE has been widely used to study the controls on global-mean temperature, and was foundational in our early understanding of climate sensitivity [Ramanathan and Coakley, 1978, Manabe and Strickler, 1964]. It is accepted that RCE is uniquely defined when the greenhouse gases and clouds are held fixed (e.g., Emanuel [1994]), but one can ask: is RCE unstable to small perturbations, with fixed insolation and surface temperature, but allowing greenhouse gases to vary?

The first affirmative answer to this question was provided by Held et al. [1993], who showed that atmospheric convection could spontaneously organize into a small

moist cluster with mean ascent, surrounded by a dry subsiding area. Since then, this unstable behavior has been referred to as the self-aggregation of convection. Its mechanisms have been studied in 3D cloud-resolving models [Tompkins, 2001, Jeevanjee and Romps, 2013, Wing and Emanuel, 2014, Muller and Bony, 2015, Holloway and Woolnough, 2016, Bretherton et al., 2005] and general circulation models [Coppin and Bony, 2015]; on an f -plane, where it systematically leads to cyclogenesis [Bretherton and Khairoutdinov, 2015, Nolan and Emanuel, 2007, Khairoutdinov and Emanuel, 2013], as well as on a β -plane, where it can generate Madden-Julian Oscillation-like disturbances [Arnold and Randall, 2015]. The weak temperature gradient (WTG) framework [Sobel et al., 2001] has proven useful to isolate this instability and study the possibility of multiple radiative-convective equilibria [Sessions et al., 2010, 2015], especially in a single column [Sobel et al., 2007, Emanuel et al., 2014], where the effects of large-scale circulation are included by allowing large-scale vertical velocities to moisten or dry the column by vertical advection. Emanuel et al. [2014] made fundamental progress by showing the instability of a two-layer atmosphere to coupled lower and upper tropospheric water vapor perturbations in the limit of high surface temperature. However, layered models are highly parameterized and only give valid expressions for radiative fluxes in the optically thin limit – in contradiction of the high surface temperature limit. Moreover, the two-layer instability criterion cannot easily be applied to observations and model outputs, which are much more highly resolved in the vertical. Consequently, we still lack a simple theory that explains when instability of RCE may occur.

This chapter poses a simple yet general criterion: if the total atmospheric radiative cooling decreases when column water vapor increases, then RCE may be unstable to growth of moist or dry perturbations. We denote this condition – of decreasing column atmospheric cooling with increasing column water vapor – as “moisture-radiative cooling instability”, or MRCI for short (section 2.2.1). MRCI is neither a necessary nor a sufficient condition for actual growth of moist and dry perturbations, because real perturbations may be amplified or damped by other processes, such as surface fluxes, moisture-convection interactions, and dynamical export or import of moist

static energy. But we believe that MRCI is a useful condition to study and describe because it is amenable to theoretical, model, and observational analysis, and because it can be expressed as a partial growth rate of moisture perturbations in the absence of other influences.

Starting from fundamental principles of radiative transfer, we show that MRCI is likely above a critical column water vapor value. Both the critical threshold as well as the growth rate, however, depend on the vertical structure of the moisture perturbation. We build a physical understanding of MRCI by starting from the clear-sky longwave radiation feedback in a gray atmosphere (section 2.2.2), and progressively adding clear-sky shortwave heating (section 2.2.3) and longwave cloud-radiation interactions (section 2.2.4). Using the rapid radiative transfer model (RRTMG), we then relax the gray approximation and show that MRCI can also be satisfied when using real-gas radiation, but the minimum column water vapor required for MRCI can be more sensitive to the vertical structure of the moisture perturbation than with gray-gas radiation (section 2.3). Finally, we combine observed atmospheric soundings with the RRTMG to show that environmental variability of water vapor in the real tropics frequently leads to clear-sky MRCI, across a range of geographic locations and seasons (section 2.4).

2.2 Theory

2.2.1 Moisture-radiative cooling instability

Starting from an equilibrium basic state, a positive column water vapor perturbation may amplify if it induces large-scale ascending motion, converging additional moisture into the column. In this section, we derive a simple evolution equation (2.6) for the perturbation atmospheric column water vapor content (in kg m^{-2}), based on coupling between the column radiative heating perturbation and the large-scale convergence or divergence of water vapor.

The column water vapor, \hat{r} , can be defined hydrostatically from the water vapor

mixing ratio r (ratio of water vapor to dry air densities):

$$\hat{r} \stackrel{\text{def}}{=} \int_0^{p_s} r(p) \frac{dp}{g}, \quad (2.1)$$

where we have introduced the atmospheric pressure p , its value p_s at the surface, and the gravity constant g . Here and elsewhere we use an overhat $\hat{}$ to indicate a density-weighted column integral. To examine the stability of a small water vapor perturbation \hat{r}' , we adopt an energetic perspective, and introduce the column moist static energy $\widehat{\text{MSE}}$, defined as:

$$\widehat{\text{MSE}} \stackrel{\text{def}}{=} \underbrace{L_v \hat{r}}_{\text{Latent heat}} + \underbrace{c_p \hat{T}}_{\text{Internal heat}} + \underbrace{\hat{\phi}}_{\text{Potential energy}}, \quad (2.2)$$

and approximately conserved by an individual air parcel during moist adiabatic processes [Arakawa and Schubert, 1974]. L_v is the latent heat of vaporization of water, c_p the specific heat capacity at constant pressure, \hat{T} the column-integrated absolute temperature and $\hat{\phi}$ the column geopotential. In the Tropics, the Coriolis force is too weak to sustain horizontal pressure and temperature gradients: the weak temperature gradient approximation [Sobel et al., 2001] holds reasonably well, and we can approximate \hat{T} and $\hat{\phi}$ as climatologically fixed. Variations of column-integrated moist static energy are thus given to first order by the latent heat variations, $L_v \hat{r}'$. In the troposphere, the only contributors to the column moist static energy budget are the total surface enthalpy flux F_s , the total atmospheric radiative cooling rate \hat{Q} (units W m^{-2}) and the advection of moist static energy [e.g., Neelin and Held, 1987]. The radiative cooling \hat{Q} is defined as positive for atmospheric cooling, and is a sum of longwave (\hat{Q}_L) and shortwave ($-\hat{Q}_S$) components.

To greatly simplify our derivation, and focus on the role of radiative heating anomalies, we set the $\widehat{\text{MSE}}$ advection to zero, yielding:

$$\frac{\partial \widehat{\text{MSE}}}{\partial t} \approx L_v \frac{\partial \hat{r}}{\partial t} = F_s - \hat{Q}. \quad (2.3)$$

Neglecting $\widehat{\text{MSE}}$ advection corresponds to an assumption of zero gross moist stability – that convergence of dry static energy exactly balances divergence of latent heat (or vice-versa) [Yu et al., 1998, Inoue and Back, 2015]. This assumption is artificial, especially on daily timescales, where the $\widehat{\text{MSE}}$ advection has been shown to be the primary driver of $\widehat{\text{MSE}}$ recharge/discharge [Inoue and Back, 2015]. However, on longer timescales (weekly/monthly), the diabatic terms F_s and \hat{Q} become of larger importance, and a tropical atmospheric column may be unstable without up-gradient MSE transport. In that spirit, RCE (denoted by overlines from now on) is an appropriate basic state for the column, since it represents a balance between the surface turbulent fluxes and radiative cooling in the absence of $\widehat{\text{MSE}}$ advection:

$$\overline{F_s} \stackrel{\text{def}}{=} \overline{\hat{Q}}. \quad (2.4)$$

To isolate the role of radiation-water vapor interaction, we fix the surface temperature and assume that the surface flux F_s stays equal to its RCE value $\overline{F_s}$ at all times. We denote the perturbations from RCE by primes. Linearizing the evolution equation (2.3) about RCE, where the balance (2.4) holds, leads to a simple evolution equation for the column water vapor perturbation \hat{r}' to first order:

$$L_v \frac{\partial \hat{r}'}{\partial t} = - \overline{\frac{\partial \hat{Q}}{\partial \hat{r}}} \hat{r}' + \text{O}[(\hat{r}')^2]. \quad (2.5)$$

From equation (2.5), we can compute the evolution of an initial perturbation in time:

$$\hat{r}'(t) = \hat{r}'(t=0) \exp(\lambda t) \quad (2.6)$$

$$\lambda = \underbrace{- \frac{1}{L_v} \overline{\frac{\partial \hat{Q}}{\partial \hat{r}}}}_{\text{Decay/Growth rate}}, \quad (2.7)$$

from which we obtain a potential linear instability criterion for moisture-radiative cooling instability (MRCI), with growth rate λ . An initial dry or moist perturbation may amplify if atmospheric radiative cooling decreases with column water vapor ($\lambda = -\overline{\partial \hat{Q} / \partial \hat{r}} > 0$). The simple mechanism of this instability is illustrated in Figure 2-

1. Note that vertical advection of MSE could be computed self-consistently within the weak temperature gradient framework, assuming that perturbation convective enthalpy fluxes are zero and that the vertical structure of perturbation radiative heating drives vertical velocities. Such a computation amounts to calculating the combined radiative and vertical-advective perturbations in the moist static energy budget. To isolate the contribution of radiative processes, we focus only on the radiative term in this chapter, although preliminary results suggest that vertical MSE advection may substantially amplify the MRCI growth rates. The following sections aim to compute $\hat{Q}(\hat{r})$ in simple but general cases, to show when and why the MRCI condition can be satisfied.

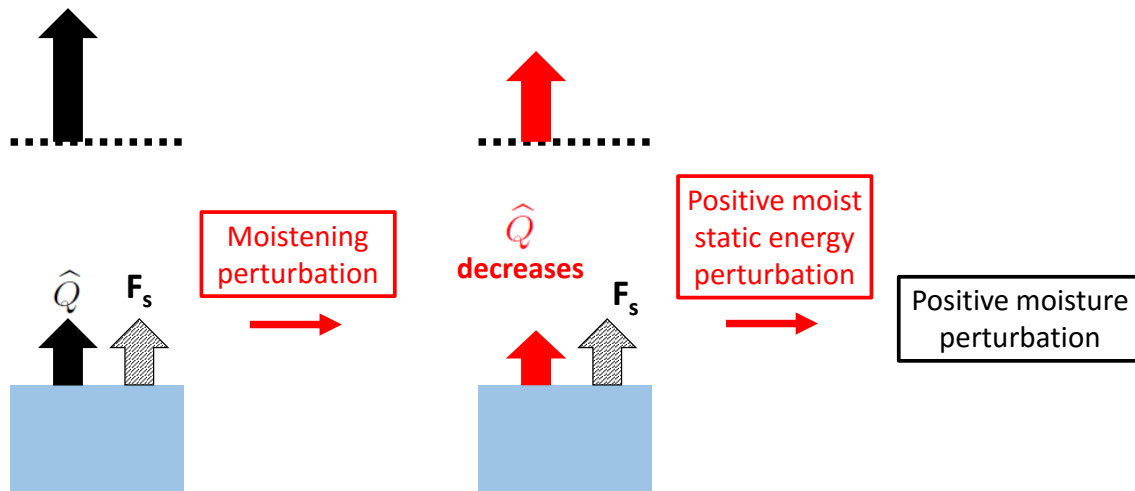


Figure 2-1: Mechanism of MRCI: A moist perturbation decreases the radiative cooling, leading to an amplification of this moist perturbation.

2.2.2 Clear-sky longwave radiation

Temperature and mixing ratio profiles

Understanding infrared radiative transfer in the atmosphere requires knowledge of the vertical structure of temperature and greenhouse gases. We will use simple analytical expressions to model Tropical temperature and water vapor profiles (e.g., Robinson and Catling [2012], Weaver and Ramanathan [1995]), informed by bi-daily

profiles from Chuuk Lagoon (Federated States of Micronesia, station 91334 PTKK), in January and over the past twenty years (January 1996/1997/.../2016; the data is retrieved from the University of Wyoming archive). The average temperature profile $T(p)$ and water vapor profile $r(p)$ are depicted in Figure 2-2.

We fit the mixing ratio profile by assuming a simple power law of the form:

$$r(p) = r_s \left(\frac{p}{p_s} \right)^n, \quad (2.8)$$

where r_s is the surface mixing ratio and n is the ratio of the pressure to the water vapor scale heights. For Chuuk Lagoon, $n \approx 3$ is a reasonable choice for this ratio, and we will use it as our reference value from now on. Note that the power law does not always capture the shape of the water vapor profile in the mid- and upper troposphere, especially when the atmospheric moisture content varies (this misfit can be seen above 300 hPa in Figure 2-2c). Furthermore, $n = 3$ is not the best fit for all tropical locations (it varies from ~ 2 -4). We also seek a simple power law fit for the temperature profile:

$$T = T_s \left(\frac{p}{p_s} \right)^{\frac{\Gamma_m R_d}{g}}, \quad (2.9)$$

where T_s is the surface temperature, R_d the specific gas constant of dry air and Γ_m is a representative average lapse rate (6.3 K km^{-1} in Figure 2-2a). Equation (2.9) can be interpreted as an all-troposphere profile with Γ_m given by the self-consistent moist adiabatic lapse rate at 500 hPa for a prescribed value of T_s . Deviations from the observed temperature profile in Figure 2-2a are less than 5 K below 200 hPa, but become much larger in the stratosphere – equation (2.9) predicts continued decrease in T with height, but shortwave absorption causes the temperature in the real atmosphere to increase with height. We will use these simple power laws for the temperature and mixing ratio profiles, together with gray radiative transfer equations, as a starting point to explore MRCI.

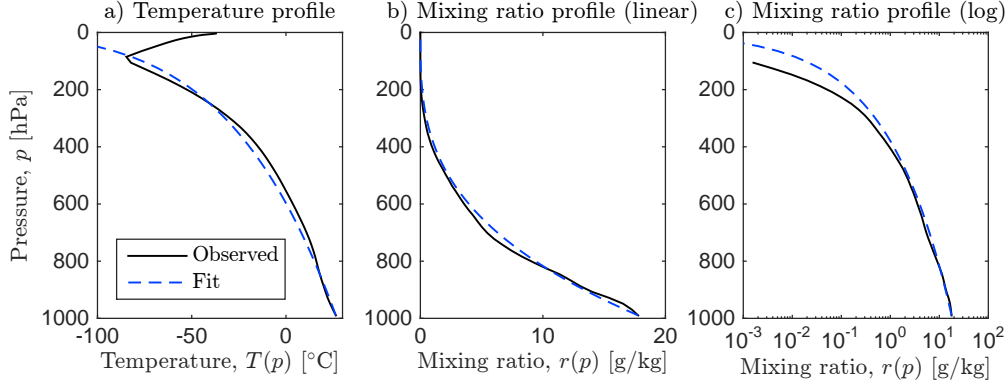


Figure 2-2: a) Temperature profile $T(p)$ and b), c) water vapor mixing ratio profile $r(p)$ in January at Chuuk Lagoon. The average observational profiles are shown in solid black lines and the idealized fits are shown in blue dashed lines; b) and c) are identical but b) has a linear scale for $r(p)$ and c) has a logarithmic scale.

Theoretical framework

We first focus on the clear-sky longwave radiation, which constitutes the bulk of the atmospheric cooling. Following Robinson and Catling [2012] and Takahashi [2009], we make several assumptions which allow us to obtain an analytical expression for $\hat{Q}_L(\hat{r})$. First, we consider a one-dimensional, plane-parallel atmosphere, and use the two-stream Schwarzschild equations [e.g., Chandrasekhar, 1960] for the upwelling and downwelling radiative fluxes (respectively \mathcal{F}_\uparrow and \mathcal{F}_\downarrow):

$$\frac{d\mathcal{F}_\uparrow}{d\tau} = \mathcal{F}_\uparrow - \sigma T^4, \quad (2.10)$$

$$\frac{d\mathcal{F}_\downarrow}{d\tau} = -(\mathcal{F}_\downarrow - \sigma T^4). \quad (2.11)$$

σ is the Stefan-Boltzmann constant, T the atmospheric temperature profile and τ the optical thickness. We assume that water vapor is the only absorbing gas in the longwave, and we make the gray approximation [e.g., Liou, 2002] with an average absorption coefficient $k_{\text{LW}} \approx 0.1 \text{ m}^2 \text{ kg}^{-1}$. The neglect of other greenhouse gases, the gray approximation, and the precise choice of k_{LW} are all significant assumptions, and we emphasize that this derivation is done for illustrative rather than exact purposes. We can then relate the differential optical thickness $d\tau$ to the differential pressure dp ,

accounting for pressure broadening of water vapor absorption strength by scaling the differential optical thickness by p/p_s :

$$d\tau = Dk_{\text{LW}}r(p) \frac{p}{p_s} \frac{dp}{g}. \quad (2.12)$$

Here, we have introduced a diffusivity factor $D = 5/3$ into the optical thickness itself, to account for the integration of the radiances over a hemisphere [Armstrong, 1968, Rodgers and Walshaw, 1966]. By combining equations (2.12), (2.8) and (2.9), it is possible to express:

- The temperature as a function of the optical thickness:

$$T = T_s \left(\frac{\tau}{\tau_s} \right)^{\alpha/4} \quad \text{where } \alpha \stackrel{\text{def}}{=} \frac{4\Gamma_m R_d}{(n+2)g}, \quad (2.13)$$

- The total optical thickness of the atmosphere as a function of the profile properties:

$$\tau_s \stackrel{\text{def}}{=} \tau(p = p_s) = \frac{Dk_{\text{LW}}p_s r_s}{(n+2)g}. \quad (2.14)$$

We can obtain the surface net longwave flux SLW, the outgoing longwave radiation OLR, and thus the atmospheric radiative cooling \hat{Q}_L by integrating equations (2.10) and (2.11). Assuming that the surface radiates like a black-body of temperature T_s and that there is no incoming longwave radiation at the top of the atmosphere yields:

$$\frac{\text{SLW}}{\sigma T_s^4} \stackrel{\text{def}}{=} \frac{\mathcal{F}_\uparrow(\tau_s) - \mathcal{F}_\downarrow(\tau_s)}{\sigma T_s^4} = \underbrace{1}_{\text{Surface} \rightarrow \text{Atmosphere}} - \underbrace{\int_0^{\tau_s} d\tau' \left(\frac{\tau'}{\tau_s} \right)^\alpha e^{-(\tau_s - \tau')}}_{\text{Atmosphere} \rightarrow \text{Surface}}, \quad (2.15)$$

$$\frac{\text{OLR}}{\sigma T_s^4} \stackrel{\text{def}}{=} \frac{\mathcal{F}_\uparrow(0) - \mathcal{F}_\downarrow(0)}{\sigma T_s^4} = \underbrace{e^{-\tau_s}}_{\text{Surface} \rightarrow \text{Space}} + \underbrace{\int_0^{\tau_s} d\tau' \left(\frac{\tau'}{\tau_s} \right)^\alpha e^{-\tau'}}_{\text{Atmosphere} \rightarrow \text{Space}}, \quad (2.16)$$

$$\frac{\hat{Q}_L}{\sigma T_s^4} \stackrel{\text{def}}{=} \frac{\text{OLR} - \text{SLW}}{\sigma T_s^4} = e^{-\tau_s} - 1 + \int_0^{\tau_s} d\tau' \left(\frac{\tau'}{\tau_s} \right)^\alpha \left(e^{-(\tau_s - \tau')} + e^{-\tau'} \right). \quad (2.17)$$

We derive these analytical forms of the radiative fluxes in appendix 2.6. The net SLW (2.15) is the blackbody emission from the surface (T_s), minus the total atmospheric

downwards emission at the surface, which increases with the temperature exponent α defined by equation (2.13). The OLR (2.16) is the sum of the surface blackbody emission that has not been absorbed by the atmosphere, and the total atmospheric upwards longwave emission at the top of the atmosphere. Finally, the longwave radiative cooling \hat{Q}_L (2.17) is the difference between the OLR and the SLW (difference between the top and bottom arrows on Figure 2-1). In order to examine \hat{Q}_L as a function of \hat{r} , and thus determine whether clear-sky longwave MRCI is satisfied, we also need to relate the column water vapor to the characteristics of the sounding. This can be done by combining equations (2.1) and (2.8):

$$\hat{r} = \frac{r_s p_s}{(n+1)g}. \quad (2.18)$$

Clear-sky longwave MRCI

We can use the results of section 2.2.1 to evaluate the sensitivity of the longwave atmospheric radiative cooling (2.17) to column water vapor. Because the water vapor mixing ratio decreases with height, we expect the radiative cooling to change less if we remove water vapor near the surface, where the atmosphere is more optically thick, than near the top of the atmosphere. Thus, we choose two simple ways of adding or removing water vapor to the column, which are both illustrated in Figure 2-3:

- a) We fix the shape of the water vapor mixing ratio profile (n), but vary its surface value r_s . Water vapor is thus mostly added or removed in the lower troposphere.
- b) We fix the surface mixing ratio (r_s) but vary its shape n . Water vapor is thus mainly added or removed in the mid-troposphere.

These variations in column water vapor can be thought of as a representation both of different RCE states about which a linear stability analysis applies, and as large-amplitude perturbations to the water vapor profile from a given RCE state. Variability of water vapor profiles in the real world is complex, and generally includes both of these idealized behaviors. We will later show, however, that water vapor variability in

the Tropics looks more like b) the case of varied shape with fixed surface mixing ratio – so the right-hand panels of subsequent Figures should be treated as more realistic.

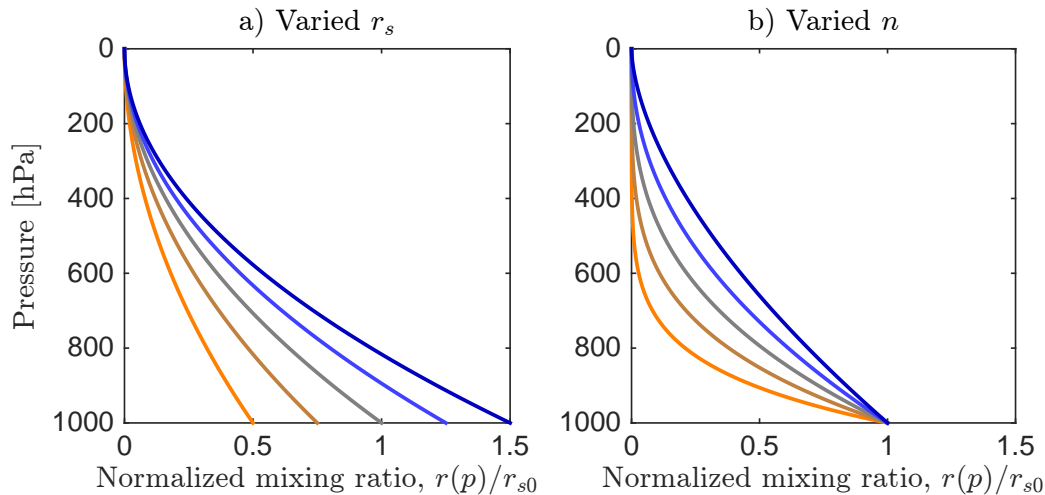


Figure 2-3: Two methods of varying column water vapor used in this chapter; a) varied mixing ratio (r_s) and fixed shape; b) varied shape ($n = 1.7, 2.2, 3.0, 4.3, 7.0$) and fixed surface mixing ratio. The reference profile is gray and the different colors represent equal increments of total column water vapor.

Looking at the contribution of the surface net longwave flux (SLW) and the outgoing longwave radiation (OLR) in Figure 2-4 gives a first understanding of the MRCI physical mechanism:

- Without water vapor ($\hat{r} = 0$), the surface directly radiates to space, and the atmospheric radiative cooling is zero. The OLR and the SLW are both at their maximal values.
- For small water vapor content, the SLW falls sharply as the boundary layer becomes opaque, and the atmosphere emits almost as much longwave radiation to the surface as it receives from the surface. For higher water vapor content, the SLW decays to zero.
- The OLR decreases much more slowly with water vapor, consistently with the observational and modeling literature (e.g. Allan and Soden [2008], Harrop and Hartmann [2015]). The OLR can be thought of as scaling with the fourth

power of the effective upward emission temperature, which decreases slowly as the atmosphere becomes optically thicker and the emission level moves upward.

- Consequently, for small water vapor content, the atmospheric radiative cooling increases with water vapor, whereas it decreases with water vapor for higher water vapor content. Thus, for gray-gas radiation, there is a critical water vapor threshold \hat{r}_{crit} , above which MRCI is satisfied.

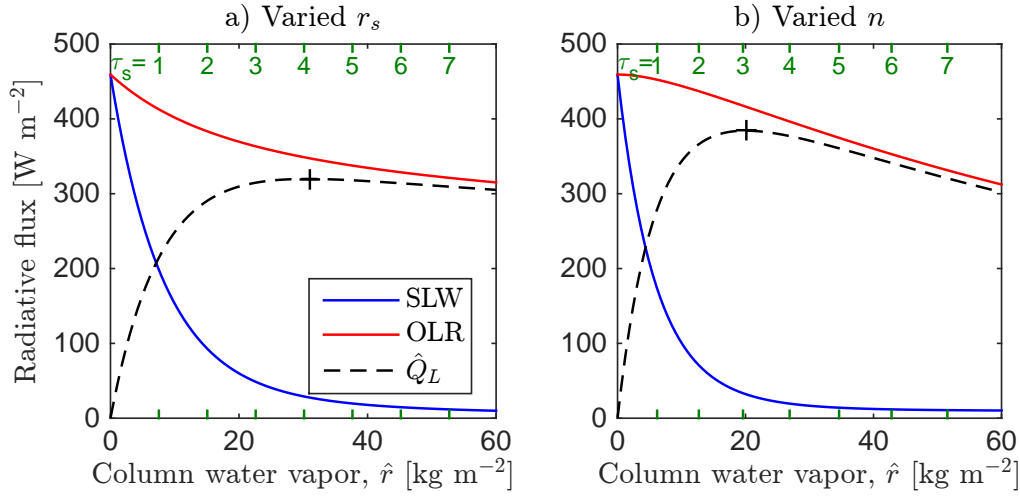


Figure 2-4: Outgoing longwave radiation (OLR), surface net longwave radiation (SLW), and longwave clear-sky radiative cooling \hat{Q}_L as a function of column water vapor \hat{r} , a) varying the surface mixing ratio at fixed shape, and b) varying the water vapor profile shape at constant surface mixing ratio. Crosses show maxima of radiative cooling, and green axis labels indicate surface optical thickness, τ_s . The surface temperature is 300K. Note the similarity to figure 4 of Takahashi [2009].

Figure 2-4 allows us to obtain the critical threshold \hat{r}_{crit} from the abscissa of the maximum (marked with crosses), and the growth rate from the slope of the curve $\hat{Q}_L(\hat{r})$. Comparing the two presented cases shows that MRCI:

- Is satisfied above a smaller critical threshold \hat{r}_{crit} at varied shape n than at varied surface mixing ratio r_s .
- Has strongest growth rates for varied shape n (typical value of $1/15$ days $^{-1}$), much larger than those at varied surface mixing ratio r_s (typical value of $1/60$

days⁻¹). The reader is referred to appendix 2.9 for the exact calculation of the growth rate in both cases.

These findings confirm that the atmosphere is more unstable to addition or removal of water vapor in the mid and upper troposphere than in the lower troposphere. The typical growth rates found for the MRCI at varied n are consistent with the numerical findings of Wing and Emanuel [2014], where the water vapor content mostly varied in the mid and upper troposphere. Since the water vapor content in RCE scales exponentially with surface temperature, we can also roughly identify a threshold surface temperature above which $\bar{r} > \hat{r}_{\text{crit}}$. To make this statement more rigorous, we verify that the functional properties of $\hat{Q}_L(\hat{r})$ do not change significantly with surface temperature due to changes in either lapse rate or surface mixing ratio (appendix 2.7). Note that these results depend on both the gray approximation and the choice of k_{LW} , and we will compare them below with calculations using real-gas radiative transfer (section 2.3).

2.2.3 Clear-sky shortwave radiation

Clear-sky shortwave radiation is always a destabilizing factor for moisture perturbations from RCE, regardless of \hat{r} or the vertical structure of the perturbation. As column water vapor increases, there is more water vapor to absorb shortwave radiation, which decreases the total radiative cooling. To incorporate shortwave radiation in our radiative model, we write the Schwarzschild equation for the downwelling shortwave radiative flux $\mathcal{F}_{\downarrow,\text{SW}}$, assuming that water vapor acts as a simple gray absorber in the shortwave:

$$\frac{d\mathcal{F}_{\downarrow,\text{SW}}}{d\tau} = -\varepsilon\mathcal{F}_{\downarrow,\text{SW}}. \quad (2.19)$$

The τ on the left side of equation (2.19) is the longwave optical thickness, so the parameter ε converts between differential shortwave and longwave optical thickness coordinates:

$$\varepsilon = \frac{d\tau_{\text{SW}}}{d\tau_{\text{LW}}} = \frac{k_{\text{SW}}}{k_{\text{LW}}\mu D}. \quad (2.20)$$

Here, $k_{\text{SW}} \approx 10^{-2} \text{ m}^2 \text{ kg}^{-1}$ represents the water vapor absorption coefficient averaged over shortwave frequencies (again chosen for illustrative and not exact purposes), and $\mu = \pi/4$ is the insolation-weighted zenith angle at the equator on the equinox [Cronin, 2014]. We integrate equation (2.19), with time-mean insolation S . The shortwave radiative heating rate \hat{Q}_S is then:

$$\frac{\hat{Q}_S}{S} \stackrel{\text{def}}{=} \frac{\mathcal{F}_{\downarrow, \text{SW}}(0) - \mathcal{F}_{\downarrow, \text{SW}}(\tau_s)}{S} = 1 - e^{-\varepsilon \tau_s}, \quad (2.21)$$

which means that the total radiative cooling rate of the atmosphere is $\hat{Q} = \hat{Q}_L - \hat{Q}_S$.

Because ε is a small number, the shortwave heating rate increases slowly with water vapor, contributing further to the MRCI studied in section 2.2.2, as we can see by the steeper slopes in Figure 2-5. The typical growth rate of MRCI increases from $1/60 \text{ days}^{-1}$ to $1/12 \text{ days}^{-1}$ for varied r_s , and from $1/15 \text{ days}^{-1}$ to $1/7 \text{ days}^{-1}$ for varied n . The threshold for MRCI \hat{r}_{crit} also decreases when shortwave absorption is taken into account (see crosses in Figure 2-5). Again, these results depend on the gray approximation and the choice of absorption coefficients, and they will be compared below with calculations using real-gas radiative transfer (section 2.3).

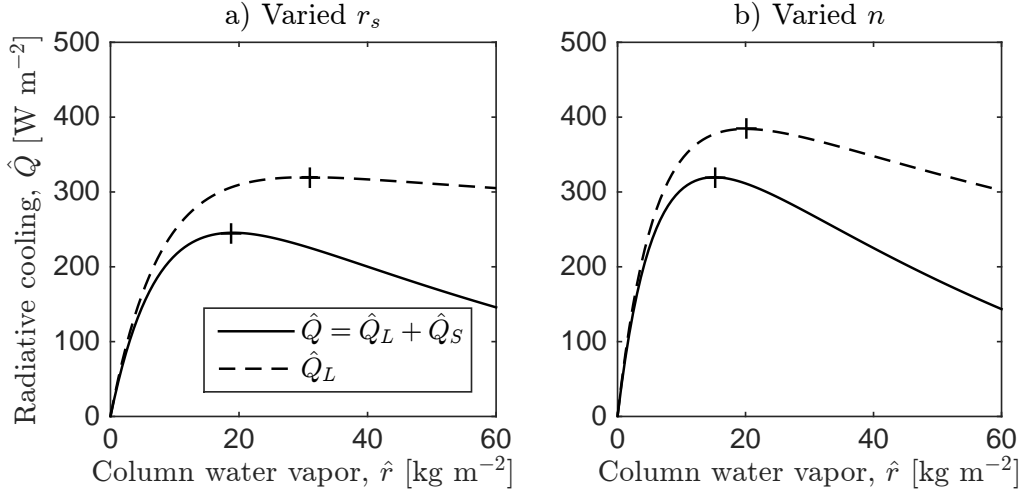


Figure 2-5: Longwave \hat{Q}_L and total \hat{Q} clear-sky radiative cooling as a function of column water vapor, a) varying the surface mixing ratio at fixed shape, and b) varying the water vapor profile shape at constant surface mixing ratio. Crosses show maxima of radiative cooling. The surface temperature is 300K.

2.2.4 Cloud longwave radiative effects

Cloud-radiation interaction has been shown to play an important role in self aggregation, and their effects can be stabilizing or destabilizing depending on the characteristics of the cloud cover [Muller and Bony, 2015, Wing and Emanuel, 2014, Wing and Cronin, 2016]. We are especially interested in recent studies that have shown that low thick clouds could be a potential mechanism for MRCI at low surface temperatures [e.g., Coppin and Bony, 2015]. After including clear-sky shortwave heating, there was still a threshold \hat{r}_{crit} below which MRCI was not satisfied. Can this threshold decrease in the presence of clouds? To address this question, we add an idealized cloud in our radiative model. Motivated by the simple idea that the cloud acts as a strong localized absorber and emitter, we approximate it as an infinitesimally thin layer, defined by its optical thickness $\Delta\tau$ and its pressure level p_c . The idealized cloud has no effect on the moist adiabatic temperature profile, but causes a step in the optical thickness profile, which is illustrated in Figure 2-6.

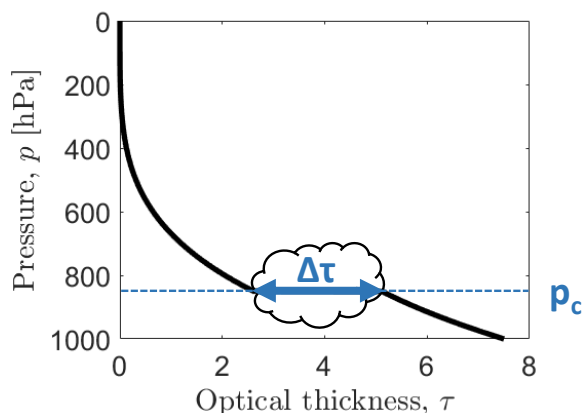


Figure 2-6: Optical thickness profile for a cloud at $p_c = 850\text{hPa}$ with cloud optical thickness $\Delta\tau = 2.5$.

The atmospheric radiative cooling in the presence of a cloud is computed in appendix 2.8 and given by equation (2.33). Note that we entirely neglect the shortwave radiative and reflective effects of clouds. To obtain a physical intuition about the cloud radiative effects, it is useful to consider two limits:

- The limit of a very optically thin cloud ($\Delta\tau \ll \tau_s, 1$). In that case, we recover

the clear-sky radiative cooling of sections 2.2.2 and 2.2.3: $\hat{Q}_L - \hat{Q}_S$.

- The limit of a very optically thick cloud ($\Delta\tau \gg 1$) in an optically thin clear-sky atmosphere ($\tau_s < 1$). In the absence of shortwave absorption, the atmospheric radiative cooling is then given by:

$$\hat{Q}_{\Delta\tau \gg 1} = \sigma(T_s^4 - 2T_c^4), \quad (2.22)$$

where T_c is the temperature of the cloud. Thus, low clouds (such that $2T_c^4 > T_s^4$) are expected to cool the atmosphere, whereas high clouds (such that $2T_c^4 < T_s^4$) warm the atmosphere.

Figure 2-7 shows the atmospheric radiative cooling in the presence of four idealized clouds, which differ by their heights (low and high) and their optical thickness (thick and thin). We see that the radiative effects of low clouds are destabilizing, reducing the critical threshold \hat{r}_{crit} and increasing the MRCI growth rate. Thick low clouds can even reduce \hat{r}_{crit} to 0. On the other hand, high clouds stabilize the atmosphere by increasing \hat{r}_{crit} and decreasing the growth rate. Cloud effects generally increase with cloud optical thickness $\Delta\tau$. Note that partial clear sky and partial cloud cover could easily be modeled by a weighted averaging of curves from Figure 2-7.

The cloud effects we discuss here refer solely to the effect of a static cloud profile on the sensitivity of atmospheric cooling to water vapor. Other stabilizing or destabilizing cloud effects can also occur due to variation of cloud amount or type with column water vapor (e.g. Harrop and Hartmann [2015]). For example, if high cloud amount or optical thickness increases with column water vapor, then \hat{Q} could decrease with increasing \hat{r} , reinforcing the MRCI growth rate. Such cloud feedbacks have been documented as important in self-aggregation [Wing and Emanuel, 2014], but elaborating on them further is beyond the scope of this work.

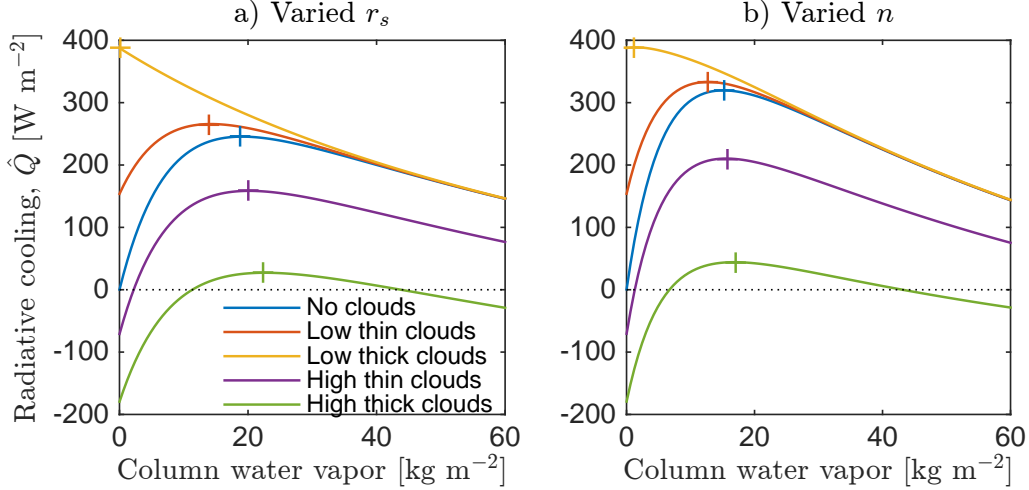


Figure 2-7: Total radiative cooling in the presence of a low ($p_c = 900\text{hPa} \Leftrightarrow T_c = 295\text{K}$), high ($p_c = 200\text{hPa} \Leftrightarrow T_c = 234\text{K}$), thick ($\Delta\tau = 5$) or thin ($\Delta\tau = 0.5$) cloud with a) varied surface mixing ratio, and b) varied shape. Crosses show maxima of radiative cooling. The surface temperature is 300K .

2.3 Real-gas radiative transfer

To better understand how the results above depend on the wavelength-dependence of water vapor absorption, we use the RRTMG model [Iacono et al., 2000, 2008, Mlawer et al., 1997] to explore the relationship between column water vapor \hat{r} and column radiative cooling \hat{Q} for idealized moisture profiles. We use the version 3.8 of the longwave and shortwave column versions of RRTMG, which is a broadband, two-stream, correlated k-distribution radiative transfer model that has been tested against line-by-line radiative transfer models, and is used in several general circulation models. We use a realistic long-term mean temperature profile from the Chuuk station, together with idealized water vapor profiles given by equation (2.8). We vary the column water vapor either by varying the surface mixing ratio r_s and holding the pressure scaling exponent n constant, or by varying the pressure scaling exponent n and holding the surface mixing ratio constant. We specify a constant CO_2 mixing ratio of 400 ppmv throughout the depth of the atmosphere, but use no other greenhouse gases.

Clear-sky longwave MRCI is much more sensitive to the vertical structure of water vapor perturbation with real-gas radiation than with gray-gas radiation. There is no

longwave instability for varied r_s and $\hat{r} < 90 \text{ kg m}^{-2}$, but with fixed r_s , MRCI is satisfied for all $\hat{r} > 15 \text{ kg m}^{-2}$ (Figure 2-8). The threshold $\hat{r}_{\text{crit}} \approx 15 \text{ kg m}^{-2}$ for MRCI in the case of varied n is at the very low end of the distribution of \hat{r} in the real Tropics. Broadly speaking, the shape of the OLR and SLW curves is similar to that in the gray-gas theory, but the net longwave radiation at the surface does not tend towards zero nearly as rapidly with increasing \hat{r} for real-gas radiative transfer. Values of SLW remain large ($\sim 50 \text{ W m}^{-2}$) even for moist atmospheres ($\hat{r} \sim 60 \text{ kg m}^{-2}$), and allow $d\text{SLW}/d\hat{r}$ to also be larger in magnitude than in the gray-gas model. Thus, because the instability is determined by the slope of OLR-SLW with \hat{r} , the failure of SLW to rapidly asymptote to zero is the key reason why the real-gas model shows greater sensitivity to the vertical structure of water vapor perturbation. The surface net longwave radiation depends strongly on near-surface specific humidity in the real atmosphere because the optical thickness of water vapor in its least absorbent parts of the spectrum – the water vapor window region of the spectrum from $\sim 8\text{-}12 \mu\text{m}$ – actually scales with the square of the vapor pressure [e.g., Cormier, Hodges, and Drummond, 2005]. The importance of the atmospheric window for surface longwave cooling motivates a two-band model for the water vapor spectrum, which allows for separate treatment of strongly-absorbing and weakly-absorbing wavelength ranges. This model of intermediate complexity, presented in appendix 2.10, gives a much better fit to Figure 2-8 than is possible for any single choice of k_{LW} , but is still simple enough for the SLW and the OLR to be expressed analytically.

Integrated column shortwave absorption is insensitive to the shape of the moisture perturbation. Including shortwave heating thus increases the instability for the case of varied n , lowering \hat{r}_{crit} to less than 10 kg m^{-2} , and pushes the case with varied r_s close to neutral stability. The total atmospheric cooling for varied r_s (solid line in Figure 2-8) actually has more than one local maximum (near 5 and 70 kg m^{-2}). Multiple local maxima in \hat{Q} can arise with real-gas radiative transfer, because different parts of the thermal spectrum become optically thick at different values of \hat{r} . As a particular spectral region becomes optically thick, it first leads to an increase in atmospheric cooling and then to a decrease (as shown by (2.17) and \hat{Q}_L in Figure 2-4). The

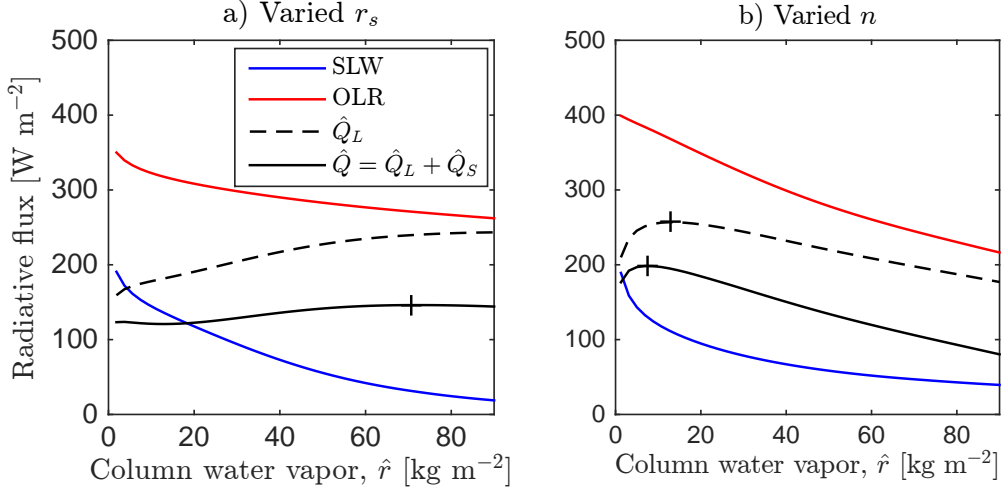


Figure 2-8: As in Figures 2-4 and 2-5, but using the RRTMG model instead of gray-gas radiative transfer. Outgoing longwave radiation (OLR), surface net longwave radiation (SLW), longwave \hat{Q}_L and total \hat{Q} clear-sky radiative cooling as a function of column water vapor, a) varying the surface mixing ratio at fixed shape, and b) varying the water vapor profile shape at constant surface mixing ratio. Crosses show maxima of radiative cooling. The surface temperature is 300K.

existence of multiple ranges of column water vapor where MRCI is satisfied may be relevant to the finding of self-aggregation in cloud-resolving simulations in snowball earth-like conditions [Abbot, 2014].

As in the case of gray radiative transfer, low clouds increase the MRCI growth rate, and high clouds decrease the MRCI growth rate (Figure 2-9). Shortwave cloud effects are included in these calculations, but do not alter the conclusions reached in section 2.2.4. Clouds most strongly influence our findings for dry profiles with varied r_s , where water vapor perturbations that would be stable in clear-sky conditions are unstable in the presence of thick low clouds.

Overall, the calculations shown here suggest that clear-sky longwave MRCI may be satisfied in the real atmosphere, but is likely sensitive to whether real variability of water vapor profiles looks more like the case of varied shape (varied n), or that of varied surface mixing ratio (varied r_s).

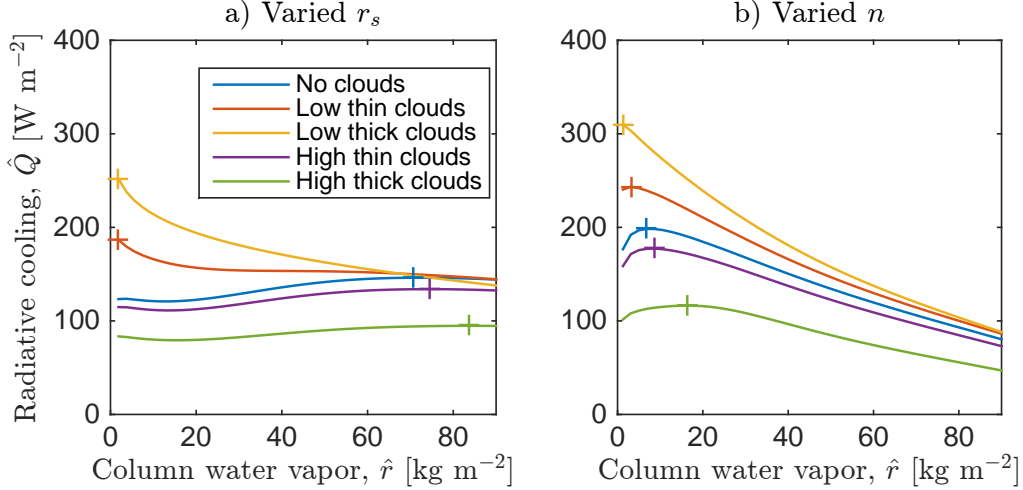


Figure 2-9: Dependence of total radiative cooling \hat{Q} on column water vapor \hat{r} in RRTMG calculations that include cloud layers, for a) varied surface mixing ratio and b) varied water vapor profile shape. The four different types of clouds correspond to those described in section 2.2.4 and Figure 2-7. The surface temperature is 300K.

2.4 Observations

2.4.1 Method

We investigate the following question: does the observed variability of Tropical water vapor lead to clear-sky MRCI? For a given meteorological station and a given month of the year, we proceed in two steps. First, we retrieve twenty consecutive years of bi-daily soundings (from the University of Wyoming archive). We eliminate the soundings that have less than 10 data points, as well as those which do not have complete data between 950 hPa and 100 hPa. The locations of the 12 stations are chosen in three distinct tropical zones, summarized in Table 2.1.

For each station, we average the temperature soundings to obtain the mean profile $T_{\text{av}}(p)$, and we examine the variability of the relative humidity in the soundings $\text{RH}(p)$. Relative humidity is defined as the ratio of the water vapor partial pressure $e(p)$ to its saturation value $e_{\text{sat}}(T, p)$:

$$\text{RH}(p) \stackrel{\text{def}}{=} \frac{e(p)}{e_{\text{sat}}(T, p)} \approx \frac{r(p)}{r_{\text{sat}}(T, p)}. \quad (2.23)$$

Table 2.1: Locations of the stations used in sounding analysis. Number of soundings used for each season indicated in the rightmost columns.

Region	Location	Station ID	Number of soundings			
			Jan	Apr	Jul	Oct
Caribbean	International airport of Barbados, Barbados	78954 TBPB	456	457	657	699
Caribbean	San Juan, Puerto Rico (US)	78526 TJSJ	1127	1105	1120	1133
Caribbean	Santo Domingo, Dominican Republic	78486 MDSD	158	190	272	301
W. Pacific	Pohnpei, Federated States of Micronesia	91348 PTPN	1150	1079	1116	1087
W. Pacific	Chuuk Lagoon, Federated States of Micronesia	91334 PTKK	1141	1116	1080	1077
W. Pacific	Guam International Airport, Guam (US)	91212 PGAC	885	947	850	781
W. Pacific	Yap Main Islands, Federated States of Micronesia	91413 PTYA	1074	1085	1072	1010
W. Pacific	Koror Island, Palau	91408 PTRO	1068	1123	1214	1127
Amazon	Manaus International Airport, Brazil	82332 SBMN	600	592	620	621
Amazon	Sao Gabriel da Cachoeira, Brazil	82107	72	72	75	58
Amazon	Santarem, Brazil	82244	157	103	111	179
Amazon	Tabatinga, Brazil	82411	94	61	85	58

We have introduced the water vapor saturation mixing ratio $r_{\text{sat}}(p)$, which is the mixing ratio above which water vapor condenses. To capture the essence of this variability, we generate three soundings for each station, based on column relative humidity \mathcal{H} :

$$\mathcal{H} \stackrel{\text{def}}{=} \frac{\hat{r}}{\hat{r}_{\text{sat}}}, \quad (2.24)$$

which is the ratio of the total column water vapor to the column-integrated saturation mixing ratio. The three soundings are:

1. Average: The ensemble average of the relative humidity profile: $\text{RH}_{\text{av}}(p)$.
2. Moist: The ensemble average of relative humidity from the moistest profiles: $\text{RH}_{\text{moist}}(p)$, defined as those with column relative humidity (2.24) one standard deviation or more above the mean ($+1\sigma$).
3. Dry: The ensemble average of relative humidity from the driest profiles: $\text{RH}_{\text{dry}}(p)$, defined as those with column relative humidity (2.24) one standard deviation or more below the mean (-1σ).

We then use the longwave and shortwave packages from the RRTMG to estimate the radiative fluxes for each case. The input to RRTMG includes:

- A standard pressure profile, with sixty levels spaced by 20.5hPa from 1000hPa to 85hPa and with a decreasing spacing above 85hPa.

- The interpolated mean temperature profile $T_{\text{av}}(p)$. We find that the temperature in profiles corresponding to RH_{av} , RH_{dry} and RH_{moist} varies by only a few tenths of a degree, and leads to only small changes in the perturbation radiative cooling (of order a few W m^{-2}). Together with our focus on radiative perturbations caused solely by water vapor variability, this justifies the use of a single average temperature profile for all three cases.
- The water vapor mixing ratio in the average, moist, and dry cases, obtained from the interpolated relative humidity levels, the exact version of definition (2.23) and Bolton’s formula for the saturation water vapor partial pressure Bolton [1980].
- Carbon dioxide with a constant mixing ratio of 4.0×10^{-4} , is the only long-lived greenhouse gas. Note that the lack of ozone decreases stratospheric shortwave absorption, resulting in an overestimate of tropospheric shortwave heating, and its sensitivity to \hat{r} .
- A solar zenith angle of $\arccos(\pi/4)$ rad, the equatorial equinox value.

Finally, we obtain the net longwave and shortwave radiative fluxes at all pressure levels (the shortwave fluxes must be multiplied by $\frac{4}{\pi^2}$ to account for the diurnal cycle and the zenith angle). We then compute the total radiative cooling by subtracting the surface net longwave flux from the top of the atmosphere net longwave flux, following definition (2.17). To summarize, this method allows us to go from environmental variability of relative humidity (RH_{av} , RH_{moist} , RH_{dry}) to environmental variability of clear-sky atmospheric radiative cooling (\hat{Q}_{av} , \hat{Q}_{moist} , \hat{Q}_{dry}), assuming that the temperature profile is unchanged and equal to its mean value $T_{\text{av}}(p)$.

2.4.2 A case study: Chuuk Lagoon

We focus on Chuuk Lagoon (Federated States of Micronesia, station 91334 PTKK); the computed mixing ratio profile used for the RRTMG input, the profile relative humidity, and its net upwards longwave and shortwave fluxes are plotted in Figure

2-10. We expect this station to be a good candidate for MRCI because column water vapor is high (on average $\hat{r} \approx 43 \text{ kg m}^{-2}$), and because the variability of water vapor is small near the surface but much larger in the mid to upper troposphere (Figure 2-10a,b). Indeed, we find MRCI at this station: $\hat{Q}_{\text{moist}} < \hat{Q}_{\text{av}} < \hat{Q}_{\text{dry}}$ (Figure 2-10a,b); this confirms that in the moist Tropics, increasing water vapor can lead to less longwave radiative cooling. Furthermore, as with section 2.2.3, the shortwave radiative heating increases with column water vapor. Total radiative cooling \hat{Q} thus decreases faster with column water vapor than the longwave radiative cooling alone, which confirms that the shortwave heating enhances MRCI in the Tropics. From equation (2.6), we can estimate the clear-sky MRCI growth rate λ :

$$\lambda_- \approx \frac{1}{L_v} \frac{\hat{Q}_{\text{dry}} - \hat{Q}_{\text{av}}}{\hat{r}_{\text{av}} - \hat{r}_{\text{dry}}} \quad (2.25)$$

$$\lambda_+ \approx \frac{1}{L_v} \frac{\hat{Q}_{\text{av}} - \hat{Q}_{\text{moist}}}{\hat{r}_{\text{moist}} - \hat{r}_{\text{av}}}. \quad (2.26)$$

For Chuuk Lagoon, we obtain growth rates of $\lambda_{-,+} = (1.6, 1.2)\text{month}^{-1}$, suggesting potential growth of moisture anomalies via MRCI with a time scale of several weeks. Given this one unstable case study, we ask: Are most tropical locations unstable to MRCI, and what are their typical MRCI growth rates?

2.4.3 MRCI growth rates in the Tropics

In this section, we present 48 case studies, where twenty consecutive years of bi-daily soundings were retrieved for each case study. We study 12 different stations spread over the Tropics (see section 2.4.1), for 4 different months of the year (January, April, July, and October). For all cases studied, the longwave and the total radiative cooling decrease with column water vapor ($\hat{Q}_{\text{dry}} > \hat{Q}_{\text{av}} > \hat{Q}_{\text{moist}}$). Thus, observed variability of water vapor is consistent with presence of MRCI at all these tropical locations. We estimate the growth rates at each of these locations from equation (2.26), and plot them as a function of column water vapor on Figure 2-11. Looking at the clear-sky longwave growth rates (Figure 2-11a), we notice that most of the longwave growth

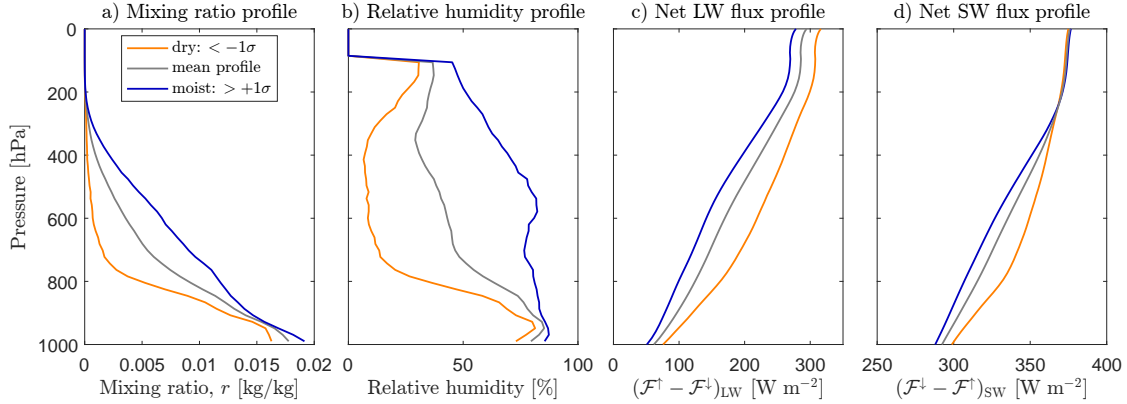


Figure 2-10: For Chuuk Lagoon station, profiles for average (gray line), $+1\sigma$ (blue line) and -1σ (orange line) conditions: (a) Computed mixing ratio profiles used for the RRTMG input (b) Relative humidity profiles (c) Net upwards longwave radiative flux (d) Net downwards shortwave radiative flux. Longwave radiative cooling values \hat{Q}_L are respectively 241 (dry: $< -1\sigma$), 233 (average), and 227 (moist: $> +1\sigma$) W m^{-2} . The shortwave radiative heating values $-\hat{Q}_S$ are respectively 76 (dry: $< -1\sigma$), 84 (average), and 89 (moist: $> +1\sigma$) W m^{-2} .

rates are below 1 month^{-1} . We also see clear geographical groups: the Caribbean soundings (blue squares with red borders) are drier than the Western Pacific ones (blue stars), which are drier than the Amazonian ones (green circles with yellow borders). Some of the highest longwave growth rates occur for the moist soundings, but the variability is too large to discern a clear trend. We have also not found a clear seasonality in MRCI growth rates, although the latter tend to be larger during the wet season at a given location.

Looking at the total clear-sky growth rates (Figure 2-11b), we see that the growth rates have increased and are now all above 1 month^{-1} . Additionally, the shortwave feedback is strongest for the driest locations. This is due to diminishing sensitivity of shortwave absorption by water vapor as column water vapor increases, as the most strongly absorbing bands saturate (see also Figure 2-8 of section 2.3). A stronger shortwave feedback in dry regions is also predicted by the gray-gas model as absorption saturates throughout the shortwave (equation (2.21) of section 2.2.3).

In conclusion, the clear-sky LW MRCI is common across the tropics but has fairly low growth rates $\lesssim 1 \text{ month}^{-1}$, but the shortwave feedback roughly doubles typical

growth rates, leading to values that are more characteristic of tropical intraseasonal disturbances. If the same method is applied to mid-latitude, or polar soundings, we find that the clear-sky longwave effects are not sufficient to destabilize the atmosphere ($\widehat{Q}_{\text{dry}} < \widehat{Q}_{\text{av}} < \widehat{Q}_{\text{moist}}$), suggesting that MRCI is unique to the Tropics. This finding owes to both the latitudinally varying shape of water vapor perturbations – varied- r_s perturbations are more common outside the Tropics – as well as to lower climatological \hat{r} values outside the tropics. Furthermore, the structural model assumption of weak temperature gradients, which implies that variations in column \widehat{MSE} are dominated by variations in $L_v \hat{r}$ and neglects horizontal advection of sensible heat, is clearly invalid outside the Tropics.

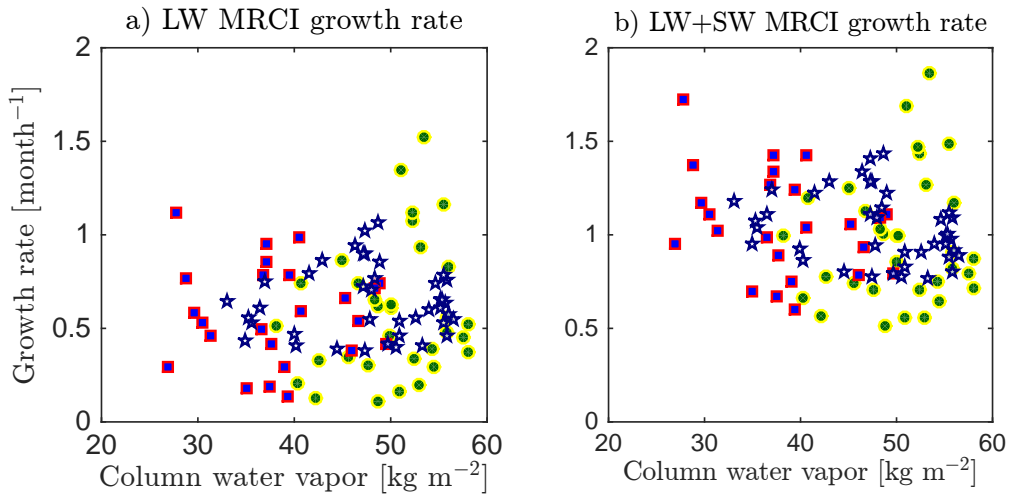


Figure 2-11: Observed MRCI growth rates based on a) slope of clear-sky longwave cooling vs. column water vapor and b) slope of clear-sky longwave plus shortwave cooling vs. column water vapor, for the Caribbean stations (blue squares with red borders) West Pacific stations (blue stars) and Amazonian stations (green circles with yellow borders)

2.5 Conclusion

We have defined a moisture-radiative cooling instability (MRCI) criterion for the tropical atmosphere; MRCI is satisfied if total column radiative cooling decreases

with increasing column water vapor. When the atmosphere is very moist, adding water vapor reduces atmospheric longwave cooling. With a smaller cooling rate, the tropical atmosphere gains energy, mainly in the form of latent heat, which increases its moisture content. In this very moist atmosphere, a dry moisture perturbation will also amplify through the opposite mechanism. In the shortwave, adding water vapor to a column increases the absorption of solar radiation, further energizing the column. Translating MRCI into an actual instability of moisture perturbations relies fundamentally on the assumption of weak temperature gradients in the tropical atmosphere, so that heating anomalies translate to vertical motion anomalies that moisten or dry the atmosphere by large-scale water vapor convergence or divergence.

We have used the gray approximation for much of the chapter for illustrative purposes, but we have also shown that MRCI operates with real-gas radiative transfer calculations. Both the gray-gas and real-gas approximations highlight the importance of the vertical structure of water vapor perturbations for MRCI. If moist and dry anomalies occur dominantly in the mid and upper troposphere, MRCI is satisfied for a larger range of column water vapor values, and its growth rates are larger. We have also shown that static clouds, especially low and thick clouds, can expand the range of column water vapor values for which MRCI is satisfied and lead to larger growth rates.

Analysis of observational soundings with a radiative transfer model suggests that MRCI is common across the real Tropics, and has growth rates of $\sim 1 \text{ month}^{-1}$. MRCI is favored in the Tropics because column water vapor values are high, and because moisture anomalies occur preferentially in the mid and upper troposphere; the boundary layer and surface humidity do not vary much.

Our key criterion for MRCI is that radiative cooling decrease with column water vapor. This criterion differs from Emanuel et al. [2014] in several ways:

- It is a bulk, vertically integrated criterion, which is simple to test against observations and model outputs.
- The occurrence of MRCI does not explicitly rely on the vertical structure of

the convective fluxes; however, its growth rate relies on the vertical structure of water vapor, and convection is important for vertical redistribution of water vapor.

- It is valid in the optically thin and the optically thick limits, and can be easily used at any surface temperature and column water vapor, particularly if real-gas radiative transfer models are used.

Our results show mixed agreement with the studies of Wing and Emanuel [2014] and Emanuel et al. [2014]. In agreement with previous work, our results with the gray approximation do suggest a threshold in RCE column water vapor below which RCE is stable. The threshold, however, is sensitive to both the basic-state clouds and the vertical structure of water vapor perturbation. Note that Emanuel et al. [2014] suggested a temperature-based instability threshold of $\sim 35\text{-}40^\circ\text{C}$, but as they used radiative transfer calculations with varied r_s to make this deduction, their temperature limit may be considerably too high. Additionally, real-gas radiative modeling suggests that multiple thresholds may exist in certain cases, as different wavelengths in the infrared become opaque at different column water vapor values. Thus, although the notion of a single temperature threshold simplifies the conceptual understanding of MRCI, it is not accurate for real-gas radiation, especially when clouds and shortwave feedbacks are included.

When MRCI is satisfied, an anomalously moist atmospheric column induces a large-scale ascent and moisture convergence. The vertical structure of this circulation can play an important role in amplifying or damping the radiation-water vapor instability [e.g., Muller and Bony, 2015]. Furthermore, our idealized model of clouds shows how MRCI can be satisfied for dry atmospheres in the presence of low thick clouds, consistent with the results of Coppin and Bony [2015] at low temperatures. It is important to note that MRCI is defined at fixed surface temperature and surface fluxes, meaning that this instability is entirely separate from the wind induced surface heat exchange mechanism [Emanuel, 1987]. Studies of self-aggregation, however, have shown that radiation and surface flux feedbacks usually act in concert early in

the process of aggregation, so MRCI may be amplified by feedbacks between column water vapor and surface turbulent fluxes [Wing and Emanuel, 2014, Wing and Cronin, 2016]. Note also that MRCI is defined at a fixed temperature profile, so there is no negative Planck feedback associated with increasing column water vapor; MRCI is not linked with the runaway greenhouse effect [Ingersoll, 1969, Pujol, 2002].

This work points to many open questions about self-aggregation and moisture-radiative cooling instability. Most pertinent to the work that we have shown here is the question: what determines the vertical structure of moisture perturbations? One approach to the problem would be to formulate the coupling between moisture, radiative cooling, and large-scale convergence of moisture as an eigenvalue problem, fixing the convective heating and moistening rates for simplicity. Preliminary investigation suggests that this is a rich problem, which may give intense non-normal growth but no unstable normal modes, due to the tendency of radiative cooling anomalies to propagate downward [e.g., Figure 4 of Emanuel et al., 2014]. Our work also suggests that observation-based investigation of the correlation between cloud and moisture anomalies would be important to constrain the magnitude of MRCI growth rates in the real world. Finally, we note that MRCI may be relevant to the regulation of climates on other worlds, with “moisture” representing a general condensible greenhouse gas (e.g., methane on Titan) – and that MRCI is likely to be of particular importance on slowly-rotating worlds with wide “tropics” in the habitable zone.

2.6 Appendix A: Analytical form of the longwave radiative fluxes

To compute the longwave radiative fluxes, the first step is to substitute the temperature as a function of the optical thickness (2.13) in the Schwarzschild equations (2.10) and (2.11), yielding:

$$\frac{d\mathcal{F}_\uparrow}{d\tau} = \mathcal{F}_\uparrow - \sigma T_s^4 \left(\frac{\tau}{\tau_s} \right)^\alpha, \quad (2.27)$$

$$\frac{d\mathcal{F}_\downarrow}{d\tau} = -\mathcal{F}_\downarrow + \sigma T_s^4 \left(\frac{\tau}{\tau_s} \right)^\alpha. \quad (2.28)$$

The boundary conditions in the longwave are:

- No downwelling flux at the top of the atmosphere: $\mathcal{F}_\downarrow(\tau = 0) = 0$.
- The surface radiates like a blackbody of temperature T_s : $\mathcal{F}_\uparrow(\tau = \tau_s) = \sigma T_s^4$.

The fixed surface temperature T_s , the total optical thickness τ_s , and the exponent α are independent of τ . Thus, we can integrate equation (2.27) from $\tau' = \tau$ to $\tau' = \tau_s$, and equation (2.28) from $\tau' = 0$ to $\tau' = \tau$:

$$\frac{\mathcal{F}_\uparrow(\tau)}{\sigma T_s^4} = e^{-(\tau_s - \tau)} + \int_\tau^{\tau_s} d\tau' \left(\frac{\tau'}{\tau_s} \right)^\alpha e^{-(\tau' - \tau)}, \quad (2.29)$$

$$\frac{\mathcal{F}_\downarrow(\tau)}{\sigma T_s^4} = \int_0^\tau d\tau' \left(\frac{\tau'}{\tau_s} \right)^\alpha e^{-(\tau - \tau')}. \quad (2.30)$$

The radiative fluxes (2.15), (2.16) and (2.17) can then be obtained from the upwelling and downwelling longwave fluxes (2.29) and (2.30).

2.7 Appendix B: Dependence of MRCI on surface temperature

MRCI is studied at fixed surface temperature \overline{T}_s , and its characteristics (e.g., its growth rate) depend directly and indirectly on \overline{T}_s . First, the moist adiabatic lapse rate

Γ_m is a function of the atmospheric temperature, and decreases with warming [e.g., Holton, 1973]. Thus, the exponent α defined by (2.13) also decreases with increasing \overline{T}_s . Second, the RCE surface mixing ratio depends on the saturation mixing ratio at the surface, which exponentially increases with increasing \overline{T}_s .

We find that the critical threshold \hat{r}_{crit} for MRCI decreases with increasing surface temperature, and typical MRCI growth rates decrease with increasing surface temperature (Figure 2-12). Physically, the atmosphere has a smaller lapse rate for higher surface temperatures, leading to a smaller change in the effective upward emission temperature for a given change in emission height. Thus, the OLR decreases less for a given moistening of the atmosphere, raising \hat{r}_{crit} and decreasing the MRCI growth rate. Effects of varying r_s with temperature are more subtle, but we have found that an increase in the lapse rate Γ_m at constant r_s , as well as an increase in r_s at constant Γ_m , both lead to an increase in \hat{r}_{crit} and a decrease in growth rate.

In Figure 2-13, we check that $\hat{r}_{\text{crit}}(T_s)$ increases slowly enough with temperature to still obtain a surface temperature threshold \overline{T}_s for MRCI, consistent with Wing and Emanuel [2014]. The typical RCE column water vapor profile as a function of \overline{T}_s was numerically computed using the toy model of Beucler and Emanuel [2016]. Note that the temperature threshold is sensitive to the water vapor profile and the cloud cover. Furthermore, the notion of a single temperature threshold only applies for gray radiation, whereas we have seen in section 2.3 that real-gas radiation can exhibit multiple thresholds or none.

2.8 Appendix C: Cloudy radiative fluxes

In Figure 2-6, we defined a cloud by its optical thickness $\Delta\tau$ and its pressure level p_c , so that the atmospheric optical thickness is given by:

$$\frac{\tau}{\tau_s} = \begin{cases} (p/p_s)^{n+2} & \text{if } p \leq p_c \\ (p/p_s)^{n+2} + \Delta\tau/\tau_s & \text{if } p \geq p_c \end{cases}. \quad (2.31)$$

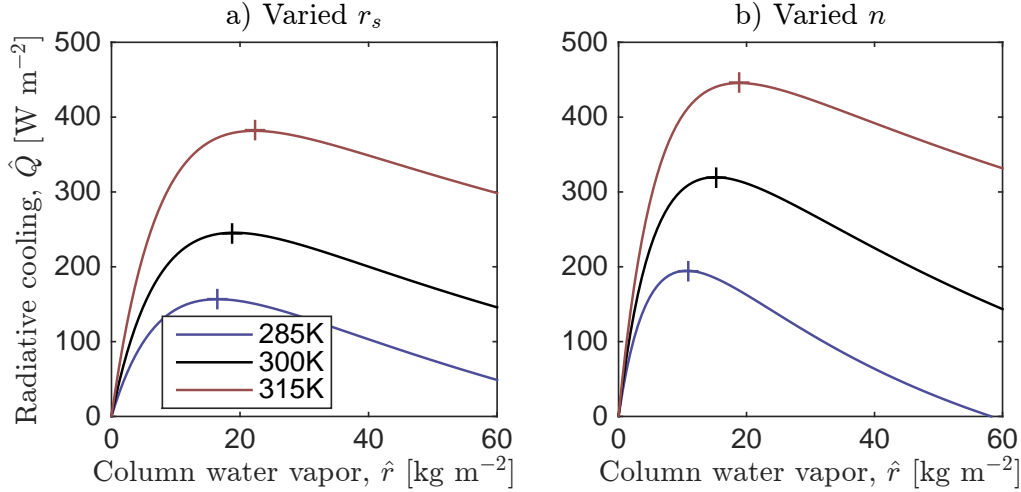


Figure 2-12: Total \hat{Q} clear-sky radiative cooling as a function of column water vapor, a) varying the surface mixing ratio at fixed shape, and b) varying the water vapor profile shape at constant surface mixing ratio, for three different choices of surface temperature. Crosses show maxima of radiative cooling.

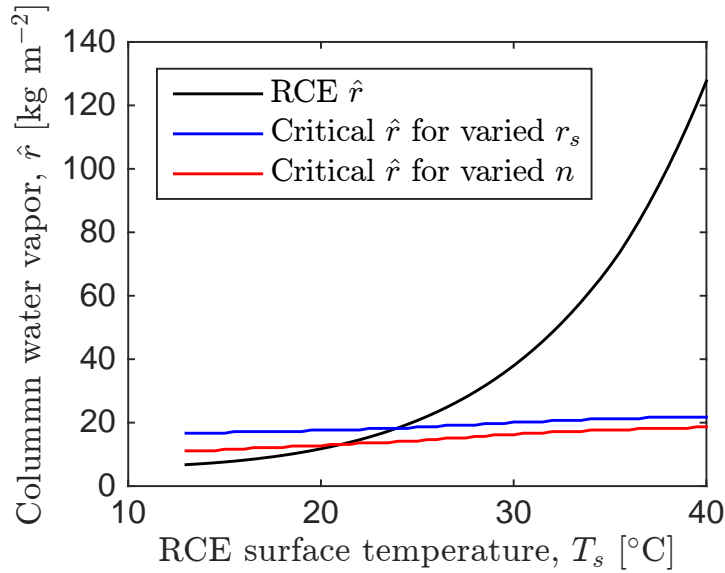


Figure 2-13: RCE column water vapor (black line) and critical column water vapor threshold \hat{r}_{crit} , as a function of the surface temperature. On the left of the intersection point, RCE is stable. On the right of the intersection point, MRCI is satisfied. We obtain approximate surface temperature thresholds of 21 $^{\circ}\text{C}$ for varied shape, and 24 $^{\circ}\text{C}$ for varied surface mixing ratio. These values should be taken as illustrative rather than exact, and are sensitive to model assumptions.

By combining the temperature profile (2.9) to the cloudy optical thickness profile (2.31), we can express the temperature as a function of the optical thickness in the presence of a cloud:

$$\frac{T}{T_s} = \begin{cases} (\tau/\tau_s)^{\alpha/4} & \text{if } \tau \leq \tau_c \\ (T_c/T_s) & \text{if } \tau_c \leq \tau \leq \tau_c + \Delta\tau \\ [(\tau - \Delta\tau)/\tau_s]^{\alpha/4} & \text{if } \tau \geq \tau_c + \Delta\tau \end{cases}.$$

We have defined the optical thickness τ_c right above the cloud:

$$\tau_c \stackrel{\text{def}}{=} \tau_s \left(\frac{p_c}{p_s} \right)^{n+2},$$

so that the cloud can be found between τ_c and $\tau_c + \Delta\tau$ in optical thickness coordinates. The cloud has a constant temperature T_c , set by the moist adiabatic temperature at pressure level p_c :

$$T_c \stackrel{\text{def}}{=} T_s \left(\frac{p_c}{p_s} \right)^{\alpha_0/4},$$

where we have defined the introduced α_0 , defined by:

$$\alpha_0 \stackrel{\text{def}}{=} (n + 2)\alpha = \frac{4\Gamma_m R_d}{g}, \quad (2.32)$$

Integrating equations (2.27) and (2.28) in the presence of a cloud, between the ground at $\tau = \tau_s + \Delta\tau$ and the top of the atmosphere at $\tau = 0$, leads to the following total

radiative cooling:

$$\begin{aligned}
\frac{\hat{Q}}{\sigma T_s^4} = & \underbrace{-1}_{\text{Surface} \rightarrow \text{Atmosphere}} + \underbrace{e^{-(\tau_s + \Delta\tau)}}_{\text{Atmosphere} \rightarrow \text{Space}} - \underbrace{\frac{S}{\sigma T_s^4} (1 - e^{-\varepsilon\tau_s})}_{\text{Shortwave absorption}} \\
& + \underbrace{\int_0^{\tau_c} d\tau' \left(\frac{\tau'}{\tau_s}\right)^\alpha \left(e^{-(\tau_s + \Delta\tau - \tau')} + e^{-\tau'}\right)}_{\text{Emission of atmosphere above cloud}} + \underbrace{\int_{\tau_c + \Delta\tau}^{\tau_s + \Delta\tau} d\tau' \left(\frac{\tau' - \Delta\tau}{\tau_s}\right)^\alpha \left(e^{-(\tau_s + \Delta\tau - \tau')} + e^{-\tau'}\right)}_{\text{Emission of atmosphere below cloud}} \\
& + 2 \underbrace{\left(\frac{T_c}{T_s}\right)^4 \sinh\left(\frac{\Delta\tau}{2}\right) \left(e^{-(\tau_c + \frac{\Delta\tau}{2})} + e^{-(\tau_s + \frac{\Delta\tau}{2} - \tau_c)}\right)}_{\text{Cloud emission}}
\end{aligned} \tag{2.33}$$

Note that we neglect the shortwave effects of the cloud entirely, using only clear-sky shortwave heating. In reality thick clouds reflect much of the incoming shortwave radiation back to space, which is then partially absorbed by the atmosphere above the cloud. This means that our model overestimates the shortwave radiative heating below the cloud, and underestimates the shortwave radiative heating above the cloud.

2.9 Appendix D: Growth rates of MRCI

According to equation (2.6), the growth rate of the instability (in units s^{-1}) is given by:

$$\overline{\left(\frac{\partial \hat{r}}{\partial \hat{r}}\right)} = -\frac{1}{L_v} \overline{\frac{\partial \hat{Q}}{\partial \hat{r}}}, \tag{2.34}$$

where the radiative cooling is given by equation (2.17) as a function of T_s , τ_s and α . We always study MRCI at fixed temperature T_s . First, we compute the growth rate at fixed shape (i.e., fixed exponent α); according to the chain rule:

$$\left(\frac{\partial \hat{r}}{\partial \hat{r}}\right)_\alpha = -\frac{1}{L_v} \left(\frac{\partial \hat{Q}}{\partial \hat{r}}\right)_\alpha = -\frac{1}{L_v} \left(\frac{\partial \tau_s}{\partial \hat{r}}\right)_\alpha \left(\frac{\partial \hat{Q}}{\partial \tau_s}\right)_\alpha. \tag{2.35}$$

By combining the expression for column water vapor (2.18) with the one for total optical thickness (2.14), we can express the total optical thickness as a function of

column water vapor and fixed parameters:

$$\tau_s = Dk \frac{n+1}{n+2} \hat{r} \Rightarrow \left(\frac{\partial \tau_s}{\partial \hat{r}} \right)_\alpha = Dk \frac{n+1}{n+2}. \quad (2.36)$$

We finally combine equations (2.35), (2.36), and use the Leibniz rule to compute the growth rate at fixed shape:

$$\begin{aligned} \frac{L_v}{kD\sigma T_s^4} \frac{n+2}{n+1} \left(\frac{\partial \dot{\hat{r}}}{\partial \hat{r}} \right)_\alpha &= - \left(\frac{\partial}{\partial \tau_s} \right)_\alpha \frac{\hat{Q}}{\sigma T_s^4} \\ &= -1 + \int_0^{\tau_s} d\tau' \left(\frac{\tau'}{\tau_s} \right)^\alpha \left[\left(1 + \frac{\alpha}{\tau_s} \right) e^{-(\tau_s - \tau')} + \frac{\alpha e^{-\tau'}}{\tau_s} \right]. \end{aligned} \quad (2.37)$$

Computing the growth rate at fixed surface mixing ratio (i.e., fixed r_s) is more involved, as both τ_s and α now vary with \hat{r} ; according to the chain rule:

$$\left(\frac{\partial \dot{\hat{r}}}{\partial \hat{r}} \right)_{r_s} = -\frac{1}{L_v} \left[\left(\frac{\partial \tau_s}{\partial \hat{r}} \right)_{r_s} \left(\frac{\partial \hat{Q}}{\partial \tau_s} \right)_\alpha + \left(\frac{\partial \alpha}{\partial \hat{r}} \right)_{r_s} \left(\frac{\partial \hat{Q}}{\partial \alpha} \right)_{\tau_s} \right]. \quad (2.38)$$

We now need to relate the exponent α to column water vapor \hat{r} and fixed parameters, which can be done by combining the definition of α (2.13) to the expression (2.1) for column water vapor:

$$\alpha = \frac{\alpha_0 \hat{r}}{\hat{r}_s + \hat{r}} \Rightarrow \left(\frac{\partial \alpha}{\partial \hat{r}} \right)_{r_s} = \frac{\alpha_0 \hat{r}_s}{(\hat{r}_s + \hat{r})^2}. \quad (2.39)$$

We have introduced two fixed parameters: the coefficient α_0 , defined by equation (2.32), and the hypothetical value of the column water vapor if the mixing ratio was equal to r_s everywhere:

$$\hat{r}_s \stackrel{\text{def}}{=} \frac{r_s p_s}{g}. \quad (2.40)$$

Combining equations (2.14), (2.18) to the definitions (2.32) and (2.40), it is possible to express τ_s as a function of \hat{r} and fixed parameters:

$$\tau_s = \frac{kD\hat{r}_s\hat{r}}{\hat{r}_s + \hat{r}} \Rightarrow \left(\frac{\partial \tau_s}{\partial \hat{r}} \right)_{r_s} = kD \left(\frac{\hat{r}_s}{\hat{r}_s + \hat{r}} \right)^2. \quad (2.41)$$

We finally combine equations (2.38), (2.39), (2.41), and use the Leibniz rule to compute the growth rate at fixed surface mixing ratio:

$$\begin{aligned}
\frac{L_v}{kD\sigma T_s^4} \left(\frac{\hat{r}_s + \hat{r}}{\hat{r}_s} \right)^2 \left(\frac{\partial \hat{r}}{\partial \hat{r}} \right)_{r_s} &= - \left[\left(\frac{\partial}{\partial \tau_s} \right)_\alpha + \frac{\alpha_0}{kD\hat{r}_s} \left(\frac{\partial}{\partial \alpha} \right)_{\tau_s} \right] \frac{\hat{Q}}{\sigma T_s^4} \\
&= -1 + \int_0^{\tau_s} d\tau' \left(\frac{\tau'}{\tau_s} \right)^\alpha \times \\
&\quad \left[\left(1 + \frac{\alpha}{\tau_s} \right) e^{-(\tau_s - \tau')} + \frac{\alpha e^{-\tau'}}{\tau_s} - \frac{\alpha_0 \log \left(\frac{\tau'}{\tau_s} \right)}{kD\hat{r}_s} \left(e^{-(\tau_s - \tau')} + e^{-\tau'} \right) \right]
\end{aligned} \tag{2.42}$$

2.10 Appendix E: Two-band longwave radiative transfer

A two-band longwave radiative transfer model can be used to distinguish between wavelengths with strong absorption and those with weak absorption, and provides a much better representation of real-gas radiative transfer for water vapor than a single gray-gas absorption coefficient. We assume that the two bands contain fractional amounts of the longwave spectrum that do not vary with temperature, as in the windowed-gray model of Weaver and Ramanathan [1995]. For strongly-absorbing wavelengths – corresponding roughly to both the pure rotational bands of water vapor at wavelengths $> 15\mu\text{m}$, and the ro-vibrational complex centered at $6.3\mu\text{m}$ – we use a large absorption coefficient $k_{\text{LW},1} = 1 \text{ m}^2 \text{ kg}^{-1}$. For weakly-absorbing wavelengths – including the major spectral window with wavelength 8-15 μm and the less important window to the shortwave side of 5 μm – we use a much smaller absorption coefficient $k_{\text{LW},2} = 0.02 \text{ m}^2 \text{ kg}^{-1}$. As these spectral regions occupy roughly equal fractions of blackbody emission at $\sim 300 \text{ K}$, the two-band longwave fluxes are simply given by an average of the broadband flux in the strongly-absorbing regions and the weakly-absorbing ones. For example, the radiative cooling is given by:

$$\hat{Q}_{L,\text{two-band}} = \frac{\hat{Q}_{L,1} + \hat{Q}_{L,2}}{2}, \tag{2.43}$$

where we have used the gray longwave radiative cooling \widehat{Q}_L given by equation (2.17), with subscripts 1 and 2 indicating that $k_{LW,1}$ is used to calculate half of the radiative cooling, and $k_{LW,2}$ is used for the other half. The two-band SLW, OLR and radiative cooling as a function of column water vapor are depicted in figure 2-14, and compare well with the real-gas radiative cooling rates (Figure 2-8). The strongly-absorbing regions saturate very quickly, which explains the sharp decrease of the SLW for small values of the column water vapor (a few kg m^{-2}). In contrast, the weakly-absorbing windows only saturate for a very large amount of column water vapor (larger than 100 kg m^{-2} , higher than values seen on Earth). As a consequence, the two-band model captures the occurrence of MRCI at varied shape (varied n), where the SLW decreases slowly enough with \hat{r} for the longwave radiative cooling \widehat{Q}_L to decrease with \hat{r} as well.

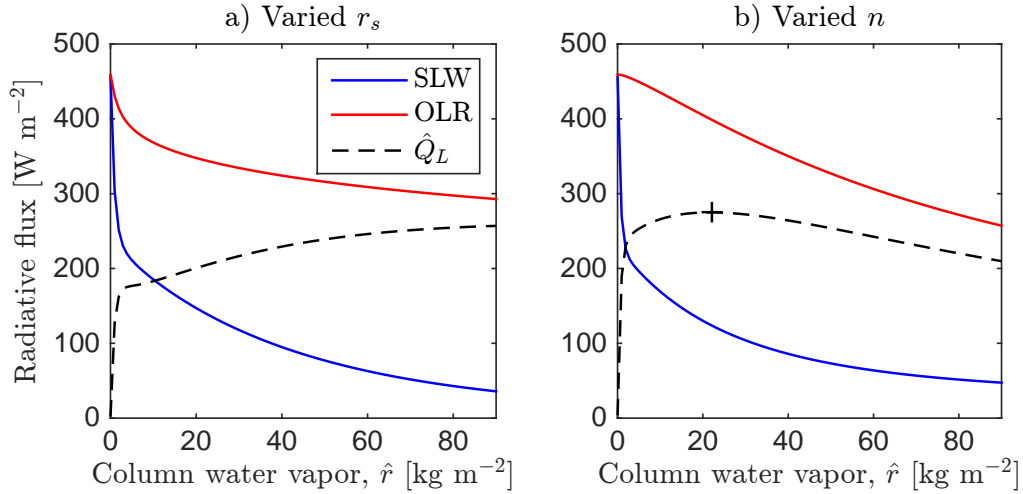


Figure 2-14: Two-band outgoing longwave radiation (OLR), surface net longwave radiation (SLW), and longwave clear-sky radiative cooling \widehat{Q}_L as a function of column water vapor \hat{r} , a) varying the surface mixing ratio at fixed shape, and b) varying the water vapor profile shape at constant surface mixing ratio. Crosses show maxima of radiative cooling.

Chapter 3

A Linear Response Framework for Radiative-Convective Instability

Abstract

Radiative-convective equilibrium (RCE) is a simple paradigm for the tropical climate, in which radiative cooling balances convective heating in the absence of lateral energy transport. Recent studies have shown that a large-scale circulation may spontaneously develop from RCE through the interactions among water vapor, radiation, and convection. This potential instability, referred to as radiative-convective instability, may be posed as a linear stability problem for the water vapor profile by combining a linear response framework with the weak temperature gradient approximation. We design two analytic models of convective linear response to moisture perturbations, which are similar to Betts-Miller and bulk-plume convection schemes. We combine these convective responses with either clear-sky gray or real-gas radiative responses. In all cases, despite consistent radiative feedbacks, the characteristics of convection dominate the vertical structure of the most unstable linear mode of water vapor perturbations. For Betts-Miller convection, the stability critically depends on a key parameter: the heating to advection of moisture conversion rate (HAM); warmer atmospheres with higher HAM exhibit more linear instability. In contrast, bulk-plume convection is stable across temperatures, but becomes linearly unstable with a moisture mode peaking in the mid-troposphere once combined to radiation, with approximate growth rates of 10 days.

3.1 Introduction

Radiative-convective equilibrium (RCE) is the state of the atmosphere in which convective heating balances radiative cooling without lateral transport of moisture or energy [e.g., review by Ramanathan and Coakley, 1978]. Although RCE is a natural basic state for the tropical atmosphere, its stability to small water vapor perturbations remains poorly understood, because of the complexity of the interaction among atmospheric water vapor, clouds, radiation, and convection. Water vapor directly interacts with radiation by changing the local emissivity of the atmosphere and the vertical structure of atmospheric radiative cooling. Furthermore, water vapor indirectly interacts with radiation by influencing the formation of clouds. Both of these interactions have the potential to amplify water vapor perturbations: they have been found to be important for spontaneous cyclogenesis [e.g., Wing et al., 2016], and the self-aggregation of convection, through mechanism denial experiments [e.g., Bretherton et al., 2005, Muller and Held, 2012, Holloway and Woolnough, 2016] and energy budgets [e.g., Wing and Emanuel, 2014, Wing and Cronin, 2016]. These interactions depend on temperature [e.g., Emanuel et al., 2014, Beucler and Cronin, 2016], clouds, and the structure of the moisture perturbation [e.g., Beucler and Cronin, 2016], making them inseparable from atmospheric convection. The interaction between water vapor and convection has been studied in the contexts of the Madden-Julian oscillation [e.g., Hannah and Maloney, 2011, Grabowski and Moncrieff, 2004] and the self-aggregation of convection in convection-permitting models [e.g., Muller and Bony, 2015, Tompkins, 2001]. The unstable nature of this interaction has been referred to as the moisture-convection feedback, and its physics remain unclear. This feedback could rely on updrafts being less cooled by entrainment in a moist environment [e.g., Tompkins, 2001, Mapes and Neale, 2011, Holloway and Neelin, 2009], or on an anomalously moist boundary layer favoring convection by increasing local buoyancy [e.g., Wing et al., 2017]. Because these interactions have been diagnosed from non-linear numerical models, their physical mechanisms are intertwined and hard to interpret, motivating the question:

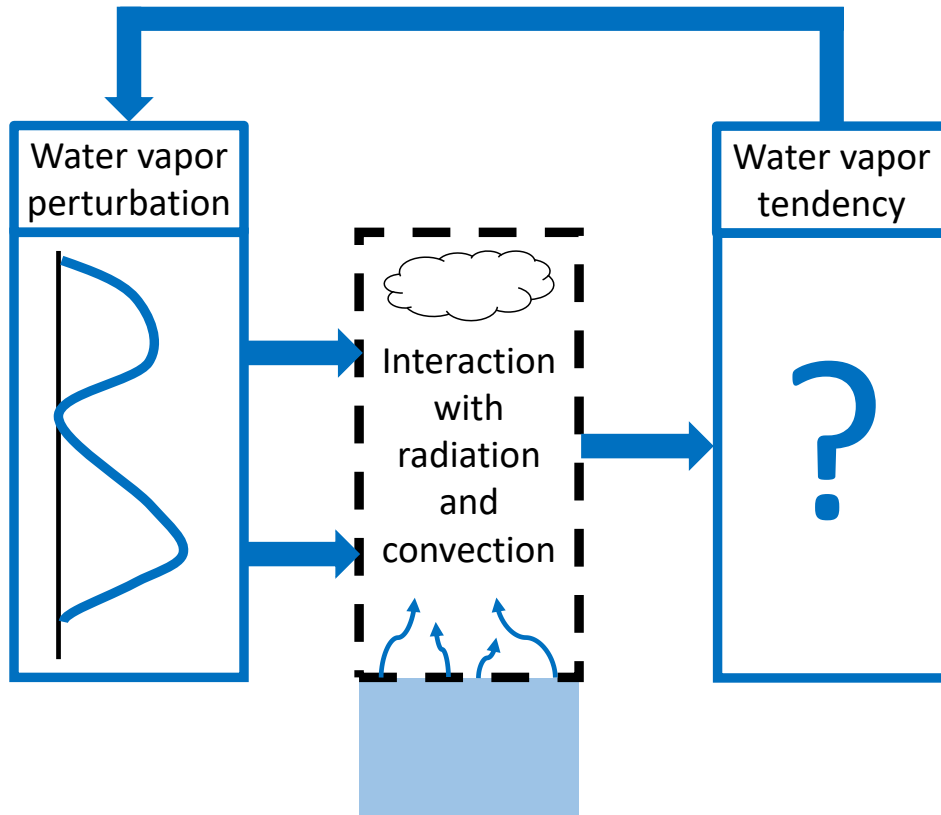


Figure 3-1: The interaction of a water vapor perturbation with atmospheric radiation and convection leads to a water vapor tendency that can amplify, damp, or move the perturbation.

What physical mechanisms govern the interactions between water vapor and convection, and between water vapor and radiation, and how do these interactions affect the evolution of a water vapor perturbation?

In this chapter, we use a bottom-up approach to diagnose the physics of the interactions among water vapor, radiation, and convection, near a basic state of RCE. To keep the problem tractable, we neglect cloud-radiation interactions and focus on clear-sky radiation. By examining the effect of a water vapor perturbation on both atmospheric convection and radiation, we predict how a water vapor perturbation would evolve over a time scale of ~ 10 days (Figure 3-1). We adopt a linear response approach to quantitatively evaluate the separate contributions from convective heating and moistening, as well as from longwave and shortwave radiative heating. We

parametrize large-scale dynamics by using the weak temperature gradient (WTG) framework [e.g., Sobel et al., 2001], where temperatures are fixed and the net residual heating from convection and radiation drives large-scale vertical motions. Each section of this chapter addresses a separate question:

(Section 3.2) How can the water vapor tendency profile be computed from the water vapor perturbation profile in the weak temperature gradient framework?

(Section 3.3) How does atmospheric convection linearly respond to water vapor perturbations?

(Section 3.4) How does atmospheric radiation linearly respond to water vapor perturbations?

(Section 3.5) How do small water vapor perturbations evolve as a consequence of their influences on atmospheric radiation and convection?

Sections 3.3 to 3.5 can be read independently, and cross-references are included when necessary.

3.2 Linear response framework

3.2.1 Linear response function

This section aims to relate the evolution of a small water vapor perturbation to its effects on radiative and convective diabatic tendencies. For that purpose, we consider a non-rotating atmospheric domain that is large enough (e.g. 100km in the Tropics) to include both a small cloudy area with deep convective ascent [typically a few percent of the total domain, e.g., Malkus et al., 1961, Bjerknes, 1938], and a large clear area with slow subsidence.

Following Arakawa and Schubert [1974], Yanai et al. [1973], we assume that the domain's dry static energy s [defined as the sum of the sensible heat and the potential energy, e.g., Yanai et al., 1973] and specific humidity q can both be approximated by their clear-sky values. Furthermore, the domain is assumed to be much smaller

than the Rossby radius of deformation and the timescale much longer (e.g. 1 day) than the gravity wave adjustment timescale, so that the weak temperature gradient approximation holds in the free troposphere. Examples of strict WTG in the literature include the neglect of the free-tropospheric temperature tendency in section 4 of Sobel and Bretherton [2000] or below equation 2 of Sobel et al. [2003], and the neglect of ΔT except for the radiative perturbation in equation A4d of *Adames and Kim* [2016]. Here, the strict version of the WTG approximation allows us to neglect the local tendency of dry static energy ($\partial s/\partial t = 0$, where t represents time). The domain-averaged free-tropospheric budgets of dry static energy and specific humidity are then given by:

$$\begin{aligned} \omega \frac{\partial s}{\partial p} &= g \left(\frac{\partial \mathcal{F}_{\text{DSE}}}{\partial p} + \frac{\partial \mathcal{F}_{\text{LW}}}{\partial p} + \frac{\partial \mathcal{F}_{\text{SW}}}{\partial p} \right), \\ \frac{\partial q}{\partial t} + \vec{u} \cdot \vec{\nabla} q + \omega \frac{\partial q}{\partial p} &= \frac{g}{L_v} \frac{\partial \mathcal{F}_{\text{LH}}}{\partial p}, \end{aligned} \quad (3.1)$$

where \vec{u} is the large-scale horizontal velocity, $\vec{\nabla}$ the horizontal gradient operator, ω the large-scale vertical velocity (in units of Pa s^{-1}), defined as the area-weighted average of the ascending motion in the cloudy zone and the subsidence motion in the clear-sky zone, p the atmospheric pressure and g is the gravitational acceleration. \mathcal{F}_{DSE} is the convective dry static energy flux, \mathcal{F}_{LW} the net longwave flux, \mathcal{F}_{SW} the net shortwave flux, and \mathcal{F}_{LH} the convective latent heat flux, all defined in units of W m^{-2} . The evaporation and condensation rates of hydrometeors are included in the convective heating and moistening tendencies. L_v is the latent heat of vaporization of water vapor, and we neglect the latent heat of fusion. Radiative-convective equilibrium (RCE) is defined as the statistically steady state of the previous equations ($\partial/\partial t = 0$), with no large vertical velocity $(\vec{\nabla}, \omega) = (\vec{0}, 0)$. From now on, we denote deviations from RCE with primes (X'), while unprimed variables (X) denote RCE. We linearize the previous equation about the basic state, RCE, by assuming that the deviations X' are small compared to the basic-state statistical mean \bar{X} . Assuming that the WTG approximation strictly holds for deviations from RCE, the

linearized version of equations 3.1 is:

$$\begin{aligned}\omega' \frac{\partial s}{\partial p} &= g \left(\frac{\partial \mathcal{F}'_{\text{DSE}}}{\partial p} + \frac{\partial \mathcal{F}'_{\text{LW}}}{\partial p} + \frac{\partial \mathcal{F}'_{\text{SW}}}{\partial p} \right), \\ \frac{\partial q'}{\partial t} + \omega' \frac{\partial q}{\partial p} &= \frac{g}{L_v} \frac{\partial \mathcal{F}'_{\text{LH}}}{\partial p}.\end{aligned}\tag{3.2}$$

Combining the two previous equations in order to eliminate ω' relates the evolution of the perturbation specific humidity to the perturbation fluxes:

$$\underbrace{\frac{\partial q'}{\partial t}}_{\text{Moisture tendency}} = \frac{g}{L_v} \left[\underbrace{\frac{\partial \mathcal{F}'_{\text{LH}}}{\partial p}}_{\text{Convective moistening}} + \alpha \left(\underbrace{\frac{\partial \mathcal{F}'_{\text{DSE}}}{\partial p}}_{\text{Convective heating}} + \underbrace{\frac{\partial \mathcal{F}'_{\text{LW}}}{\partial p}}_{\text{Longwave heating}} + \underbrace{\frac{\partial \mathcal{F}'_{\text{SW}}}{\partial p}}_{\text{Shortwave heating}} \right) \right],\tag{3.3}$$

where we have introduced the non-dimensional parameter α that relates heating sources to vertical advection of water vapor:

$$\alpha \stackrel{\text{def}}{=} -\frac{L_v \partial q / \partial p}{\partial s / \partial p} > 0.\tag{3.4}$$

This parameter has been previously introduced by Chikira [2014], studied in the context of the Madden-Julien oscillation moisture-convective feedback in Wolding et al. [2016], and corresponds to the ratio $-M_q/M_s$ in equations 1 and 2 of Sobel et al. [2003]. From now on, we refer to α as the heating-to-advection-of-moisture (HAM) conversion factor (it is positive-definite so long as dry static energy increases with height and specific humidity decreases with height). HAM is essentially an exchange rate between the heating rate and the latent heat tendency in WTG; a value greater than 1 indicates that 1 W kg⁻¹ of heating will translate into more than 1 W kg⁻¹ of latent heat tendency due to vertical advection by WTG-derived vertical motion. Since $\alpha \stackrel{\text{def}}{=} 1 - (\partial \text{MSE} / \partial p) (\partial s / \partial p)^{-1}$, where $\text{MSE} \stackrel{\text{def}}{=} s + L_v q$ is the moist static energy, a decrease of moist static energy with height implies $\alpha > 1$, whereas an increase of moist static energy with height implies $\alpha < 1$. Tropical profiles of moist static energy generally have a "C" shape of moist static energy with a mid-tropospheric minimum; $\alpha > 1$ below this minimum and $\alpha < 1$ above it. $1 - \alpha$ is closely related to the

local definition of normalized gross moist stability (see equation 2 of Kuang [2012]), which usually corresponds to convective amplification when negative through the net import of moisture in the lower troposphere. Finally, although we will assume a base RCE state for the rest of this study, this framework could be generalized to a base state with mean velocity (\vec{u}, \bar{w}) by adding $\vec{u} \cdot \vec{\nabla}q + \bar{w}\partial q/\partial p$ on the left-hand side of the moisture equation 3.1, $\vec{u} \cdot \vec{\nabla}q' + \bar{w}\partial q'/\partial p$ on the left-hand side of the moisture equation 3.2, and $-\vec{u} \cdot \vec{\nabla}q' - \bar{w}\partial q'/\partial p$ on the right-hand side of equation 3.3.

In summary, equation 3.3 states that under the WTG approximation, specific humidity is changed directly by the local perturbation convective moistening, and also by the local perturbation convective, longwave and shortwave heating rates through the effect they have on the large-scale vertical velocity. Furthermore, equation 3.3 gives a framework to study the linear instability of water vapor perturbations. RCE is an equilibrium state, meaning that the right-hand side of equation 3.3 is zero in RCE. Therefore, the behavior of small water vapor perturbations is determined by the value of the Jacobian in RCE [as long as it does not have eigenvalues with zero real parts, e.g., Hartman, 1960]:

$$\frac{\partial}{\partial q'} \left[\frac{\partial q'}{\partial t} \right]_{\text{RCE}} = \frac{g}{L_v} \left[\frac{\partial^2 \mathcal{F}_{\text{LH}}}{\partial p \partial q'} + \alpha \left(\frac{\partial^2 \mathcal{F}_{\text{DSE}}}{\partial p \partial q'} + \frac{\partial^2 \mathcal{F}_{\text{LW}}}{\partial p \partial q'} + \frac{\partial^2 \mathcal{F}_{\text{SW}}}{\partial p \partial q'} \right) \right]_{\text{RCE}}, \quad (3.5)$$

where the subscript RCE means that the bracketed quantities are evaluated in radiative-convective equilibrium, in which $q' = 0$ by definition. Equation 3.5 is the WTG continuous version of equations (7) and (25) of [Emanuel et al., 2014], respectively valid for a finite number of layers and two layers. If the Jacobian has at least one eigenvalue with positive real part, RCE may be unstable to small water vapor perturbations. In models and observations, we work on discrete pressure levels, motivating the introduction of the discrete counterpart to the Jacobian: the linear response matrix.

3.2.2 Linear response matrix

We start by defining discrete levels of the atmosphere: $i = 1, 2, \dots, N$. For short time periods following a small water vapor perturbation, we expect the atmosphere

to respond linearly, and the discrete version of equation 3.5 is:

$$\frac{dq'_i}{dt} = \sum_{j=1}^N M_{ij} \cdot q'_j, \quad (3.6)$$

where q'_j is the specific humidity perturbation at a level j , dq'_i/dt the specific humidity tendency in response to that perturbation at a level i , and M the linear response matrix in units s^{-1} , defined as the discrete counterpart of the continuous Jacobian. The linear response function approach has been used by Kuang [2010] to study convectively-coupled waves, and also by Herman and Kuang [2013] to study the moistening and heating responses of several convective parameterizations. Here, the atmospheric temperature profile is fixed, making the linear response function a single two-dimensional matrix rather than a set of four matrices as in the work by Kuang [2010, 2012]. The interpretation of our single linear response matrix is described in Figure 3-2. In a model with equally-spaced pressure levels, the column-integrated growth rate of a localized perturbation at level p_j , \widehat{M}_j (in s^{-1}) may be directly computed from the linear response matrix:

$$\widehat{M}_j = \sum_{i=1}^N M_{ij}. \quad (3.7)$$

Using this matrix, we can predict the evolution of the structure and magnitude of a small water vapor perturbation $q'_i(t)$ as:

$$q'_i(t) = (\exp Mt)_{ij} \cdot q'_j(t=0) \quad (3.8)$$

for small times, where we have exponentiated the linear response matrix:

$$\exp Mt \stackrel{\text{def}}{=} \sum_{n=0}^{\infty} \frac{(Mt)^n}{n!}.$$

If M has at least one eigenvalue with positive real part, RCE may be unstable to a small initial perturbation $q'_j(t=0)$. From equation 3.6, we see that equal moist and

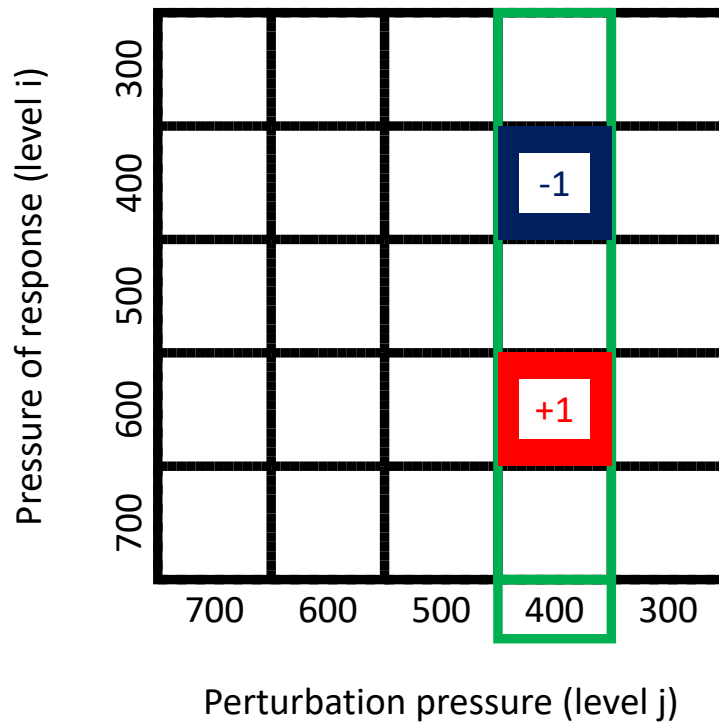


Figure 3-2: Guide to reading the linear response matrix M : The horizontal axis is the pressure at which water vapor is perturbed (p_j , in hPa), while the vertical axis is the pressure of the water vapor response (p_i , in hPa). In the example depicted above, water vapor is perturbed at $p_j = 400$ hPa, and the water vapor tendency response can be read in the green column. At the local perturbation level $p_i = 400$ hPa, a negative matrix element indicates that a perturbation would decay in time; below the perturbation level at $p_i = 600$ hPa, a positive matrix element indicates that a perturbation would amplify in time. In this simple case, a water vapor perturbation at 400 hPa would be moved to 600 hPa at a unit rate.

dry perturbations yield opposite responses, which is a consequence of using a linear framework. Therefore, an atmospheric model should produce symmetric responses to opposite-signed perturbations if it is working in its linear range, which allows testing of the linear assumption [(e.g., appendix B1 of Herman and Kuang, 2013)]. In order to gain more insight into the interactions among water vapor, radiation, and convection, we decompose M into four components by writing the discrete counterpart of equation 3.5:

$$\underbrace{M}_{\text{Linear response}} = \underbrace{M_{\text{LH}} + M_{\text{DSE}}}_{\text{Convective response}} + \underbrace{M_{\text{LW}} + M_{\text{SW}}}_{\text{Radiative response}}, \quad (3.9)$$

where M_{LH} is the convective moistening response, M_{DSE} the convective heating response, M_{LW} the longwave heating response and M_{SW} the shortwave heating response. We have incorporated the evaporation and condensation of hydrometeors in the convective response, which is valid as long as the perturbations are small enough not to saturate the domain at any level. Because the atmosphere is assumed to be close to RCE, there is no advective response on the right-hand side of equation 3.9. In RCE, gross moist stability [see Yu et al., 1998, Inoue and Back, 2015] is undefined, as there is no horizontal flow ($\vec{u} = 0$). However, once the system is perturbed, gross moist stability is internally determined by the vertical structure of the perturbation. If this internally-determined gross moist stability is negative, a column-integrated moist static energy perturbation may grow spontaneously, potentially indicating an unstable moisture-convection feedback. Some such scenarios of unstable moisture-convection feedback would be unphysical, if they occurred from a basic state with zero moist available potential energy. This could happen because of limitations of both the strict WTG approximation and convective parameterizations, neither of which necessarily enforces the physical requirement that circulations develop due to conversion of available potential energy to kinetic energy. The definition of moist available potential energy [e.g., Stansifer et al., 2017] is subtle, however, and further consideration of such possible unphysical moisture-convection instabilities is left as a subject for future work. We will now proceed to compute the linear response matrix in idealized and numerical models of convection and radiation.

3.3 Linear response of convection

The goal of this section is to gain physical insight into the linear convective response, defined as the sum of the convective moistening response M_{LH} and the convective heating response M_{DSE} . For that purpose, we analyze realistic convective responses from cloud-permitting simulations, before calculating analytic WTG linear convective responses based on toy models of convection similar to two widely used convective schemes.

3.3.1 Convection in cloud-permitting models

Linear response matrix of a cloud-permitting model

We start by analyzing realistic linear response matrices derived from a cloud-permitting model and provided by Zhiming Kuang following the methodology he described in Kuang [2010]. The System for Atmospheric Modeling [SAM Khairoutdinov et al., 2003] is run to RCE in a $128 \times 128 \text{km}^2$ square domain with 2km horizontal resolution and 28 vertical levels, as described in section 4 of Kuang [2012]. Kuang [2012] ran all simulations using a surface temperature of 301.15K, and integrated the perturbed runs for as long as 10,000 days to minimize the noise level of the linear response matrices. We calculate the WTG convective response matrix by adapting equation 3.3 to the convective responses of moisture to moisture perturbations (dq/dt from q') (in s^{-1}) and temperature to moisture perturbations (dT/dt from q') (in K/s per kg/kg) [respectively figures 8b and 8c from Kuang, 2012]:

$$\underbrace{M_{\text{LH}}}_{\text{Convective moistening}} = \left(\frac{dq}{dt} \text{ from } q' \right) \quad | \quad \underbrace{M_{\text{DSE}}}_{\text{Convective heating}} = \alpha \frac{c_p}{L_v} \left(\frac{dT}{dt} \text{ from } q' \right), \quad (3.10)$$

where c_p is the specific heat capacity of dry air at constant pressure and the HAM α is calculated from the mean thermodynamic profiles of the SAM RCE simulation of Kuang [2012]. The linear convective response, sum of the convective moistening

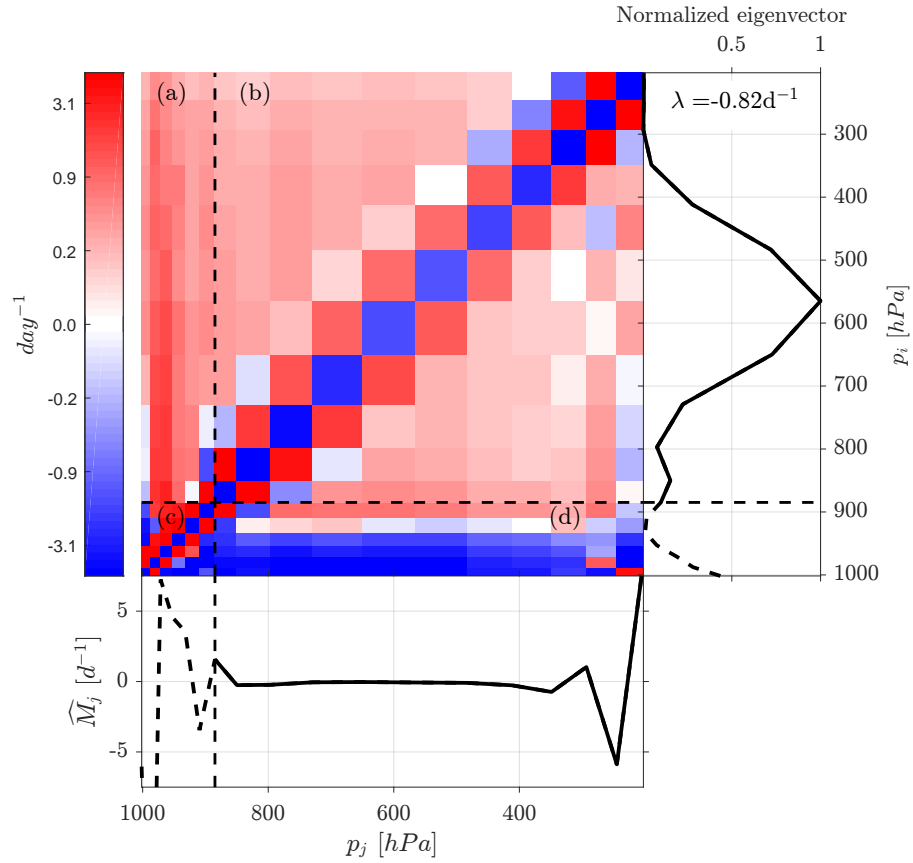


Figure 3-3: Linear convective matrix from the linear response matrices of Kuang [2012], where the HAM has been evaluated from the mean state of the simulation. The top of the boundary layer, identified as the relative humidity maximum in the lower troposphere, is indicated with dashed black lines. (Bottom panel) Vertically-integrated growth rate (\widehat{M}_j in day^{-1}). (Right panel) Eigenvector corresponding to the leading eigenvalue real part λ , normalized to have a maximum of 1.

and heating responses, is depicted in figure 3-3. We subdivide the convective linear response into four regions:

- (a) The strong free-tropospheric convective heating resulting from boundary-layer moisture perturbations,
- (b) The free-tropospheric convective heating and moistening responses to free-tropospheric moisture perturbations,
- (c) The local response to boundary-layer moisture perturbations (dominated by water vapor mixing),
- (d) The cooling and drying of the boundary layer resulting from free-tropospheric moisture perturbations.

Although combining convective heating and moistening responses into a single WTG response is always mathematically possible, it does not directly inform us on the evolution of water vapor perturbations in the boundary layer where WTG breaks down because of horizontal buoyancy gradients (regions a,c,d). In this study, we focus on explaining the free-tropospheric response to free-tropospheric perturbations (region b) and its consequences for the linear stability of water vapor perturbations. It is possible to separate the convective response into three separate components:

1. A local drying of moisture perturbations (blue diagonal), with strong local mixing of water vapor (red squares right above and right below the blue diagonal),
2. A tropospheric-uniform convective heating, which decreases with height due to the modulation by the HAM profile (red lower-right triangle and small part of the red upper-left triangle),
3. A combination of convective heating and moistening above the diagonal (most of the red upper-left triangle).

The combination of these three components leads to a stable convective response in RCE (the leading real eigenvalue is -0.82day^{-1}), consistent with the stability of RCE

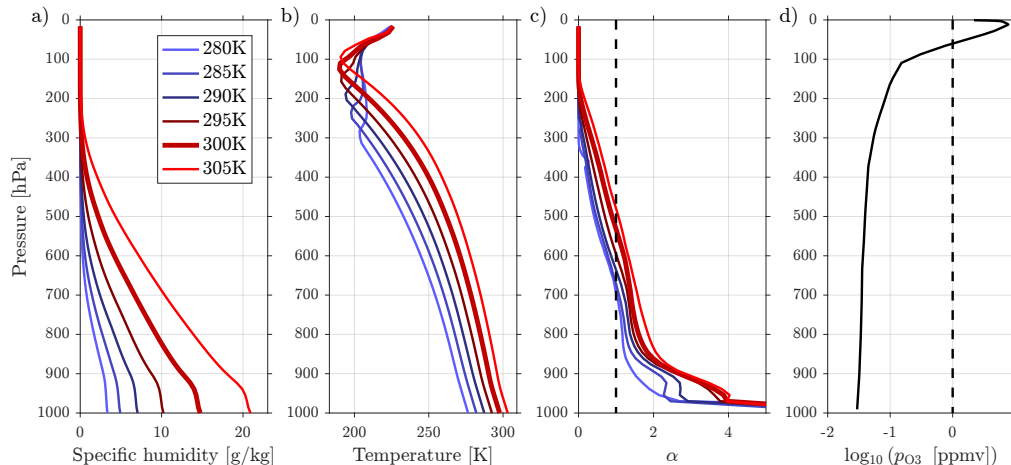


Figure 3-4: Vertical profiles of (a) specific humidity (in g/kg), (b) temperature (in K), (c) HAM and (d) log 10 of the ozone volume concentration (in ppmv) in the SAM simulations ran by Tristan Abbott.

in Kuang’s cloud-permitting simulations. Constructing convective responses and combining them with radiative responses for a variety of basic states is computationally expensive and difficult to interpret in cloud-permitting simulations. Therefore, we proceed to the construction of simple convective responses that mimic the two components of more realistic responses. Before doing so, we calculate different basic RCE states for our simple convective models from cloud-permitting simulations.

Radiative-convective equilibria from cloud-permitting simulations

To provide basic states of temperature and specific humidity, we use simulations of RCE conducted by Tristan Abbott on the Engaging computational cluster at MIT, using version 6.10.6 of the SAM cloud-permitting model. The surface temperature varies from 280K to 305K in increments of 5K between simulations. The horizontal domain is 96×96 grid cells with 1 km horizontal resolution, while the stretched vertical grid has 64 levels, with eight levels below 1km and 500m vertical resolution above 3km. The upper boundary is a rigid lid at 28km height, and a sponge layer from 19km to 28km prevents excessive gravity wave reflection off of the top of the model domain.

Insolation is set to an equinoctial diurnal cycle at 19.45 degrees North, producing a time-mean insolation of 413.6Wm^{-2} . We use the radiation code from the National Center for Atmospheric Research Community Atmosphere Model version 3 Collins et al. [2006] and set the carbon dioxide mixing ratio to 355ppmv, and the ozone mixing ratio to the standard tropical profile in SAM in all simulations. Microphysics are parameterized with the SAM single-moment microphysics scheme, documented in Khairoutdinov et al. [2003]. No large-scale forcing of winds, temperature, or moisture is imposed in any simulations. In these simulations, convection remains disaggregated (referred to as “pop-corn” convection), and the thermodynamic profiles (shown in figure 3-4) are averaged in space and time over 60 days after a 40 day spin-up. The column water vapor varies from 7.9kg.m^{-2} to 68.7kg.m^{-2} from the coldest to warmest surface temperature (Figure 3-4a). The temperature profile is close to a moist adiabatic profile in the lower troposphere and progressively approaches a dry adiabat near the tropopause (Figure 3-4b). Finally, the HAM profile is very large in the boundary layer (with values up to 10 near the surface), decreases below 1 in the lower to mid-troposphere before asymptoting to 0 near the tropopause (Figure 3-4c). Only the warmest surface temperature has a free-tropospheric-averaged α larger than 1. The reference simulation for sections 3.3 and 3.4 uses a surface temperature of 300K and is denoted with a thicker line in figure 3-4. Its column water vapor is 44.5kg.m^{-2} , column relative humidity 84%, tropopause pressure 121hPa, tropopause temperature 190K, and its HAM has a mean free-tropospheric value of 0.91. The standard tropical ozone profile in SAM (Figure 3-4d) has a column ozone of 5.3g.m^{-2} ; its mixing ratio reaches a minimum of 30ppbv at the surface and a maximum of 7.8ppmv in the upper atmosphere.

Toy models of convective response

Starting from the 300K reference simulation, we construct Betts-Miller-like and bulk-plume-like convective linear responses, with our schemes designed so that tendencies of water vapor and temperature are zero in the reference state. The 2 toy models provide meaningful linear responses about the same basic state under the WTG ap-

proximation, responses we can then directly compare. For brevity, we refer to the 2 toy models as simply “Betts-Miller” and “bulk-plume” schemes, keeping in mind that we have chosen toy models over their more realistic counterparts and traded realism for analytical tractability. Since the eigenvalues of radiative-convective instability are very sensitive to the convective response, this choice is a first step that provides novel physical insight.

3.3.2 Betts-Miller scheme

Description

The Betts-Miller convective scheme Betts and Miller [1986, 1993], commonly used as a minimal model of moist convection [e.g., Frierson, 2007], computes precipitation and convective tendencies based on the deviation of the temperature and water vapor profiles from reference values in a convectively unstable atmosphere. In the free troposphere, the scheme relaxes moisture and temperature perturbations to zero in time τ_{BM} , where τ_{BM} is a parameter of the scheme (typically a few hours). In order to conserve the moist static energy of the convecting layer, the scheme shifts the temperature profile in time τ_{BM} , by a uniform amount $(\Delta T)_{\text{BM}}$ given by:

$$(\Delta T)_{\text{BM}} = \frac{1}{c_p(p_b - p_t)} \int_{p_t}^{p_b} (c_p T_{\text{BM}} + L_v q_{\text{BM}}), \quad (3.11)$$

where c_p is the specific heat constant of dry air at constant pressure, L_v the latent heat of vaporization of water vapor, p_b the pressure at the top of the planetary boundary layer, p_t the tropopause pressure, T_{BM} the temperature perturbation from the Betts-Miller reference profile and q_{BM} the specific humidity perturbation from the Betts-Miller reference profile.

Linear response

The theoretical framework of section 3.2 provides two simplifying constraints. First, we can linearize equation 3.11 about RCE and note that: $(T'_{\text{BM}}, q'_{\text{BM}}) = (T', q')$.

Second, under the WTG approximation, the temperature perturbation T' is zero. Since the convective heating is given by the tendency of $(\Delta T)_{\text{BM}}$, its perturbation solely depends on the moisture perturbation q' .

In order to evaluate the linear response of the Betts-Miller scheme, we introduce a water vapor perturbation q'_j in a thin pressure layer $[p_j - \Delta p/2, p_j + \Delta p/2]$, for which the pressure thickness Δp is much smaller than the pressure level p_j . The pressure level p_j is above the top of the boundary layer, defined as the level of maximal relative humidity (928hPa for the reference profile), and below the tropopause, defined as the level of minimal temperature (188hPa for the reference profile). We assume that the whole atmosphere between these two levels is convecting. In response to the water vapor perturbation q'_j , the scheme relaxes q'_j to zero in time τ_{BM} , corresponding to a local damping of the water vapor perturbation. Therefore, the convective moistening response matrix (in units s^{-1}) is given by:

$$(M_{\text{LH}})_{ij} \stackrel{\text{def}}{=} \frac{1}{q'_j} \left(\frac{dq'_i}{dt} \right)_{\text{BM}} = \underbrace{-\frac{\delta_{ij}}{\tau_{\text{BM}}}}_{\text{Local drying}}, \quad (3.12)$$

where i is the response level, j the perturbation level, BM a subscript denoting the action of the Betts-Miller scheme and δ_{ij} the Kronecker symbol, defined as 1 if $i = j$ and 0 otherwise. In contrast, the convective heating in response to the perturbation moistening is equally distributed over all layers of the atmospheric column, corresponding to the following convective heating response:

$$(M_{\text{DSE}})_{ij} \stackrel{\text{def}}{=} \frac{\alpha_i}{L_v q'_j} \frac{c_p (\Delta T)'_{\text{BM}}}{\tau_{\text{BM}}} = \underbrace{\frac{\alpha_i}{\tau_{\text{BM}}} \frac{\Delta p}{p_b - p_t}}_{\text{Heating everywhere}}, \quad (3.13)$$

where M_{DSE} is the convective heating response matrix (in units s^{-1}), α_i the HAM (equation 3.4) evaluated at the response level p_i , and $(p_b - p_t)$ the thickness of the free troposphere. Figure 3-5 represents the convective linear response of the Betts-Miller scheme with SAM RCE profiles as our basic state. Thus, the response of the Betts-Miller scheme to moist perturbations can be separated in two parts:

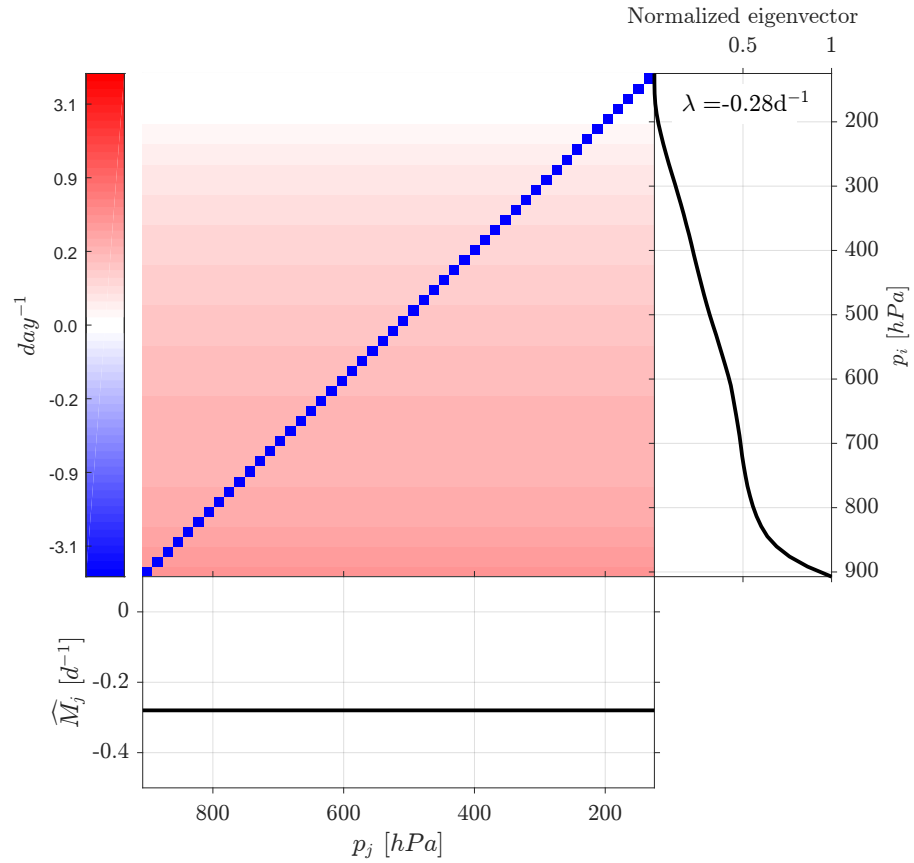


Figure 3-5: Betts-Miller linear convective matrix for $\tau_{\text{BM}} = 3$ hours, where the HAM has been evaluated from the reference SAM RCE profile. (Bottom panel) Vertically-integrated growth rate (\widehat{M}_j in day^{-1}). (Right panel) Eigenvector corresponding to the leading eigenvalue real part λ , normalized to have a maximum of 1.

- A local convective drying along the diagonal, where perturbations are removed in time τ_{BM} .
- A tropospherically-uniform convective heating which has a growth rate that decreases with height due to modulation by the HAM profile (equation 3.13).

3.3.3 Bulk plume equations

Description

Most of the parameterizations that represent precipitating convection use bulk schemes, which model an ensemble of different cumulus elements as a small number of entraining-detraining plumes. Plant [2009] reviews the theoretical basis for different bulk parameterizations and spectral parameterizations (e.g. Arakawa and Schubert [1974]). Here, we start with a simplified form of the bulk-plume equations for a single updraft plume developed by Yanai et al. [1973], which has been used by Romps [2014] in order to estimate the moisture profile from specified entrainment, detrainment, and mass flux profiles:

$$-g \frac{\partial m}{\partial p} = e - d, \quad (3.14)$$

$$-g \frac{\partial (mq^*)}{\partial p} = eq - dq^* - c, \quad (3.15)$$

$$-g \frac{\partial (mq)}{\partial p} = eq - dq^*, \quad (3.16)$$

$$-g \frac{\partial [m(s + L_v q^*)]}{\partial p} = e(s + L_v q) - d(s + L_v q^*), \quad (3.17)$$

where g is the gravitational acceleration, m is the cloud updraft mass flux (in units $\text{kg}\cdot\text{m}^{-2}\cdot\text{s}^{-1}$), p is the hydrostatic pressure, (e, d, c) are the entrainment, detrainment and condensation rates (in units s^{-1}), q^* is the saturation specific humidity, and q is the environmental specific humidity. To keep the model analytically tractable, we have neglected thermodynamical details of the bulk plume model, including:

- The weight of the condensate on the right-hand side of the mass equation 3.14, which is reasonable for small values of q^* .
- The evaporation of condensate on the right-hand side of the environmental moisture equation 3.16, which assumes that any condensate instantly falls to the surface without re-evaporating in the clear-sky environment. This is a poor approximation to reality, as clear-sky re-evaporation balances the difference between convective heating and radiative cooling in RCE.

- The difference between the dry static energy of the clouds and the environment [neutral buoyancy assumption if virtual effects are ignored, e.g., Singh and O’Gorman, 2013], which affects the right-hand side of the moist static energy equation 3.17.
- The mixing between the neutral air of the troposphere and the stably stratified air of the stratosphere, which can occur through convective overshooting and gravity wave breaking.

Basic state

Assuming that the bulk-plume equations apply, we aim at diagnosing the equilibrium updraft mass flux, detrainment, entrainment and condensation rates from RCE moisture and temperature profiles. In appendix A.1, we show that the bulk-plume equations lead to a unique set of solutions for the equilibrium convective profiles:

$$m(p) = \frac{\widehat{Q}_{\text{BP}} \cdot \mathcal{I}(p)}{L_v q_{\text{def}}}, \quad (3.18)$$

$$e(p) = \frac{g \widehat{Q}_{\text{BP}} \cdot \mathcal{I}(p)}{L_v^2 q_{\text{def}}^2} \frac{\partial (s + L_v q^*)}{\partial p}, \quad (3.19)$$

$$d(p) = \frac{g \widehat{Q}_{\text{BP}} \cdot \mathcal{I}(p)}{L_v q_{\text{def}}^2} \frac{\partial q}{\partial p}, \quad (3.20)$$

$$c(p) = -\frac{g \widehat{Q}_{\text{BP}} \cdot \mathcal{I}(p)}{L_v^2 q_{\text{def}}^2} \frac{\partial s}{\partial p}, \quad (3.21)$$

where \widehat{Q}_{BP} is the total free-tropospheric atmospheric cooling (a free parameter of our simple bulk-plume model), p_b is the pressure at the top of the planetary boundary layer; we have introduced the function \mathcal{I} :

$$\mathcal{I}(p) \stackrel{\text{def}}{=} \exp \left[\int_{p_b}^p \frac{dp'}{L_v q_{\text{def}}(p')} \frac{\partial s(p')}{\partial p'} \right],$$

as well as the saturation deficit q_{def} :

$$q_{\text{def}} \stackrel{\text{def}}{=} (q^* - q). \quad (3.22)$$

Taking the reference SAM RCE profiles as RCE leads to the convective profiles shown in Figure 3-6.

Although our simple model captures the order-of-magnitude of convective properties overall [e.g., Figures 5 and 6 of Pauluis and Mrowiec, 2013], the entrainment rates can artificially take negative values in the upper troposphere and at the top of the boundary layer, where the saturated moist static energy decreases with height. This limitation of the entrainment diagnostics remains if ice precipitation is taken into account [e.g., equation 22 of Pauluis and Mrowiec, 2013] or if we take into account the weight of condensate and/or the re-evaporation of condensates in the clear-sky environment (not shown). Taking into account troposphere-stratosphere mixing, the preferential detrainment of plumes with low saturated moist static energy, or cloud-top mixing would (at least partly) correct this issue, but these details are beyond the scope of our simple bulk-plume model.

Linear response

The steady equations 3.14, 3.15, 3.16 and 3.17 do not constrain the (time-dependent) linear response of our simple bulk-plume model. For simplicity, analytic tractability, and since the moisture perturbations are small and free-tropospheric, we assume that the additional water vapor behaves as a passive tracer to evaluate the response of our bulk-plume toy model. Note that this approximation would not be valid in the boundary layer, as shown in panel (a) of Figure 3-3, nor for large free-tropospheric perturbations that would inhibit or enhance deep convection. This approximation ignores perturbations in the convective ensemble properties (m, e, d, c) , which remain at their RCE values computed in section 3.3.3 during the linear response. In a more realistic bulk-plume model, the transient evolution of the system would depend on other equations, such as the mass-flux closure equation. We evaluate this passive

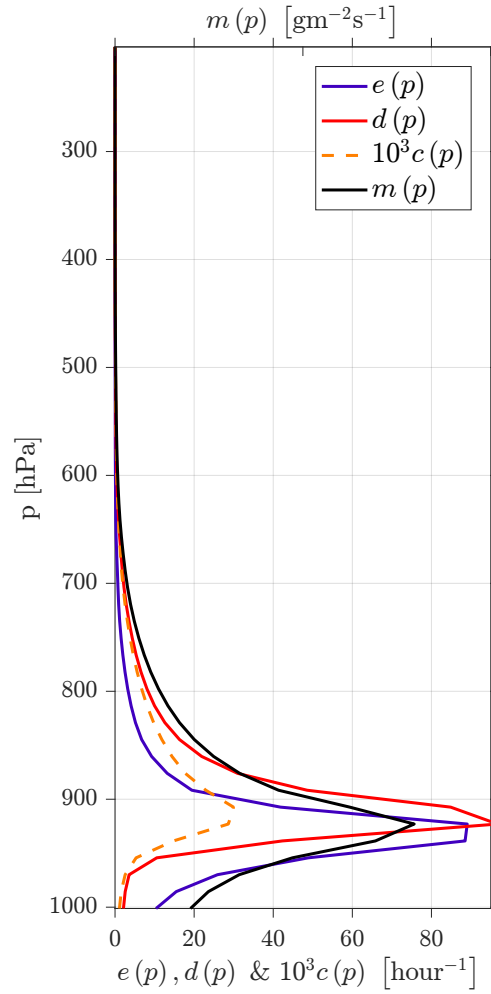


Figure 3-6: Entrainment and detrainment rate profiles (in hour^{-1}) and condensation rate profile (in month^{-1}) in RCE, as diagnosed from the reference SAM RCE temperature and moisture profiles.

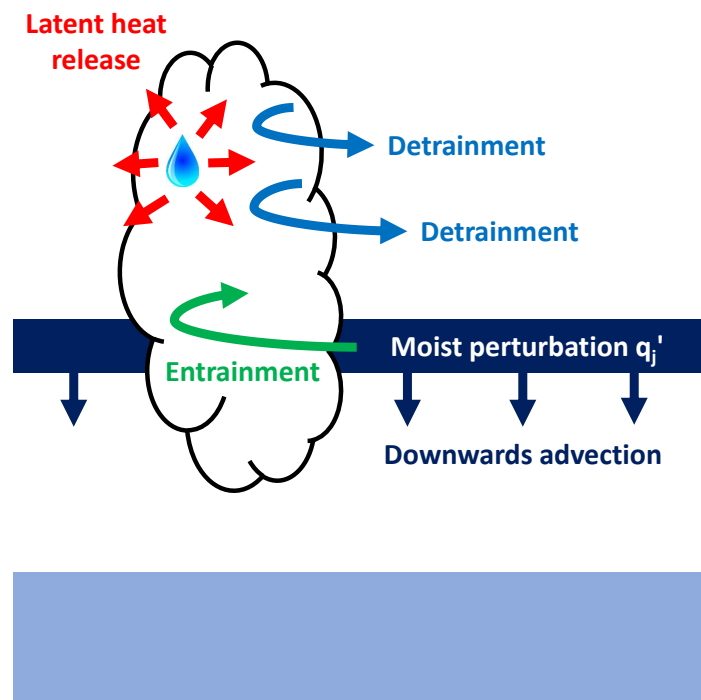


Figure 3-7: The moist perturbation at level p_j is entrained in the cloudy updraft, where it detrains and releases latent heat through condensation at level $p_{i>j}$ above the perturbed level. The moist perturbation is also advected downwards to level p_{j-1} by the subsidence mass flux.

tracer linear response in four steps, following Figure 3-7:

1. We introduce a perturbation q'_j in a thin convecting layer $[p_j - \Delta p/2, p_j + \Delta p/2]$, with entrainment: $e_j = e(p_j)$, where e is the RCE entrainment profile given by equation 3.19.
2. We assume that the perturbation q'_j is entrained into the convective plume at a rate e_j from the perturbation level p_j and this entrained portion of the water vapor perturbation is communicated to all levels above: $p_i < p_j$.
3. At a given level p_i within the plume, the perturbation q'_j condenses at a rate proportional to the local RCE condensation rate at that level: $c_i = c(p_i)$, and detrains at a rate proportional to the RCE detrainment rate $d_i q_i^* = (dq^*)(p_i)$. The proportionality constant is uniform in the convecting layer and related to the entrainment rate at the perturbation level.
4. Finally, the environmental perturbation is also advected downwards by the local subsidence mass flux $-m_i = -m(p_i)$.

In appendix A.2, we show that the convective moistening response M_{LH} and the convective heating response M_{DSE} are respectively given by:

$$(M_{\text{LH}})_{ij} = e_j \left[\underbrace{-\delta_{ij}}_{\text{Entrained moisture}} + \underbrace{\frac{d_i q_i^* \delta_{i>j}}{\sum_{i>j} (d_i q_i^* + c_i)}}_{\text{Detrained moisture above}} \right] + \underbrace{\frac{g m_j [\delta_{i(j-1)} - \delta_{ij}]}{\Delta p}}_{\text{Downwards advection}}, \quad (3.23)$$

$$(M_{\text{DSE}})_{ij} = \underbrace{\frac{e_j \alpha_i c_i \delta_{i>j}}{\sum_{i>j} (d_i q_i^* + c_i)}}_{\text{Latent heating above}}, \quad (3.24)$$

where δ_{ij} is 0 if $i \neq j$ and 1 if $i = j$, $\delta_{i>j}$ is 0 if $i \leq j$ and 1 if $i > j$, and $\delta_{j(i-1)}$ is 0 if $i \neq j - 1$ and 1 if $i = (j - 1)$.

The linear convective response is depicted in Figure 3-8, while the separate convective moistening and heating responses can be found in appendix A.2. Overall, the

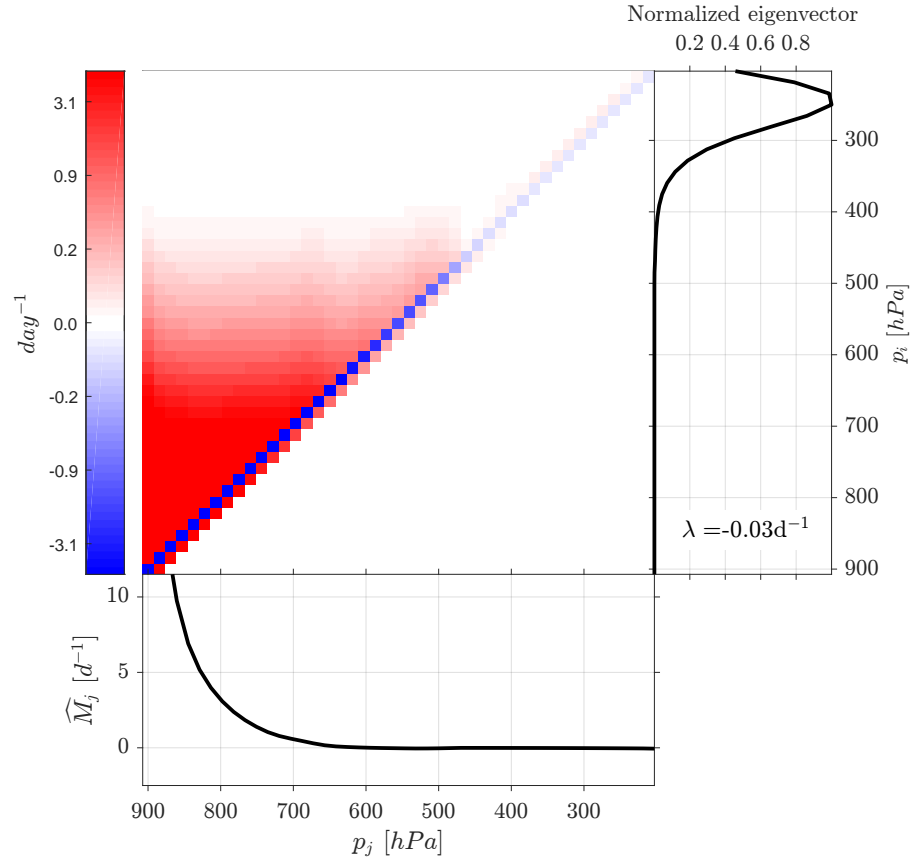


Figure 3-8: Bulk-plume linear convective matrix ($M_{\text{LH}} + M_{\text{DSE}}$) for $\widehat{Q}_{\text{BP}} = 150 \text{ W m}^{-2}$. (Bottom panel) Vertically-integrated growth rate (\widehat{M}_j in day^{-1}). (Right panel) Eigenvector corresponding to the leading eigenvalue real part λ , normalized to have a maximum of 1 (note that the leading eigenvalue here is negative, so it represents the slowest-decaying mode).

response of the bulk-plume scheme to moist perturbations can be separated in three parts:

- A local drying (blue diagonal) due to the entrainment of water vapor in the plume and its downwards advection by the subsiding mass flux.
- A growth of the perturbation above the perturbation level (red upper-left part of the matrix) due to the detrainment of the moist plume as well as the latent heating within the plume. This component of the response scales like the detrainment and condensation rate profiles from bottom to top, and like the local entrainment rate profile from left to right.
- A moistening right below the perturbation level (red below the diagonal) due to the downwards advection of the moist perturbation by the subsidence mass flux.

The Betts-Miller and bulk-plume convective responses both conserve moist static energy: they locally damp the perturbation, and re-distribute it everywhere in the case of the Betts-Miller scheme and upwards in the case of the bulk-plume scheme. Unlike convection, radiation diabatically heats the column, which may enhance moist static energy perturbations even when the HAM profile is uniform [e.g., Beucler and Cronin, 2016]).

3.4 Linear response of radiation

In this section, we compute the linear response of longwave radiation M_{LW} and that of shortwave radiation M_{SW} using analytical and real-gas radiative transfer models. We use the same tropical basic state as in section 3.3.

3.4.1 Two-stream model of longwave radiation

The framework introduced here generalizes the analytical framework introduced in Beucler and Cronin [2016] by allowing the water vapor profile to vary freely and

writing the differential optical thickness $d\tau$ as a product of a general function f_1 of pressure and a general function f_2 of specific humidity:

$$d\tau = \kappa f_1(p) f_2(q) \frac{dp}{g}, \quad (3.25)$$

where the gray longwave absorption coefficient κ has the units $\text{m}^2 \text{kg}^{-1}$, and dp is the differential atmospheric pressure. Beucler and Cronin [2016] accounted for pressure broadening of water vapor in a simple fashion by choosing $\kappa = 0.17 \text{ m}^2 \text{kg}^{-1}$, $f_1(p) = p/p_s$, $f_2(q) = q$, where p_s is the surface pressure, and we make the same choice in this section. From the two-stream Schwarzschild equation for a one-dimensional plane-parallel atmosphere (equations (10) and (11) of Beucler and Cronin [2016]), we can write the longwave convergence in pressure coordinates $d\mathcal{F}_{\text{LW}}/dp$ (in $\text{Wm}^{-2}\text{hPa}^{-1}$) as the product of the longwave convergence in optical thickness coordinates (in W m^{-2}) with the differential optical thickness (in hPa^{-1}):

$$\frac{d\mathcal{F}_{\text{LW}}}{dp} = \frac{d(\mathcal{F}_{\uparrow} - \mathcal{F}_{\downarrow})}{dp} = \underbrace{(\mathcal{F}_{\uparrow} + \mathcal{F}_{\downarrow} - 2\sigma T^4)}_{\text{LW convergence}} \overbrace{\frac{\kappa f_1 f_2}{g}}^{\text{Diff opt thickness}}, \quad (3.26)$$

where \mathcal{F}_{\uparrow} and \mathcal{F}_{\downarrow} are respectively the upwelling and downwelling radiative fluxes (in W m^{-2}), σ is the Stefan-Boltzmann constant and T is the atmospheric temperature. In appendix B.1, we show that the linear longwave response can be written as the sum of two components:

$$(M_{\text{LW}})_{ij} = \underbrace{\frac{\kappa \alpha_i}{L_v} \left[f_1 \left(\frac{df_2}{dq} \right)_{q=0} \right]_{p_j}}_{\text{Opt thick pert}} \left\{ \text{LW}_{\text{local},ij} + \overbrace{\frac{\kappa \Delta p (f_1 f_2)_{p_i}}{g}}^{\text{Local opt thickness}} \text{LW}_{\text{non-local},ij} \right\}. \quad (3.27)$$

Their general expression and physical interpretation for a moist perturbation $q'_j > 0$ are:

1. A local increase in the radiative cooling, due to the increase of the local emis-

sivity:

$$\text{LW}_{\text{local},ij} = (\mathcal{F}_{\uparrow} + \mathcal{F}_{\downarrow} - 2\sigma T^4)_{p_i} \delta_{ij}, \quad (3.28)$$

2. A non-local term that has different signs above and below the perturbation:

$$\text{LW}_{\text{non-local},ij} = \underbrace{\exp(-|\tau_i - \tau_j|)}_{\text{Transmissivity}} \left[-(\mathcal{F}_{\uparrow})_{p_j} \delta_{i>j} - (\mathcal{F}_{\downarrow})_{p_j} \delta_{i<j} + \sigma T_j^4 \delta_{i \neq j} \right], \quad (3.29)$$

where τ_i is the optical thickness of the atmosphere between p_i and space, τ_j is the optical thickness of the atmosphere between p_j and space, and T_j is the atmospheric temperature at the perturbation level. Above the perturbation level ($i > j$), the upwelling flux received from the perturbation $(\mathcal{F}_{\uparrow})_{p_j}$ decreases because the moist perturbation absorbs some of the upwelling atmospheric radiation below it. Below the perturbation level ($i < j$), the downwelling flux received from the perturbation $(\mathcal{F}_{\downarrow})_{p_j}$ decreases because the moist perturbation absorbs some of the downwelling atmospheric radiation above it. In return, the perturbation emits radiative energy up and down at a rate σT_j^4 . Because the atmospheric temperature decreases with height, the emission term σT_j^4 exceeds the radiative flux $(\mathcal{F}_{\downarrow})_{p_j}$ received from above but is less than the radiative flux $(\mathcal{F}_{\uparrow})_{p_j}$ received from below. Therefore, we expect the net longwave convergence to decrease above the perturbation level and to increase below it for a positive moisture perturbation. The amplifying radiative linear response resulting from the non-local heating perturbation below a moist perturbation (or cooling perturbation below a dry perturbation) is referred to as the radiative amplification effect.

Figure 3-9a shows the longwave linear response for a surface optical thickness of 5.4, which matches the net radiative cooling as computed in SAM and is a reasonable tropical value corresponding to column water vapor values of 40 kg m^{-2} in the simple model of Beucler and Cronin [2016]. The local increase is cooling (LW_{local}) appears as a blue diagonal throughout the troposphere, except near the tropopause where the gray-radiation skin temperature exceeds the atmospheric temperature, leading to local

heating and pointing to one limitation of the gray model. The decrease in radiation received from the ground is prevalent in the lower troposphere, and corresponds to the blue area above the bottom left corner of the matrix. The damping linked to the decrease in radiation received from the atmosphere is largest right above and right below the diagonal, and explains why the blue zone above the diagonal extends to the mid-troposphere. The radiative amplification term is larger than the damping terms and well-distributed below the perturbation level. Water vapor molecules below a moist perturbation emit less radiation to space, resulting in a net heating below the perturbation level. For lower-tropospheric perturbations, the three damping terms on the right-hand side of equation 3.27 are prevalent in the sum, and $\widehat{M}_j < 0$. However, \widehat{M}_j becomes positive in the case of mid to upper-tropospheric perturbations, for which the radiative amplification term is largest. The potential growth of column-integrated perturbations through their unstable interaction with longwave radiation has been extensively studied in Beucler and Cronin [2016], and referred to as moisture-radiative cooling instability. Note that the toy radiative model presented in equation 28 of Emanuel et al. [2014] is a specific case of our gray model in the limit of two optically-thin atmospheric layers. This framework provides fundamental understanding for the gray part of the clear-sky real-gas radiative response, and gives an idea of the cloud longwave radiative response, for which the gray approximation holds better. The reader interested in the assumptions made in order to compute the optical thickness profile for Figure 3-9 is referred to appendix B.3.

3.4.2 One-stream model of shortwave radiation

Following Beucler and Cronin [2016], we adopt a simple one-stream model of radiation with the generalized optical thickness given by equation 3.25:

$$\mathcal{F}_{\text{SW}} = \mathcal{S}e^{-\varepsilon\tau}, \quad (3.30)$$

where \mathcal{F}_{SW} is the downwelling shortwave flux (in Wm^{-2}), \mathcal{S} the solar constant, τ the optical thickness and ε the factor relating the longwave to shortwave optical thick-

ness. Assuming that ε does not vary with pressure to first order, the shortwave flux convergence is simply given by:

$$-\frac{d\mathcal{F}_{\text{SW}}}{dp} = \underbrace{\frac{\kappa\varepsilon f_1 f_2}{g}}_{\text{Diff opt thickness}} \mathcal{F}_{\text{SW}}. \quad (3.31)$$

In appendix B.2, we show that the linear shortwave response can be written as the sum of two terms:

$$(M_{\text{SW}})_{ij} = \frac{\kappa\alpha_i (\mathcal{F}_{\text{SW}})_{p_i}}{L_v} \underbrace{\left[\varepsilon f_1 \left(\frac{df_2}{dq} \right)_{q=0} \right]_{p_j}}_{\text{Opt thick pert}} \left[\underbrace{\delta_{ij}}_{\uparrow \text{Local emissivity}} - \frac{\overbrace{\kappa\Delta p \cdot \varepsilon \cdot (f_1 f_2)_{p_i}}^{\text{Local opt thickness}}}{g} \underbrace{\delta_{i < j}}_{\downarrow \text{Rad received}} \right], \quad (3.32)$$

1. A local increase in the radiative heating, due to the increase of the local emissivity.
2. A decrease in the solar radiation received below the perturbation level.

The shortwave linear response matrix is depicted in Figure 3-9b. The local increase in radiative heating corresponds to the red diagonal and is attenuated by the decrease in received solar radiation below the perturbation level. Because the atmosphere is optically thin in the shortwave, the strength of the linear response is mostly affected by the local value of the product αf_1 , which increases strongly with pressure. Therefore, \widehat{M}_j is greatest in the lower troposphere and quickly decays for higher perturbations. Although the gray model qualitatively exhibits the basic physics of the linear radiative response, different water vapor spectral bands saturate at different humidity levels, and we use of a full radiative model in order to yield accurate results in section 3.4.3.

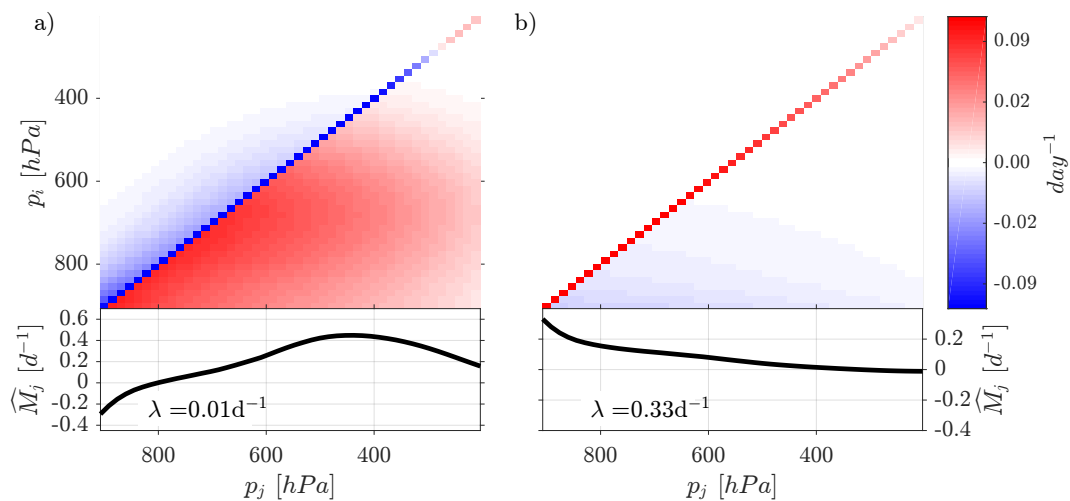


Figure 3-9: (a) Longwave linear response matrix (in $month^{-1}$) and vertically integrated longwave growth rate (in day^{-1}) plotted against perturbation level (in hPa). (b) Shortwave linear response and vertically integrated shortwave growth rate. The total optical thickness of the free troposphere is 6 in the longwave and 0.5 in the shortwave. It corresponds to a net free-tropospheric cooling of 215 W m^{-2} . The analytical matrices, with leading real eigenvalues λ , have both been tested against a numerical version of the two-stream Schwarzschild model.

3.4.3 Real-gas radiative transfer

Method

In order to take into account the full water vapor absorption spectrum, we use the RRTMG model Iacono et al. [2000, 2008], Mlawer et al. [1997] to compute the response of the atmosphere to small water vapor perturbations. Following Beucler and Cronin [2016], we use version 4.85 of the longwave and version 3.9 of the shortwave column versions of RRTMG, a broadband, two-stream, correlated k-distribution radiative transfer model, that has been tested against line-by-line radiative transfer models. The RCE water vapor and temperature profiles are once again the observed January SAM RCE profiles, and have 60 levels in the vertical. To match the clear-sky radiative transfer of the SAM base state as closely as possible, we also specify a constant carbon dioxide mixing ratio of 355ppmv and use the standard SAM tropical ozone mixing ratio profile depicted in Figure 3-4d. The solar zenith angle is chosen to be $\arccos(\pi/4)$ rad, the insolation-weighted equatorial equinox value. The linear radiative responses are obtained in 4 steps:

1. We use RRTMG in order to compute the structure of the longwave and shortwave radiative fluxes from the RCE greenhouse gas and temperature profiles.
2. We perturb the RCE water vapor profile level by level. 64 “moistened” profiles are produced, by adding 1% to the specific humidity at each level. Similarly, 64 “dried” profiles are produced by removing 1% from the RCE specific humidity at each level.
3. For each perturbed profile, we use RRTMG to compute the structure of longwave and shortwave radiative fluxes. We multiply the shortwave fluxes by a constant factor to account for the diurnal cycle and match the total shortwave heating in SAM (the factor is close to $4/\pi^2$, which would exactly account for an insolation-weighted zenith angle).
4. By subtracting the RCE radiative fluxes to the perturbed radiative fluxes, we obtain the perturbation radiative fluxes, from which we compute the longwave

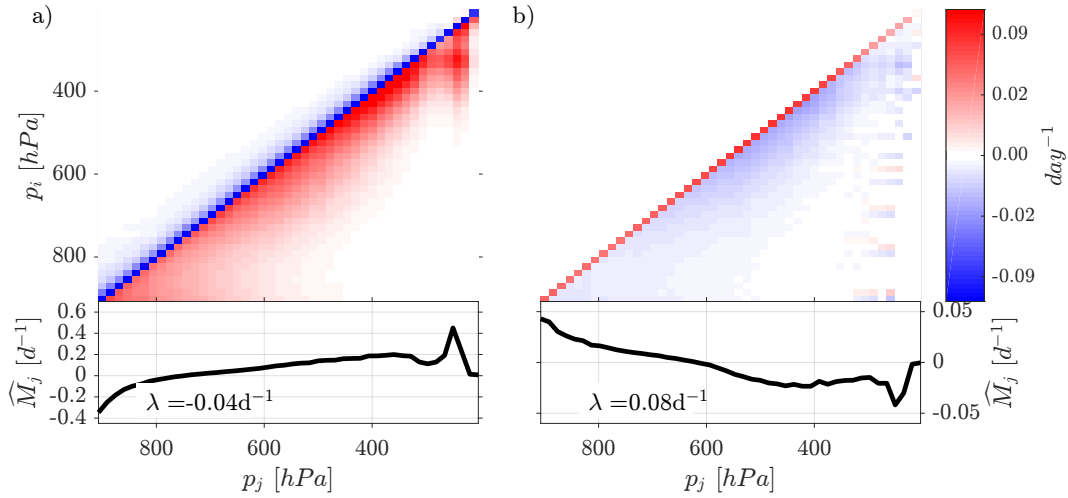


Figure 3-10: (a) Longwave linear response matrix (in month⁻¹) and vertically integrated longwave growth rate (in day⁻¹) plotted against perturbation level (in hPa). (b) Shortwave linear response and vertically integrated shortwave growth rate. The HAM has been evaluated from the reference SAM RCE profile. The leading real eigenvalue λ of each matrix is indicated in the corresponding bottom panel.

and shortwave linear responses matrices following equations 3.3 and 3.6.

Results

The longwave and shortwave linear response matrices are respectively depicted in Figure 3-10a and 3-10b. The total radiative linear response matrix is qualitatively similar to the clear-sky radiative responses obtained by Emanuel et al. [2014] for a negative moisture perturbation, with a radiative amplification effect concentrated below the diagonal that expands as surface temperature increases. For the SAM RCE reference profile, the total longwave radiative cooling is 211 W m^{-2} and the total shortwave radiative heating 61 W m^{-2} , leading to a net cooling of 150 W m^{-2} , which is the standard value we use for \widehat{Q}_{BP} in the bulk-plume model (section 3.3.3). The vertically-integrated response is negative for lower-tropospheric perturbations, and grows as the longwave amplification effect becomes larger to values of order 0.5 day^{-1} for perturbations near the tropopause. The shortwave effect is opposite and reaches -0.05 day^{-1} for perturbations near the tropopause. The main difference when

going from a gray-gas to a real-gas model of radiation is the sharp amplification of the response growth rates near the tropopause. There, the most absorbing bands of water vapor (large κ) contribute to longwave cooling and shortwave heating. Therefore, small water vapor perturbations will change the optical thickness by a greater amount per unit mass perturbation in water vapor amount.

3.5 Linear evolution of small water vapor perturbations

In this section, we combine the Betts-Miller convective response (referred to as BM, see section 3.3.2) and the bulk-plume convective response (referred to as BP, see section 3.3.3) with the real-gas radiative response (referred to as RRTM, see section 3.4.3), in order to obtain the full linear response and study the linear evolution of small water vapor perturbations. The total Betts-Miller response matrix $M_{\text{BM+RRTM}}$ and the total bulk-plume response matrix $M_{\text{BP+RRTM}}$ are given by:

$$M_{\text{BM+RRTM}} = M_{\text{BM}} + M_{\text{RRTM}}, \quad (3.33)$$

$$M_{\text{BP+RRTM}} = M_{\text{BP}} + M_{\text{RRTM}}, \quad (3.34)$$

where M_{BM} is the Betts-Miller convective response (sum of the responses given by equations 3.12 and 3.13) for the Betts-Miller timescale $\tau_{\text{BM}} = 3h$, M_{BP} is the bulk-plume convective response (sum of the responses given by equations 3.23 and 3.24) for the radiative cooling parameter computed from the RRTM model, and M_{RRTM} is the RRTM radiative response (sum of the longwave and shortwave responses shown in Figure 3-10). We show in Appendix C that the results of this section are robust across a wide range of convective parameters τ_{BM} and \hat{Q}_{BP} .

From section 3.2.1, we remember that the linear response matrix may be linearly unstable if its leading eigenvalue real part is greater than zero. In Figure 3-11a, we compute the leading eigenvalue real part of each matrix for different values of the

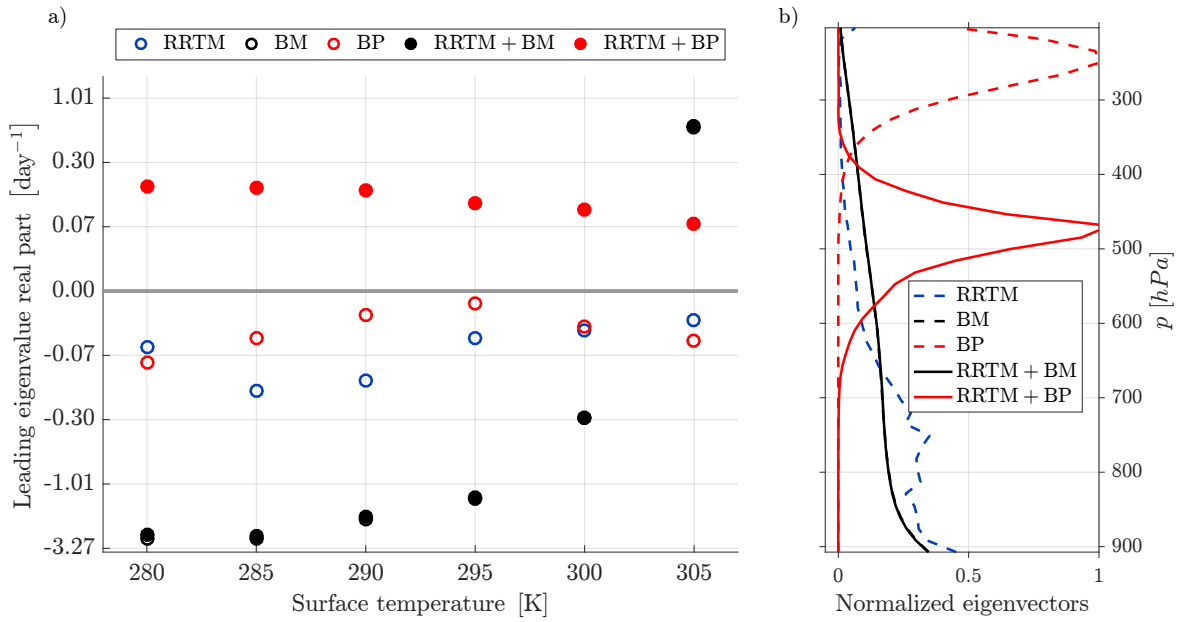


Figure 3-11: (a) Leading eigenvalue real part (in day^{-1}) as a function of the RCE surface temperature (in K). (b) Corresponding eigenvectors for the 300K reference case: Radiative response alone (RRTM), Betts-Miller response alone (BM, $\tau_{\text{BM}} = 3\text{hours}$), bulk-plume response alone (BP, $\widehat{Q}_{\text{BP}} = 150 \text{ W m}^{-2}$), and their sums (RRTM+BP) & (RRTM+BM). The lines for (BM) and (RRTM+BM) are indistinguishable. The eigenvectors have been normalized to have the same pressure-average.

surface temperature:

- (RRTM) For the reference SAM RCE profile, the leading eigenvalue real part corresponds to a decay time scale of 27 days; there is no pure linear instability from radiation alone. Because the radiative linear response matrix is mostly lower triangular, with a strictly negative diagonal corresponding to strong local cooling, water vapor perturbations are displaced downwards and eventually damped out in the absence of convection, though they may initially amplify as they are displaced through non-normal growth. Except for the 280K case, the decay timescale increases with temperature, suggesting that the clear-sky radiation's damping effect is less pronounced in warmer climates. Finally, we find that the clear-sky radiative feedback can be linearly unstable if the RCE relative humidity profile is artificially dried, due to the upper-tropospheric radiative amplification effect. For readability purposes, the results are not shown in Figure 3-11 but provided to the reader in the corresponding MATLAB script.
- (BM) In the WTG framework, Betts-Miller convection is linearly unstable if and only if the mean free-tropospheric HAM is larger than 1 (analogous to a negative gross moist stability). This condition is only satisfied for the 305K simulation, in which the specific humidity remains above 5g/kg and the HAM remains above 1 in the lower troposphere (see panels a and c of figure 3-4). In the unstable case (305K), the perturbation latent heating in the lower troposphere induces strong upward motion because $\alpha > 1$ there, leading to the unstable growth of lower to mid-tropospheric water vapor perturbations. In the stable case (all cases but 305K), these perturbations are damped because a larger mass of the atmosphere has: $\alpha < 1$, which makes the convective drying effect overcome the latent heating effect. Mathematically, we prove in appendix A.3 that the leading eigenvalue real part of the Betts-Miller linear response is proportional to the vertical average of HAM minus 1 (see equation 3.43), which increases with surface temperature as can be seen on figure 3-11. This growth rate is exactly reached for a water vapor perturbation profile that is proportional to

the HAM profile.

- (RRTM+BM) Adding the radiative response reinforces the local and upper-tropospheric perturbation’s damping. However, the stability of the combined linear response matrix is barely distinguishable from that of the convective response alone for Betts-Miller timescales as short as 3 hours.
- (BP) The bulk-plume response is mostly upper triangular, with a strictly negative diagonal corresponding to local drying through the entrainment of the water vapor perturbation. The decay timescale of the bulk-plume convective response is approximately equal to the minimal entrainment value, as the leading eigenvalue real part is close (within $\sim 20\%$ in our case) to $-\min_p [e(p)]$, where e is the entrainment profile (see appendix A.3). Therefore, bulk-plume convection is always linearly stable on its own. The dependence of the leading eigenvalue real part on surface temperature is weak, consistent with the weak dependence of the entrainment minimum on surface temperature.
- (RRTM+BP) The combination of the bulk-plume convective response with the radiative response is linearly unstable for all surface temperatures. Physically, lower-tropospheric perturbations are carried upwards by the plume where they can reinforce through the radiative amplification effect identified in equation 3.29. Upper-tropospheric perturbations can also amplify mid-tropospheric perturbations through radiative amplification, which are then carried upwards in the plume. Mathematically, the combination of an upper and a lower triangular matrices with positive off-diagonal values can allow part of the spectrum to become positive.

The leading eigenvalue real part informs us about the linear growth rate of each response matrix. We now focus on the vertical structure of water vapor perturbations. The evolution of a given perturbation can be found by exponentiating the linear response matrix, following equation 3.8. If we compute the growth rate of column water vapor perturbations, we find that the leading eigenvalue real part can be

used as a predictor of the order of magnitude of the growth rate on a time scale of order days. For the first few hours, the transient growth rate of water vapor perturbations is very dependent on their initial shape. After a few days, dominant vertical modes appear, which mathematically correspond to the eigenvectors associated with the leading eigenvalue real part of each convective response. These eigenvectors, depicted in Figure 3-11b, are the HAM profile for M_{BM} and an upper tropospheric bulge for M_{BP} ; they grow at a rate given by the corresponding leading eigenvalue real parts λ_{BM} and λ_{BP} . In contrast, the purely radiative response (RRTM) damps the perturbation in the upper troposphere, as radiative cooling is increased above the perturbation level, and in the lower troposphere, where the radiative amplification term is smallest. When combined with Betts-Miller convection (RRTM+BM), radiation slightly damps the upper-tropospheric perturbation, which can not be seen by eye in Figure 3-11b. However, the bulk-plume scheme moves the moist lower-tropospheric perturbation upwards in the mid-troposphere, where the radiative amplification effect is largest. This means that the perturbation grows faster when bulk-plume convection and radiation are added (RRTM+BP). The perturbation decays in the lower troposphere, where it is entrained upwards, and in the upper troposphere, where it is advected downwards. In both cases, the convection scheme dominates the pattern of vertical moisture perturbation response. Thus, the (RRTM+BM) & (BM) eigenvectors are indistinguishable, while the (RRTM+BP) & (BP) eigenvectors are close in the lower troposphere. As a closing point, we remind the reader that these eigenvectors are all computed in terms of specific humidity; eigenvectors expressed in terms of relative humidity would in all cases be strongly weighted towards the upper troposphere, where the reference-state q is small.

3.6 Conclusion

In section 3.2, we developed a theoretical framework to compute the response of RCE to small water vapor perturbations in WTG: The resulting linear response function (equation 3.5) is the sum of the convective moistening, convective heating, longwave

heating and shortwave heating linear response functions. The linear response function can be represented as a two-dimensional matrix (equation 3.9), which can be exponentiated in order to compute the evolution of water vapor perturbations for short times. In section 3.3, we calculated analytic responses of two toy models of the convective linear response: a Betts-Miller-like scheme, which re-distributes a local moisture perturbation to the rest of the atmosphere in the form of convective heating, and a bulk-plume-like scheme, which sends a moisture perturbation upwards. Comparing our responses with those obtained by Kuang [2012] (Figures 8c and 8d), the Betts-Miller response is similar to the response of a cloud-permitting model in an elongated domain (aspect ratio larger than 20), whereas the response of the same model in a square domain resembles the bulk-plume response. Additionally, the convective response studied in section 3.3 presents characteristics of both convective toy models, as confirmed by its eigenmode peaking at 575hPa (right panel of figure 3-3), which is the arithmetic mean of the bulk-plume’s mode 250hPa peak and the Betts-Miller’s mode 900hPa peak (right panel of figure 3-11). This suggests that the physical insight obtained in section 3.3 could be used to understand the more intricate physics of cloud resolving model responses. In section 3.4, we investigated the physics of the clear-sky radiative response using the Schwarzschild equations. The response includes a local damping of moisture perturbations and a radiative amplification effect of mid-tropospheric perturbations in the lower troposphere. We also quantitatively evaluated the clear-sky response by using a real-gas radiative transfer model, and found large non-gray radiative feedbacks in the upper troposphere. Section 3.5 shows that despite the damping effect of the radiative response, it could amplify the unstable convective response in the bulk-plume case. In contrast, the Betts-Miller response’s stability depends on the mean free-tropospheric HAM, which increases with temperature, causing linear instability above surface temperatures of 300K.

Although this work explores the physics of the interaction between water vapor, convection and clear-sky radiation in depth, two critical elements of the response are lacking: the cloud response and the surface temperature response. The first re-

quires knowledge of how cloudiness responds to water vapor perturbations (which is mediated by convection and also depends on microphysical factors such as the background cloud condensation nuclei profile) and of how cloudiness affects the radiative heating profile. Preliminary results indicate that the cloud longwave response significantly enhances the longwave radiative amplification effect described in this study, making RCE more prone to linear instability. The second is an air-sea interaction problem, exploring the interaction between atmospheric moisture and surface temperature gradients, which could be relevant for monsoonal intraseasonal oscillations [e.g., Sengupta et al., 2001, Vecchi and Harrison, 2002] and help better understand coupled general circulation model results [e.g., Coppin and Bony, 2017].

This work connects with results from convection-permitting modeling by showing that despite the robustness of radiative thermodynamic feedbacks, the evolution and structure of water vapor perturbations is extremely sensitive to the linear response of convection. Even when convection is not parameterized, its linear response can differ greatly across model geometries [Kuang, 2012], and this may connect with the known sensitivity of aggregation to many aspects of convection-permitting model setup, including resolution and subgrid parameterizations [e.g., Muller and Held, 2012, Tompkins et al., 2017]. Our findings may thus help to explain why the self-aggregation of convection in cloud-permitting models is finicky: the convective linear response is critical, and we still do not fully understand what controls it. Decomposing the full linear response into a Betts-Miller-type response, a bulk-plume-type response (using the mean HAM profile), and a radiative response could provide insight into the early stages of self-aggregation and help explain why the peak of the main moisture mode can be found in the mid-troposphere.

3.7 Appendix A: Linear response of the bulk-plume equations

3.7.1 A.1. Basic state

In order to eliminate the variations of the updraft mass flux m with pressure p , we combine equations 3.19, 3.20 and 3.21 with equation 3.18:

$$gm \frac{\partial q^*}{\partial p} = c + eq_{\text{def}}, \quad (3.35)$$

$$gm \frac{\partial q}{\partial p} = dq_{\text{def}}, \quad (3.36)$$

$$gm \frac{\partial (s + L_v q^*)}{\partial p} = L_v eq_{\text{def}}, \quad (3.37)$$

where we have assumed that the in-cloud dry static energy was equal to the environmental dry static energy (neutral buoyancy assumption) and introduced the saturation deficit q_{def} defined in equation 3.22. Subtracting equation 3.37 to equation 3.36 and using equation 3.18 leads to a first order differential equation for the updraft mass flux:

$$\frac{1}{m} \frac{\partial m}{\partial p} = -\frac{1}{q_{\text{def}}} \left(\frac{\partial q_{\text{def}}}{\partial p} + \frac{1}{L_v} \frac{\partial s}{\partial p} \right). \quad (3.38)$$

The vertically integrated energetic balance requires that the free-tropospheric convective heating (equal to the convective flux at the top of the boundary layer) balances the free-tropospheric radiative cooling $\widehat{Q}_{\text{BP}} > 0$:

$$\frac{L_v}{g} \int_{p_b}^p c = L_v m(p_b) q_{\text{def}}(p_b) = \widehat{Q}_{\text{BP}},$$

leading to the unique solution 3.18 for the updraft mass flux, as long as the free troposphere is not saturated in RCE ($\forall p, q < q^*$). The entrainment, detrainment and condensation rates can be obtained by combining equations 3.37, 3.36 and 3.35 to equation 3.18.

3.7.2 A.2. Linear response

In order to compute the convective moistening and heating resulting from the moist perturbation q'_j , we follow the steps listed in section 3.3.3:

- Step 3: The convective drying tendency due to the entrainment of the moist perturbation in the plume can be written:

$$\left(\frac{dq'_i}{dt}\right)_{\text{Ent}} = -e_j q'_j \delta_{ij}. \quad (3.39)$$

- Step 4: The convective moistening due to the detrainment of water vapor from the plume (above the perturbation level) is:

$$\left(\frac{dq'_i}{dt}\right)_{\text{Det}} = \mathcal{C}_{\text{Det}} e_j q'_j d_i q_i^* \delta_{i>j}, \quad (3.40)$$

while the convective heating due to the condensation of water vapor in the plume (above the perturbation level) is:

$$L_v \left(\frac{dq'_i}{dt}\right)_{\text{Con}} = \mathcal{C}_{\text{Con}} e_j q'_j c_i \delta_{i>j}, \quad (3.41)$$

where \mathcal{C}_{Det} and \mathcal{C}_{Con} are proportionality constants. We have assumed that these two constants were equal ($\mathcal{C}_{\text{Det}} = \mathcal{C}_{\text{Con}} = \mathcal{C}$). Using the conservation of the water vapor perturbation q'_j yields:

$$\left(\frac{dq'_i}{dt}\right)_{\text{Ent}} = \sum_{i>j} \left[\left(\frac{dq'_i}{dt}\right)_{\text{Det}} + \left(\frac{dq'_i}{dt}\right)_{\text{Con}} \right] \quad (3.42)$$

Combining equations 3.39, 3.40, 3.41 and 3.42 allows us to express the proportionality constant \mathcal{C} as a function of the detrainment and condensation rates:

$$\mathcal{C} = \frac{1}{\sum_{i>j} (d_i q_i^* + c_i)}.$$

- Step 5: The downwards advection of the perturbation by the subsidence mass

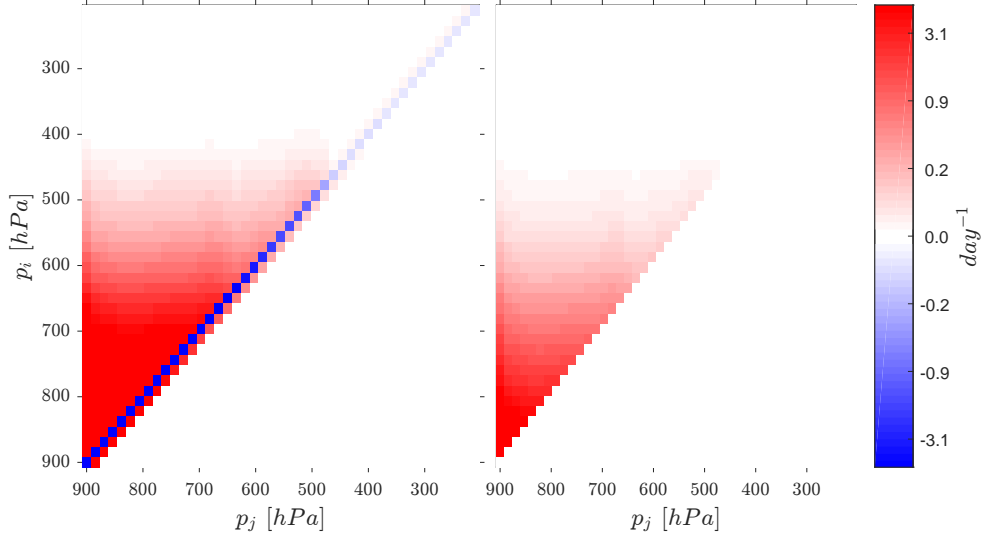


Figure 3-12: (a) Convective moistening (M_{LH}) and (b) Convective heating (M_{DSE}) linear response matrices, in units day^{-1} .

flux can be written using an upwind advection scheme. At the perturbation level ($i = j$):

$$\left(\frac{dq'_i}{dt}\right)_{\text{Adv}} = -q'_j \frac{gm_j}{\Delta p} \delta_{ij},$$

while below the perturbation level ($i = j - 1$):

$$\left(\frac{dq'_i}{dt}\right)_{\text{Adv}} = q'_j \frac{gm_j}{\Delta p} \delta_{i(j-1)}.$$

The full convective moistening response (equation 3.23) and convective heating response (equation 3.24) are then computed by using their definition:

$$(M_{\text{LH}})_{ij} = \frac{1}{q'_j} \left[\left(\frac{dq'_i}{dt}\right)_{\text{Ent}} + \left(\frac{dq'_i}{dt}\right)_{\text{Det}} + \left(\frac{dq'_i}{dt}\right)_{\text{Adv}} \right],$$

$$(M_{\text{DSE}})_{ij} = \frac{\alpha_i}{q'_j} \left(\frac{dq'_i}{dt}\right)_{\text{Con}}.$$

Because of the limits of our simple bulk-plume model, the entrainment rate is negative right above the top of the boundary layer and in parts of the upper troposphere, which would yield inconsistent linear responses. This problem is addressed by

replacing the negative values of e_j with the closest positive value of the entrainment rate that can be found below the level p_j .

3.7.3 A.3. Leading eigenvalue of the convective response matrices

We approximate the spectrum of the bulk-plume linear response matrix M_{BP} (sum of the responses given by equations 3.23 and 3.24) by the spectrum of the upper triangular matrix with the following diagonal:

$$(M_{\text{BP}})_{ii} + (M_{\text{BP}})_{(i-1)i} = -e_i.$$

In practice, this approximation is justified when the size of M_{BP} is large enough for its neighboring diagonal coefficients to be close:

$$\left| (M_{\text{BP}})_{ii} - (M_{\text{BP}})_{(i+1)(i+1)} \right| \ll |(M_{\text{BP}})_{ii}|.$$

The spectrum of an upper triangular matrix is given by its diagonal values: $e_i > 0$, which means that the leading eigenvalue real part of the bulk-plume linear response λ_{BP} is approximately given by:

$$\lambda_{\text{BP}} \approx -\min_p [e(p)].$$

For completeness, we compute the leading eigenvalue of the Betts-Miller linear response M_{BM} (sum of the responses given by equations 3.12 and 3.13). According to Gershgorin circle theorem, the spectrum of M_{BM} lies in the disc of center:

$$(M_{\text{BM}})_{ii} = \frac{1}{\tau_{\text{BM}}} \left(-1 + \frac{\alpha_i \Delta p}{p_b - p_t} \right),$$

and radius:

$$R_i = \sum_{j \neq i} \left| (M_{\text{BM}})_{ij} \right| = \frac{\Delta p}{\tau_{\text{BM}} (p_b - p_t)} \sum_{j \neq i} \alpha_j.$$

Therefore, an upper bound for the real part of the spectrum of M_{BM} is:

$$\lambda_{\text{BM}} = (M_{\text{BM}})_{ii} + R_i = \frac{1}{\tau_{\text{BM}}} \left(\underbrace{\frac{\Delta p}{p_b - p_t} \sum_j \alpha_j}_{\text{Vertical average } \alpha} - 1 \right). \quad (3.43)$$

This upper bound is reached for the eigenvector α_i , which proves that λ_{BM} is the exact leading eigenvalue real part of the Betts-Miller linear response.

3.8 Appendix B: Linear response of the Schwarzschild equations

3.8.1 B.1. Two-stream model of longwave radiation

First, we linearize the longwave flux convergence, given by equation 3.26, about RCE:

$$\frac{g}{\kappa} \frac{d\mathcal{F}_{\text{LW}}'}{dp} = f_1 f_2' (\mathcal{F}_{\uparrow} + \mathcal{F}_{\downarrow} - 2\sigma T^4) + f_1 f_2 (\mathcal{F}_{\uparrow}' + \mathcal{F}_{\downarrow}') \quad , \quad (3.44)$$

To quantitatively evaluate the second term of equation 3.44, we can:

1. Perturb the analytical solutions computed in Beucler and Cronin [2016] about RCE.
2. Use fundamental properties of the two-stream Schwarzschild equations, written below:

$$\frac{d\mathcal{F}_{\uparrow}}{d\tau} = \mathcal{F}_{\uparrow} - \sigma T^4 \quad , \quad \frac{d\mathcal{F}_{\downarrow}}{d\tau} = -\mathcal{F}_{\downarrow} + \sigma T^4. \quad (3.45)$$

The first method is straightforward but mathematically technical; here we adopt the second method to gain physical insight into gray radiative transfer. Let's start with the upwelling flux \mathcal{F}_{\uparrow} and integrate its Schwarzschild equation from the optical

thickness τ_j of a level p_j to the optical thickness τ_i of a level p_i :

$$\underbrace{(\mathcal{F}_\uparrow)_{\tau_i}}_{\text{Flux i}} = \underbrace{e^{-(\tau_j - \tau_i)}}_{\text{Transmittivity i} \rightarrow \text{j}} \left[\underbrace{(\mathcal{F}_\uparrow)_{\tau_j}}_{\text{Flux j}} + \underbrace{\sigma \int_{\tau_i}^{\tau_j} T^4 e^{-\tau'} d\tau'}_{\text{Atm emission i} \rightarrow \text{j}} \right]. \quad (3.46)$$

We now introduce an optical thickness perturbation τ'_j around the level p_j by introducing a water vapor perturbation q'_j in a thin pressure layer $[p_j - \Delta p/2, p_j + \Delta p/2]$ for which $\Delta p \ll p_j$. Our goal is to find the radiative response: $(\mathcal{F}_\uparrow + \mathcal{F}'_\uparrow)_{\tau_i}$ at the response level p_i . The bottom boundary condition is that the surface flux equals the (constant) terrestrial blackbody emission:

$$(\mathcal{F}_\uparrow)_{\tau_s} = \sigma T_s^4 = (\mathcal{F}_\uparrow + \mathcal{F}'_\uparrow)_{\tau_s + \tau'_j}.$$

We distinguish two cases:

1. If the perturbation level p_j is above the response level p_i , both the transmissivity and the atmospheric emission from the surface to the response level are unchanged. Writing equation 3.46 between the surface and response levels shows that the radiative response is unchanged: $(\mathcal{F}'_\uparrow)_{\tau_i + \tau'_j} = 0$.
2. If the perturbation level p_j is below the response level p_i , we first write equation 3.46 between the response level and right above the perturbation level:

$$\underbrace{(\mathcal{F}_\uparrow + \mathcal{F}'_\uparrow)_{\tau_i}}_{\text{Flux i}} = \underbrace{e^{-(\tau_j - \tau_i)}}_{\text{Transmittivity i} \rightarrow \text{j}} \left[\underbrace{(\mathcal{F}_\uparrow + \mathcal{F}'_\uparrow)_{\tau_j}}_{\text{Flux j}} + \underbrace{\sigma \int_{\tau_i}^{\tau_j} T^4 e^{-\tau'} d\tau'}_{\text{Atm emission i} \rightarrow \text{j}} \right], \quad (3.47)$$

where the temperature profile in optical thickness space $T(\tau)$ is unperturbed because we are above the perturbation level. Subtracting equation 3.46 to 3.47

relates the perturbation fluxes at levels p_i and p_j :

$$\underbrace{(\mathcal{F}'_{\uparrow})_{\tau_i}}_{\text{Perturbation flux i}} = \underbrace{e^{-(\tau_j - \tau_i)}}_{\text{Transmittivity i} \rightarrow \text{j}} \underbrace{(\mathcal{F}'_{\uparrow})_{\tau_j}}_{\text{Perturbation flux j}} . \quad (3.48)$$

Then, we write equation 3.46 between the surface and right below the perturbation level, use the fact that the temperature profile does not change in pressure space, and use equation 3.46 between the surface and level p_j before the perturbation was introduced:

$$\begin{aligned} \underbrace{(\mathcal{F}_{\uparrow} + \mathcal{F}'_{\uparrow})_{\tau_j + \tau'_j}}_{\text{Flux below pert}} &\stackrel{\text{Equation 3.46}}{=} \underbrace{e^{-(\tau_j - \tau_s)}}_{\text{Transmittivity s} \rightarrow \text{j}} \left[\underbrace{(\mathcal{F}_{\uparrow} + \mathcal{F}'_{\uparrow})_{\tau_s + \tau'_j}}_{\text{Surface flux}} + \underbrace{\sigma \int_{\tau_j + \tau'_j}^{\tau_s + \tau'_j} (T + T')^4 e^{-\tau'} d\tau'}_{\text{Atm emission s} \rightarrow \text{j}} \right] \\ &\stackrel{T(p) = (T + T')(p)}{=} \underbrace{e^{-(\tau_j - \tau_s)}}_{\text{Transmittivity s} \rightarrow \text{j}} \left[\underbrace{(\mathcal{F}_{\uparrow})_{\tau_s}}_{\text{Surface flux}} + \underbrace{\sigma \int_{\tau_j}^{\tau_s} T^4 e^{-\tau'} d\tau'}_{\text{Atm emission s} \rightarrow \text{j}} \right] \\ &\stackrel{\text{Equation 3.46}}{=} \underbrace{(\mathcal{F}_{\uparrow})_{\tau_j}}_{\text{Flux before pert}} . \end{aligned} \quad (3.49)$$

We can now express the perturbation flux at level j as a function of the total

flux at level j to first order:

$$\begin{aligned}
(\mathcal{F}'_{\uparrow})_{\tau_j} &\stackrel{\text{First order}}{=} (\mathcal{F}'_{\uparrow})_{\tau_j+\tau'_j} \\
&\stackrel{\text{Equation 3.49}}{=} (\mathcal{F}_{\uparrow})_{\tau_j} - (\mathcal{F}_{\uparrow})_{\tau_j+\tau'_j} \\
&\stackrel{\text{First order}}{=} - \left(\frac{d\mathcal{F}_{\uparrow}}{d\tau} \right)_{\tau_j} \tau'_j \\
&\stackrel{\text{Equation 3.45}}{=} \left[\sigma T_j^4 - (\mathcal{F}_{\uparrow})_{\tau_j} \right] \tau'_j \\
&\stackrel{\text{Equation 3.25}}{=} \left[\sigma T_j^4 - (\mathcal{F}_{\uparrow})_{\tau_j} \right] \frac{\kappa (f_1 f'_2)_{\tau_j}}{g} \\
&\stackrel{\text{First order}}{=} \frac{\kappa}{g} \left(f_1 \frac{df_2}{dq} \right)_{\tau_j} \left[\sigma T_j^4 - (\mathcal{F}_{\uparrow})_{\tau_j} \right] q'_j \\
(\mathcal{F}'_{\uparrow})_{\tau_j} &\stackrel{\text{Equation 3.48}}{=} \frac{\kappa}{g} \left(f_1 \frac{df_2}{dq} \right)_{\tau_j} e^{-|\tau_i-\tau_j|} \left[\sigma T_j^4 - (\mathcal{F}_{\uparrow})_{\tau_j} \right] q'_j
\end{aligned} \tag{3.50}$$

It is possible to use a similar reasoning for the downwelling flux and find that:

1. If the perturbation level p_j is above the response level p_i , the downwelling flux is perturbed, and to first order:

$$(\mathcal{F}'_{\downarrow})_{\tau_i} = \frac{\kappa}{g} \left(f_1 \frac{df_2}{dq} \right)_{\tau_j} e^{-|\tau_i-\tau_j|} \left[\sigma T_j^4 - (\mathcal{F}_{\downarrow})_{\tau_j} \right] q'_j. \tag{3.51}$$

2. If the perturbation level p_j is below the response level p_i , the downwelling flux is unchanged.

Combining equations 3.44, 3.50 and 3.51 leads to the longwave linear response (equation 3.27) by using its definition:

$$(M_{\text{LW}})_{ij} \stackrel{\text{def}}{=} \frac{g\alpha_i}{L_v q'_j} \left(\frac{d\mathcal{F}_{\text{LW}}'}{dp} \right)_{p_i}. \tag{3.52}$$

3.8.2 B.2. One-stream model of shortwave radiation

First, we linearize the shortwave flux convergence, given by equation 3.31, about RCE:

$$- \frac{g}{\kappa} \frac{d\mathcal{F}_{\text{SW}}'}{dp} = \varepsilon f_1 f'_2 \mathcal{F}_{\text{SW}} + \varepsilon f_1 f_2 \mathcal{F}'_{\text{SW}}, \tag{3.53}$$

This time, we directly perturb the analytical solution for the downwelling shortwave flux:

$$\frac{\mathcal{F}_{\text{SW}}}{\mathcal{S}} = e^{-\varepsilon\tau}, \quad (3.54)$$

$$\frac{\mathcal{F}'_{\text{SW}}}{\mathcal{S}} = e^{-\varepsilon\tau} \left(e^{-\varepsilon\kappa g^{-1} \int_0^p f_1 f'_2} - 1 \right). \quad (3.55)$$

Then again, we introduce a water vapor perturbation q'_j in a thin pressure layer $[p_j - \Delta p/2, p_j + \Delta p/2]$, for which $\Delta p \ll p_j$, and use the smallness of $\Delta p/p_j$ to simplify the form of the perturbation fluxes at a given level p_i :

$$\left(\frac{\mathcal{F}'_{\text{SW}}}{\mathcal{S}} \right)_{p_i} = e^{-\varepsilon\tau_i} \frac{\varepsilon\kappa\Delta p}{g} (f_1 f'_2)_{p_j} \delta_{i < j}. \quad (3.56)$$

Combining equations 3.53 and 3.56 leads to the shortwave linear response (equation 3.32) by using its definition:

$$(M_{\text{SW}})_{ij} \stackrel{\text{def}}{=} -\frac{g\alpha_i}{L_v q'_j} \left(\frac{d\mathcal{F}_{\text{SW}}'}{dp} \right)_{p_i}. \quad (3.57)$$

3.8.3 B.3. Choice of the optical thickness

For consistency with Beucler and Cronin [2016], we represent the optical thickness for Figure 3-9 using the following functions of pressure in equations 3.25 and 3.30:

$$\kappa = 0.17 \text{m}^2 \cdot \text{kg}^{-1}, \quad f_1(p) = \frac{p}{p_s}, \quad f_2(q) = q, \quad \varepsilon(p) \approx 0.077.$$

This choice assumes a simple pressure broadening of water vapor, neglects the greenhouse effects of gas other than water vapor, and estimates the total shortwave absorption using equation 20 of Beucler and Cronin [2016]. The net radiative cooling (sum of equations 17 and 21 in Beucler and Cronin [2016]) as a function of the free-tropospheric optical thickness is depicted in Figure 3-13, as well as its longwave and shortwave components. The net radiative cooling (black line) matches the radiative cooling computed by RRTM (150 Wm^{-2}) for two choices of the absorption coefficient: $\kappa = (0.022, 0.17) \text{m}^2 \cdot \text{kg}^{-1}$, corresponding to two surface optical thicknesses

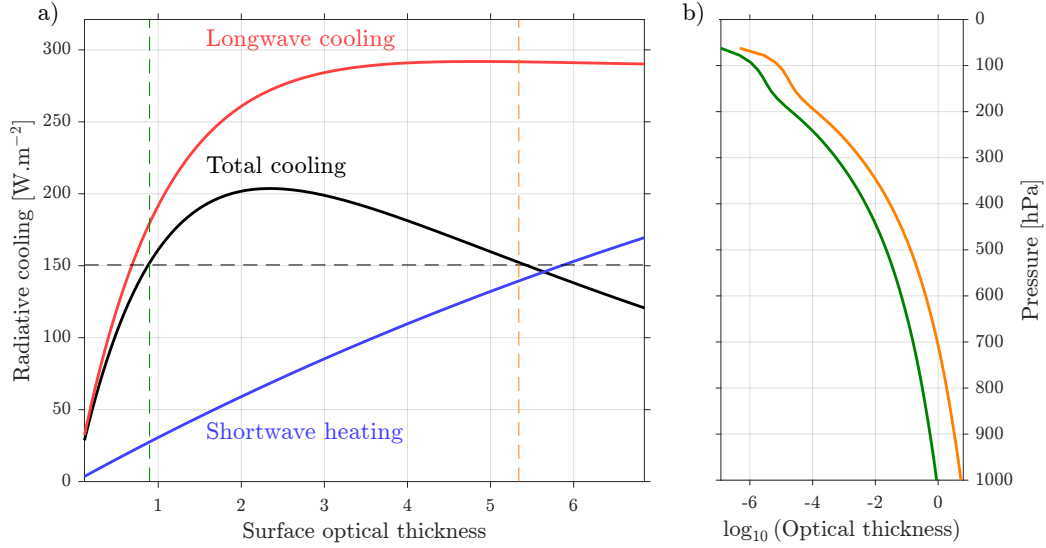


Figure 3-13: (a) Free-tropospheric longwave cooling (red line) and shortwave heating (blue line) and total net radiative cooling (black line) in $\text{W}\cdot\text{m}^{-2}$, versus surface optical thickness. The net radiative cooling in SAM is denoted with a dotted black line, and intersects the total radiative cooling of the gray model for two values of the surface optical thickness (denoted with green and orange vertical dotted lines). (b) Logarithm 10 of optical thickness profile in pressure space when the absorption coefficient is $\kappa = 0.022\text{m}^2\cdot\text{kg}^{-1}$ (green line) and $\kappa = 0.17\text{m}^2\cdot\text{kg}^{-1}$ (orange line).

of (0.8 , 5.4). For the gray radiative linear response matrix, we choose the optically thick solution $\kappa = 0.17\text{m}^2\cdot\text{kg}^{-1}$ (orange lines), for which the radiative cooling decreases with surface optical thickness and moisture radiative-cooling instability can occur [Beucler and Cronin, 2016].

3.9 Appendix C: Sensitivity to convective model parameters

In this section, we investigate how the stability of the linear response depends on the convective parameters τ_{BM} and \hat{Q}_{BP} . Following section 3.5, we combine the Betts-Miller convective response and the bulk-plume convective response with the real-gas radiative response in order to obtain the full linear response and study the

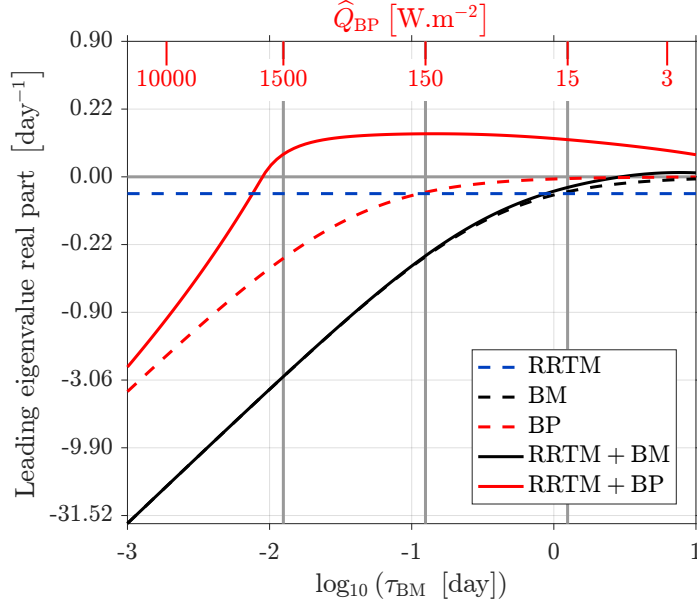


Figure 3-14: Leading eigenvalue real part of the 300K linear response (in day^{-1}) as a function of $\log_{10} \tau_{\text{BM}}$ (in hours, for the RRTM+BM and BM cases) and \hat{Q}_{BP} (in W m^{-2} , for the RRTM+BP and BP cases). The scale for τ_{BM} and the scale for \hat{Q}_{BP} are aligned so that the responses depicted on figure 3-5 (BM, $\tau_{\text{BM}} = 3$ hours) and 3-7 (BP, $\hat{Q}_{\text{BP}} = 150 \text{ W m}^{-2}$) fall on the same vertical line (central vertical gray line). The two other vertical gray lines indicate the range of realistic convective parameters.

linear evolution of small water vapor perturbations. The total Betts-Miller response matrix $M_{\text{BM}+\text{RRTM}}$ and the total bulk-plume response matrix $M_{\text{BP}+\text{RRTM}}$ are given by:

$$M_{\text{BM}+\text{RRTM}}(\tau_{\text{BM}}) = M_{\text{BM}}(\tau_{\text{BM}}) + M_{\text{RRTM}}, \quad (3.58)$$

$$M_{\text{BP}+\text{RRTM}}(\hat{Q}_{\text{BP}}) = M_{\text{BP}}(\hat{Q}_{\text{BP}}) + M_{\text{RRTM}}, \quad (3.59)$$

where the Betts-Miller convective response M_{BM} depends on the Betts-Miller timescale τ_{BM} and the bulk-plume convective response M_{BP} depends on the radiative cooling parameter \hat{Q}_{BP} , while the radiative response M_{RRTM} remains unchanged for a fixed surface temperature.

In figure 3-14, we define the range of realistic convective parameters as τ_{BM} between 0.3 and 30 hours, and $\hat{Q}_{\text{BP}} = 150$ between 15 and 1500 W m^{-2} . Over this wide range of convective parameters, none of the leading eigenvalue real parts change sign.

The combined RRTM and bulk-plume response is the only linearly unstable response with an average growth rate of 10.0 days over the realistic range of parameters.

Chapter 4

A Budget for the Size of Convective Self-aggregation

Abstract

There is no consensus on the physical mechanisms controlling the scale at which convective activity organizes near the Equator. Here, we introduce a diagnostic framework relating the evolution of the length scale of convective aggregation to the net radiative heating, the surface enthalpy flux, and horizontal energy transport. We evaluate these expansion tendencies of convective aggregation in twenty high-resolution cloud-permitting simulations of radiative-convective equilibrium. While both radiative fluxes contribute to convective aggregation, the net longwave radiative flux operates at large scales (1000-5000 km) and stretches the size of moist and dry regions, while the net shortwave flux operates at smaller scales (500-2000 km) and shrinks it. The surface flux expansion tendency is dominated by convective gustiness, which acts to aggregate convective activity at smaller scales (500-3000 km).

4.1 Introduction

To first order, the size of extra-tropical storms is set by the Rossby deformation radius, which scales inversely with the Coriolis parameter. However, what sets the scale at which convective activity organizes near the Equator, where the Coriolis parameter is small, remains an open question. Observations of monsoonal depressions (e.g. Figure 12 of Houze [1989]) and the Madden-Julian oscillation (e.g. Figure 3b of Zhang [2005]) indicate that convectively active regions near the Equator span scales from 100 km to

15,000 km, but we lack a simple framework that would combine internal and external influences on the scale of these regions.

Fundamental understanding of convection has been bolstered by simulating radiative-convective equilibrium, an idealized state of the Tropical atmosphere in which radiative cooling balances convective heating in the absence of lateral energy transport (e.g. review by Ramanathan and Coakley [1978]) using cloud-permitting models (e.g. Tompkins and Craig [1998]) and general circulation models with parametrized convection (e.g. Held et al. [2007]). High-resolution cloud-permitting simulations of non-rotating convection show the clustering of convective activity despite homogeneous boundary forcing; this phenomenon has been referred to as convective self-aggregation (e.g. Held et al. [1993], Bretherton et al. [2005]). Studies to date with square domains in three-dimensional cloud-permitting models, without rotation, have found at most one cluster in the self-aggregated state, regardless of the domain size. With only a single cluster in aggregated square domains, the length scale of self aggregation in such simulations does not correlate with other parameters such as resolution (e.g. Muller and Held [2012]) or surface temperature (e.g. Wing and Emanuel [2014]), limiting our physical understanding of the length scale of convective aggregation. However, using the Regional Atmospheric Modeling System, Posselt et al. [2012] showed that non-rotating simulations which used elongated-channel geometry exhibited multiple aggregated areas. Wing and Cronin [2016] came to the same conclusion using the System for Atmospheric Modeling (SAM). Arnold and Randall [2015] and Coppin and Bony [2015] showed that aquaplanet simulations using the Goddard Earth observing System Atmospheric General Circulation Model and the IPSL-CM5A-LR General Circulation Model, respectively, exhibited multiple convective clusters when run with parametrized convection. The same is true for more realistic aquaplanet simulations that include planetary rotation and latitudinal sea surface temperature gradients (e.g. Bretherton and Khairoutdinov [2015]). These recent findings suggest that the length scale L of convective aggregation may be regulated by physical mechanisms, rather than artifacts of the model configuration, in some simulations – and thus within the reach of physical understanding.

Since resolving both moist turbulent convective activity (1-10 km scale) and the scale of moist and dry regions associated with large-scale overturning circulations (100-1000 km scale) is computationally expensive, identifying the physical mechanisms that set the length scale L of moist and dry regions remains an active research area. In the context of an aquaplanet model with parameterized convection, Grabowski and Moncrieff [2004] have proposed that the length scale associated with moisture-convection feedback on intra-seasonal timescales is related to the large-scale subsidence drying. By taking the product of the typical horizontal wind speed ($\sim 5 \text{ m s}^{-1}$) and a subsidence drying timescale ($\sim 10 \text{ d}$), they obtain a value $L \sim 5000 \text{ km}$. In the context of elongated-channel simulations, Wing and Cronin [2016] proposed that L is the distance needed to re-moisten a subsiding air parcel in the boundary layer, which scales as the ratio of the boundary layer height ($\sim 1 \text{ km}$) to the surface enthalpy exchange coefficient ($\sim 2 \times 10^{-3}$), leading to typical values of 500 km. However, this simple scaling does not capture the decrease of length scale observed when the radiation scheme is changed [see Figure 7 of Wing and Cronin, 2016] from the radiative transfer module of the National Center for Atmospheric Research Community Atmosphere Model version 3 [CAM, Collins et al., 2006] to the Rapid Radiative Transfer Model [RRTM, Iacono et al., 2008]. In the context of two-dimensional cloud-permitting simulations with SAM, Yang [2017] proposed that L scales like the product of the boundary layer height ($\sim 1 \text{ km}$), the square root of the boundary layer density variations due to humidity variations ($\sim \sqrt{10^{-3}}$, referred to as the virtual effect), and a combined parameter that includes momentum damping in the boundary layer, stratification and radiative cooling at the top of the boundary layer (5×10^{-4}). Although this scaling yields the correct order of magnitude for L ($\sim 1500 \text{ km}$), the theory requires knowledge of density and radiative cooling variations at the top of the boundary layer. The underlying physical mechanism proposed by Yang [2017] has been refined by Arnold and Putman [2018] in the context of the Goddard Earth Observing System Atmospheric General Circulation Model, who suggested that density variations in the boundary layer due to temperature variations constrain L to be less than 3000-4000 km through boundary layer momentum balance.

The previous theories predict the order of magnitude of L and some of its dependencies (surface temperature, boundary layer properties, etc.) by assuming a dominant physical mechanism a priori. This chapter takes an alternative approach by formulating a budget for L and diagnosing the contributions to its evolution from different processes in three-dimensional cloud-permitting simulations with interactive radiation, surface fluxes and large-scale dynamics. We ask:

How do radiation, surface enthalpy fluxes and advection contribute to the emergence and evolution of a dominant length scale for convective aggregation?

In the spirit of the spectral analysis done in Arnold and Randall [2015] and in sections 5-7 of Bretherton and Khairoutdinov [2015], we develop a spectral diagnostic framework for the evolution of L in section 4.2, and identify the controlling physical mechanisms from the results in section 4.3.

4.2 Method

Our goal is to quantify the roles of radiation, surface fluxes and advection in selecting the length scale of convective organization. First, we define a length scale L for convective aggregation from the spatial spectrum of moist static energy (section 4.2.1). Then, we formulate a spectral budget that relates the evolution of L to the vertically-integrated moist static energy fluxes (section 4.2.2). We evaluate the radiative, surface flux and advective terms of this budget in a set of three-dimensional, cloud-permitting simulations across a range of sea surface temperatures, using SAM (section 4.2.3).

4.2.1 Definitions

We use the column-integrated frozen moist static energy H – interchangeably referred to as MSE in this chapter – as a proxy for the organization of convection. H has units J m^{-2} and is defined as the sum of column internal energy, potential energy and

latent heat:

$$H \stackrel{\text{def}}{=} \int_0^{p_s} \frac{dp}{g} \left(\underbrace{c_p T}_{\text{Sensible heat}} + \underbrace{gz}_{\text{Potential energy}} + \underbrace{L_v q}_{\text{Lat. heat vap}} - \underbrace{L_f q_i}_{\text{Lat. heat fusion}} \right), \quad (4.1)$$

where p_s is the surface pressure, dp the differential pressure, g the gravity constant, c_p the specific heat capacity of dry air at constant pressure, T the absolute temperature, z the geopotential height, L_v the latent heat of vaporization, q the specific humidity, L_f the latent heat of fusion and q_i the condensed ice water mixing ratio. When convection is statistically homogeneous (a.k.a. "pop-corn" convection), then H is also statistically homogeneous. However, when convection starts to organize, a large-scale overturning circulation develops (e.g. Muller and Bony [2015]). Regions of large-scale upwelling are moister (higher H) and have more active convection, while regions of large-scale downwelling are drier (lower H) and have less active convection. Therefore, a natural size for the organization of convection is the distance between regions of negative and positive spatial MSE anomalies. To gain a physical understanding of what sets this distance L , we formally define it as the spectral mean of the wavelength, weighted by the spatial power spectrum φ of H :

$$L \stackrel{\text{def}}{=} \frac{\langle \lambda \varphi \rangle}{\langle \varphi \rangle}, \quad (4.2)$$

where the wavelength λ is defined from the modulus $\|\mathbf{k}\|$ of the wave vector \mathbf{k} in n dimensions as:

$$\lambda = \frac{2\pi\sqrt{n}}{\|\mathbf{k}\|}. \quad (4.3)$$

The spatial spectrum of H , φ , is defined from the MSE spatial Fourier transform \hat{H} :

$$\varphi \stackrel{\text{def}}{=} \hat{H} \hat{H}^*, \quad (4.4)$$

$$\hat{H} \stackrel{\text{def}}{=} \frac{1}{(2\pi)^{n/2}} \int_{\mathbf{0}}^{\mathbf{L}^{\text{dom}}} \exp(-i\mathbf{k} \cdot \mathbf{x}) H(\mathbf{x}) d\mathbf{x}, \quad (4.5)$$

where \widehat{H}^* is the complex conjugate of \widehat{H} , \mathbf{x} is the horizontal position vector in n dimensions and ι is the unit imaginary number, $\iota^2 = -1$ (note that we later use i as an index to refer to distinct processes). In equation 4.5, the domain is assumed to be rectangular and to span from the origin of the coordinate system $\mathbf{x} = \mathbf{0}$ to the opposite corner of the domain $\mathbf{x} = \mathbf{L}_{\text{dom}}$. To improve the readability of equation 4.2, we have introduced the spectral average $\langle \cdot \rangle$:

$$\langle X \rangle \stackrel{\text{def}}{=} \frac{\int_{\mathbf{k}_0}^{\mathbf{k}_N} X(\mathbf{k}) d\mathbf{k}}{\int_{\mathbf{k}_0}^{\mathbf{k}_N} d\mathbf{k}}, \quad (4.6)$$

where \mathbf{k}_0 is the wavenumber with smallest non-zero magnitude and \mathbf{k}_N is the Nyquist wavenumber. In a rectangular three-dimensional model of horizontal domain size (L_x, L_y) and resolution (dx, dy) , the integration bounds are $\mathbf{k}_0 = 2\pi(L_x^{-1}, L_y^{-1})$ and $\mathbf{k}_N = \pi(dx^{-1}, dy^{-1})$. In applying equation 4.3 to a three-dimensional domain with equal horizontal lengths $L_x = L_y$, the pre-factor $2\pi\sqrt{2}$ ensures that L equals the segment length L_x if all the power φ is concentrated in the largest wave vector \mathbf{k}_0 . In this study, we have made a simple choice for the definition of L given by equation 4.2. Alternatively, we could have used the integral scale: $2\pi\sqrt{n} \langle \varphi \rangle / \langle \|\mathbf{k}\| \varphi \rangle$ to measure the scale of MSE spatial anomalies (e.g. equation 8.45 of Vallis [2006] and equations 7-8 of Wing and Cronin [2016]). It is possible to generalize the definition of L to: $L \stackrel{\text{def}}{=} 2\pi\sqrt{n} \langle \|\mathbf{k}\|^p \varphi \rangle^{1/q} \langle \|\mathbf{k}\|^{p+q} \varphi \rangle^{-1/q}$, where $(p, q) \in \mathbb{Z}^2$ are integers. Note that $(p, q) = (-1, 1)$ in our definition of L (equation 4.2). The choice of (p, q) determines the relative weighting of the different parts of the spectrum φ . For example, if $(p+1)$ is larger than the spectral slope s such that $\varphi \sim \|\mathbf{k}\|^{-s}$, then L is determined by the small-scale contributions to the MSE spectrum, while L is dominated by the large-scale contributions to the MSE spectrum if $(p+q+1)$ is smaller than s . Therefore, L cannot describe the MSE spectrum in its full complexity, and we compare different choices for L in appendix A. Nevertheless, having a single metric $L(t)$ to quantify the spatial organization of MSE reduces the problem to a single time-dependent variable, and we proceed to relate its time-evolution to the fluxes of MSE.

4.2.2 Budgets

Frozen moist static energy budget

The column frozen moist static energy H is conserved under vertical convective mixing, and altered by the net moist static energy flux (in Wm^{-2}) through the boundaries of the atmospheric column in consideration. The total flux is the sum of the net radiative flux at the top and bottom of the atmosphere \dot{H}_{rad} , the net surface enthalpy flux \dot{H}_{sf} , and the horizontal flux of moist static energy \dot{H}_{adv} (referred to as the advective flux and defined as the mass-weighted column integral of the three-dimensional advection of local frozen moist static energy). The evolution equation of H can be written:

$$\frac{\partial H}{\partial t} = \dot{H}_{\text{lw}} + \dot{H}_{\text{sw}} + \dot{H}_{\text{sf}} + \dot{H}_{\text{adv}}, \quad (4.7)$$

where t is time (in s). When averaged in space and time, the net longwave flux \dot{H}_{lw} is negative as the atmosphere cools to space, the net shortwave flux \dot{H}_{sw} positive as the atmosphere absorbs solar radiation, and the surface enthalpy flux \dot{H}_{sf} positive as the surface enthalpy is greater than the enthalpy of the air above it. In RCE, these three tendencies balance out to zero in the absence of horizontal MSE fluxes \dot{H}_{adv} . As an atmospheric circulation develops, the MSE advective flux \dot{H}_{adv} becomes positive if there is a net MSE import into the column, and negative in the case of a net MSE export. Equation 4.7 holds for all length scales, which means that at a given scale, the value of each flux increases or decreases the MSE at that scale. This statement can be made mathematically explicit by working in spectral space.

Budget for the spatial spectrum of frozen moist static energy

To derive the budget for the spatial spectrum of frozen moist static energy φ , we start by taking the time-derivative of its definition (equation 4.4):

$$\frac{\partial \varphi}{\partial t} \stackrel{\text{def}}{=} \frac{\partial \left(\widehat{H}^* \widehat{H} \right)}{\partial t} = 2\text{Re} \left(\widehat{H}^* \frac{\partial \widehat{H}}{\partial t} \right), \quad (4.8)$$

where Re refers to the real part of a complex number. We then take the spatial Fourier transform of the frozen moist static energy's budget (equation 4.7):

$$\frac{\partial \widehat{H}}{\partial t} = \frac{\partial \widehat{H}}{\partial t} = \widehat{H}_{\text{lw}} + \widehat{H}_{\text{sw}} + \widehat{H}_{\text{sf}} + \widehat{H}_{\text{adv}}. \quad (4.9)$$

Substituting equation 4.9 into equation 4.8 yields:

$$\frac{\partial \varphi}{\partial t} = \dot{\varphi}_{\text{lw}} + \dot{\varphi}_{\text{sw}} + \dot{\varphi}_{\text{sf}} + \dot{\varphi}_{\text{adv}}, \quad (4.10)$$

where each spectral tendency $\dot{\varphi}_i$ is related to the corresponding flux \dot{H}_i via:

$$\forall i, \quad \dot{\varphi}_i = 2\text{Re} \left\{ \widehat{H}^* \widehat{H}_i \right\}, \quad (4.11)$$

where $\forall i$ indicates that equation 4.11 is valid for each individual process \dot{H}_i . Note that we use i hereafter as a general subscript to refer to any of the processes that modify H : longwave radiation, shortwave radiation, surface fluxes, or advection. Equation 4.10 relates the evolution of the spectrum φ to the spectral tendencies $\dot{\varphi}_i$ for each wave vector \mathbf{k} .

Convective aggregation length scale budget

To derive the budget for the convective aggregation length scale L , we start by taking the logarithmic time-derivative of its definition (equation 4.2):

$$\frac{1}{L} \frac{\partial L}{\partial t} \stackrel{\text{def}}{=} \frac{1}{\langle \lambda \varphi \rangle} \left\langle \lambda \frac{\partial \varphi}{\partial t} \right\rangle - \frac{1}{\langle \varphi \rangle} \left\langle \frac{\partial \varphi}{\partial t} \right\rangle \quad (4.12)$$

We then substitute the right-hand side of the φ -evolution equation 4.10 into equation 4.12. This allows us to write the right-hand side of equation 4.12 as a sum of individual expansion tendencies (in units m s^{-1}), which we refer to as the budget for the convective aggregation length scale L :

$$\frac{\partial L}{\partial t} = \dot{L}_{\text{lw}} + \dot{L}_{\text{sw}} + \dot{L}_{\text{sf}} + \dot{L}_{\text{adv}}. \quad (4.13)$$

Note that we use ‘rate’ to describe the relative growth or decay (in inverse time units) of the total MSE spatial variance $\langle\varphi\rangle$ (aggregation rate) or the convective aggregation length scale L (expansion rate), while ‘tendency’ refers to the time-derivative of a variable. According to equation 4.12, each expansion rate is given by:

$$\begin{aligned}\forall i, \frac{\dot{L}_i}{L} &= \frac{\langle\lambda\dot{\varphi}_i\rangle}{\langle\lambda\varphi\rangle} - \frac{\langle\dot{\varphi}_i\rangle}{\langle\varphi\rangle} \\ &= \frac{\langle\dot{\varphi}_i\rangle}{\langle\varphi\rangle} \left(\frac{\langle\lambda\dot{\varphi}_i\rangle}{\langle\dot{\varphi}_i\rangle} \frac{\langle\varphi\rangle}{\langle\lambda\varphi\rangle} - 1 \right)\end{aligned}\tag{4.14}$$

The tendencies of L , given by equation 4.14, can be re-written as:

$$\forall i, \dot{L}_i = \underbrace{\frac{\langle\dot{\varphi}_i\rangle}{\langle\varphi\rangle}}_{\text{Aggregation rate}} \underbrace{(\mathcal{L}_i - L)}_{\text{Length scale factor}},\tag{4.15}$$

$$\mathcal{L}_i \stackrel{\text{def}}{=} \frac{\langle\lambda\dot{\varphi}_i\rangle}{\langle\dot{\varphi}_i\rangle},\tag{4.16}$$

where \mathcal{L}_i is the length scale associated with the spectral tendency $\dot{\varphi}_i$, analogous to the convective aggregation length scale L (equation 4.2), but based on the tendency of the spectrum of H due to a particular physical process, rather than on the spectrum of H itself. To build intuition about what sets \mathcal{L}_i , we consider three examples:

1. A diabatic process that linearly damps spatial MSE anomalies H' at a rate α , such as the enthalpy disequilibrium component of the surface flux: $\dot{H}_{\text{dis}} \approx -\alpha H'$. Following equation 4.11, its spectral tendency linearly damps the MSE spectrum for non-zero wave vectors: $\dot{\varphi}_{\text{dis}} = 2\text{Re} \left\{ \widehat{H}^* (-\alpha H) \right\} = -2\alpha\varphi$. Finally, equation 4.16 yields: $\mathcal{L}_{\text{dis}} = \langle -2\alpha\varphi\lambda \rangle / \langle -2\alpha\varphi \rangle = L$, showing that a scale-neutral diabatic process that acts to linearly damp or amplify the MSE anomaly has the same scale L as the MSE anomaly itself.
2. A scale-selective process that preferentially amplifies MSE anomalies at large scales, such as the net longwave flux convergence: $\widehat{H}_{\text{lw}} = \alpha (\lambda/\lambda_0)^\mu \widehat{H}'$, where α, μ and λ_0 are constant positive rate, longwave spectral exponent and characteristic wavenumber, respectively. Following equation 4.11, its spectral tendency

is strongest at large scales: $\dot{\varphi}_{1w} = 2\text{Re} \left\{ \widehat{H}^* \alpha (\widehat{\lambda/\lambda_0})^\mu H \right\} = 2\alpha (\lambda/\lambda_0)^\mu \varphi$. At this point, it is useful to note that except for small wave vectors, the MSE spectrum quickly decays with the wave vector amplitude: $\varphi = \varphi_0 \lambda^s$, where φ_0 is a constant spectral amplitude and we require the spectral slope s be strictly larger than 2. Typically, $s \approx 3$ above wavenumber $(2\pi) L^{-1}$, as can be seen in panel 6b of Wing and Cronin [2016]; if the spectral slope s was smaller than 2, our definition of the convective aggregation length scale L would depend on the model's horizontal grid spacing through the Nyquist wave vector \mathbf{k}_N . The diabatic length scale for that scale-selective process is calculated using equation 4.16:

$$\frac{\mathcal{L}_{1w}}{L} = \frac{\langle \lambda \dot{\varphi}_{1w} \rangle \langle \varphi \rangle}{\langle \dot{\varphi}_{1w} \rangle \langle \lambda \varphi \rangle} = \frac{\langle \lambda^{\mu+s+1} \rangle \langle \lambda^s \rangle}{\langle \lambda^{\mu+s} \rangle \langle \lambda^{s+1} \rangle} \approx 1 + \underbrace{\frac{\mu}{(\mu+s)(s-1)}}_{>1}. \quad (4.17)$$

Therefore, a process i that amplifies MSE anomalies at large scales has an associated length scale \mathcal{L}_i larger than the MSE anomaly scale L , by a factor that depends on the MSE spectral slope s and the spectral exponent of the process, μ .

3. A scale-selective process that preferentially amplifies MSE anomalies at small scales, such as the net shortwave flux convergence. By applying the previous model and equation 4.17 to the case of a constant negative spectral exponent $\mu \in]-s, 0[$, the length scale \mathcal{L} associated with that process is smaller than the MSE anomaly scale L .

Equation 4.15 allows us to interpret each tendency \dot{L}_i as a product of two factors. In appendix A.2, we prove that the factor $\langle \dot{\varphi}_i \rangle / \langle \varphi \rangle$ is equal to the growth rate of moist static energy spatial variance in inverse time units (e.g. the terms on the right-hand side of equation 4 of Wing and Cronin [2016]; see sections 3.1-3.4 of Wing et al. [2017] for a review of their physical interpretation). The second factor is a length scale factor that vanishes if the convective aggregation length scale L equals the length scale \mathcal{L}_i .

We focus on the physical interpretation of equation 4.15 in section 4.2.5.

4.2.3 Simulation design

We use a series of twenty simulations to understand the dependence of the radiative, surface flux and advective expansion tendencies on the surface temperature, radiation scheme and domain geometry. Following Wing and Cronin [2016], radiative-convective equilibrium (RCE) is simulated using version 6.8.2 of SAM (e.g. Khairoutdinov et al. [2003]); we contrast the characteristics of the cloud-permitting experiments in table 4.1. Seventeen of the twenty simulations were provided by Allison Wing; the reader interested in the setup and general characteristics of the long-channel simulations is referred to sections 3 and 4 of Wing and Cronin [2016], respectively, while the characteristics of the square simulation are described in sections 7.2 and 7.5 of Wing and Cronin [2016]. The big square-domain simulation uses the same set-up as the square-domain simulations (Allison Wing, personal communication). We also run 3 mechanism denial experiments (MD), in which the radiative heating, the surface enthalpy fluxes, and both the radiative heating and the surface enthalpy fluxes, are horizontally homogenized at each vertical level and at the beginning of each timestep. The evolution of the moist static energy field H , averaged over the short dimension of the channel for these 3 experiments, is depicted in Figure 4-1, as well as the evolution of L . The evolution of the moist static energy field H of the three square experiments is depicted in Figure 4-2, along with the corresponding MSE anomaly scale L .

Acronym	LC	MD	SQ	BSQ
# simulations	14	3	2	1
T_s (K)	280/285/.../310	300	305	305
Dom. size (km)	12 288 × 192	12 288 × 192	1536 × 1536	3072 × 3072
Radiation	CAM/RRTM	CAM	CAM/RRTM	RRTM

Table 4.1: Characteristics of the twenty cloud-permitting experiments used in this chapter. From top to bottom: Acronym given to the series of simulations (LC: Long-channel domain, MD: Mechanism-denial experiments, SQ: Square domain, BSQ: Big square domain), number of simulations in each series, fixed surface temperature T_s , domain size and radiation scheme.

4.2.4 Calculation of the budget terms

Hourly-averages of H and the diabatic fluxes \dot{H}_{lw} , \dot{H}_{sw} , \dot{H}_{sf} are computed every hour, using their values at every time step. We call the radiation module every six minutes, calculate hypothetical radiative heating profiles without clouds for diagnostic purposes, and obtain longwave and shortwave “clear-sky” radiative fluxes: \dot{H}_{lwcs} , \dot{H}_{swcs} . The advective flux, \dot{H}_{adv} , is computed as a residual from equation 4.7. We verify that \dot{H}_{adv} calculated as a residual has the same behavior as \dot{H}_{adv} computed from the three-dimensional fields of H and velocity (for the standard experiment LC300 with CAM radiation, the domain-averaged aggregation feedback $\langle \dot{\varphi}_{adv} \rangle$ matches within 20% if we use three-dimensional snapshots in time of H and velocity to compute \dot{H}_{adv} directly). We calculate the Fourier transform of H and the MSE tendencies \dot{H}_i using the MATLAB Fast Fourier Transform, which uses the C library FFTW (e.g. Frigo and Johnson [2005]). For the LC and MD simulations, the spatial variability in the long direction is more than 10 times the spatial variability in the short direction once convection has aggregated. Therefore, we average H and \dot{H}_i in the short direction before computing one-dimensional Fourier transforms in the long direction to calculate the moist static energy spectrum φ and the spectral tendencies $\dot{\varphi}_i$. The spectral tendencies $\dot{\varphi}_i$ would have more power at smaller wavelengths λ if the Fourier trans-

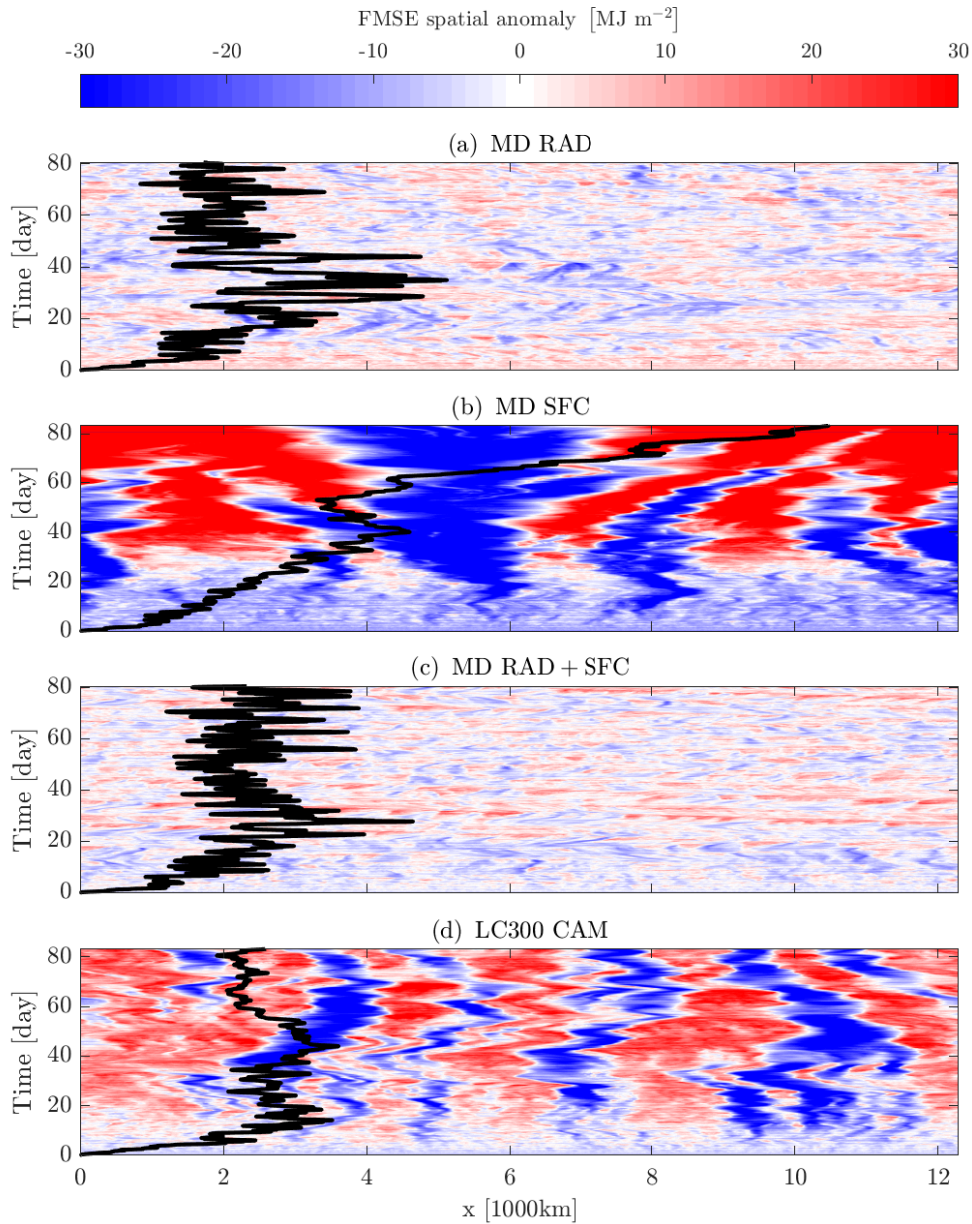


Figure 4-1: Hovmüller diagram of the frozen moist static energy spatial anomaly H' (in MJ m⁻²) for the three MD experiments and the control LC300 CAM experiment. The vertical axis is time (in days) and the horizontal axis is x (in 1000km). The anomaly has been spatially-averaged in the y -direction. The distance between the left vertical axis and the thick, black line represents the one-dimensional time-varying convective aggregation length scale $L(t)$ (in 1000km, defined in equation 4.2).

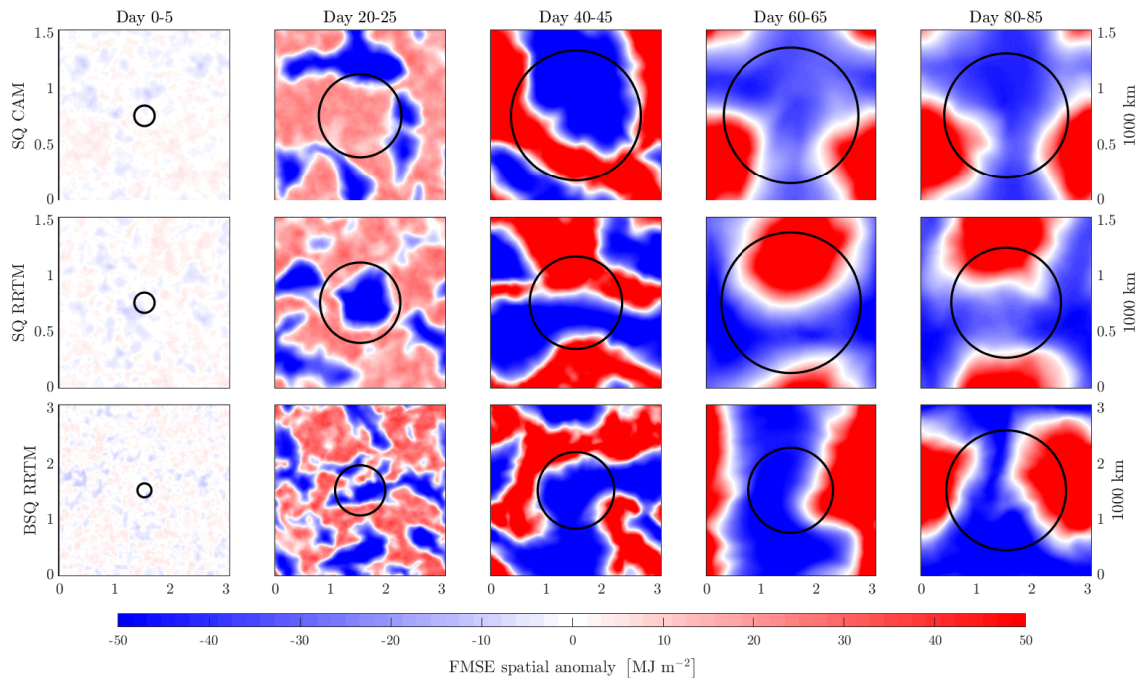


Figure 4-2: Snapshots of the frozen moist static energy spatial anomaly H' , averaged in time over periods of five days (in MJ m^{-2}) for the two SQ experiments and the BSQ experiment. For each snapshot of the doubly-periodic square domain, the horizontal axis is x (in 1000km) and the vertical axis is y (in 1000km). The radius of each black circle represents the two-dimensional time-varying convective aggregation length scale $L(t)$ (in 1000km, defined in equation 4.2).

form in the long direction was applied before averaging in the short direction, which would be less representative of the y-averaged spatio-temporal variability depicted in Figure 4-1. For the SQ and BSQ simulations, we compute two-dimensional Fourier transforms of H and \dot{H}_i in the horizontal to obtain φ and $\dot{\varphi}_i$. In all cases, following equation 4.6, we integrate φ and $\dot{\varphi}_i$ between the smallest non-negative wavenumber and the Nyquist wavenumber to compute L and \dot{L}_i .

4.2.5 Interpretation of the expansion tendency

For a given process (e.g., net longwave heating \dot{H}_{lw}), equation 4.15 relates:

1. The longwave expansion tendency \dot{L}_{lw} , in units m s^{-1} . This tendency can be interpreted as the velocity at which longwave radiation stretches (if $\dot{L}_{lw} > 0$) or shrinks (if $\dot{L}_{lw} < 0$) the size of moist and dry regions (see equation 4.13).
2. The longwave aggregation rate $\langle \dot{\varphi}_{lw} \rangle / \langle \varphi \rangle$, in units day^{-1} , which is the longwave contribution to the rate of increase in MSE spatial variance (a standard metric for the rate at which convection aggregates, e.g. section 3 of Wing et al. [2017]). If $\langle \dot{\varphi}_{lw} \rangle > 0$, the moist static energy spatial variance is reinforced and convection aggregates. If $\langle \dot{\varphi}_{lw} \rangle < 0$, the moist static energy field is smoothed and convection disaggregates.
3. The convective aggregation length scale L , which measures the typical size of moist and dry regions (see equation 4.2).
4. The longwave length scale \mathcal{L}_{lw} , which measures the scale at which the longwave heating acts to aggregate convection.

If the aggregation tendency is positive ($\langle \dot{\varphi}_{lw} \rangle > 0$) and acts at a larger scale than the convective aggregation length scale ($\mathcal{L}_{lw} > L$), then L will exponentially relaxes towards \mathcal{L}_{lw} , corresponding to a stretching ($\dot{L}_{lw} > 0$). We illustrate this case in Figure 4-3 and summarize the interpretation of equation 4.15 for all sign cases in Table 4.2.

	Small-scale: $\mathcal{L}_i < L$	Large-scale: $\mathcal{L}_i > L$
Aggregation: $\langle \dot{\varphi}_i \rangle > 0$	Shrinking: $\dot{L}_i < 0$	Stretching: $\dot{L}_i > 0$
Disaggregation: $\langle \dot{\varphi}_i \rangle < 0$	Stretching: $\dot{L}_i > 0$	Shrinking: $\dot{L}_i < 0$

Table 4.2: Guide for interpreting equation 4.15 which relates the expansion tendencies \dot{L}_i to the aggregation rates $\langle \dot{\varphi}_i \rangle / \langle \varphi \rangle$ and the diabatic scales \mathcal{L}_i .

Aggregation at smaller scales $\mathcal{L}_i < L$ will make L exponentially relax towards \mathcal{L}_i , corresponding to a shrinking (top-left case: $\dot{L}_i < 0$). When the aggregation rate is negative (second row), \mathcal{L}_i represents the scale at which MSE power is most strongly damped and acts as a repeller for the scale L of MSE anomalies: repelling from small-scales leads to a stretching (bottom-left case: $\dot{L}_i > 0$) while repelling from large-scales leads to a shrinking (bottom-right case: $\dot{L}_i < 0$). Finally, when a process \dot{H}_i acts at a scale \mathcal{L}_i that is equal to the convective aggregation scale L , then it does not affect the scale of convective activity and $\dot{L}_i = 0$.

4.3 Results

We show the evolution of the convective aggregation length scale L in section 4.3.1 and the evolution of the tendencies \dot{L}_i and $\dot{\varphi}_i$ in section 4.3.2. We then investigate the physics of the radiative (section 4.3.3) and of the surface flux (section 4.3.4) tendencies.

4.3.1 Convective aggregation length scales

All experiments are initiated with a horizontally homogeneous state and small thermal noise ($\sim 0.05\text{K}$ at the surface, decaying to zero at an elevation of 500 meters), and therefore start with very small MSE anomalies (less than 0.1MJ m^{-2}). A horizontally homogeneous state implies small L (left of Figure 4-4a) and small degree of aggregation (left of Figure 4-4b). As convection organizes, the MSE power spectrum is:

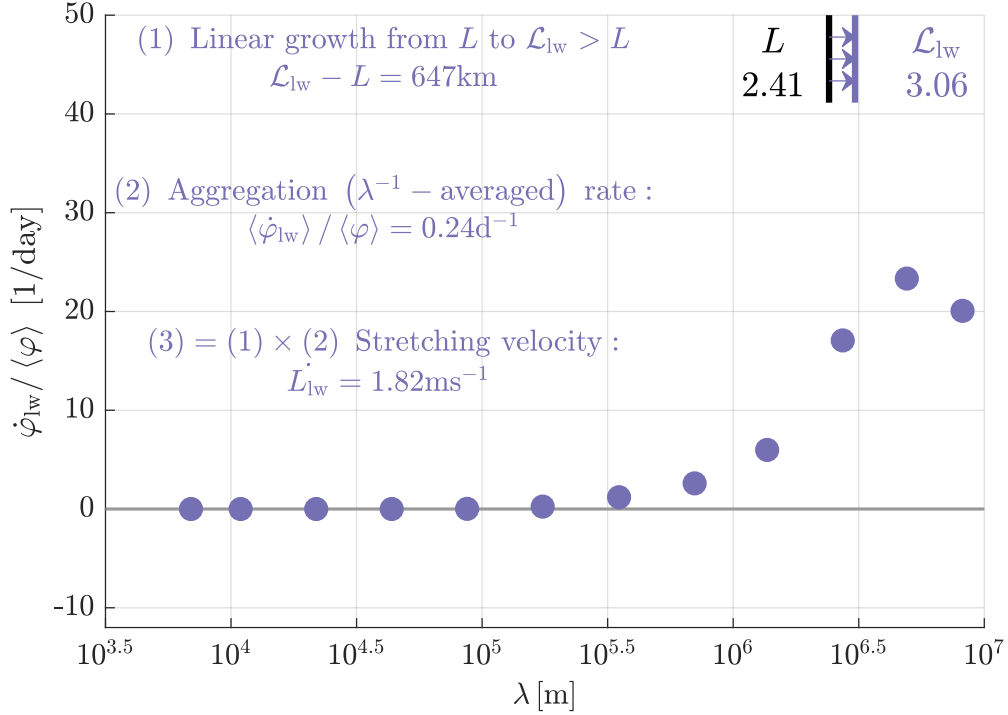


Figure 4-3: We use the time-averaged data from the first 30 days of the LC300 simulation as an example.

(Black line) Time-averaged convective aggregation length scale L (in day^{-1}).

(Blue line) Length scale \mathcal{L}_{lw} of the longwave tendency $\dot{\varphi}_{lw}$.

(1-Arrows) Longwave radiation tries to “stretch” the convective aggregation length scale L to its preferred length scale \mathcal{L}_{lw} , because $\langle \dot{\varphi}_{lw} \rangle > 0$ and $\mathcal{L}_{lw} > L$.

(2-Dots) Normalized longwave spectral rates $\dot{\varphi}_{lw} / \langle \varphi \rangle$ (in day^{-1}) for each wavelength λ (in 1000 km). The spectral-average of the spectral rates equals the longwave aggregation rate $\langle \dot{\varphi}_{lw} \rangle / \langle \varphi \rangle$ (in day^{-1}).

(3-expansion tendency) The combination of the positive longwave aggregation rate $\langle \dot{\varphi}_{lw} \rangle / \langle \varphi \rangle > 0$ with the growth from L to $\mathcal{L}_{lw} > L$ leads to a positive longwave expansion tendency $L_{lw} > 0$.

- Enriched overall, which increases the spectrally-averaged MSE power $\langle\varphi\rangle$, or equivalently the spatial MSE anomalies (first month of Figure 4-4b).
- Preferentially enriched at long wavelengths, which increases the MSE anomaly scale L (first month of Figure 4-4a).

In physical space, MSE anomalies amplify, which is referred to as convective self-aggregation. In the long-channel experiments (e.g. Figure 4-1d), aggregated bands appear on the Hovmoller diagram, while aggregated moist and dry “blobs” appear in the square-geometry experiments (Figure 4-2). The convective aggregation length scale L (marked with black lines in both figures) reasonably follows the average MSE anomaly size, and a discussion on the advantages of different definitions of L can be found in appendix A. Based on the degree of aggregation, it is conceptually useful to distinguish two phases:

- A “growth phase”, in which convection aggregates and MSE spatial anomalies increase. To simplify the comparison among different experiments, we define this phase as the first month of the simulation (until the end of the 30th day). In the reference simulation LC300CAM, the weekly-averaged MSE spatial standard deviation at the end of the first month is 14.8MJ m^{-2} , 84% of the time-averaged MSE standard deviation after the first month of simulation (17.6MJ m^{-2}).
- A “mature phase”, in which convection has reached a statistically steady degree of aggregation, and MSE spatial anomalies have relatively small oscillations compared to their large time-averaged value (indicated with parenthesis in Figure 4-4).

We will use this breakdown into two temporal phases when presenting time-averaged data in the rest of the chapter. The length scale L , however, does not closely follow this same evolution:

- During the first week or two, L grows rapidly as high and low-MSE regions appear.

- After that, L has large-amplitude oscillations as MSE power is exchanged between the longest wavelengths. Because our definition 4.2 gives the largest weight to the longest wavelength, L is very sensitive to MSE power exchange between the two longest wavelengths (domain size and half-domain size). Consequently, cold simulations (LC280CAM, LC280RRTM, LC285CAM) and the MD SFC experiment, which have a significant amount of MSE power in the longest wavelength, can undergo very large changes despite having reached a statistically steady degree of aggregation.

In the “mature phase”, the LC experiments which have colder surface temperatures and use the CAM radiation scheme generally have larger L , but the largest values of L are seen in the experiment where surface fluxes are horizontally homogenized (MD SFC, where L is still growing after 80 days of simulation). By contrast, the experiments in which radiative heating is made horizontally homogeneous (MD RAD and MD RADSFC, see purple lines in Figure 4-4), exhibit very weak aggregation given their surface temperature of 300K. Finally, the square domain experiments (SQ) have the smallest L , despite being strongly aggregated given their surface temperatures of 305K. For these experiments, L may still be limited by the domain size, which is suggested by the fact that the BSQ experiment’s MSE anomaly scale L (dotted black line in Figure 4-4a) is almost twice as large as its SQ counterpart (dotted gray line in Figure 4-4b). Furthermore, L equals half the domain size in both cases during the mature phase, consistent with the cluster occupying half of the domain in Figure 4-2. The spatial organization of convection in the long-channel setting is relatively insensitive to the domain size as long as the domain’s aspect ratio remains large, which is discussed in section 7.5 of Wing and Cronin [2016]. To understand what causes L to vary so much, we now study the evolution of its diabatic tendencies \dot{L}_i .

4.3.2 Evolution of the length scale diabatic tendencies

We start by focusing on the LC300 CAM experiment, for which the evolution of $L(t)$ is depicted using a green line in Figure 4-4. The total forcing \dot{L}_{tot} (in m s^{-1}),

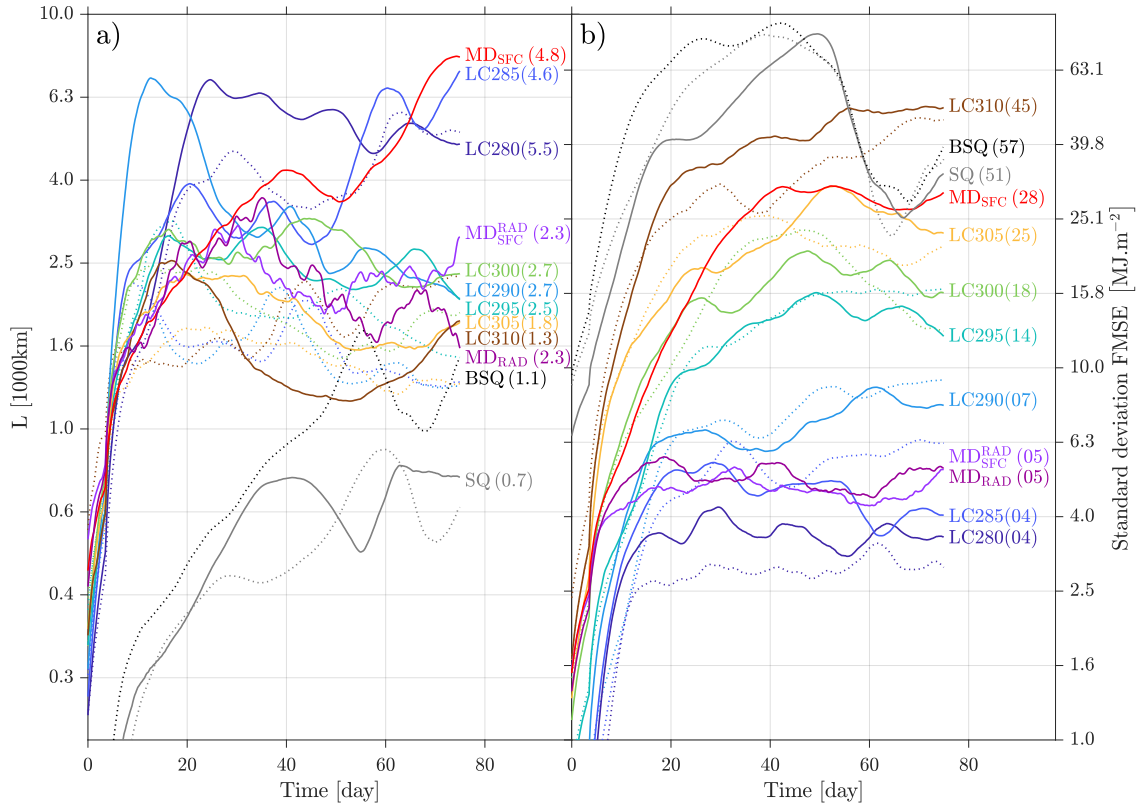


Figure 4-4: Evolution of (a) the convective aggregation length scale L (in 1000 km, defined in equation 4.2) and (b) the spatial standard deviation of MSE (in $\text{MJ}\cdot\text{m}^{-2}$) during the 75 days of each experiment. The solid lines represent the experiments using the CAM radiation schemes, and are identified using the acronyms defined in table 4.1 and the value of the fixed surface temperature. The dotted lines represent the experiments using the RRTM radiation scheme. We indicate the time-averaged value in the mature phase using parentheses, and use a time-moving-average of 1 week before plotting each variable.

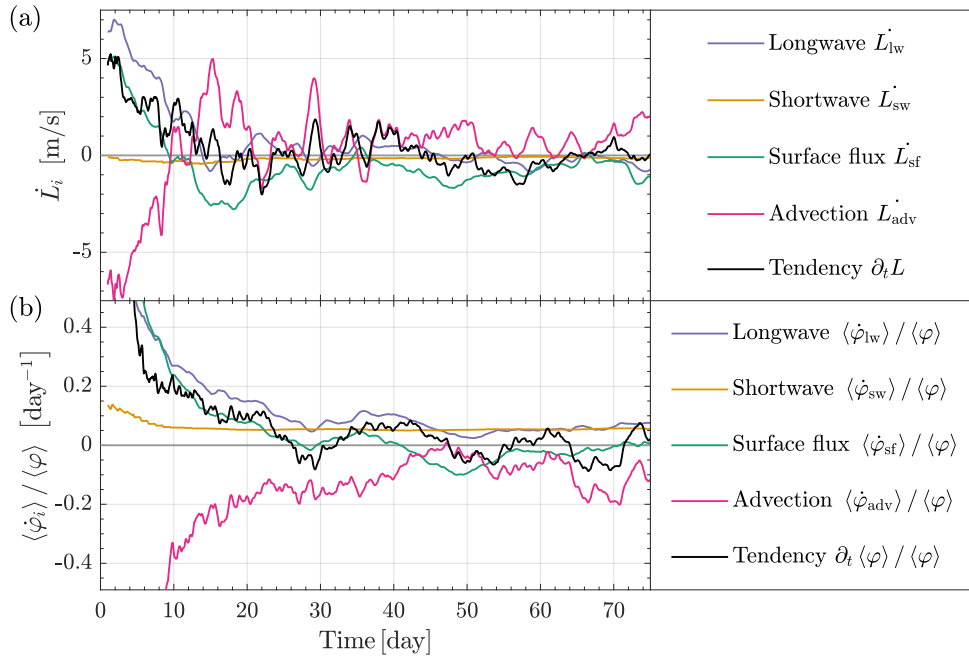


Figure 4-5: (a) Evolution of the expansion tendency \dot{L}_i (in ms^{-1} , on the right-hand side of equation 4.13) during the 75 days of experiment LC300 CAM. (b) Evolution of the aggregation rate $\langle \dot{\varphi}_i \rangle / \langle \varphi \rangle$ (in day^{-1}) in LC300 CAM. Lines in both subplots are smoothed using a time-moving-average of 1 week.

represented with a black line in Figure 4-5a, is equal to the tendency of L in time. Therefore, it is positive when L grows ($t < 14.3$ day), and oscillates around zero afterwards ($t > 14.3$ day). Because the variability of L is large in the mature phase, the amplitude of these oscillations sometimes exceeds that of \dot{L}_{tot} during the growth phase, challenging the idea of a uniquely-defined stationary size for convectively active regions during the mature phase. Following equation 4.13, \dot{L}_{tot} can be decomposed into four expansion tendencies. The longwave tendency \dot{L}_{lw} (blue line) stretches L at an average velocity of 1.8 m s^{-1} during the first month and has an overall neutral effect afterwards. By contrast, the shortwave tendency \dot{L}_{sw} (orange line) shrinks L at an average velocity of 0.25 m s^{-1} during the first month and 0.13 m s^{-1} afterwards. The surface flux tendency \dot{L}_{sf} stretches L for the first 12 days of the simulation before shrinking L for the rest of the simulation. Finally, the advective tendency \dot{L}_{adv} exhibits the opposite behavior to \dot{L}_{sf} in this particular case. During the growth phase, \dot{L}_{adv} shrinks L at an average velocity of 0.54 m s^{-1} because it homogenizes MSE more at large scales than at small scales (bottom-right case of Table 4.2, consistent with the spectral HÄüvmmoller plots of Arnold and Randall [2015]), while \dot{L}_{adv} stretches L at an average velocity of 0.93 s^{-1} during the mature phase because it homogenizes MSE more at small scales than at large scales (bottom-left case of Table 4.2): The reader interested in the scale-by-scale MSE spectral tendencies $\dot{\varphi}_{\text{adv}}$ is referred to appendix D. It is instructive to compare the evolution of the length scale and aggregation tendencies for the same simulation (see Figure 4-5b and Figure 4e of Wing and Cronin [2016] for the evolution of the aggregation rates in time, calculated from the MSE spectrum and spatial anomalies, respectively). The longwave and shortwave aggregation tendencies are always positive, the advective aggregation tendency always negative, and the surface flux aggregation tendency transitions from positive to negative rates. Note that the amplitude of the moist static energy spectral tendencies $\langle \dot{\varphi}_i \rangle$ (in units $\text{J}^2 \text{ m}^{-4} \text{ s}^{-1}$) increases less rapidly than the amplitude of the MSE spectrum $\langle \varphi \rangle$ (in units $\text{J}^2 \text{ m}^{-4}$) as convection organizes, explaining why the amplitude of the aggregation rates $\langle \dot{\varphi}_i \rangle / \langle \varphi \rangle$ (in inverse time units) decreases with time.

Figure 4-6 summarizes the length scale and aggregation tendencies in both the growth phases and the mature phases of all twenty simulations. The horizontal axis represents the expansion rate $\left(\dot{L}_i/L\right)$, with a stretching effect to the right and a shrinking effect to the left of the zero line. The vertical axis represents the aggregation rate $(\langle\dot{\varphi}_i\rangle/\langle\varphi\rangle)$, with an aggregating effect above and a disaggregating effect below the zero line. Using the position of each moist static energy flux in $\left(\dot{L}_i/L, \langle\dot{\varphi}_i\rangle/\langle\varphi\rangle\right)$ space, we can extend our observations from the 300 K CAM-radiation long channel simulation to different sea surface temperatures, radiation schemes and geometries:

1. The longwave flux (blue markers) has positive length scale and aggregation rates during the first month across all simulations.
2. The shortwave flux (orange markers) has negative length scale and positive aggregation rates at all time across all simulations. We see a sharp dependence on surface temperature: rates for warm surface temperature simulations are significantly smaller than their cold surface temperature counterparts.
3. During the growth phase, the surface enthalpy flux (green markers) has large positive expansion and aggregation rates. During the mature phase, both rates become negative, with two notable exceptions. The mechanism denial experiments in which radiation is homogenized (MD RAD and MD RADSFC) maintain positive expansion and aggregation rates from surface fluxes in the mature phase, consistent with the weak aggregation of convection (see Figure 4-1a). In the square experiments, the aggregation rate becomes negative while the expansion rate remains positive.
4. Finally, the advective flux (pink markers) exhibits the largest variability. In most simulations, advection shrinks L in the growth phase and damps the convective aggregation at all times. It has the opposite effect on L in the simulations with hottest sea surface temperature, as it can stretch L during the mature phase. Both SQ and BSQ simulations have stretching yet disaggregating advective tendencies during the first month of the simulation. In the BSQ simulation,

the surface enthalpy fluxes are responsible for balancing out the large advective stretching rate \dot{L}_{adv}/L in the mature phase, since $\dot{\varphi}_{adv}$ homogenizes small scales faster than large scales in the BSQ geometry.

The last two sections investigate the sign and amplitude of aggregation and expansion rates from radiative and surface enthalpy fluxes.

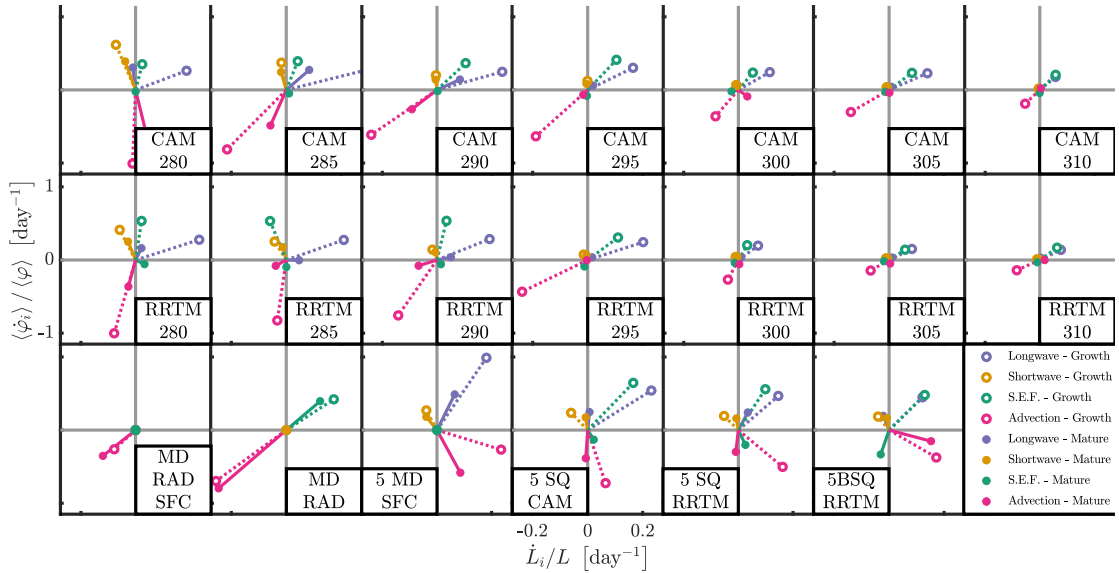


Figure 4-6: Representation of the twenty experiments in $(\dot{L}_i/L, \langle \dot{\varphi}_i \rangle / \langle \varphi \rangle)$ space. The aggregation and expansion rates have been time-averaged over the first month (Growth phase, depicted with dotted lines and empty circles) or later months (Mature phase, depicted with full lines and filled circles) of each experiment. Colors indicate different MSE fluxes: Longwave (blue), Shortwave (orange), Surface enthalpy flux (green) and advective flux (pink). All subplots use the same scale for both axis.

4.3.3 Radiative rates

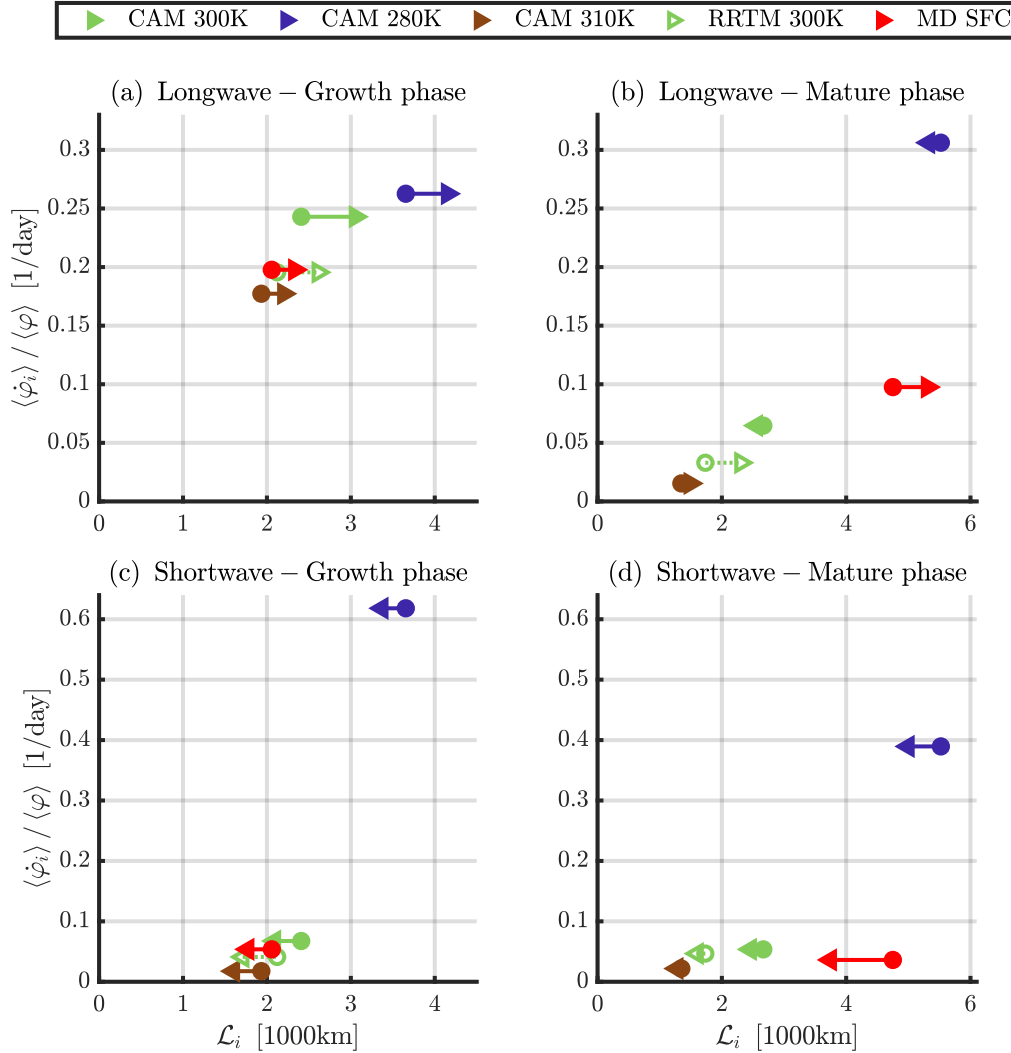


Figure 4-7: Representation of five characteristic experiments in $(\mathcal{L}_i, \langle \dot{\varphi}_i \rangle / \langle \varphi \rangle)$ space. The longwave and shortwave rates have been time-averaged over the growth phases ((a) and (c) respectively) and mature phases ((b) and (d) respectively) of each simulation. The arrows go from the time-averaged convective length scale L (represented with a circle) to the radiative length scale \mathcal{L}_i , and represent the length scale growth of each experiment (an arrow to the right corresponds to $\dot{L}_i > 0$). The color code is that of Figure 4-4.

Since the radiative aggregation tendencies are positive across all simulations ($\langle \dot{\phi}_{1w} \rangle > 0$ and $\langle \dot{\phi}_{sw} \rangle > 0$, except during the first week of some cold simulations), radiation acts to pull the length scale of aggregation towards the radiative length scale (first line of Table 4.2). On the one hand, we find that the longwave length scale \mathcal{L}_{1w} usually exceeds the convective aggregation length scale L during the growth phase, as shown in panels 4-7a. Therefore, the longwave tendency in the growth phase forces L towards a larger scale \mathcal{L}_{1w} , and $\dot{L}_{1w} > 0$ across all simulations and phases as shown by the right-pointing arrows in the top-left panel. Even if the clear-sky longwave tendency contributes up to a third of the aggregation tendency $\langle \dot{\phi}_{1w} \rangle$ at low temperature, its expansion tendency is always small relative to the total expansion tendency because the scale of water vapor anomalies is very close to the MSE anomaly scale. This is not the case in the mature phase (Figure 4-7b), during which the longwave length scale \mathcal{L}_{1w} may be smaller than the MSE anomaly scale L , resulting in a shrinking according to the top-left case of Table 4.2. On the other hand, we find that the shortwave length scale \mathcal{L}_{sw} is smaller than L during both phases, as shown in panels 4-7c and 4-7d. Therefore, the shortwave tendency forces L towards a smaller scale \mathcal{L}_{sw} and $\dot{L}_{sw} < 0$ across all simulations and phases. The shortwave expansion tendency \dot{L}_{sw} is also dominated by the “cloudy” contribution because the clear-sky shortwave diabatic scale is so close to the MSE anomaly scale. Although a full analysis of the interaction between cloud radiation and convection is beyond the scope of this chapter, we speculate that the contrast in longwave and shortwave length scales occurs due to the relative roles and spatial power spectra of clouds at different heights. Spectral analysis reveals that the net longwave heating is more coherent with column ice water, while the net shortwave heating is more coherent with column liquid water and column water vapor, which can be seen in Figure 4-11 of Appendix D. These results suggest that the net longwave heating variability is primarily dictated by high clouds, while the net shortwave heating variability is primarily dictated by low and mid-level clouds. High clouds are produced primarily by outflow from deep convection, which can spread far from the scattered convective cores, while low clouds are produced primarily by smaller-scale shallow-convective processes, giving us a first hint as to why

$\mathcal{L}_{\text{sw}} < L < \mathcal{L}_{\text{lw}}$. We refer the reader to section 6.2 of Bretherton and Khairoutdinov [2015] for a complementary discussion on this topic.

4.3.4 Surface flux rates

At first glance, the surface flux expansion tendency \dot{L}_{sf} is more challenging to interpret. The aggregation tendency changes sign across time and length scales, preventing us from using \mathcal{L}_{sf} as a tool to interpret \dot{L}_{sf} . Following section 5.2 of Wing and Emanuel [2014], we decompose the surface enthalpy flux spatial anomaly into 3 contributions. Assuming a standard aerodynamic formula for the surface enthalpy flux, it can be written as the product of two factors:

$$\text{SF} = \rho C_k U_s \times \Delta k, \quad (4.18)$$

where SF is the total surface enthalpy flux (in W m^{-2}), ρ is the near-surface air density (in kg m^{-3}), C_k is the surface enthalpy exchange coefficient, U_s is the surface wind speed (in m s^{-1}) and Δk is the air-sea enthalpy disequilibrium. We introduce the spatial-averaging operator $\langle \rangle_{\mathbf{x}}$ (see equation 4.33 in appendix A.2) and denote spatial anomalies with primes ($'$). By decomposing the two factors in equation 4.18 into their spatial means and anomalies, we decompose SF' into 3 terms:

$$\begin{aligned} \text{SF}' &\stackrel{\text{def}}{=} \text{SF} - \langle \text{SF} \rangle_{\mathbf{x}} \\ &= \underbrace{(\rho C_k U_s)' \langle \Delta k \rangle_{\mathbf{x}}}_{\text{Surface wind speed}} + \underbrace{\langle \rho C_k U_s \rangle_{\mathbf{x}} \Delta k'}_{\text{Enthalpy disequilibrium}} + \underbrace{(\rho C_k U_s)' \Delta k' - \langle \rho C_k U_s \rangle_{\mathbf{x}} \langle \Delta k \rangle_{\mathbf{x}}}_{\text{Eddy term}}. \end{aligned} \quad (4.19)$$

We apply this same decomposition to the aggregation and expansion surface flux rates, which is shown in Figure 4-8. Figure 4-8a shows that the wind and disequilibrium aggregation rates are each consistent in sign for the whole simulation, while the eddy aggregation rate is negligible at all times. Convectively active zones exhibit more convective gustiness, making the wind aggregation tendency always positive. Meanwhile, convectively active zones are moister and have a smaller enthalpy disequilibrium, keeping the disequilibrium aggregation tendency negative. During the

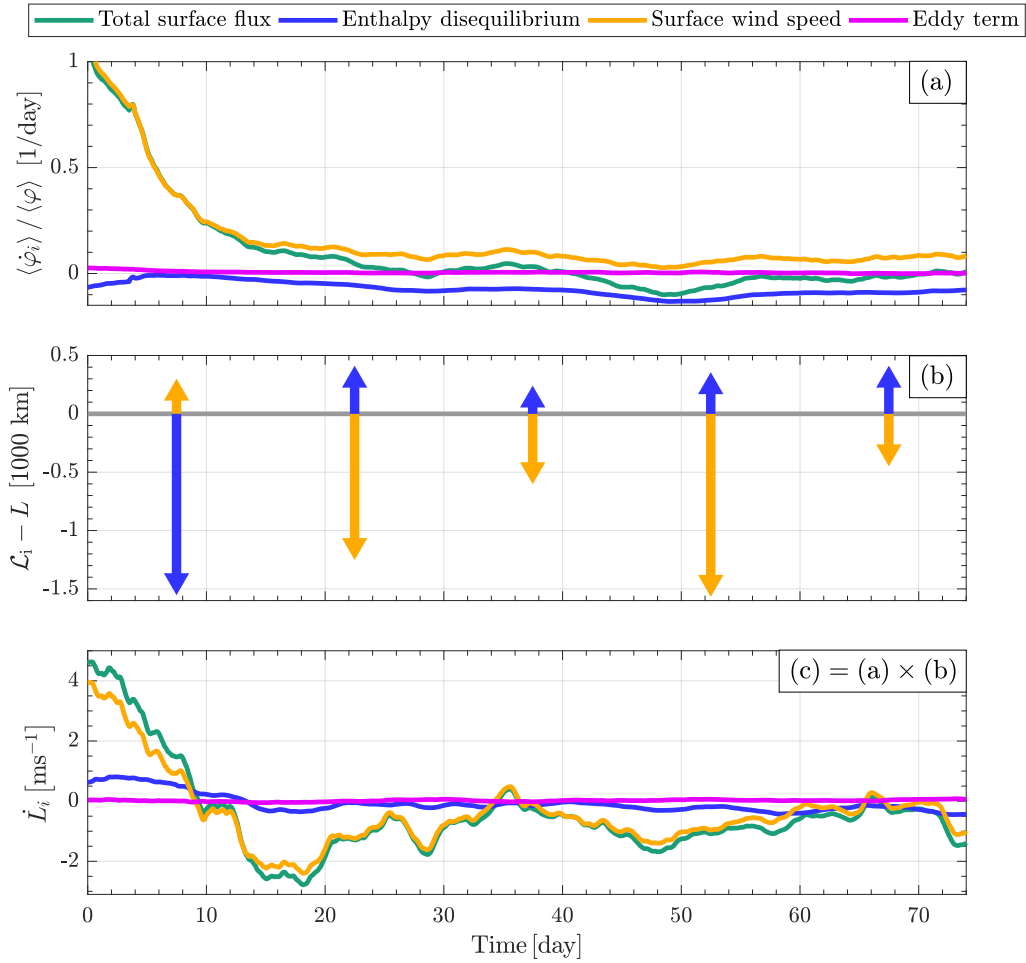


Figure 4-8: Decomposition of the surface flux aggregation rate (a), difference between diabatic length scale and MSE anomaly scale (b) and expansion tendency (c) for the LC300 CAM experiment. Panels (a) and (c) use a running time-average of 1 week while panel (b) shows length scale differences computed using 15 day time-averages. According to equation 4.15, the expansion rate (c) can be obtained by multiplying the aggregation rate (a) by the length scale difference (b).

growth phase, the wind aggregation rate dominates over the two other aggregation rates, and the total aggregation rate is positive. During the mature phase, the two aggregation rates oppose each other and the total aggregation rate switches from positive to negative, as the disequilibrium rate becomes more and more negative. This finding is consistent with results from square-domain non-rotating simulations presented in this chapter and panel 5d of Wing et al. [2016]; panel 5c of Wing et al. [2016] suggests that the positive surface wind speed feedback dominates for all times in simulations of rotating convection (in which tropical cyclones form). We plot the length scale factor of equation 4.15 in Figure 4-8b. Since the wind and disequilibrium aggregation rates are single-signed, the interpretation of their diabatic length scales \mathcal{L}_i is easier. The evolution of $L_{\text{wind}}^{\dot{}}$ (depicted in Figure 4-8c) follows from the first line of table 4.2: For $t < 12$ day, the surface wind speed component of the surface flux aggregates convection at larger scales and stretches L (analogous to $L_{\text{lw}}^{\dot{}}$), while for $t > 12$ day, it aggregates convection at smaller scales and shrinks L (analogous to $L_{\text{sw}}^{\dot{}}$). The surface wind speed component of the surface flux includes contributions from both the large-scale circulations that develop throughout the simulation, and convective gustiness. We find that $\mathcal{L}_{\text{wind}}$ quickly becomes smaller than L as convection aggregates and L grows (Orange arrows in Figure 4-8b), suggesting that convective gustiness dominates the surface wind speed spectral tendency $\dot{\phi}_{\text{wind}}$. While both aggregation tendencies $\langle \dot{\phi}_{\text{wind}} \rangle$ and $\langle \dot{\phi}_{\text{dis}} \rangle$ have the same order of magnitude, the enthalpy disequilibrium flux acts at the scale of MSE anomalies. Its diabatic length scale \mathcal{L}_{dis} is then close to L , and the amplitude of its expansion tendency is significantly smaller than the surface wind expansion tendency ($|L_{\text{dis}}^{\dot{}}| \ll |L_{\text{wind}}^{\dot{}}|$). Therefore, the evolution of the wind expansion tendency $L_{\text{wind}}^{\dot{}}$ explains the evolution of the surface flux expansion tendency $L_{\text{sf}}^{\dot{}}$ to first order; the disequilibrium tendency slightly stretches L during the growth phase and slightly damps it during the mature phase.

4.4 Conclusion

We have developed a budget that relates the evolution of the convective aggregation length scale (defined in section 4.2.1) to the vertically-integrated moist static energy fluxes (section 4.2.2). We have used a set of cloud-permitting three-dimensional simulations (section 4.2.3) to evaluate (section 4.2.4) and interpret (section 4.2.5) the different terms of this budget across different experiments. In section 4.3.1, we have divided the evolution of convective aggregation into two phases: a growth phase during which convection self-aggregates, and a mature phase during which the size of moist and dry regions depends on the characteristics of the simulation. In section 4.3.2, we have characterized the aggregation and expansion tendencies across experiments, and have investigated the values of the radiative and surface flux rates in sections 4.3.3 and 4.3.4. The surface temperature dependence of the expansion rates is summarized in Figure 4-9:

1. The first-month-averaged longwave expansion rates $\left(\dot{L}_{\text{lw}}/L\right)$ decrease with surface temperature following the decrease in longwave aggregation rates $\langle\dot{\varphi}_{\text{lw}}\rangle/\langle\varphi\rangle$. The aggregation rate decrease comes from a decrease in column ice, as well as an increase in the degree of aggregation with surface temperature. Aggregation rates are higher for the CAM than RRTM radiation scheme, which can be traced back to larger net cloudy radiative heating aggregation rates when the CAM radiation scheme is used. In the long-channel setting, the net cloudy longwave heating is the crucial ingredient for convection to aggregate, as confirmed by the low degree of aggregation in the MD RAD and MD RADSFC experiments. The mature-phase-averaged longwave expansion rates $\left(\dot{L}_{\text{lw}}/L\right)$ also decrease with surface temperature, and may even become slightly negative for the CAM radiation scheme, as the longwave diabatic length scale \mathcal{L}_{lw} becomes smaller than the scale L of MSE anomalies.
2. The shortwave expansion rates $\left(\dot{L}_{\text{sw}}/L\right)$ become less negative as surface temperature increases. The net shortwave heating is always dominated by its clear-sky component; as temperature increases, this component becomes more and more

prevalent. Since the clear-sky shortwave flux acts at the MSE anomaly scale to good approximation, it does not have any shrinking effect and \dot{L}_{sw} becomes closer and closer to zero.

3. The initial surface enthalpy flux expansion rate $\left(\dot{L}_{\text{sf}}/L\right)$ increases with surface temperature, mostly due to an increase in the wind-induced component of the latent heat flux expansion rate with surface temperature. That increase comes from a change in the spectral shape of the surface flux spectral tendency $\dot{\varphi}_{\text{sf}}$, since the first-month-averaged surface enthalpy flux aggregation rates $\langle\dot{\varphi}_{\text{sf}}\rangle/\langle\varphi\rangle$ decrease with surface temperature: In Figure 4-6, the green empty circles shift to the bottom-right of $\left(\dot{L}_{\text{sf}}/L, \langle\dot{\varphi}_{\text{sf}}\rangle/\langle\varphi\rangle\right)$ space as surface temperature increases. The mature-phase-averaged surface enthalpy flux expansion rate $\left(\dot{L}_{\text{sf}}/L\right)$ switches from positive at low surface temperatures, for which the enthalpy disequilibrium component prevails, to negative at higher surface temperatures because of the wind component's spectral peak below the MSE anomaly scale L (see Appendix 4.8). The strong shrinking effect of surface enthalpy fluxes is what prevents MSE power from being transferred to the longest wavelength in the long-channel setting, as confirmed by the MD SFC experiment exhibiting the largest L that keeps increasing after three months of simulation.
4. Finally, the advective flux always has a shrinking effect during the first month, except in square domain geometry simulations where it has a stretching effect because it disaggregates convection at small scales (see Figure 4-6). It shifts from shrinking to stretching with surface temperature during the mature phase as it homogenizes MSE at smaller and smaller scales.

For each flux, we represent the expansion rate's temporal variability with error bars, which heights equal three standard deviations divided by the sample size's square root. If the temporal variability had a Gaussian distribution, these error bars would be equal to three times the root-mean-squared error on the time-averaged expansion rates. The largest variability arises from the advective and longwave expansion rates during the first month of the simulations, with the advective rate potentially becoming

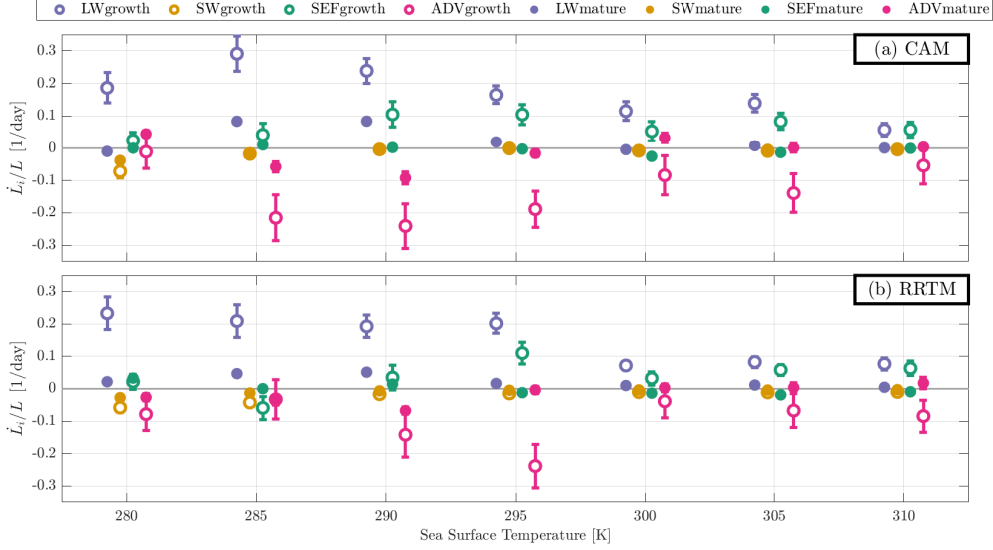


Figure 4-9: Expansion rate (in 1/day) versus sea surface temperature for the long-channel experiments using the (a) CAM and (b) RRTM radiation schemes. The rates are time-averaged during the first month (Growth phase, empty circles) and later months (Mature phase, filled circles) of each simulation; we use error bars to indicate three standard deviations normalized by the sample size’s square root. Each color corresponds to a MSE flux: Longwave (blue), Shortwave (orange), Surface enthalpy flux (green) and Advective flux (pink).

positive as its spectral peak shifts to smaller wavelengths. Note that the dependence of the expansion tendencies with surface temperature is more visible if we use metrics that give more weight to smaller wavelengths, such as the integral scale studied in Appendix A.

By relating local physical processes to large-scale convective organization, this budget emphasizes the need to better understand individual spectral tendencies $\dot{\varphi}_i(\mathbf{k})$. We still lack a fundamental physical explanation for the value of cloud radiative spectral tendencies, which are key players in setting the size and intensity of moist and dry regions. Furthermore, the influence of radiative tendencies on the organization of convection in the real world remains a topic of active research, as inhomogeneous boundary feedbacks and external shear make the physical processes harder to distinguish in practice. The framework presented here focuses on the expansion tendencies rather than a static aggregated state, which is a step towards diagnosing clustering feedbacks in the real world where the constantly-evolving size of moist and dry regions

challenges the idea of a single MSE anomaly scale. In cloud-permitting simulations, a framework to decompose spectral advective tendencies into their deep, shallow and diabatically-driven components could also help bridge this gap by isolating the indirect role of diabatic processes through the circulation they induce (e.g. Holloway and Woolnough [2016]). Finally, we have explored the surface temperature dependence of convective organization; making the surface temperature interactive will be a necessary step to connect cloud-permitting simulations with the real world, especially given how the interaction between the atmosphere and a shallow slab-ocean affects the organization of convection (e.g. Hohenegger and Stevens [2018] for a Convection-Permitting study and Coppin and Bony [2017] for a recent General Circulation Model study). Overall, our work underscores the need to observe and simulate surface fluxes, radiative and advective fluxes across the 1km-1000km range of scales to better understand the characteristics of turbulent moist convection.

4.5 Appendix A: Alternative definitions of L

4.5.1 A.1. Comparison of spectrally-defined scales to the auto-correlation length scale

In this article, we adopt the intuitive definition 4.2 of the convective aggregation length scale. This definition can be generalized to $L \stackrel{\text{def}}{=} 2\pi\sqrt{n} \langle \|\mathbf{k}\|^p \varphi \rangle^{1/q} \langle \|\mathbf{k}\|^{p+q} \varphi \rangle^{-1/q}$, with the choice of (p, q) determining which parts of the MSE spectrum are given the most weight. In this appendix, we compare three cases of this general definition:

1. The power spectrum-weighted-averaged wavelength, which is the definition used in the main text:

$$(p, q) = (-1, 1) \Rightarrow L \stackrel{\text{def}}{=} \frac{2\pi\sqrt{n}}{\langle \varphi \rangle} \left\langle \frac{\varphi}{\|\mathbf{k}\|} \right\rangle, \quad (4.20)$$

2. The integral scale, which is a standard definition in the turbulence literature

(e.g. equation 8.45 of Vallis [2006]):

$$(p, q) = (1, -1) \Rightarrow K^{-1} \stackrel{\text{def}}{=} \frac{2\pi\sqrt{n}\langle\varphi\rangle}{\langle\|\mathbf{k}\|\varphi\rangle}, \quad (4.21)$$

3. The geometric mean of the two previous definitions:

$$(p, q) = \left(-\frac{1}{2}, \frac{1}{2}\right) \Rightarrow \sqrt{LK^{-1}} \stackrel{\text{def}}{=} 2\pi\sqrt{n}\sqrt{\frac{\langle\varphi/\|\mathbf{k}\|\rangle}{\langle\|\mathbf{k}\|\varphi\rangle}}. \quad (4.22)$$

A fourth plausible choice of length scale in our comparison is the spatial auto-correlation scale of the MSE field $L_\varphi(t)$, defined as the e-folding length of the autocorrelation function (e.g. section 8.10 of Dunn [2005]). In one-dimension, $L_\varphi(t)$ can be defined from the normalized inverse Fourier transform ϕ of the MSE power spectrum φ as:

$$L_\varphi(t) \stackrel{\text{def}}{=} \min_x \{x : \phi(x, t) < \exp(-1)\}, \quad (4.23)$$

$$\phi(x, t) \stackrel{\text{def}}{=} \frac{\int_{k_0}^{k_N} \exp(ikx) \varphi(k, t) dk}{\int_{k_0}^{k_N} \varphi(k, t) dk}. \quad (4.24)$$

Note that the definition of L_φ can yield unrealistic large values when the power spectrum φ is concentrated at low wave numbers, which is the case during the mature phase of our simulations. In that case, we set unrealistic large values, typically greater than the domain size, to their nearest realistic neighbor. Furthermore, if the oscillations of ϕ in x cross the hard threshold $\exp(-1)$ rapidly, there is ambiguity in the physical meaning of L_φ , even if we choose the smallest solution and define a unique value for L_φ . For these reasons, we believe L_φ is too ill-defined to be used as a systematic metric when studying the physics of convective aggregation in our simulations. Nevertheless, L_φ is a standard metric for the scale of spatial anomalies, and we compare it to L , K^{-1} and $\sqrt{LK^{-1}}$ for our reference LC300CAM simulation in Figure A1.

Because L gives the most weight to the longest wavelengths, it is the largest metric for the scale of MSE spatial anomalies. Furthermore, it is the closest metric to the

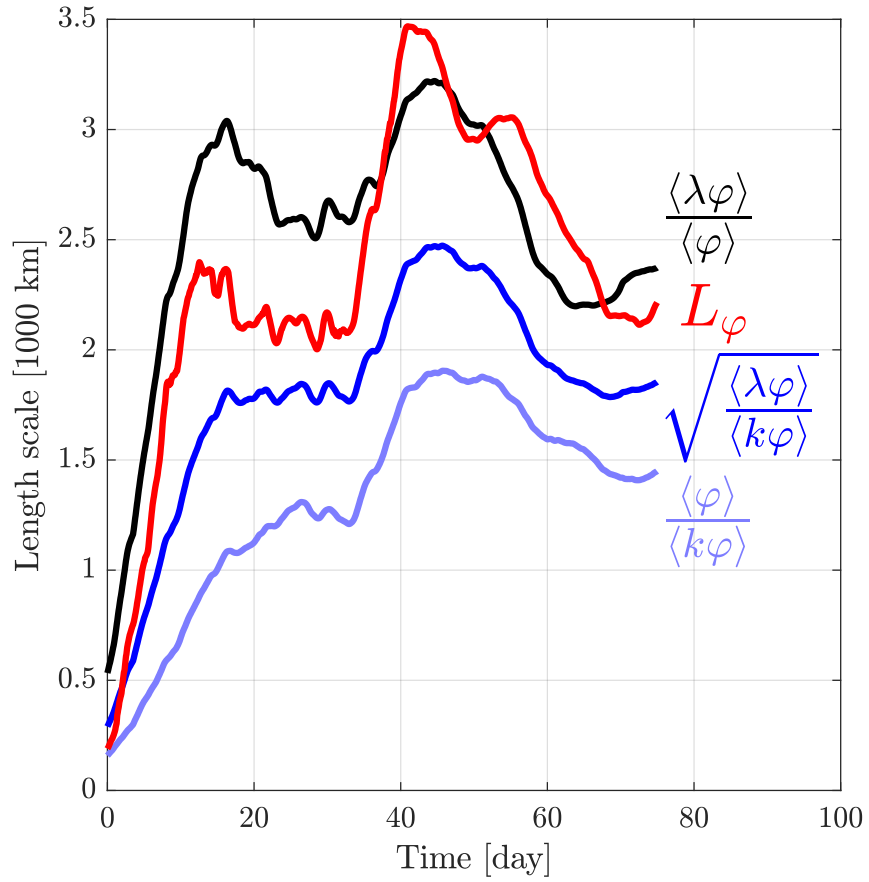


Figure 4-10: (Black line) $L(t)$, (Red line) $L_\varphi(t)$, (Blue line) $\sqrt{LK^{-1}}(t)$ and (Sky blue line) $K^{-1}(t)$ (in 1000 km) versus time (in days) for the reference LC300CAM simulation.

auto-correlation scale L_φ . The two other metrics both capture the low-frequency time-evolution of the auto-correlation scale (growing-decaying-growing-decaying), suggesting that their budgets may contribute to our understanding of the MSE spectrum evolution. Therefore, we derive a budget for the integral MSE scale $K^{-1}(t)$ in the next sub-section A.2. One notable shortcoming of the integral scale K^{-1} arises in square-domain geometries and non-aggregated simulations. Because the spectral slope in square domain geometries oscillates around $\varphi \sim \|\sqrt{k^2 + l^2}\|^{-3}$ in the SQ and BSQ simulations, where (k, l) are the components of the two-dimensional wave vector \mathbf{k} , the average:

$$\langle \|\mathbf{k}\|\varphi \rangle \stackrel{\text{def}}{=} \frac{\int_{k_0}^{k_N} dk \int_{l_0}^{l_N} dl \times \sqrt{k^2 + l^2} \times \varphi(k, l)}{\int_{k_0}^{k_N} dk \int_{l_0}^{l_N} dl \times \varphi(k, l)} \quad (4.25)$$

may depend on the domain's resolution through (k_N, l_N) . The same issue arises in non-aggregated simulations, where the spectral slope s of $\varphi \sim k^{-s}$ may be smaller than 2. This dependence limits the physical understanding that we can obtain from the K^{-1} -budget for the LC CAM, LC RRTM, and MD SFC experiments.

4.5.2 A.2. Budget for the integral moist static energy scale

This section derives a budget for the integral MSE scale K^{-1} , similar to the convective aggregation length scale derived in section 4.2.2. We start by deriving a budget for $K \stackrel{\text{def}}{=} \langle \|\mathbf{k}\|\varphi \rangle / \langle \varphi \rangle$, by following the exact steps of section 4.2.2 and substituting $\lambda \mapsto \|\mathbf{k}\|$. By analogy to equations 4.13, 4.15 and 4.16, we can write the evolution of K as a sum of diabatic tendencies \dot{K}_i , defined as the product of the aggregation tendency with a growth length scale factor towards the diabatic integral wave number \mathcal{K}_i :

$$\frac{\partial K}{\partial t} = \dot{K}_{\text{lw}} + \dot{K}_{\text{sw}} + \dot{K}_{\text{sef}} + \dot{K}_{\text{adv}}, \quad (4.26)$$

$$\forall i, \dot{K}_i = \frac{\langle \dot{\varphi}_i \rangle}{\langle \varphi \rangle} (\mathcal{K}_i - K) \quad | \quad \mathcal{K}_i \stackrel{\text{def}}{=} \frac{2\pi\sqrt{n} \langle \|\mathbf{k}\|\dot{\varphi}_i \rangle}{\langle \dot{\varphi}_i \rangle}. \quad (4.27)$$

The budget for the integral scale K^{-1} can be derived by using a logarithmic derivative:

$$\frac{1}{K^{-1}} \frac{\partial K^{-1}}{\partial t} = -\frac{1}{K} \frac{\partial K}{\partial t} \Rightarrow \frac{\partial K^{-1}}{\partial t} = \sum_{i=\text{lw,sw,sef,adv}} (K^{-1})_i, \quad (4.28)$$

$$\forall i, (K^{-1})_i = \underbrace{\frac{\langle \dot{\varphi}_i \rangle}{\langle \varphi \rangle}}_{\text{Aggregation rate}} \overbrace{K^{-1} \left(1 - \frac{K^{-1}}{\mathcal{K}_i^{-1}} \right)}^{\text{Length scale factor}}. \quad (4.29)$$

The length scale factor in equation 4.29 is analogous to its counterpart in equation 4.16 because each flux (i) forces the MSE integral scale K^{-1} towards its intrinsic integral scale \mathcal{K}_i^{-1} , but it differs in its functional form: the growth is now logistic rather than exponential. This modifies the interpretation of the diabatic integral scale \mathcal{K}_i^{-1} as summarized in Table 4.3, analogous to Table 4.2.

	Small scale: $0 < \mathcal{K}_i^{-1} < K^{-1}$	Large-scale: $\mathcal{K}_i^{-1} > K^{-1}$	Negative scale: $\mathcal{K}_i^{-1} < 0$
Aggregation: $\langle \dot{\varphi}_i \rangle > 0$	Shrinking: $(K^{-1})_i < 0$	Stretching: $(K^{-1})_i > 0$	“Super stretching”: $(K^{-1})_i > 0$
Disaggregation: $\langle \dot{\varphi}_i \rangle < 0$	Stretching: $(K^{-1})_i > 0$	Shrinking: $(K^{-1})_i < 0$	“Super shrinking”: $(K^{-1})_i < 0$

Table 4.3: Guide for interpreting equation 4.29, which relates the integral scale tendencies $(K^{-1})_i$ to the aggregation tendencies $\langle \dot{\varphi}_i \rangle / \langle \varphi \rangle$ and the diabatic integral scales \mathcal{K}_i^{-1} .

When a flux \dot{H}_i acts at a scale \mathcal{K}_i^{-1} that is equal to the MSE integral scale K^{-1} , then it does not affect the scale of convective activity and $(K^{-1})_i = 0$; the singular case $\mathcal{K}_i^{-1} = 0$ would correspond to an infinite integral scale tendency $(K^{-1})_i$. When the scale \mathcal{K}_i^{-1} is negative (possible because the spectral tendencies $\dot{\varphi}_i$ can be double-signed), there are two possible cases:

1. If the aggregation tendency $\langle \dot{\varphi}_i \rangle$ is positive, then the stretching $(K^{-1})_i > 0$ is larger than the stretching for any positive \mathcal{K}_i^{-1} greater than the scale of aggregation (referred to as “Super stretching”):

$$(K^{-1})_i (\mathcal{K}_i^{-1} < 0) > (K^{-1})_i (\mathcal{K}_i^{-1} > K^{-1}) > 0 \quad . \quad (4.30)$$

2. If the aggregation tendency $\langle \dot{\varphi}_i \rangle$ is negative, then the amplitude of the shrinking

is larger than the amplitude of the shrinking for any positive \mathcal{K}_i^{-1} smaller than the scale of aggregation (referred to as ‘‘Super shrinking’’):

$$(\dot{K}^{-1})_i (\mathcal{K}_i^{-1} < 0) < (\dot{K}^{-1})_i (\mathcal{K}_i^{-1} \in]0, K^{-1}[) < 0 \quad . \quad (4.31)$$

These cases can only occur in a sustained context when a process acts to damp MSE variability over one range of spatial scales and amplify it across another range, and when the MSE spatial variance over the range of damped scales is maintained by other processes (so that its weighting in equation 4.11 does not vanish as time passes).

The qualitative conclusions regarding the role of each diabatic flux in setting the scale of MSE anomalies are insensitive to the choice of L or K^{-1} as a metric, except for the MD RAD, MD RAD+SFC, SQ and BSQ simulations for which K depends on the simulation’s resolution. The reader interested in a more quantitative comparison is referred to the article’s MATLAB scripts: using the ‘‘User’s choice’’ options, each figure of the main text can be remade using the budget for K rather than for L .

4.6 Appendix B: Equivalence of the moist static energy variance and power spectrum budgets

First, consider two real-valued functions of position, $f(\mathbf{x})$ and $g(\mathbf{x})$ that are periodic with zero average on a rectangular domain extending from the origin ($\mathbf{x} = \mathbf{0}$) to ($\mathbf{x} = \mathbf{L}_{\text{dom}}$). We will prove that:

$$\langle fg \rangle_{\mathbf{x}} = \mathcal{N} \left\langle \text{Re} \left(\widehat{f} \widehat{g}^* \right) \right\rangle_{\mathbf{k}}, \quad (4.32)$$

where $\widehat{f}(\mathbf{k})$ and $\widehat{g}(\mathbf{k})$ are the spatial Fourier transforms of f and g , defined in equation 4.5, and \mathcal{N} a constant that depends on the size and resolution of the integration domain. We have introduced the averaging operators in physical space:

$$\langle X \rangle_{\mathbf{x}} \stackrel{\text{def}}{=} \frac{\int_{\mathbf{0}}^{\mathbf{L}_{\text{dom}}} X(\mathbf{x}) d\mathbf{x}}{\int_{\mathbf{0}}^{\mathbf{L}_{\text{dom}}} d\mathbf{x}}, \quad (4.33)$$

and spectral space:

$$\langle X \rangle_{\mathbf{k}} \stackrel{\text{def}}{=} \frac{\int_{\mathbf{k}_0}^{\mathbf{k}_N} X(\mathbf{k}) d\mathbf{k}}{\int_{\mathbf{k}_0}^{\mathbf{k}_N} d\mathbf{k}}, \quad (4.34)$$

where the spectral domain extends from the wavenumber with smallest modulus $\mathbf{k} = \mathbf{k}_0$ to the Nyquist wavenumber $\mathbf{k} = \mathbf{k}_N$. The proof can be done in four steps:

1. Assuming (f, g) are square-integrable functions, we can prove Parseval's lemma regarding the scalar product of square integrable functions:

$$\begin{aligned} \int_{\mathbf{0}}^{\mathbf{L}^{\text{dom}}} f(\mathbf{x}) g(\mathbf{x}) d\mathbf{x} &= \int_{\mathbf{0}}^{\mathbf{L}^{\text{dom}}} f(\mathbf{x}) g(\mathbf{x})^* d\mathbf{x} \\ &= \frac{1}{(2\pi)^n} \int_{\mathbb{R}^n} d\mathbf{x} \int_{\mathbb{R}^n} d\mathbf{k} e^{-i\mathbf{k}\cdot\mathbf{x}} \hat{f}(\mathbf{k}) \int_{\mathbb{R}^n} d\mathbf{k}' e^{+i\mathbf{k}'\cdot\mathbf{x}} \hat{g}(\mathbf{k}')^* \\ &= \frac{1}{(2\pi)^n} \int_{\mathbb{R}^n} \int_{\mathbb{R}^n} \int_{\mathbb{R}^n} d\mathbf{x} d\mathbf{k} d\mathbf{k}' \cdot e^{i(\mathbf{k}'-\mathbf{k})\cdot\mathbf{x}} \hat{f}(\mathbf{k}) \hat{g}(\mathbf{k}')^* \\ &= \int_{\mathbb{R}^n} \int_{\mathbb{R}^n} d\mathbf{k} d\mathbf{k}' \cdot \delta(\mathbf{k} - \mathbf{k}') \hat{f}(\mathbf{k}) \hat{g}(\mathbf{k}')^* \\ &= \int_{\mathbb{R}^n} d\mathbf{k} \hat{f}(\mathbf{k}) \hat{g}(\mathbf{k})^* \\ &= \int_{\mathbb{R}_+^n} d\mathbf{k} \hat{f}(\mathbf{k}) \hat{g}(\mathbf{k})^* + \int_{\mathbb{R}_-^n} d\mathbf{k} \hat{f}(\mathbf{k}) \hat{g}(\mathbf{k})^* \end{aligned} \quad (4.35)$$

where we have introduced the Dirac delta function δ and the n-dimensional real number set \mathbb{R}^n .

2. Since the functions (f, g) are real-valued, their Fourier transforms verify:

$$\hat{f}(-\mathbf{k}) = \hat{f}(\mathbf{k})^* \quad , \quad \hat{g}(-\mathbf{k}) = \hat{g}(\mathbf{k})^* \quad (4.36)$$

3. In the last line of step 1, we have broken the integral over \mathbb{R}^n in two parts: an integral over the positive numbers (\mathbb{R}_+^n) and an integral over the negative numbers (\mathbb{R}_-^n). Using step 2, we can change variables and transform the integral

over \mathbb{R}_-^n into an integral over \mathbb{R}_+^n :

$$\begin{aligned}
\int_{\mathbb{R}^n} d\mathbf{k} \widehat{f}(\mathbf{k}) \widehat{g}(\mathbf{k})^* &= \int_{\mathbb{R}_+^n} d\mathbf{k} \widehat{f}(\mathbf{k}) \widehat{g}(\mathbf{k})^* + \int_{\mathbb{R}_-^n} d\mathbf{k} \widehat{f}(-\mathbf{k})^* \widehat{g}(-\mathbf{k}) \\
&= \int_{\mathbb{R}_+^n} d\mathbf{k} \widehat{f}(\mathbf{k}) \widehat{g}(\mathbf{k})^* + \int_{\mathbb{R}_+^n} d\mathbf{k} \widehat{f}(\mathbf{k})^* \widehat{g}(\mathbf{k}) \\
&= 2 \int_{\mathbb{R}_+^n} d\mathbf{k} \cdot \text{Re} \left[\widehat{f}(\mathbf{k}) \widehat{g}(\mathbf{k})^* \right]
\end{aligned} \tag{4.37}$$

4. The product (fg) is periodic in \mathbf{x} and its average is the same over \mathbb{R}^n and $[\mathbf{0}, \mathbf{L}_{\text{dom}}]$:

$$\int_{\mathbb{R}^n} (fg)(\mathbf{x}) d\mathbf{x} = \int_{\mathbf{0}}^{\mathbf{L}_{\text{dom}}} (fg)(\mathbf{x}) d\mathbf{x} = \langle fg \rangle_{\mathbf{x}} \int_{\mathbf{0}}^{\mathbf{L}_{\text{dom}}} d\mathbf{x} \tag{4.38}$$

Furthermore, if we work in the context of a model with finite resolution, we set the signal to zero above the Nyquist wavenumber: $(\widehat{f\widehat{g}^*})(\|\mathbf{k}\| > \|\mathbf{k}_N\|) = \mathbf{0}$. Additionally, since (f) and (g) have zero \mathbf{x} -average, $(\widehat{f})(\mathbf{k} = \mathbf{0}) = \mathbf{0}$, $(\widehat{g}^*)(\mathbf{k} = \mathbf{0}) = \mathbf{0}$, so $(\widehat{f\widehat{g}^*})(\mathbf{k} = \mathbf{0}) = \mathbf{0}$, and we can write:

$$\int_{\mathbb{R}_+^n} \text{Re}(\widehat{f\widehat{g}^*})(\mathbf{k}) d\mathbf{k} = \int_{\mathbf{k}_0}^{\mathbf{k}_N} \text{Re}(\widehat{f\widehat{g}^*})(\mathbf{k}) d\mathbf{k} = \left\langle \text{Re}(\widehat{f\widehat{g}^*}) \right\rangle_{\mathbf{k}} \int_{\mathbf{k}_0}^{\mathbf{k}_N} d\mathbf{k}. \tag{4.39}$$

We conclude by using the result from step 3:

$$\begin{aligned}
\int_{\mathbb{R}^n} f(\mathbf{x}) g(\mathbf{x}) d\mathbf{x} &= 2 \int_{\mathbb{R}_+^n} d\mathbf{k} \cdot \text{Re} \left[\widehat{f}(\mathbf{k}) \widehat{g}(\mathbf{k})^* \right] \\
\langle fg \rangle_{\mathbf{x}} \int_{\mathbf{0}}^{\mathbf{L}_{\text{dom}}} d\mathbf{x} &= 2 \left\langle \text{Re}(\widehat{f\widehat{g}^*}) \right\rangle_{\mathbf{k}} \int_{\mathbf{k}_0}^{\mathbf{k}_N} d\mathbf{k}
\end{aligned} \tag{4.40}$$

$$\langle fg \rangle_{\mathbf{x}} = \mathcal{N} \left\langle \text{Re}(\widehat{f\widehat{g}^*}) \right\rangle_{\mathbf{k}} \quad | \quad \mathcal{N} \stackrel{\text{def}}{=} 2 \int_{\mathbf{k}_0}^{\mathbf{k}_N} d\mathbf{k} / \int_{\mathbf{0}}^{\mathbf{L}_{\text{dom}}} d\mathbf{x} \tag{4.41}$$

which proves identity 4.32.

We are now ready to apply the identity 4.32 to the moist static energy spatial variance budget terms (e.g. Wing and Emanuel [2014]). The budget considers zonal deviations

of physical variables X , defined as:

$$X' \stackrel{\text{def}}{=} X - \langle X \rangle_{\mathbf{x}}. \quad (4.42)$$

Both X' and Y' are doubly-periodic on $[0, \mathbf{L}_{\text{dom}}]$ and have zero \mathbf{x} -average, which allows us to use the identity 4.32. First, by applying the identity 4.32 to $f = g = H'$, we see that the spectral-mean of the spectrum φ is proportional to the spatial variance of H , $\text{var}H \stackrel{\text{def}}{=} \langle H'H' \rangle_{\mathbf{x}}$:

$$\langle \varphi \rangle_{\mathbf{k}} = \mathcal{N} \cdot \text{var}H. \quad (4.43)$$

By taking a logarithmic time-derivative of identity 4.32, we see that if normalized, the spectral-mean evolution of the spectrum φ equals the evolution of $\text{var}H$:

$$\frac{1}{\langle \varphi \rangle_{\mathbf{k}}} \left\langle \frac{\partial \varphi}{\partial t} \right\rangle_{\mathbf{k}} = \frac{1}{\text{var}H} \frac{\partial (\text{var}H)}{\partial t}, \quad (4.44)$$

$$\sum_{i=\text{lw,sw,sf,adv}} \frac{\langle \dot{\varphi}_i \rangle_{\mathbf{k}}}{\langle \varphi \rangle_{\mathbf{k}}} = \sum_{i=\text{lw,sw,sf,adv}} \frac{(\dot{\text{var}H})_i}{\text{var}H}, \quad (4.45)$$

$$\sum_{i=\text{lw,sw,sf,adv}} \frac{\left\langle \text{Re} \left\{ \widehat{H}^* \widehat{H}_i \right\} \right\rangle_{\mathbf{k}}}{\langle \varphi \rangle_{\mathbf{k}}} = \sum_{i=\text{lw,sw,sf,adv}} \frac{\left\langle H' \dot{H}'_i \right\rangle_{\mathbf{x}}}{\text{var}H}. \quad (4.46)$$

The identity 4.32 allows us to go one step further by proving an equivalence between physical and spectral space for each individual tendency. For a given flux $i = \text{lw,sw,sf,adv}$, we choose $f = \dot{H}_i$ and $g = H'$; combining identity 4.32 to identity 4.43 shows that the normalized spectral coherence between MSE and flux (i) equals the normalized spatial correlation between MSE and flux (i):

$$\forall i, \quad \frac{\left\langle \text{Re} \left\{ \widehat{H}^* \widehat{H}_i \right\} \right\rangle_{\mathbf{k}}}{\langle \varphi \rangle_{\mathbf{k}}} = \frac{\left\langle H' \dot{H}'_i \right\rangle_{\mathbf{x}}}{\text{var}H} \quad (4.47)$$

This means that the physical understanding of how each process contributes to $\text{var}H$ (e.g. sections 3.1-3.4 of Wing et al. [2017]) carries over to how each process contributes to the average of φ in spectral space.

4.7 Appendix C: Summary table for all experiments

Var↓ Exp→	CAM280	CAM285	CAM290	CAM295	CAM300	CAM305	CAM310
$(L)_{G/M}$ [1000km]	3.7/5.5	2.8/4.6	4.6/2.7	2.2/2.5	2.4/2.7	2.0/1.8	1.9/1.3
$(\langle\dot{\varphi}_i\rangle/\langle\varphi\rangle)_G$ d^{-1}	0.3 0.6 0.4 -1.0	0.3 0.4 0.4 -0.8	0.2 0.2 0.4 -0.6	0.3 0.1 0.4 -0.6	0.2 0.1 0.2 -0.4	0.2 0.0 0.2 -0.3	0.2 0.0 0.2 -0.2
$(\langle\dot{\varphi}_i\rangle/\langle\varphi\rangle)_M$ d^{-1}	0.3 0.4 -0.0 -0.7	0.3 0.2 -0.0 -0.5	0.1 0.1 -0.0 -0.3	0.1 0.1 -0.1 -0.1	0.1 0.1 -0.0 -0.1	0.0 0.0 -0.0 -0.0	0.0 0.0 -0.0 0.0
$(10 \dot{L}_i/L)_G$ d^{-1}	1.9 -0.7 0.2 -0.1	2.9 -0.2 0.4 -2.2	2.4 -0.0 1.0 -2.4	1.6 -0.0 1.0 -1.9	1.1 -0.1 0.5 -0.8	1.4 -0.1 0.8 -1.4	0.6 -0.0 0.6 -0.5
$(10 \dot{L}_i/L)_M$ d^{-1}	-0.1 -0.4 0.0 0.4	0.8 -0.2 0.1 -0.6	0.8 -0.0 0.0 -0.9	0.2 -0.0 -0.0 -0.2	-0.0 -0.0 -0.3 0.3	0.1 -0.0 -0.1 0.0	0.0 -0.0 -0.0 0.0
$(\mathcal{L}_i)_G$ [1000km]	4.2 3.4 4.1 3.6	4.4 2.6 2.8 3.1	7.5 4.3 4.9 5.7	3.1 2.1 2.4 2.6	3.1 2.1 2.4 2.5	2.7 1.5 2.3 2.5	2.2 1.6 2.1 2.1
$(\mathcal{L}_i)_M$ [1000km]	5.3 5.0 5.6 5.2	5.8 4.2 4.4 4.9	4.4 2.6 1.6 3.7	3.3 2.4 2.6 3.0	2.6 2.5 5.9 1.8	2.2 1.6 2.8 1.8	1.5 1.3 1.4 1.6
Var↓ Exp→	RRTM280	RRTM285	RRTM290	RRTM295	RRTM300	RRTM305	RRTM310
$(L)_{G/M}$ [1000km]	2.6/4.4	1.7/1.5	1.5/1.5	2.2/1.8	2.1/1.7	1.5/1.4	1.5/2.0
$(\langle\dot{\varphi}_i\rangle/\langle\varphi\rangle)_G$ d^{-1}	0.3 0.4 0.5 -1.0	0.3 0.3 0.5 -0.8	0.3 0.1 0.5 -0.8	0.2 0.1 0.3 -0.4	0.2 0.0 0.2 -0.3	0.2 0.0 0.1 -0.1	0.1 0.0 0.2 -0.1
$(\langle\dot{\varphi}_i\rangle/\langle\varphi\rangle)_M$ d^{-1}	0.2 0.3 -0.1 -0.4	-0.0 0.2 -0.1 -0.1	0.0 0.1 -0.1 -0.1	0.0 0.1 -0.1 -0.0	0.0 0.0 -0.0 -0.1	0.0 0.0 -0.0 -0.0	0.0 0.0 -0.0 -0.0
$(10 \dot{L}_i/L)_G$ d^{-1}	2.3 -0.6 0.2 -0.8	2.1 -0.4 -0.6 -0.3	1.9 -0.2 0.3 -1.4	2.0 -0.1 1.1 -2.4	0.7 -0.1 0.3 -0.4	0.8 -0.1 0.6 -0.7	0.8 -0.1 0.6 -0.8
$(10 \dot{L}_i/L)_M$ d^{-1}	0.2 -0.3 0.3 -0.3	0.5 -0.1 0.0 -0.4	0.5 -0.1 0.1 -0.7	0.2 -0.0 -0.1 -0.0	0.1 -0.0 -0.1 0.0	0.1 -0.0 -0.2 0.0	0.0 -0.0 -0.1 0.2
$(\mathcal{L}_i)_G$ [1000km]	3.4 2.4 2.9 2.7	2.4 1.5 1.3 1.6	2.2 1.3 1.4 1.6	3.5 1.8 2.5 3.0	2.6 1.7 2.0 2.1	2.2 0.9 1.9 2.1	2.3 -0.0 2.0 2.5
$(\mathcal{L}_i)_M$ [1000km]	4.8 3.9 2.3 4.6	-20.2 1.4 1.5 2.4	3.7 1.4 1.2 2.9	2.7 1.7 2.1 2.4	2.3 1.6 2.3 1.7	1.9 1.3 3.1 1.3	2.4 1.7 2.6 -22.8
Var↓ Exp→	MD RAD SFC	MD RAD	MD SFC	SQ CAM	SQ RRTM	BSQ RRTM	
$(L)_{G/M}$ [1000km]	2.2/2.3	2.2/2.3	2.1/4.8	0.4/0.8	0.4/0.7	0.5/1.1	
$(\langle\dot{\varphi}_i\rangle/\langle\varphi\rangle)_G$ d^{-1}	0.0 0.0 0.0 -0.3	0.0 0.0 0.4 -0.7	0.2 0.1 0.0 -0.1	0.1 0.0 0.1 -0.1	0.1 0.0 0.1 -0.1	0.1 0.0 0.1 -0.1	
$(\langle\dot{\varphi}_i\rangle/\langle\varphi\rangle)_M$ d^{-1}	0.0 0.0 0.0 -0.4	0.0 0.0 0.4 -0.8	0.1 0.0 0.0 -0.1	0.0 0.0 -0.0 -0.1	0.0 0.0 -0.0 -0.1	0.0 0.0 -0.1 -0.0	
$(10 \dot{L}_i/L)_G$ d^{-1}	0.0 0.0 0.0 -0.8	0.0 0.0 1.7 -2.6	0.4 -0.1 0.0 0.5	0.5 -0.1 0.3 0.1	0.3 -0.1 0.2 0.3	0.2 -0.1 0.3 0.3	
$(10 \dot{L}_i/L)_M$ d^{-1}	0.0 0.0 0.0 -1.2	0.0 0.0 1.2 -2.5	0.1 -0.1 0.0 0.2	0.0 -0.0 0.0 -0.0	0.1 -0.0 0.1 -0.0	-0.0 -0.0 -0.1 0.3	
$(\mathcal{L}_i)_G$ [1000km]	N/A N/A N/A 3.3	N/A N/A 3.0 3.1	2.3 1.8 N/A 1.1	0.5 0.4 0.4 0.3	0.4 0.3 0.4 0.2	0.6 0.4 0.5 0.3	
$(\mathcal{L}_i)_M$ [1000km]	N/A N/A N/A 3.2	N/A N/A 3.0 3.0	5.3 3.7 N/A 3.9	0.8 0.7 0.6 0.8	0.8 0.7 0.6 0.7	1.0 1.0 1.2 0.0	

Table 4.4: For each experiment (Exp), variables (Var) from top to bottom are: Time-averaged convective aggregation scale L (in 1000 km) during the growth phase (subscript G) and the mature phase (subscript M), time-averaged aggregation rate during the growth phase $(\langle\dot{\varphi}_i\rangle/\langle\varphi\rangle)_G$ (in day^{-1}), time-averaged aggregation rate during the mature phase $(\langle\dot{\varphi}_i\rangle/\langle\varphi\rangle)_M$ (in day^{-1}), 10 times the time-averaged expansion rate during the growth phase $(\dot{L}_i/L)_G$ (in day^{-1}), 10 times the time-averaged expansion rate during the mature phase $(\dot{L}_i/L)_M$ (in day^{-1}), time-averaged diabatic length scale during the growth phase $(\mathcal{L}_i)_G$ (in 1000 km), and time-averaged diabatic length scale during the mature phase $(\mathcal{L}_i)_M$ (in 1000 km). i represents a generic flux in the legend; in practice, fluxes are listed in the following order: Longwave Shortwave Surface enthalpy flux Advective flux.

4.8 Appendix D: Spectral moist static energy tendencies and cloud water coherence

In this appendix, we compare the distribution of the MSE power spectral tendencies $\dot{\varphi}_i$ across wavelengths λ (Figure 4-11a) to the spectral coherence of cloud water (Figure 4-11b) and the spectral tendencies $\dot{\varphi}_i$ of the surface enthalpy flux components listed in equation 4.19 (Figure 4-11c). Following definition 4.6, the tendencies are normalized using the wavenumber-averaged MSE power spectrum $\langle\varphi\rangle$, the inverse wavelength λ^{-1} and a wavenumber pre-factor, so that the spectra can be visually integrated over the logarithmic scale to yield the aggregation rate (in s^{-1}):

$$\underbrace{\left(\int_{k_0}^{k_N} dk\right)^{-1}}_{\text{Pre-factor}} \times \int_{k_0}^{k_N} \underbrace{\frac{\dot{\varphi}_i}{\lambda \langle\varphi\rangle}}_{\text{Pow. sp. tendency}} \underbrace{\frac{2\pi\sqrt{ndk}}{\|\mathbf{k}\|}}_{\text{Diff. log. scale}} \stackrel{\text{def}}{=} \underbrace{\frac{\langle\dot{\varphi}_i\rangle}{\langle\varphi\rangle}}_{\text{Aggregation rate}}. \quad (4.48)$$

The cloud water spectral coherence with MSE, depicted in Figure 4-11b, is defined analogously to the MSE spectral tendency $\dot{\varphi}_i$: In equation 4.11, we substitute the spatial Fourier transform of the cloud water path (in kg/m^2) for the spatial Fourier transform \widehat{H}_i of the MSE flux $\{i\}$ (in W/m^2). We then multiply the cloud coherence by the latent heat of vaporization of water vapor L_v (in units J kg^{-1} , evaluated using standard atmospheric temperature conditions) to make it unitless.

The diabatic length scale \mathcal{L}_i of each flux $\{i\}$ is the centroid of the dots, and is indicated with a vertical line in the upper part of each panel. During the first month of the simulation:

- The longwave flux operates at the largest scale, larger than the MSE anomaly scale.
- The MSE anomaly scale is very close to the MSE advection scale as convection aggregates.
- The shortwave flux operates at the smallest scale, below the MSE anomaly scale, resulting in the shortwave shrinking effect.

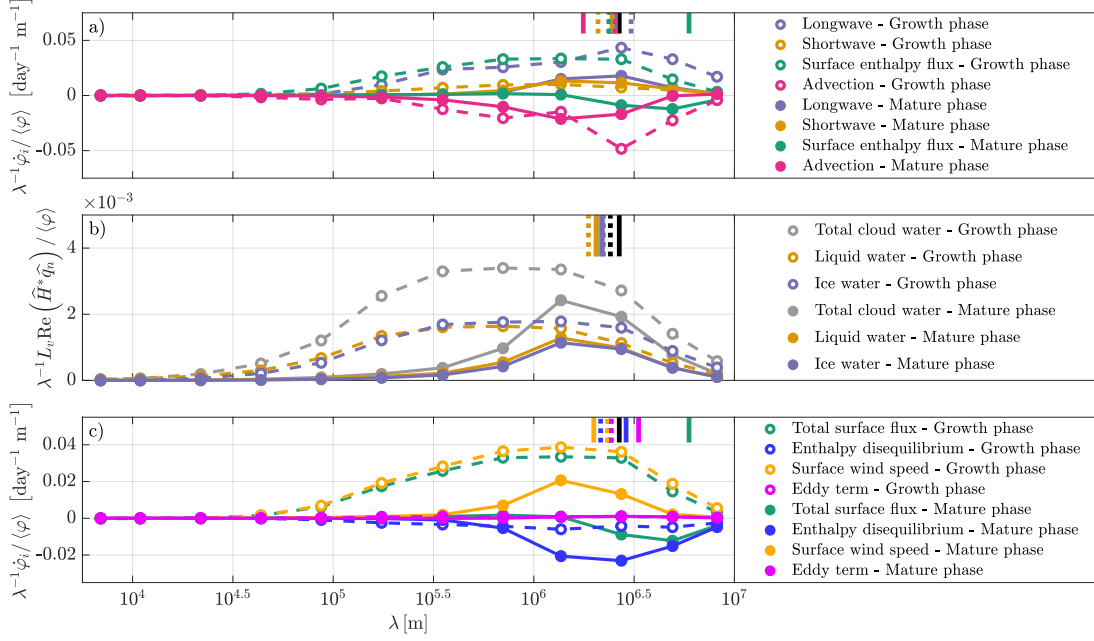


Figure 4-11: (a) Normalized power spectral tendencies (in day/m) of the longwave (blue), shortwave (orange), surface enthalpy (green) and advective (pink) fluxes of MSE during the growth (first month of simulation) and mature (last months of simulation) phases of the reference LC300CAM simulation. (b) Normalized spectral coherence (unitless) between MSE and cloud water concentration: Total cloud water (gray), liquid (orange) and ice (blue) water. (c) Normalized power spectral tendencies (in day/m) of the total surface enthalpy flux (green), enthalpy disequilibrium component (blue), surface wind speed component (orange) and eddy term (pink). The total normalization factor used in all three panels is equal to $\left(\lambda \langle \varphi \rangle \int_{\mathbf{k}_0}^{k_N} dk\right)^{-1}$. All spectra are octave-averaged (dots) and plotted versus wavelength (in m) on a logarithmic scale. The diabatic length scale \mathcal{L}_i (in m) corresponding to each flux is indicated with a dotted vertical line (growth phase) and a full line (mature phase). For reference, the convective aggregation length scale L (in m) is depicted with a dotted black line (growth phase) and a full black line (mature phase).

- The cloud water coherence spectrum shows that ice prevails over liquid water at scales larger than ~ 300 km, consistent with the longwave flux adding MSE power at larger scales than the shortwave flux.
- The surface enthalpy flux operates at a larger than smaller scale than the MSE anomaly scale. From the decomposition of the surface enthalpy flux during the first month, the shape of the surface enthalpy flux is mostly determined by its surface wind component, with a broad peak between ~ 1000 km and ~ 3000 km.

In contrast, during the last months of the simulation:

- The longwave and shortwave fluxes operate at scales closer to the MSE anomaly scale, and the tendencies are more peaked, between ~ 1000 km and ~ 5000 km.
- The ice and liquid water spectra are also more similar to each other, as well as more peaked.
- The advective flux removes MSE power at all scales and peaks below the MSE anomaly scale. Therefore, it preferentially removes power at smaller scales, homogenizing small scale MSE anomalies faster than large-scale ones. This explains the stretching effect of advection in the reference LC300CAM case.
- The surface enthalpy fluxes add MSE power through the surface wind effect up to ~ 2000 km and remove energy through the enthalpy disequilibrium effect above that scale. As a result, the diabatic length scale is artificially large because the surface enthalpy flux aggregation tendency $\langle \dot{\varphi}_{sf} \rangle$ is double-signed. It is then easier to think of the single-signed components of the surface enthalpy flux: the surface wind component adds power with a peaked spectrum centered around ~ 2000 km, while the surface enthalpy disequilibrium component removes power with a broader spectrum centered around ~ 3000 km.

Chapter 5

Are Convective-Aggregation Mechanisms Relevant for the Transient Zonal Variability of Precipitable Water in the Tropics?

Abstract

Recent planetary-scale cloud-resolving models resolve the transfer of moist static energy variability between the convective scale ($\sim 10\text{km}$) and the large-scale circulation in the Tropics ($\sim 10,000\text{km}$), yet we lack simple metrics to compare this multi-scale energy transfer to observations of the tropical atmosphere. Here, we generalize the spectral spatial budget of moist static energy to relate the transient zonal variability of precipitable water to convective-aggregation mechanisms in realistic models and observations. Using a hierarchy of six high-resolution models and observations, we find that the interaction between radiative cooling and water can reinforce transients of precipitable water near the Equator. Surface enthalpy fluxes weaken precipitable water transients across scales in realistic products of the atmosphere, similarly to idealized simulations that exhibit aggregated convection. Our preliminary results suggest that convective-aggregation mechanisms modulate precipitable water variance below the planetary scale ($\sim 10,000\text{km}$), while providing a framework to understand thermodynamic discrepancies between high-resolution observations and models.

5.1 Introduction

The variability of precipitable water (PW) along a latitude circle, referred to as zonal variability, shapes tropical weather and climate. On meteorological timescales, the intensity of extreme precipitation events depends on the humidity of the surrounding environment, e.g. for mesoscale convective systems (LeMone et al. [1998]) and tropical cyclones (Hill and Lackmann [2009]). On climatic timescales, the zonal variability of PW is linked to the equator-to-pole energy transport (e.g. via its correlation with the divergence of the latent heat flux or with the surface enthalpy fluxes, Trenberth et al. [2002]) and to climate sensitivity through cloud and water vapor feedbacks (e.g. via its link to the Walker circulation, Feldl et al. [2014]). To facilitate the discussion, we separate PW into three components: A spatiotemporal mean PW_0 , a stationary anomaly $\overline{PW}(x)$ defined as the time-averaged zonal anomaly of PW, and a residual $PW'(x, t)$ referred to as the transient anomaly:

$$\underbrace{PW(x, t)}_{\text{Total}} = \underbrace{PW_0}_{\text{Mean}} + \underbrace{\overline{PW}(x)}_{\text{Stationary}} + \underbrace{PW'(x, t)}_{\text{Transient}}. \quad (5.1)$$

Characteristics of the stationary PW anomaly (e.g. Figure 5-1a) can be attributed to external influences: The highest values of PW are found over the “Pacific warm pool”, whereas the lowest values are found over the cold Eastern tropical Pacific, and the mountain ranges of South America and Africa. By contrast, the transient variability of PW near the Equator is more difficult to interpret because it is tied to tropical weather across a wide range of spatial scales: convective activity at the $\sim 10\text{km}$ scale, mesoscale convective complexes at the $\sim 100\text{km}$ scale (e.g. review by Houze [2004]), tropical depressions at the $\sim 1000\text{km}$ scale, and the Madden-Julian Oscillation (e.g. review by Zhang [2005]) as well as the Asian monsoon (e.g. Webster et al. [1998]) at the planetary scale ($\sim 10,000\text{km}$). These disturbances may all be modulated non-linearly by the stationary PW features, adding another level of complexity to PW transients.

Thanks to recent computational progress, we can explicitly simulate transients

of PW across the 10 – 10,000km scale range by running high-resolution full-physics models with resolutions comparable to the cloud-scale, referred to as cloud-permitting models (CPM), on planetary-scale domains. When CPM are run on large enough domains, PW self-organizes into moist and dry regions even in the absence of external forcing, such as planetary rotation, surface inhomogeneities or large-scale wind shear (e.g. Held et al. [1993], Muller and Bony [2015]). This emergent property of moist thermodynamics, referred to as “convective self-aggregation” (e.g. reviews by Wing et al. [2017], Holloway et al. [2017]), suggests that a significant fraction of the transient variability of PW near the Equator may arise from internal thermodynamic processes rather than external processes, such as surface characteristics or teleconnections with the mid-latitudes. Since the physical mechanisms of convective self-aggregation have been extensively studied in the context of idealized CPM with fixed surface temperatures, quantitatively comparing convective-aggregation processes in CPM and observations may deepen our understanding of how transient PW anomalies grow and decay.

Explicit comparisons of convective aggregation in observations and CPM are rare because the degree to which idealized CPM configurations represent the real world is still debated. Using satellite data, Tobin and Roca [2012] showed that ($10^\circ \times 10^\circ$) longitude-latitude boxes which had larger degrees of convective organization also exhibited lower values of PW and larger outgoing longwave radiation, consistent with idealized CPM experiments (e.g. Wing and Emanuel [2014]). Holloway et al. [2017] used data from the Nauru meteorological station and showed that the long-channel configuration of Wing and Cronin [2016] had more realistic distributions of PW and vertical velocity than traditional square-domain CPM. Additionally, Stein et al. [2017] showed that for a given large-scale precipitation rate and vertical motion, anvil clouds decreased with the degree of aggregation in satellite data, while low clouds and precipitation efficiency increased with it. Recently, Holloway [2017] used the moist static energy spatial variance budget to show that akin to idealized CPM simulations, interactive radiation maintained aggregation while moist static energy advection disaggregated convection. Motivated by the recent availability of global

CPM data with Earth-like configurations, we seek to leverage the scale-resolving moist static energy framework of Beucler and Cronin [2018] to compare convective organization in observations and planetary-scale high-resolution models of the atmosphere. We ask: Are the convective-aggregation mechanisms studied in this thesis relevant for the transient variability of PW in the Tropics?

In this chapter, we generalize the scale-resolving framework of Chapter 4 to transient PW anomalies to (1) quantify how convective-aggregation mechanisms organize PW transients between the cloud and planetary scales, in idealized and realistic datasets of the tropical atmosphere, and (2) understand thermodynamic discrepancies between high-resolution observations and models. We detail the methods in section 5.2, describe our preliminary results in section 5.3 and discuss the implications and limits of our work in section 5.4.

5.2 Methods

5.2.1 Data characteristics

To diagnose convective-aggregation feedbacks in the real tropical atmosphere, we use observations (ERA and CERES) and a state-of-the-art general circulation model with prescribed surface temperatures from the same time period (GFDL). To relate these diagnosed feedbacks to convective-aggregation mechanisms identified in idealized CPM, we compare the relation between diabatic fluxes and PW in these three datasets to three CPMs with configurations of increasing realism: Non-rotating long-channel with an ocean surface (LC), Rotating near-global rectangle with an ocean surface (NG), and Spherical rotating Earth with realistic land-mass (DYAMOND). We summarize the datasets characteristics in Table 5.1 and describe them in more details below.

Acronym	Type	Domain	Time period
ERA	Meteorological reanalysis	Spherical Earth (spectral)	1Jan2010-31Dec2014
CERES	Satellite observations	Earth	1Jan2010-31Dec2014
GFDL	Global atm. model	Cubed-spherical Earth	1Jan2010-31Dec2014
DYAMOND	Global CPM with land	Cubed-spherical Earth	8Aug2016-10Sep2016
LC	Channel non-rotating CPM	$12,288 \times 192\text{km}^2$	80 days
NG	Near-global rotating CPM	$40,360 \times 10,000\text{km}^2$	1 year

Acronym	Model zonal resolution	Data temporal resolution
ERA	27.5km	1hour
CERES	110km	6hour
GFDL	275km	1day
DYAMOND	4.3km	30min
LC	3km	2.5hour
NG	156.25km	1.2day

Table 5.1: Dataset acronym, type, time period, model zonal resolution and temporal resolution of the data used in this study.

ERA We use data from European Centre for Medium-Range Weather Forecasts Re-Analysis (ERA) version 5 (Hennermann and Guillory [2018]), which was produced by assimilating observational data in version CY41R2 of the Integrated Forecast System. The new reanalysis dataset has better hydrological cycle and sea surface temperatures in the Tropics and is calibrated for climate applications.

CERES We use data from the Clouds & Earth’s Radiant Energy Systems (CERES, Wielicki et al. [1996]) “CERES SYN1deg Ed4A” dataset, which provides diurnally-complete top-of-atmosphere and surface radiative fluxes by using sixteen geostationary satellite as well as the National Aeronautics and Space Administration’s Moderate Resolution Imaging Spectroradiometer.

GFDL We use data from the control experiment for the Geophysical Fluid Dynamics Laboratory’s (GFDL) Global Atmosphere Model version 4.0, with prescribed surface temperatures from ERA5 reanalysis. The performance of the control experiment is described in Zhao et al. [2018a], while the full model description can be found in Zhao et al. [2018b]. The radiative transfer code has been updated from the GFDL radiative transfer code by fitting simulations line-by-line using recent spectroscopy databases, while the convective scheme is a double-plume model (shallow and deep, see section 4 of Zhao et al. [2018b]), in which the deep plume is strongly constrained by environmental humidity.

DYAMOND We use data from the DYnamics of the Atmospheric general circulation Modeled On Non-hydrostatic Domains (DYAMOND) inter-comparison project: DYAMOND experiments are initialized with ERA5 reanalysis data on August 1st 2016, and run until September 10th 2016 with prescribed surface temperatures from ERA5. Here, we focus on the DYAMOND run of the most recent version of the System for Atmospheric Modeling, with a lat-lon grid with 4.25 km grid-spacing at the Equator and a time step of 7.5 seconds. The model uses a simplified land model with vegetation and interactive soil, described in Lee and Khairoutdinov [2015].

LC We use data from a suite of three long-channel (LC) experiments at fixed surface temperature of 300K, with version 6.8.2 of the System for Atmospheric Modeling CPM (Khairoutdinov et al. [2003]), referred to as LC300CAM, MDRAD and MDSFC in Beucler and Cronin [2018]. The control simulation LC300CAM was run by Allison Wing and is thoroughly described in Wing and Cronin [2016].

NG We use data from a suite of three near-global (NG) experiments at fixed surface temperature of 300K with full planetary rotation rate, that uses version 6.10.6 of the System for Atmospheric Modeling CPM (Khairoutdinov et al. [2003]), referred to as CTRL, HOM-RAD and HOM-SFC in Khairoutdinov and Emanuel [2018].

5.2.2 Transient precipitable water variance budgets

In this section, we derive approximate budgets for the zonal variability of transient PW, starting from the budget for column frozen moist static energy H , defined as the sum of column latent heat, sensible heat and potential energy (in units J m^{-2}). H evolves in response to the net moist static energy fluxes F through the boundaries of the atmospheric column in consideration (in W m^{-2}), namely the net radiative flux RAD , the surface enthalpy flux SF and the advection of moist static energy through the column's boundaries ADV :

$$\frac{\partial H}{\partial t} = \sum_{F=RAD,SF,ADV} F \stackrel{\text{(WTG)}}{\approx} L_v \frac{\partial PW}{\partial t}, \quad (5.2)$$

where L_v is the latent heat of vaporization of water vapor and $\partial/\partial t$ is the Eulerian time-derivative at a fixed location. We have approximated the column sensible heat and potential energy as steady using the strict weak temperature approximation (WTG) and neglected the small column latent heat of fusion. To derive a budget for the transient variance of PW, we multiply both sides of equation 5.2 by the transient anomaly PW' of PW, which yields:

$$L_v \frac{\partial}{\partial t} \overbrace{(PW'PW')}^{\text{Transient variance}} = \sum_{F=RAD,SF,ADV} 2 \left(\overbrace{PW'F'}^{\text{Transient-Transient}} + \underbrace{PW'\bar{F}}_{\text{Transient-Stationary}} + \overbrace{PW'F_0}^{\text{Transient-Mean}} \right), \quad (5.3)$$

where F' represents transient moist static energy fluxes, \bar{F} stationary moist static energy fluxes and F_0 spatiotemporally-averaged moist static energy fluxes. Equation 5.3 relates the local growth of transient PW anomalies to their zonal covariance with energy fluxes F , including net radiative flux RAD , surface enthalpy fluxes SF and horizontal advection of moist static energy ADV . The right-hand side of equation 5.3 contains three terms. The generation of variance from the interaction between transient PW and transient energy fluxes is the only non-zero term in zonally-symmetric models of the atmosphere, such as the LC and NG configurations. In realistic configurations, the stationary and mean energy fluxes do not sum to zero, and the interaction

between transient PW anomalies and stationary energy fluxes can generate PW transients on time scales shorter than the time period used to define the temporal average \bar{X} . To quantify the preferred scales of PW variance input and removal, we turn to the spectral framework of Chapter 4: We introduce the zonal spectrum $\widehat{X}(k, t)$ of a variable $X(x, t)$, where k is the zonal wavenumber, by Fourier-transforming $X(x, t)$ in the x-direction. We Fourier-transform equation 5.2 in the x-direction and multiply both sides by the complex conjugate of the PW transient spectrum \widehat{PW}'^* to yield an approximate budget for the transient power spectrum of PW:

$$L_v \frac{\partial}{\partial t} \overbrace{\left(\widehat{PW}'^* \widehat{PW}' \right)}^{\text{Transient power sp.}} = \sum_{F=RAD, SF, ADV} 2 \left[\overbrace{\text{Re} \left(\widehat{PW}'^* \widehat{F}' \right)}^{\text{Transient-Transient}} + \underbrace{\text{Re} \left(\widehat{PW}'^* \widehat{F} \right)}_{\text{Transient-Stationary}} \right]. \quad (5.4)$$

Note that the term $\text{Re} \left(\widehat{PW}'^* \widehat{F}_0 \right)$ is zero because the Fourier transform of the constant F_0 is a delta function at wavenumber $k = 0$ and the Fourier transform of the PW anomaly PW' is zero at $k = 0$. At a given zonal scale λ , a positive coherence between PW' and energy flux zonal anomalies increases the power spectrum of PW' , while a negative coherence decreases the power spectrum of PW' .

5.2.3 Statistical and spectral analyses

The present analysis requires three fields: precipitable water, net atmospheric radiative heating and surface enthalpy fluxes. Because we are interested in zonal variability near the Equator, the fields are first averaged over the North-South dimension, from 15°S to 15°N (the fields are averaged over the short extent of the domain in the y-direction for the LC configuration). Changing 15° to 10° or 20° does not affect the conclusions of the paper. To facilitate the comparison between different datasets, we restrict the time series of ERA, CERES and GFDL to the same time period (January 1st 2010 - December 31st 2014), and only keep the “aggregated phase” of idealized CPM LC and NG, i.e. the time series after the PW temporal variance reaches its first local maximum (typically a few weeks). We also restrict ERA and CERES to

the DYAMOND time period of (August 8th 2016 - September 10th 2016) and present the results of their comparison in Appendix 5.5. We correlate transient fields at every time step before time-averaging the covariances to yield the right columns of Figures 5-1 and 5-4. We diurnally-average the PW and flux transients, create the histogram of PW' in Figure 5-2a using the MATLAB “histcounts” binning algorithm with automatic bin width choice, and keep the same bins to condition each energy flux on PW in Figures 5-2b,c. The same operation is repeated on the total fields to yield Figure 5-5. We calculate the zonal spectra of each variable using the MATLAB Fast Fourier Transform “fft” algorithm, which uses the C library FFTW Frigo and Johnson [2005]. The power spectra and cross-spectral density fields are calculated at every time step before being time-averaged to create Figures 5-3a,b,c. Finally, we apply rectangular window filters to the zonal spectra of PW and energy fluxes to obtain the right panels of Figures 5-2 and 5-5.

5.3 Preliminary results

5.3.1 Interaction between water vapor, radiation and convection

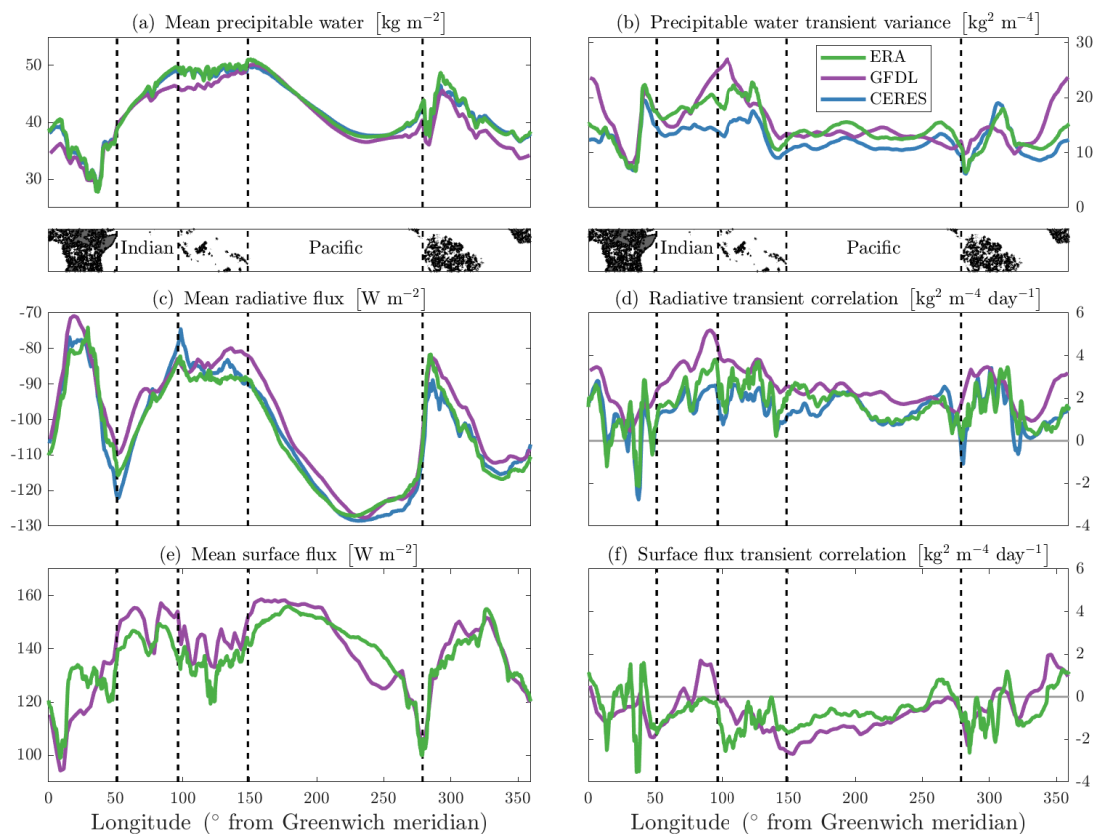


Figure 5-1: Time-mean PW (a) and moist static energy fluxes (c,e), time-mean transient variance of PW (b) and twice the time-mean covariance between transient PW and transient surface enthalpy fluxes (d,f) versus longitude for ERA, CERES and GFDL for the five years 2010-2014.

We can measure PW differences between datasets using a simple temporal average, and Figure 5-1a shows a persistent dry bias of the GFDL over Africa and the Eastern Indian Ocean compared to observational products (Zhao et al. [2018a]). Since DYAMOND was only run for one month, we compare it to observations separately in Appendix 5.5. Discrepancies between GFDL, ERA and CERES become more ap-

parent when calculating higher moments of the PW field, which are more directly connected to extreme precipitation events (e.g. Bretherton et al. [2004]): Figure 5-1b shows that GFDL exhibits a higher time-averaged variance of PW transients ¹ than both ERA and CERES (zonal mean of $15.3\text{kg}^2 \text{m}^{-4}$ versus $14.4\text{kg}^2 \text{m}^{-4}$ and $12.3\text{kg}^2 \text{m}^{-4}$), motivating the question: What physical processes set the variance of PW transients?

Since horizontal variations in free-tropospheric temperature are weak in the Tropics, internal thermodynamic processes create variability dominantly through the interaction between water vapor and energy fluxes from radiation, convection and advection. If the convergence of energy fluxes is larger in moister regions, moist regions become moister through the ascending motion driven by the anomalous enthalpy input (e.g. Holloway and Woolnough [2016]). This moist instability of the tropical atmosphere may lead to growth of PW transient anomalies in time and space until the net variance input by diabatic fluxes equilibrates with the large-scale export and small-scale mixing of enthalpy.

Using equation 5.3, we correlate the transient PW and radiative heating fields to show that the interaction between radiation and PW maintains PW transients around the globe (see Figure 5-1d). This result could not be obtained by simply correlating the stationary patterns of PW (Figure 5-1a) and radiative heating (Figure 5-1c): Unlike transient anomalies, steady anomalies act to remove PW variance over Africa, where radiative cooling and PW is low. Similarly, Figure 5-1f shows that the transient covariance between PW and surface fluxes weaken PW transients over the “Pacific warm pool”, while the stationary maxima of PW and surface fluxes at this location maintain steady PW anomalies (Figures 5-1a and 5-1c). The sum of transient diabatic covariances zonally-averages to $1.0\text{kg}^2 \text{m}^{-4} \text{day}^{-1}$ for ERA, with values as high as $4.7\text{kg}^2 \text{m}^{-4} \text{day}^{-1}$ over the Indian Ocean. At this rate, the time-average variance of transient PW anomalies could be created in ~ 2 weeks from a state of rest, if not for the destruction of variance through advective pro-

¹rigorously defined as $\langle \text{PW}'\text{PW}' \rangle_{2010-2014}$, where $\langle X \rangle_{2010-2014}$ is the temporal average of a variable $X(t)$ over the 2010-2014 time period.

cesses². By comparison, the sum of total radiative and surface flux zonal covariances averages to $\sum_F (\overline{PW'} + \overline{PW}) (\overline{F'} + \overline{F}) = 4.4\text{kg}^2 \text{m}^{-4} \text{day}^{-1}$, with maxima of $\approx 10\text{kg}^2 \text{m}^{-4} \text{day}^{-1}$ over the Indian Ocean, suggesting that a non-negligible portion of the PW variance arises from internal (transient diabatic fluxes) versus external (e.g. stationary surface temperature gradients) processes.

We further investigate how convective-aggregation mechanisms may vary across PW and scales by calculating statistics of transient diabatic fluxes conditioned on transient PW for all six datasets (shown in Figure 5-2a).

Convective-aggregation mechanisms rely on the relation between the net radiative fluxes and PW: If radiative heating increases with PW, then PW anomalies may grow by interacting with the radiation field. In an atmospheric column, the net radiative fluxes are determined by the complex vertical distribution of temperature and radiatively-active molecules. Because zonal gradients in temperature and trace molecules other than atmospheric water are weak in the Tropics (Sobel et al. [2001]), we take a statistical approach and bin the transient radiative fluxes on transient PW. Focusing on ERA reanalysis in Figure 5-2b, the variability of radiative heating for a given value of PW, as measured by the inter-quartile range (vertical green bars), is smaller than the overall change of radiative heating with PW. Therefore, the effect of PW on radiative heating is visible across regions of different transient PW anomalies. This result holds for the six datasets which exhibit similar inter-quartile range, but we only show the ERA inter-quartile range in Figure 5-2b for readability purposes. Although the relation between total radiative cooling and total PW is non-monotonic (see Appendix 5.6, consistent with Chapter 2), we find that transient radiative heating anomalies grow almost linearly with transient PW anomalies in all datasets but LC³.

²Averaging equation 5.3 over the 2010-2014 time period predicts that the transient covariances must sum to zero over the 2010-2014 time period:

$$0 \approx \frac{L_v}{2} \frac{PW'PW' (31\text{Dec}2014) - PW'PW' (1\text{Jan}2010)}{5 \text{ years}} = \sum_{F=RAD,SF,ADV} 2 \langle PW'F' \rangle_{2010-2014}. \quad (5.5)$$

³Since the LC configuration is zonally symmetric, transient PW equal total anomalies. Since the distribution of PW in LC has a large variance, it contains PW values as small as 20kg m^{-2} , for which radiative cooling increases with PW.

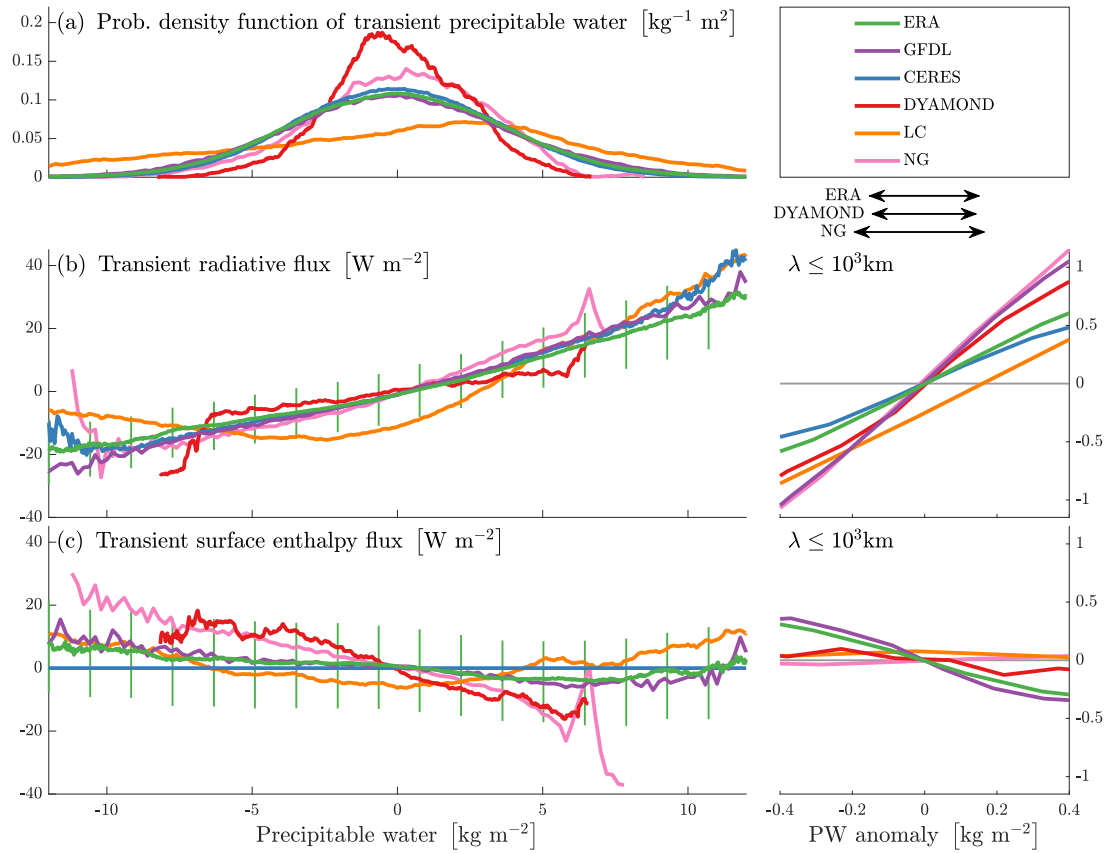


Figure 5-2: (a) Probability density function of transient PW and (b-c) Expected value of diurnally-averaged transient diabatic fluxes conditioned on PW for all datasets. For ERA, we indicate the inter-quartile range of the fluxes conditioned on PW with vertical green lines. The right panels show the anomalous fluxes conditioned on anomalous PW after applying a rectangular window-filter to only keep the zonal variability at scales below one thousand kilometers, with black double-arrows indicating the inter-quartile range of filtered transient PW anomalies for different datasets.

Following the methodology of Chapter 2, we define a radiative-instability growth rate by normalizing the slope of the radiation-PW relation using the latent heat of vaporization of water vapor. We find a growth rate of 0.07day^{-1} for ERA in the $\mp 5\text{kg m}^{-2}$ range, similar to the cloudy growth rates predicted in Chapter 2. The relatively large variability of surface fluxes at constant PW in Figure 5-2c suggests that in realistic configurations, the interaction between surface fluxes and PW may not lead to the growth, maintenance or strong decay of PW transients.

The relation between transient diabatic fluxes and PW anomalies significantly changes across zonal scales, as shown on the right panels of Figure 5-2. In idealized configurations (LC and NG), radiative heating consistently creates PW variance below zonal scales of $1,000\text{km}$, with an average instability rate as high as $\approx 0.08\text{day}^{-1}$ over the $\mp 0.4\text{kg m}^{-2}$ range of PW anomalies for NG. In realistic configurations (ERA, GFDL and CERES), the radiative instability rate of $+0.04\text{day}^{-1}$ is largely compensated by the removal of PW variance by surface fluxes at the rate of 0.03day^{-1} . The large decrease in moist instability rates from the planetary scale to the mesoscale ($100 - 1,000\text{km}$) motivates the use of zonal spectra to quantify the preferred scales of PW variance input and removal.

5.3.2 Zonal Spectra of Convective-Aggregation Feedbacks

We use the spectral budget for PW transients (equation 5.4) to (1) quantify the scale-by-scale input of PW variance by each diabatic flux and (2) compare the thermodynamics of models and observations across scales. We measure the variance of PW at each zonal scale λ using the zonal power spectrum of PW between the cloud-scale $\lambda \approx 10\text{km}$ and the planetary-scale $\lambda \approx 40,000\text{km}$, depicted in Figure 5-3a for all six datasets. We can distinguish two ranges: Below the zonal scale $\lambda \approx 1,000\text{km}$, the PW power spectrum grows sharply with λ , following a $\lambda^3 \sim k^{-3}$ slope, where $k \stackrel{\text{def}}{=} (2\pi)\lambda^{-1}$ is the zonal wavenumber. At these smaller scales, the right panels of Figure 5-2 suggests that diabatic fluxes act to reinforce PW zonal structures, while the local transport of enthalpy smoothes out PW zonal structures so as to maintain a k^{-3} spectral slope. Above a scale $\lambda_0 < 10,000\text{km}$ that depends on the dataset and

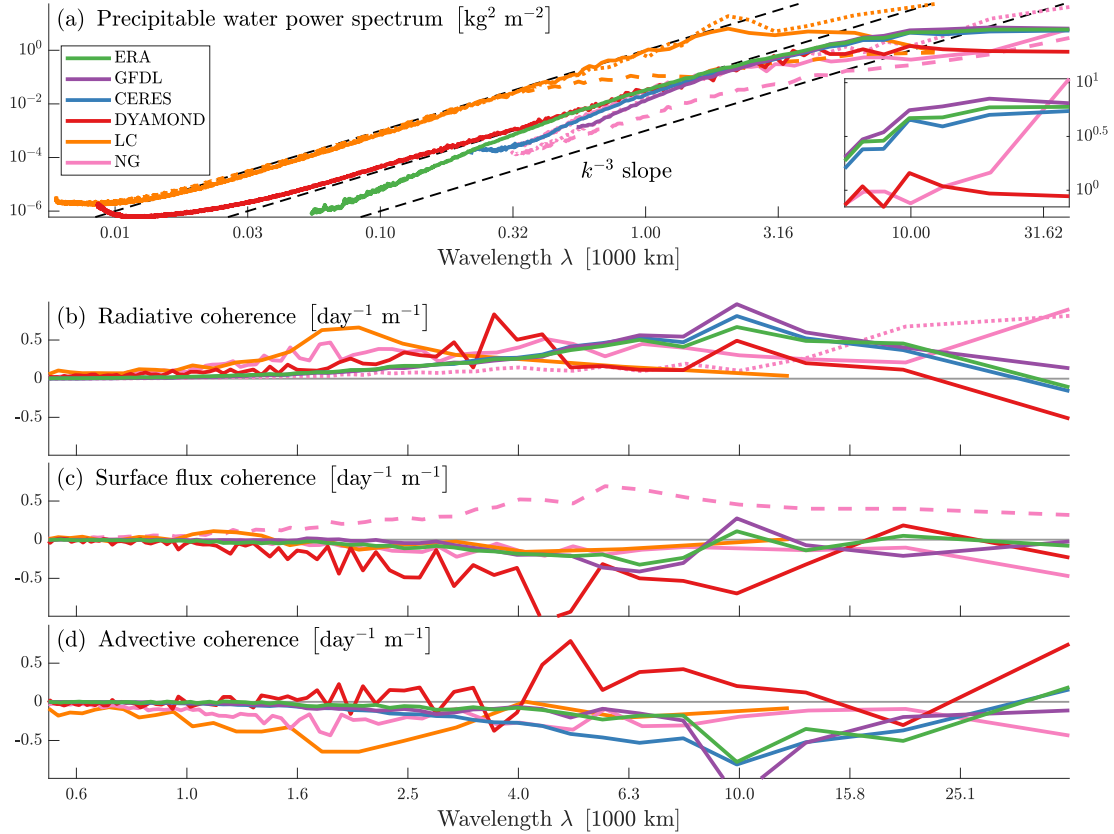


Figure 5-3: (a) PW transient power spectrum versus wavelengths for all datasets. For LC and NG, we additionally plot mechanism denial experiments with uniform radiation using dashed lines, and with uniform surface fluxes using dotted lines, respectively. (b-d) Moist static energy flux spectral cross-spectral densities, multiplied by 2.

is well-measured by the integral scale of the PW power spectrum (see Appendix A of Chapter 4), the PW power spectrum flattens. A notable exception is NG, which exhibits large PW power at the longest wavelength $\lambda \approx 40,000\text{km}$, consistent with the strong Madden-Julian-Oscillation signal observed in this simulation Khairoutdinov and Emanuel [2018]. Therefore, we observe moist and dry transients below the largest scale, prompting the question: What determines the shape of the PW spectrum at large scales?

Idealized CPM experiments are powerful tools to approach that question as they can test the causal effect of different thermodynamic processes on the PW spectrum. We focus on two mechanism-denial experiments developed in the context of convective

self-aggregation: Simulations in which radiation is made horizontally uniform at every time step (dashed line), and simulations in which surface fluxes are made uniform at each time step (dotted line). When radiation is made uniform, convection does not aggregate at large scales, and λ_0 is small, corresponding to small PW structures of a few hundred kilometers. In contrast, convection aggregates at very large scales when surface fluxes are made uniform and λ_0 is large. Although Figure 5-5a shows that the water vapor distributions of idealized and realistic datasets differ, the k^{-3} slope is robust across experiments and datasets, including the non-rotating LC configuration and the mechanism-denial experiments. This suggests that (1) the zonal variability of PW from the cloud-scale to the $\approx 1,000\text{km}$ scale may be explained without invoking planetary rotation arguments and that (2) changes of the diabatic fluxes-PW relation affect the scale λ_0 at which the PW spectrum flattens but not the mesoscale k^{-3} slope since all mechanism-denial experiments retain it. The changes in λ_0 suggest that the interaction between radiative heating and PW across scales may help PW organize at large scales, while the interaction between surface fluxes and PW may remove variance at these large scales. We quantitatively measure this multi-scale interaction by using the cross-spectral density between the zonal spectrum of transient PW \widehat{PW}' and the zonal spectrum of transient energy fluxes \widehat{F}' (equation 5.4), averaged over the entire time period of each dataset.

Figure 5-3b shows that radiative cross-spectral density is positive across scales, and largest at the planetary-scale, in both idealized and realistic configurations. Radiative heating thus creates PW variance at large zonal scales, consistent with the radiative-PW instability of moist atmospheres (e.g. Kuang [2018], Beucler and Cronin [2018]). Therefore, DYAMOND, which has anomalously small radiative cross-spectral density at scales above $\approx 5,000\text{km}$, has the smallest PW power spectrum above $\approx 5,000\text{km}$ among all realistic configurations. The surface enthalpy flux cross-spectral density across scales, depicted in Figure 5-3c, is of special interest as Figure 5-2c shows that CPM and realistic datasets predict different surface flux-PW relations. In idealized models, the surface flux cross-spectral density tends to be overly positive when PW is not organized at large scales, which translates to a strong positive cross-spectral

density for the NG mechanism denial experiments across scales (dashed pink line in Figure 5-3c). As convection organizes at scales of $\approx 1,000\text{km}$, the surface flux cross-spectral densities of aggregated CPM become negative: Over a given surface type (land or ocean) and at fixed surface temperature, moister regions have smaller near-surface enthalpy disequilibrium and therefore smaller surface enthalpy fluxes (e.g. Wing et al. [2017]). Realistic datasets also remove PW variance between the $\approx 1,000\text{km}$ and the $\approx 10,000\text{km}$ scales, suggesting that the convective-aggregation mechanisms identified in idealized CPM may operate at these scales, although external factors such as synoptic-scale dry intrusions could also be removing PW variance by increasing surface enthalpy fluxes (e.g. Bretherton and Khairoutdinov [2015]). The surface flux cross-spectral density in realistic datasets becomes closer to zero above the $\approx 10,000\text{km}$ scale, suggesting that the interaction between transient PW and stationary diabatic fluxes becomes more important at planetary scales. Finally, we infer the advective cross-spectral density as a residual from the diabatic flux cross-spectral densities in Figure 5-3d, and find that horizontal advection smooths out PW transients at all scales, with the exception of DYAMOND which requires further investigation.

5.4 Discussion

As computational progress allows more and more convection-resolving models to be run at the global scale, we need to create more and more physically-meaningful metrics, such as the radiation-PW relation depicted in Figure 5-2b, to test them for operational purposes, whether it be numerical weather forecast or long-term climate predictions. Because these relations change across spatial scales, we can leverage spectral analysis to compare behaviors in observations and models of different configurations and resolutions. Common characteristics, such as the radiative instability growth rate of $1/(2\text{week})$, the k^{-3} slope of the PW power spectrum in Figure 5-3a, or the variance input by diabatic fluxes between $1,000\text{km}$ and $10,000\text{km}$, suggest that non-rotating idealized simulations can help explain the spatial variability of PW in

the Tropics. Statistically significant differences, such as the lack of radiative coherence in the DYAMOND model (Figure 5-3b) or the overestimated transient cross-spectral densities in the GFDL model (Figure 5-1), can help improve high-resolution modeling of the tropical atmosphere through data assimilation (e.g. Rodell et al. [2004]) or statistical learning (e.g. Gentine et al. [2018]) of local (e.g. aircraft, Marengo et al. [1998]) and global (e.g. satellite, Adler et al. [2003]) observations. Intriguing results encourage deeper investigations: The linear relation between transient radiative heating and transient PW (Figure 5-2b) suggests that moist PW transients affect radiative heating at the same rate regardless of their environment, which could be verified by conditioning the three-dimensional cloudy and clear-sky radiative fluxes on transient PW. The transient surface fluxes - transient PW relation (Figure 5-2c) and the total surface fluxes - total PW relation (Figure 5-5c) have opposite slopes in the case of DYAMOND, pointing to non-linear feedbacks between surface fluxes, water vapor and the large-scale circulation.

Our preliminary results, although promising, require more careful analysis before we can confirm the relevance of convective-aggregation mechanisms for transient PW variability in the Tropics. Throughout this chapter, we have only considered time-averaged budgets of transient PW variability, and thus overlooked the interaction between transient PW anomalies and the stationary anomalies of diabatic fluxes. This interaction can be large on short time scales, which could nuance the suggestions of Figure 5-2. For instance, moist instabilities that rely on the interaction between transient radiation and transient PW may mostly contribute to the maintenance of transient PW structures (e.g. amplification of the Madden-Julian oscillation), while stationary features of diabatic fluxes could be responsible for triggering PW transients (e.g. initiation of the Madden-Julian oscillation). Conditioning the observed relation between diabatic fluxes and PW on surface type (e.g. land versus ocean) or geographical region (e.g. West Pacific versus East Pacific) could be a first step towards quantifying the interaction between stationary diabatic flux anomalies and transient PW anomalies.

5.5 Appendix A: Comparison between DYAMOND and observations

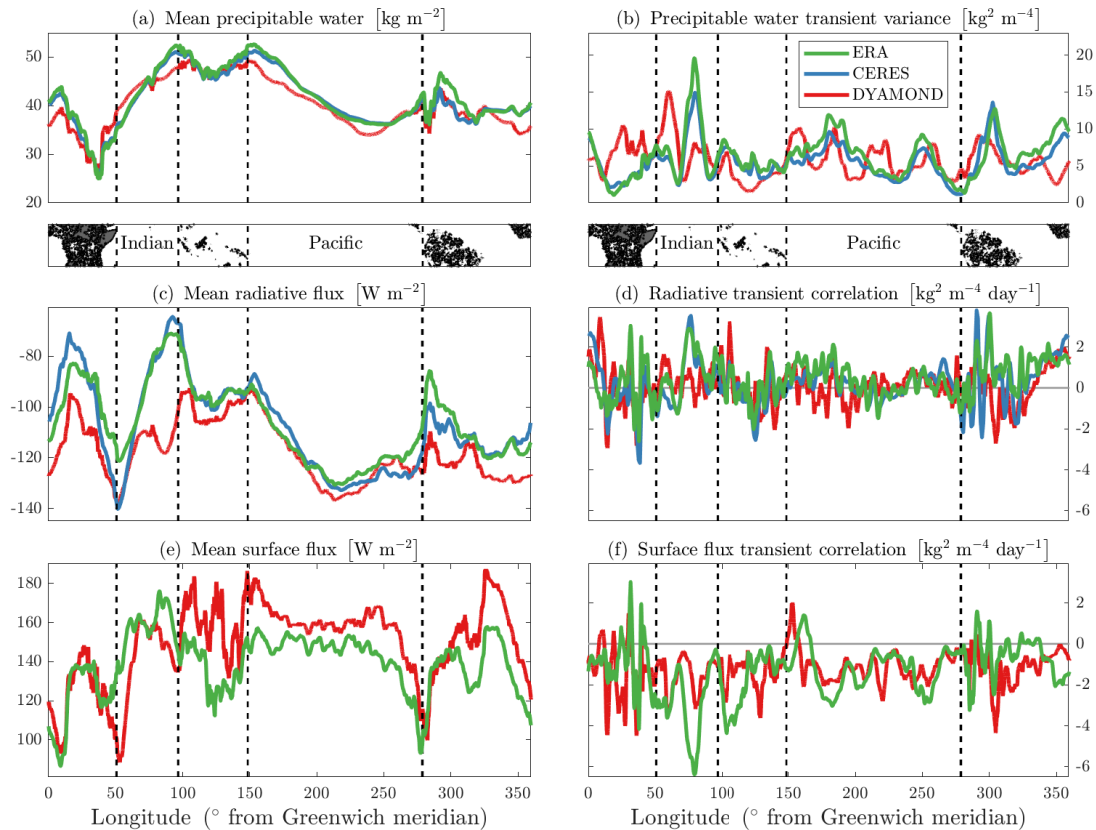


Figure 5-4: Time-mean PW (a) and diabatic fluxes (c,e), time-mean transient variance of PW (b) and twice the time-mean covariance between transient PW and transient surface diabatic fluxes (d,f) versus longitude for ERA, CERES and DYAMOND for the time period: Aug 8th 2016 - Sep 10th 2016.

5.6 Appendix B: Relation between total diabatic fluxes and precipitable water

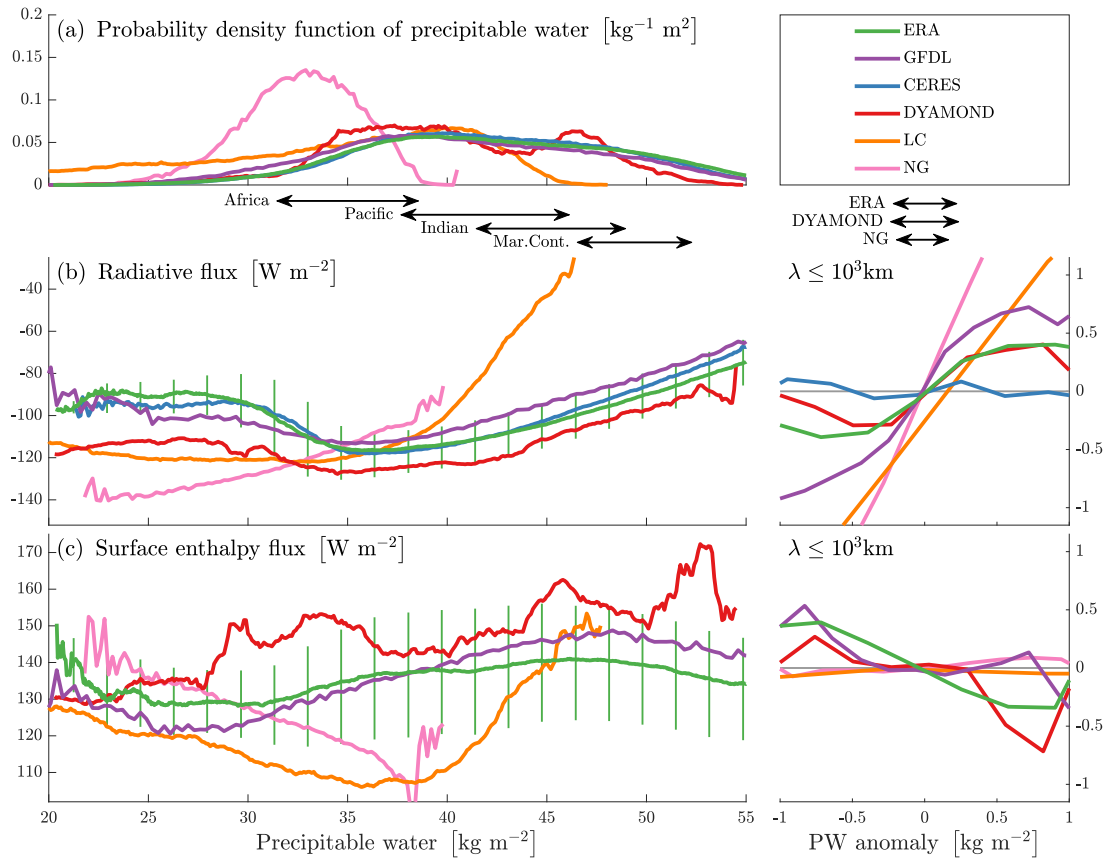


Figure 5-5: (a) Probability density function of PW, with black double-arrows indicating the inter-quartile range of PW over specific regions and (b-c) Expected value of diurnally-averaged diabatic fluxes conditioned on PW for all datasets. For ERA, we indicate the inter-quartile range of the fluxes conditioned on PW with vertical green lines. The right panels show the anomalous fluxes conditioned on anomalous PW after applying a rectangular window-filter to only keep the zonal variability at scales below one thousand kilometers, with black double-arrows indicating the inter-quartile range of filtered PW anomalies for different datasets.

Chapter 6

Conclusion

6.1 Introduction

More than half of the Earth's population is projected to live in the Tropics by 2050¹. Better understanding of the hydrological cycle in the Tropics thus has immense societal value, whether it be to better predict extreme precipitation events (e.g. Allan and Soden [2008]), droughts (e.g. Seneviratne et al. [2012]), or even the propagation of infectious diseases (e.g. Metcalf et al. [2017]). To predict future tropical climate, we cannot solely rely on observations and statistical models of the present climate for at least two reasons:

1. Mean tropical surface temperatures are projected to warm by $\sim 1.5 - 2^\circ\text{C}$ by 2050 and $\sim 5 - 9^\circ\text{C}$ by 2200 in the business-as-usual scenario (RCP 8.5 using 1986-2005 as the base period for temperatures, Figure 12.11 of IPCC [2014]). Because of this warming, precipitable water (PW) will reach values that have never been observed since the advent of satellites. For instance, PW values as high as 100kg m^{-2} ($\approx 1\%$ of the total atmospheric column mass) are less than (+1) standard deviation from the mean in the long-channel configuration with a surface temperature of 310K!
2. It can be misleading to use fluctuations within the present climate, such as El

¹defined as the region between 23.5°S and 23.5°N , according to Edelman et al. [2014] based on world population prospects data from the population division of the United Nations.

Nino and the Southern Oscillation, to infer what may happen in the future (e.g. Schneider et al. [2010]). For instance, the observed surface temperature threshold for deep convection in the current climate (e.g. Folkins and Braun [2003]) depends on large-scale properties of the atmosphere, such as the static stability (e.g. Neelin et al. [2009]).

Therefore, we must rely on high-resolution Earth-system modeling to predict future tropical climate. These models cannot simply be tuned to the present climate: they must rely on physical principles and be evaluated against observations using methods that reveal their underlying biases. In that spirit, the present thesis has used variables commonly generated by realistic models to build theories of tropical thermodynamics and new diagnostic frameworks for convective organization. We hope that some of these frameworks will be useful to develop or evaluate future global climate models, and that the physical mechanisms of radiative-convective instability will be a step towards deeper understanding of the tropical atmosphere.

6.2 Key results

Faithful to its title, the present thesis studies the interaction between atmospheric water vapor, radiation and convection across scales in models and observations. We summarize the key results relating to each component of this interaction below, and refer the reader interested in a linear summary to section 1.2.

Interaction between longwave radiation and water vapor In Chapter 2, we have shown that longwave cooling is non-monotonic vis-a-vis of PW: For small values of PW, longwave cooling increases with PW because the concentration of emitters increases. However, above a critical PW threshold, longwave cooling decreases with PW because water vapor molecules in the lower troposphere cannot cool as effectively to space, physical mechanism that we refer to as “radiative amplification effect”. Decreasing cooling to space by adding energy in the form of water vapor can drive an overturning circulation that leads to a positive feedback between water vapor and

longwave radiation. This behavior holds for clear-sky longwave radiation, whether it be gray or realistic, and may be enhanced in the presence of clouds. We have used observed soundings of the tropical atmosphere to show that the tropical atmosphere is in the unstable range of this longwave-PW interaction. In Chapter 3, we have quantified the level-by-level interaction between water vapor and longwave radiative heating, using both gray and realistic radiation. We have rigorously quantified the “radiative amplification effect”, that leads to a decrease in radiative cooling when water vapor is added in the upper troposphere. In Chapter 4, we have diagnosed the scale-by-scale MSE variance input from clear-sky and cloudy longwave radiation using a series of cloud-permitting simulation. We have found that longwave radiative cooling is the main contributor to the aggregation and expansion of water vapor perturbations in idealized simulations of convective self-aggregation, which we mostly attribute to ice clouds using additional mechanism-denial experiments in Appendix A. Finally, we have shown in Chapter 5 that longwave radiation also creates PW variance at large zonal scales in realistic products of the atmosphere, and that the non-monotonicity of the longwave-PW relation holds for both clear-sky and cloudy radiation.

Interaction between shortwave radiation and water vapor In Chapter 2, we have shown that clear-sky shortwave absorption contributes to radiative-PW instability because moist regions absorb more solar radiation than dry regions, and have quantified this effect in observed soundings of the tropical atmosphere. In Chapter 3, we have shown that level-by-level interactions between shortwave heating and water vapor lead to a local absorption effect, slightly compensated by the cooling of water vapor molecules below the absorbing molecules because of the reduced incoming solar flux. In Chapter 4, we have shown that shortwave radiative heating helps convection aggregate, while making moist and dry regions smaller because it acts at the scale of shallow clouds and water vapor. In Appendix A, we have shown that the shortwave heating effect is large enough to aggregate convection on its own, which we refer to as clear-sky aggregation.

Interaction between radiation and convection We have explicitly studied the interaction between radiation and convection in Chapter 3: Although convection dominates the evolution of the water vapor profile, consistent radiative feedback may interact with bulk-plume convection to reinforce water vapor perturbations in the mid-troposphere. This interaction depends on the structure of convection, and is favored when convection transports energy upwards, which can then amplify water vapor in the mid-troposphere through the “radiative amplification effect”.

Interaction between convection and water vapor The interaction between convection and water vapor, commonly referred to as moisture-convection feedback, is explicitly studied in Chapter 3. Under the weak temperature gradient approximation, we have shown that the column-integrated HAM determines the stability of the interaction between water vapor and Betts-Miller convection. In Appendix B, we have shown that the local value of HAM determines the stability of the interaction between water vapor and convective downdrafts by controlling the relative effect of convective cooling and moistening on water vapor perturbations. In contrast, we have found that the stability of moisture-convective feedback depends on the entrainment rate for bulk-plume convection.

Interaction between surface fluxes and water vapor This interaction can fall under the umbrella of convection-water vapor interactions, since the column-integral of convective enthalpy fluxes is the net surface enthalpy flux. In Chapter 4, we have shown that the wind component of the surface flux aggregates convection at the small scale of convective gustiness, while the enthalpy disequilibrium component of the surface flux tends to remove variance at the scale of moist and dry regions. As a consequence, the total surface enthalpy flux initially helps convection aggregate, while disaggregating and shrinking PW structures once convection has aggregated. In Chapter 5, we have shown that in realistic products of the atmosphere, surface fluxes remove the variance associated to PW transients across scales, similarly to surface fluxes in idealized and aggregated simulations of convection.

6.3 Directions for future research

Atmospheric physics and tropical meteorology are rich fields, and listing general directions for future research would not fit in this conclusion. Instead, we focus on topics that have been omitted from the present thesis by asking: If this thesis had three more chapters, what would they look like?

6.3.1 Organization of convection over an interactive surface

Chapter 5 underlines important differences between convective feedbacks over different types of surfaces: In the real world, land surfaces and oceans with strong near-surface stratification (e.g. the Bay of Bengal during Boreal Winter, Mahadevan et al. [2016]) behave differently from idealized surfaces of infinite heat capacity, a behavior largely overlooked in this thesis. Recent general-circulation (Coppin and Bony [2017]) and cloud-permitting (Hohenegger and Stevens [2018]) studies have shown that the presence of an interactive surface adds variability to radiative-convective equilibrium, and prevents the formation of steady moist and dry regions through feedbacks between surface fluxes and the circulation. The long-channel configuration used in Chapter 4 and Appendix A could be generalized to an interactive surface to validate the previous findings and explore the scale-dependence of these surface fluxes-circulation feedbacks, with the caveat that RCE takes much longer to equilibrate with an interactive surface (e.g. Cronin and Emanuel [2013]). The different spatial variability obtained with an interactive surface could then be compared with the observed variability of PW over surfaces of smaller heat capacity, for instance by isolating the results of Chapter 5 over land.

6.3.2 Role of radiation and convection during extreme events

Tropical cyclones

Using cloud-permitting models, Wing et al. [2016] has found that convective-aggregation feedbacks may play a leading-order role in the spontaneous genesis of tropical cyclones.

Although latent heat fluxes can lead to cyclogenesis without the help of radiative feedbacks, Muller and Romps [2018] have simulated a “radiative cyclone” driven by the interaction between gradients in radiative fluxes and rotating dynamics. Radiation can influence the rate of cyclone intensification through the differential longwave cooling between the developing cloudy disturbance and the cloud-free environment (e.g. Nicholls [2015]), or when shortwave heating changes surface temperatures, which in turn affect the latent heat fluxes (e.g. Sobel et al. [2018]). The recent progress in modeling tropical cyclones using high-resolution cloud-permitting models is an opportunity to generalize the spectral MSE budgets in Chapter 4 to tropical cyclones. Using the spectral MSE budget, we could study how surface enthalpy fluxes and radiation change the intensity and structure of a tropical cyclone: For example, cyclone size changes using a Hankel transform in the radial direction, or forcing of asymmetries using the azimuthal MSE spectrum. Note that in the case of tropical cyclones, the MSE budget may be complemented by the radial momentum equation, in which the dominant flow is set by the balance between the Coriolis force, the centrifugal acceleration and the geopotential gradient.

Monsoonal depressions

Monsoonal depressions are cyclonic vortices with typical radii nearing 1000km [Godbole, 1977] and high precipitation rates, that account for roughly half of the total South Asian monsoonal rain [Yoon and Chen, 2005, Stano et al., 2002]. Because monsoonal depressions are inadequately represented in global climate models [Praveen et al., 2015] that cannot accurately resolve convection and clouds, little is known about the physical mechanisms leading to the formation and intensification of monsoonal depressions, and how these mechanisms depend on the environment. While it was thought that counter-propagating waves in the lower and upper atmosphere could phase-lock and induce mutual growths in a precipitating atmosphere [Salvekar et al., 1986, Aravequia et al., 1995], Cohen and Boos [Cohen and Boos, 2016] recently found that the necessary criterion for their instability [Charney and Stern, 1962] did not agree with modern meteorological reanalysis products. Rather, monsoonal de-

pressions resemble vertical vortices such as tropical depressions in the Eastern Pacific [Serra et al., 2008, Rydbeck et al., 2016], with cold centers and strong wind anomalies in the lower troposphere [Hunt et al., 2016, Adames and Ming, 2018]. These recent findings suggest that progress in modeling monsoonal depressions can be made by adapting methods from the tropical cyclogenesis community. Based on the near-global configuration of Chapter 5, we could run series of three-dimensional, cloud-permitting simulations in a domain centered around the Equator including planetary rotation and a background MSE gradient, to spin up organized convection into monsoonal depressions. These simulations could test the influence of dynamic and thermodynamic processes that have been hypothesized to play crucial roles in monsoonal depression genesis, including meridional gradients in zonal winds, zonal shear, and the spatial variability of diabatic fluxes and surface friction. Better understanding the conditions under which monsoonal depressions form would improve our ability to forecast them and help identify missing physical processes in operational weather and climate models.

Appendix A

Impact of cloud radiation on the organization of non-rotating convection

A.1 Experimental design

This appendix is a technical report of new results that have been obtained while investigating the physical mechanisms of convective self-aggregation. The long-channel configuration, described in Chapter 4, is used as a numerical laboratory to test the causal effect of different mechanisms on the organization of non-rotating convection, from the cloud-scale (~ 10 km) to the planetary scale ($\sim 10,000$ km). We list 27 of our experiments in Table A.1, informally referred to as a “zoo of convective aggregation” because of their diverse convective characteristics, and describe the new configurations in more detail below. The output of all experiments is available on the MIT Engaging cluster.

Category	#	Characteristics
Surface temperature	7	Fixed surface temperature varied from 280K to 310K in 5K increments
Radiation scheme	7	Radiation scheme switched to RRTM using same surface temperatures
Diabatic fluxes	3	Horizontally uniform radiation and/or surface enthalpy fluxes
Microphysical scheme	2	Microphysical scheme switched to NA5 and double-moment at 300K
Uniform cloud radiation	3	Horizontally uniform radiation from clouds, liquid water only and ice only
Zero cloud radiation	3	Zero radiation from clouds, liquid water only and ice only
No re-evaporation	2	No re-evaporation of rainfall with/without uniform diab. fluxes

Table A.1: List of long-channel experiments available on the MIT Engaging cluster. From left to right: Category, number, characteristics of experiments and useful references when applicable.

- The experiments testing the effect of surface temperature, radiation scheme and horizontally uniform diabatic fluxes are analyzed in Chapter 4.
- We change the microphysical scheme used in SAM from the single-moment scheme of Khairoutdinov et al. [2003] to the “NOSEDAALIQ5” (NA5) set-up of Lopez et al. [2009] and the double-moment scheme of Morrison et al. [2005], that were developed to increase the realism of cloud-radiative effects and cloud microphysical processes, respectively. The differences between these microphysical schemes is extensively described by Lutsko and Cronin [2018] in the context of precipitation efficiency.
- Since cloud radiation is critical to organize convection at large scales (e.g. Beucler and Cronin [2018]), we test the effect of making cloud radiation uniform by horizontally homogenizing the liquid concentration, the ice concentration and the total cloud concentration in the SAM radiation scheme (rad_full.f90).
- Arnold and Putman [2018] tested the effect of making the ice and liquid radiation zero in a limited-area general circulation model: This motivates a second set of three experiments, where we make the liquid concentration, the ice concentration and the total cloud concentration zero in the SAM radiation scheme (rad_full.f90).

- Finally, we test the effect of cold pools by turning off the re-evaporation of precipitation (in `precip_proc.f90`), which leads to strong and stationary aggregation features. These features become even stronger when we make radiation and surface fluxes horizontally uniform.

A.2 Results

In this section, we use the methodology developed in section 4.2 to analyze 12 experiments that exhibit different degrees of aggregation and convective aggregation scales.

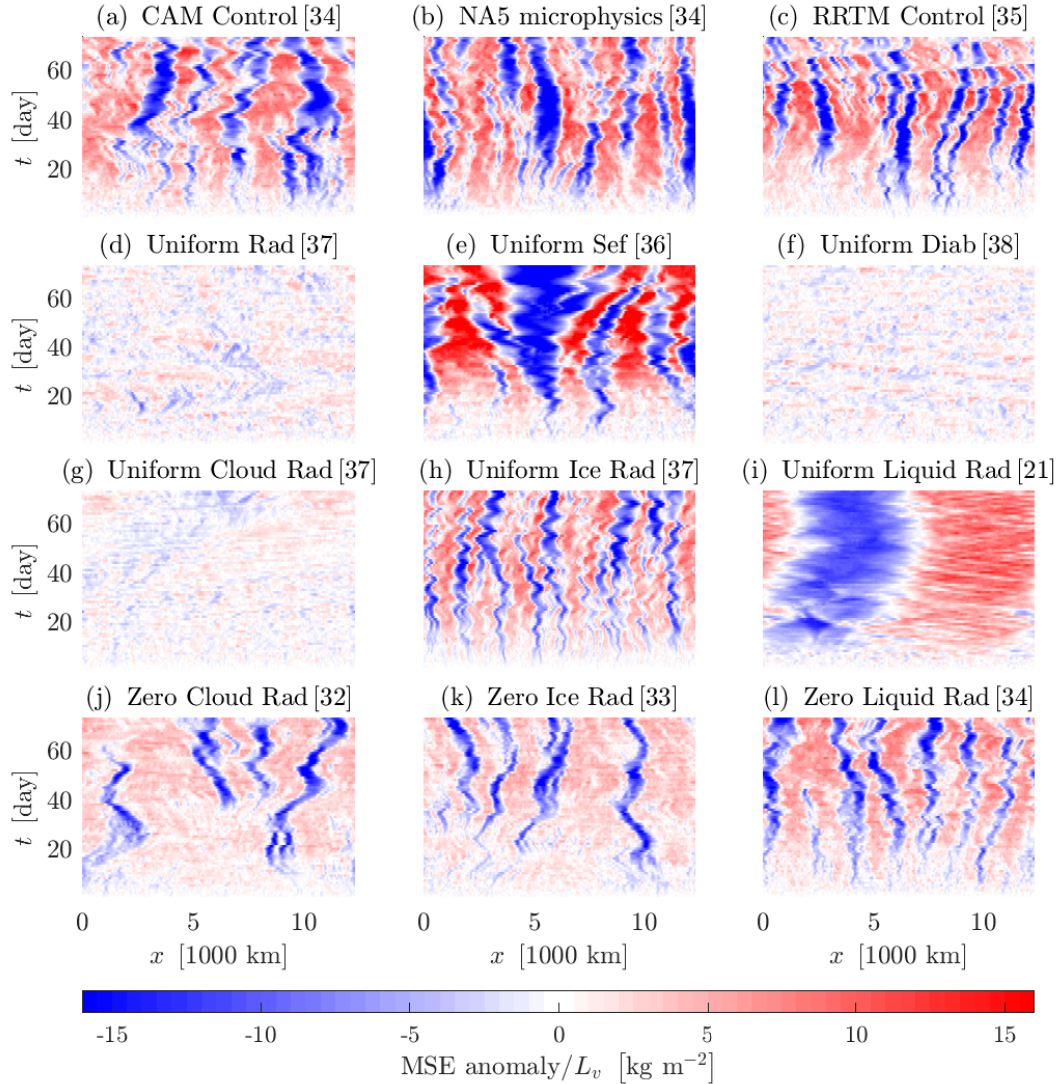


Figure A-1: Hovmoller plots of anomalous moist static energy. The anomaly was taken from the spatial mean moist static energy at each time step, and normalized by the latent heat of vaporization to yield units of kg m^{-2} . The average column water vapor during the last week of each simulation is indicated in the subplot’s titles using square brackets.

Figure A-1 shows the evolution of column moist static energy (MSE) anomalies, averaged over the short direction of the long channel:

- Switching the microphysics scheme from single-moment to NA5 (a to b) slightly increases the MSE variance, while the change is barely noticeable when switch-

ing to the double moment scheme (not shown).

- The dependence of convective aggregation on the radiation scheme (c), and the mechanism denial experiments where diabatic fluxes are made horizontally uniform (d,e,f), are analyzed in Chapter 4.
- If cloud radiation is made uniform, convection does not aggregate (g). In contrast, when ice radiation only is made uniform (h), aggregation aggregates at a smaller scale than the control experiment.
- Interestingly, when we make liquid radiation uniform (i), we recover the “binary” self-aggregation behavior, where a single “blob” occupies the entire domain and the climate dries significantly: the average column water vapor drops by 50% compared to the control experiment! This result challenges the concept of a fixed upper bound for the size of convective cluster, suggested by Arnold and Putman [2018] in the context of a limited-area general circulation model.
- Another surprising aspect of these experiments is the large difference in convective organization between horizontally-uniform and zero cloud radiation (g and j). This difference underlines the importance of the base-state radiative cooling for convective organization, as clear-sky aggregation preferentially occurs in the absence of stationary cloudy radiative fluxes. Similarly, the absence of uniform liquid radiation in (l) prevents ice radiation from cascading the MSE variance at the largest scale (i).

To quantify the input of MSE variance power φ across wavelengths λ by different diabatic fluxes, we integrate equation (4.10) in time between the beginning ($t = 0$) and the end ($t = 75d$) of each simulation. The variance created over the simulation time is the sum of the longwave, shortwave, surface fluxes and advective spectral tendencies $\dot{\varphi}_i$, integrated over the 75 days of the simulation:

$$\underbrace{\varphi(t = 75d) - \varphi(t = 0)}_{\text{Total variance created}} = \underbrace{\int_0^{75d} dt' (\dot{\varphi}_{\text{lw}} + \dot{\varphi}_{\text{sw}} + \dot{\varphi}_{\text{sef}} + \dot{\varphi}_{\text{adv}})(t')}_{\text{Variance input from each diabatic flux}} \quad (\text{A.1})$$

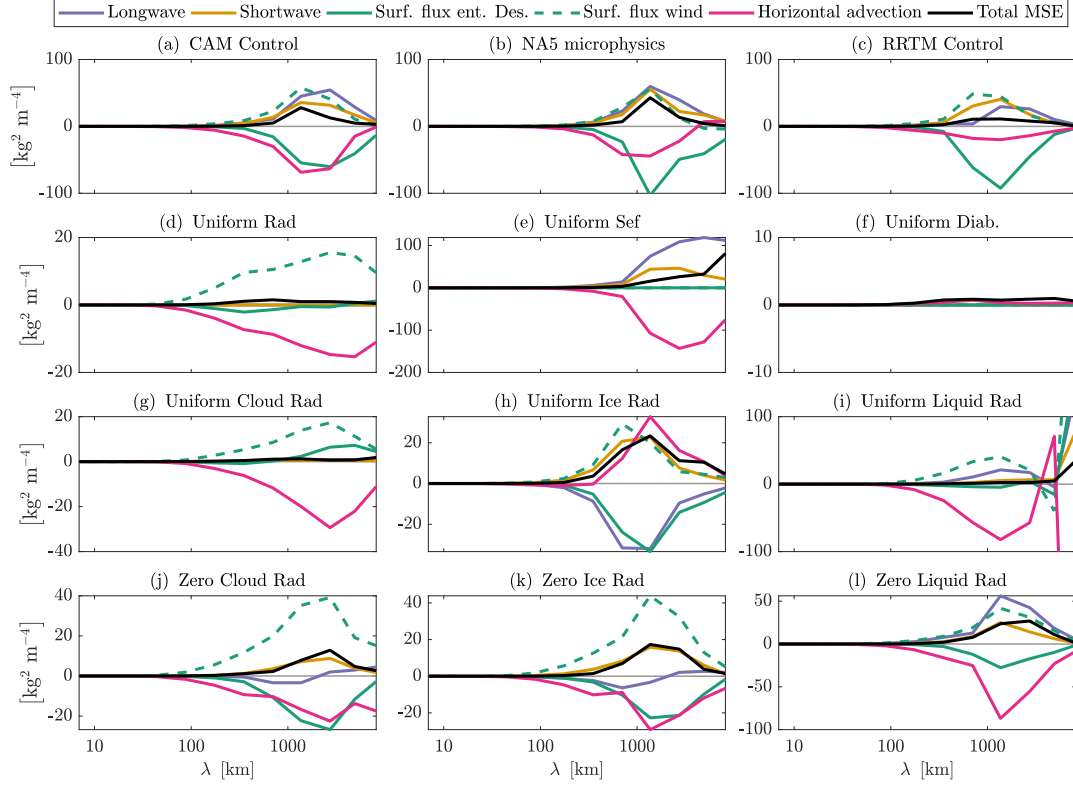


Figure A-2: Normalized variance input from each term of equation A.1 over the 75 days of each simulation. The total variance tendency is obtained by integrating each curve over the logarithmic wavelength scale.

Comparing the spectral MSE budgets between different simulations in Figure A-2 allows to deepen our understanding of the MSE spectral tendencies analyzed in Chapter 4:

- It is mostly the longwave radiative flux from ice clouds that contributes to the longwave aggregating and expansion effects (blue lines in panels i and l). On its own, the clear-sky longwave cooling removes variance at the $\sim 1,000\text{km}$ scale and adds variance at the $\sim 10,000\text{km}$ scale (see blue line in panel j), which can be attributed to the non-monotonic behavior of the clear-sky longwave cooling - column water vapor relation studied in Chapter 2. The longwave cooling from liquid clouds is in the range where cooling increases with column water vapor, leading to a large removal of MSE variance over a broad range of wavelengths.

- The shortwave spectral tendency is less affected by clouds, as most of it is clear-sky shortwave absorption. It can maintain convective aggregation at smaller scales ($\sim 1,000\text{km}$) on its own, as shown by simulations (h) and (j).
- Following section 4.3.4, surface enthalpy fluxes can be separated into two main components with opposite behaviors: a surface wind speed component and an enthalpy disequilibrium component. The enthalpy disequilibrium component acts to remove variance at the MSE anomaly scale: To a good approximation, the variance removal by surface enthalpy fluxes is opposite and proportional to the MSE variance created over the simulation time. In contrast, the surface wind speed component creates variance at smaller scale and can help MSE anomalies develop initially, although this tendency is not large enough to aggregate convection on its own (e.g. simulations d and g).
- Finally, horizontal advection always removes variance, usually at a slightly smaller scale than the MSE anomaly scale. The only exception is the uniform ice radiation simulation, for which longwave cooling removes variance. This suggests that a large part of the horizontal advection of MSE may be driven by low-level gradients in longwave cooling.

Overall, these experiments confirm the potentially large impact of cloud radiation on the hydrological cycle and provide a framework to study questions at the intersection of meteorology and climate, such as the the importance of the thermodynamic environment for the mesoscale convective complexes that form within the moist and dry regions and the effect of microphysical parametrizations on convective organization.

Appendix B

Linear Response of a Full-physics Column Model

B.1 Introduction

The following section takes one step towards the real world by applying the linear response framework of chapter 3 - section 2 to a full-physics column model. Because the column model is calibrated to work on climatological (~ 100 day) rather than convective (~ 3 hours) time scales, both the methodology and the results are complex. The reader may skip this section without missing fundamental aspects of radiative-convective instability.

B.2 Experimental design

We choose to construct the linear response matrix of the MIT single-column model, first described in Renno et al. [1994], because it conserves column moist static energy and its convection scheme (see Emanuel and Zivkovic-Rothman [1999], Emanuel [1991]) includes unsaturated downdrafts, which have not been explicitly parametrized in the toy models of Chapter 3. Its radiation scheme is based off the European Center for Medium Weather Forecasts forecasting system Morcrette [1991], Fouquart and Bonnel [1980]. We run the model with a tropospheric resolution of 25hPa and a

total of 60 vertical levels. It has fully interactive radiation, convection, and water vapor, and we call the radiative and convective routines at every timestep. Although the model produces cloud, we deactivate cloud-radiation interactions to focus on the clear-sky response matrices. We also deactivate the parametrization for convective gustiness, as well as the corresponding Reynolds corrections in temperature and moisture. To avoid abrupt and nonlinear jumps in the deep convective profiles, we relax the level of neutral buoyancy in time, so that it linearly responds to convection with a one-hour lag:

$$\frac{\partial p_{\text{NB}}}{\partial t} = \frac{p_{\text{NB,Emanuel}} - p_{\text{NB}}}{\tau_{\text{NB}}}, \quad (\text{B.1})$$

where $p_{\text{NB,Emanuel}}$ is the level of neutral buoyancy as calculated by the Emanuel convective routine, p_{NB} is the “relaxed” level of neutral buoyancy and $\tau_{\text{NB}} = 1\text{hours}$ is the chosen relaxation timescale. Our experiment consists of 5 steps:

1. We run the model to RCE. The initial conditions are climatological temperature and specific humidity profiles from the tropical Western-Pacific island of Chuuk-Lagoon (Micronesia), and we use a monthly-averaged ozone profile from ERA-Interim reanalysis Dee et al. [2011] (spatially-averaged in the $(2^\circ \times 2^\circ)$ box centered around Chuuk Lagoon, during the month of January 2016). The only other greenhouse gas is carbon dioxide, assumed to be well-mixed, with a constant volume concentration of 400ppmv. We prescribe a fixed surface wind of 5ms^{-1} and a fixed sea surface temperature of 300K. Other relevant parameters for this run are described in Table B.1. The temperature and specific humidity profiles adjust to a unique statistical equilibrium, independent of the initial climatological profile. In this equilibrium, the time-averaged dry static energy and water vapor forcings are zero on timescales longer than 3 days.
2. To capture the statistical nature of RCE, we select 100 snapshots of RCE in time, and perturb each of their water vapor profiles level by level. For each water vapor profile, 38 “moistened” profiles are created by adding 1% to the specific humidity at each level between the top of the subcloud layer and the

level of neutral buoyancy, one level at a time. Similarly, 38 "dried" profiles are produced by removing 1% from the RCE specific humidity at each level.

3. We run the RCE profile and each perturbed profile one time-step forward, with a strict enforcement of the weak temperature gradient approximation. In this framework, the residual heating in the free troposphere is exactly compensated by the large-scale vertical advection. The atmospheric radiation, convection, and radiation are fully interactive. The dry static energy and water vapor forcings are outputted to compute the four components of the linear response: convective moistening, convective heating, longwave heating and shortwave heating.
4. We select 10 linear responses to describe the response of RCE. Because of the extreme sensitivity of local entrainment to water vapor perturbations, the convection scheme often responds nonlinearly, in spite of the smallness of perturbations. For consistency, we only select the linear responses, which produce the same response to within 20% of the Frobenius norm for the +1% and the -1% perturbations. Within the subset of linear responses (approximately half of the total set), we use the Metropolis Monte-Carlo algorithm (Metropolis et al. [1953], generalized by Hastings [1970]) to pick 10 time-steps from the RCE that minimize the residual heating rate at each level (i.e., that give the closest statistical fit to the RCE state).
5. We ensemble-average the 10 linear response matrices. Then, we subtract the non-perturbed run from each perturbed run to isolate the effect of the water vapor perturbation by removing the small drift present in each RCE snapshot.
6. We repeat steps 1-5 for four different fixed sea surface temperatures between 290K and 310K.

Parameter	Value	Units
Auto-conversion threshold	1.1	mg/g
Convective momentum transport coefficient	0.7	
Critical temperature for precipitation	-55.0	°C
Entrainment parameter	1.5	
Evaporation coefficient of rain	0.9	
Evaporation coefficient of snow	0.6	
Fraction of precipitation falling outside the clouds	0.12	
Fractional area of unsaturated downdrafts	0.05	
Gust factor for surface fluxes	5.0	m.s ⁻¹
Length of integration for RCE runs	400.0	day
Pressure fall speed of rain	50.0	Pa.s ⁻¹
Pressure fall speed of snow	5.0	Pa.s ⁻¹
Quasi-equilibrium relaxation coefficient α_{QE}	0.015	kg.m ⁻² .s ⁻¹ .K ⁻¹
Quasi-equilibrium relaxation coefficient DAMP	0.05	
Solar constant	1360	W.m ⁻²
Surface albedo	0.10	
Timestep	180	s

Table B.1: Parameters used in the MIT single-column model

B.3 Results

In this section, we present the linear response matrix and its components. The matrices presented below are ensemble-average responses to a 1% moistening; as the response is linear for small perturbations, the matrices resulting from a 1% drying are nearly indistinguishable. To physically interpret these matrices, we have outputted the sub-components of the convective heating and moistening, following equations 27 and 29 of Emanuel [1991]. Since we are interpreting linear physics, the processes for the 1% drying case are the exact opposite of the processes for the 1% moistening case, presented below.

B.3.1 Radiative-convective equilibrium

The ensemble-averaged RCE profiles are shown in FigureB-1: The specific humidity profile (Figure B-1a) resembles typical tropical moisture profiles (e.g. Figure 2 of [Beucler and Cronin, 2016] or [Ciesielski et al., 2003]), with a surface value of 15.6g/kg and a column-integrated content of 35.7kg.m⁻². The temperature profile

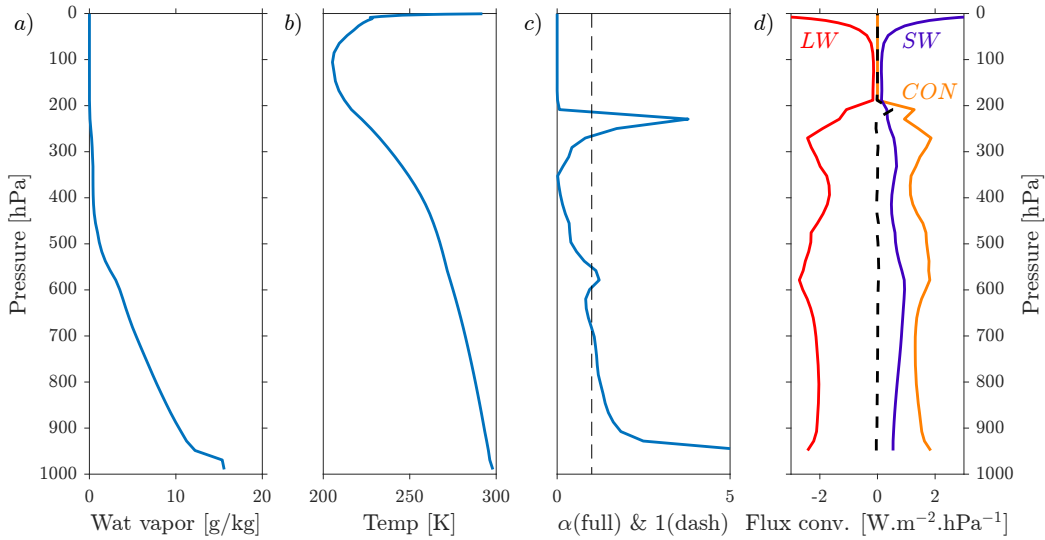


Figure B-1: (a) Specific humidity (in g/kg), (b) HAM (c) temperature (in K) and (d) flux convergence (in $\text{W}\cdot\text{m}^{-2}\cdot\text{hPa}^{-1}$) profiles. In panel (d), the longwave radiative heating is red, the shortwave radiative heating blue, the convective heating orange, and the total convergence flux is represented with a dotted black line. The profiles are ensemble averages of the 10-members chosen to represent radiative-convective equilibrium. The surface temperature is fixed to 300K and cloud-radiation interactions are deactivated.

(Figure B-1b) is moist-adiabatic in the lower and mid-troposphere (below 400hPa), with an average tropospheric lapse rate of 5.8K/km and a tropopause pressure of 100hPa. The stratosphere in the top 100hPa of the model includes strong shortwave heating associated with the prescribed ozone profile. The atmosphere is in radiative-convective equilibrium from the surface (1000hPa) to the level of neutral buoyancy (approximately 200hPa), as the convective heating and shortwave heating perfectly compensate the longwave cooling at each level. From the level of neutral buoyancy to the top of the model (0hPa), the atmosphere is in radiative equilibrium: the shortwave heating balances the longwave heating, and the convective heating is zero.

B.3.2 Convective response

The convective response (Figure B-2) is defined as the sum of the convective moistening (M_{LH}) and the convective heating (M_{DSE}) responses (see Figure B-3 for the decomposition). Water vapor perturbations at a given level are diffused to the two

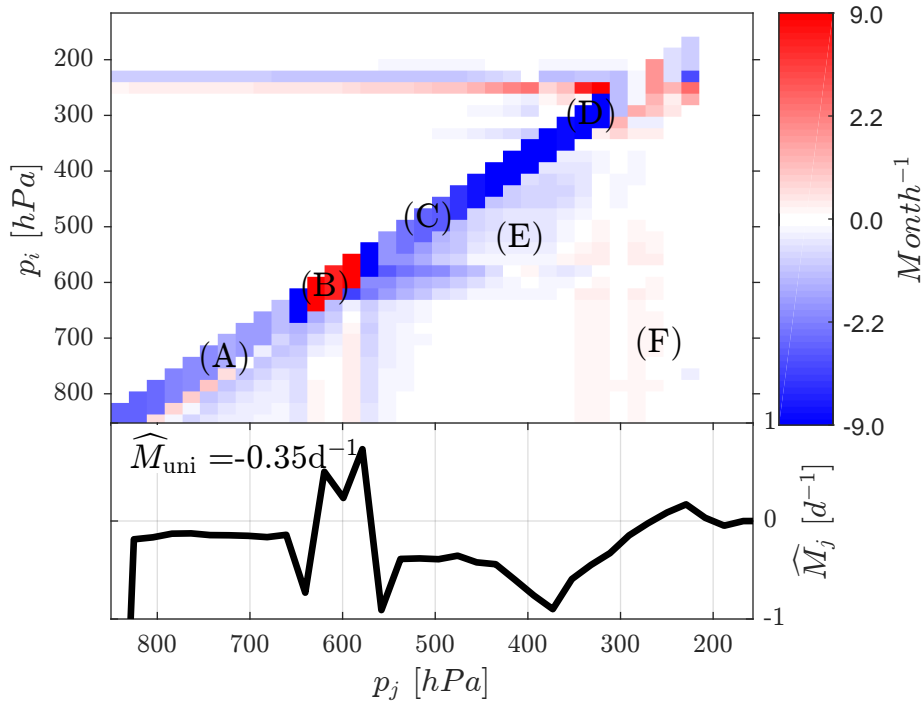


Figure B-2: (Top) Convective component of the linear response matrix ($M_{LH} + M_{DSE}$), in units month^{-1} . (Bottom) Vertically-integrated growth rates (in units day^{-1}) versus perturbation level (in hPa).

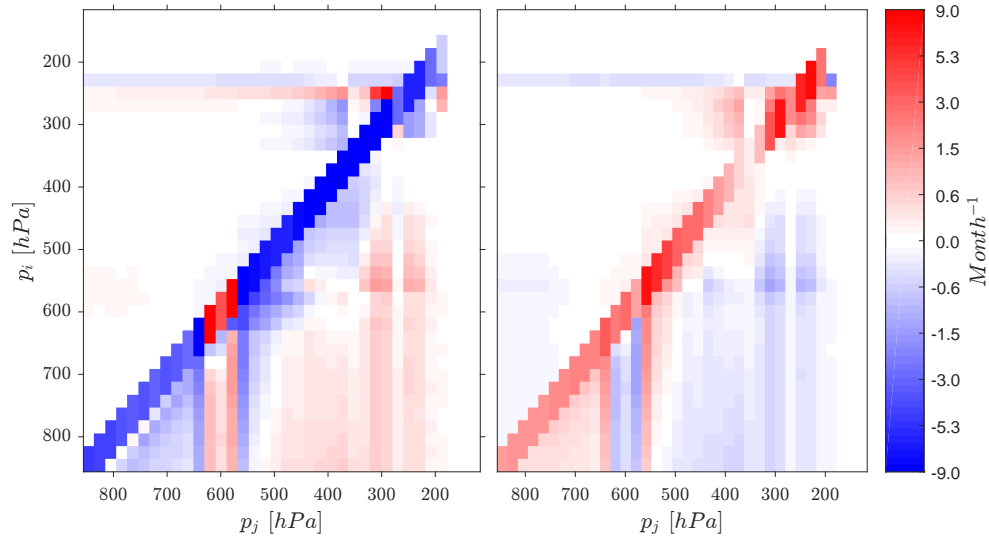


Figure B-3: (a) Convective moistening (M_{LH}) and (b) Convective heating (M_{DSE}) linear response matrices, in units month^{-1} .

adjacent levels on a very short (~ 4 hours) time-scale. Therefore, we average each growth rate on the diagonal with the two neighboring growth rates, to focus on effects other than local mixing. The different regions of the matrix exhibit different physical behaviors. Overall, the main effect of perturbing water vapor is to change the partial re-evaporation rate E (in s^{-1}) of cloudy water into the clear-sky environment. Moistening the environment decreases the humidity difference between the cloudy and clear-sky areas, and thus decreases the re-evaporation rate (in mathematical terms: $\partial E/\partial q' < 0$). According to the last equation of chapter 3 - section 2.1, the water vapor growth rate associated to a change in re-evaporation is:

$$\frac{g}{L_v} \left(\underbrace{\frac{\partial^2 \mathcal{F}_{\text{LH}}}{\partial p \partial q'}}_{\text{Moistening}} + \alpha \underbrace{\frac{\partial^2 \mathcal{F}_{\text{DSE}}}{\partial p \partial q'}}_{\text{Latent heating}} \right)_{\text{RCE}} = (1 - \alpha) \left(\frac{\partial E}{\partial q'} \right)_{\text{RCE}}, \quad (\text{B.2})$$

where α is the HAM. According to equation B.2, there are three possible situations:

1. $\alpha < 1$: The drying effect of decreasing re-evaporation overcomes the heating effect, leading to a damping of water vapor perturbations.
2. $\alpha = 1$: The drying effect of decreasing re-evaporation perfectly compensates the heating effect, consistent with zero change in the local moist static energy.
3. $\alpha > 1$: The heating effect of decreasing re-evaporation overcomes the drying effect, leading to an amplification of water vapor perturbations.

The leading physical mechanisms of each region are identified by breaking down the convective heating and moistening into their sub-components, following equations 27 and 29 of Emanuel [1991]:

(A) The local lower tropospheric response exhibits mildly positive growth rates, as $\alpha > 1$. The re-evaporation effect is partially compensated by a decrease in water vapor entrainment.

(B) We see strong positive growth rates for the local response at 600hPa, where HAM peaks above one. The re-evaporation effect adds to the moistening effect of the unsaturated downdrafts, which are locally damped by the moisture perturbation.

(C) In the upper troposphere, the local response is a damping of water vapor perturbations, as $\alpha < 1$. Additionally, the perturbation advection of water vapor by in-cloud updrafts dries the atmosphere more than it brings dry static energy in to moisten it (since $\alpha < 1$).

(D) For this particular sounding, HAM peaks around 250hPa and exceeds 1, leading to a strongly positive growth rate.

(E) The effect of mid-tropospheric perturbations is to dry the lower-troposphere, through an increase in the intensity of unsaturated downdraft amplification and an increase in the advection of moisture by in-cloud updrafts.

(F) The effect of upper tropospheric perturbations is to slightly moisten the lower troposphere through a small decrease in re-evaporation rates ($\alpha > 1$).

The general characteristics of the response are insensitive to the entrainment parameter in the Emanuel scheme (not shown): Although the value of the convective growth rates depends weakly on the entrainment parameter, the physical mechanisms of the linear response are qualitatively unchanged.

B.3.3 Radiative response

The radiative response (Figure B-4) is defined as the sum of the longwave cooling (M_{LW}) and the shortwave heating (M_{SW}) responses (see Figure B-5 for the decomposition). The physical mechanisms of this response can be separated in four components, all dominated by the longwave effect:

(A) A strong local longwave cooling: Adding water vapor locally increases the emissivity of the atmospheric layer, making it cool to space faster.

(B) A significant indirect longwave heating effect: The levels below the moist perturbation emit less longwave radiation to space, resulting in a net heating. If integrated in the vertical, this remote longwave heating effect overcomes the local cooling effect, and the reader is referred to [Beucler and Cronin, 2016] for more details on this positive feedback.

(C) This indirect longwave heating effect is largest in the upper troposphere (above 330hPa). In this part of the atmosphere, the HAM has a large peak that exceeds

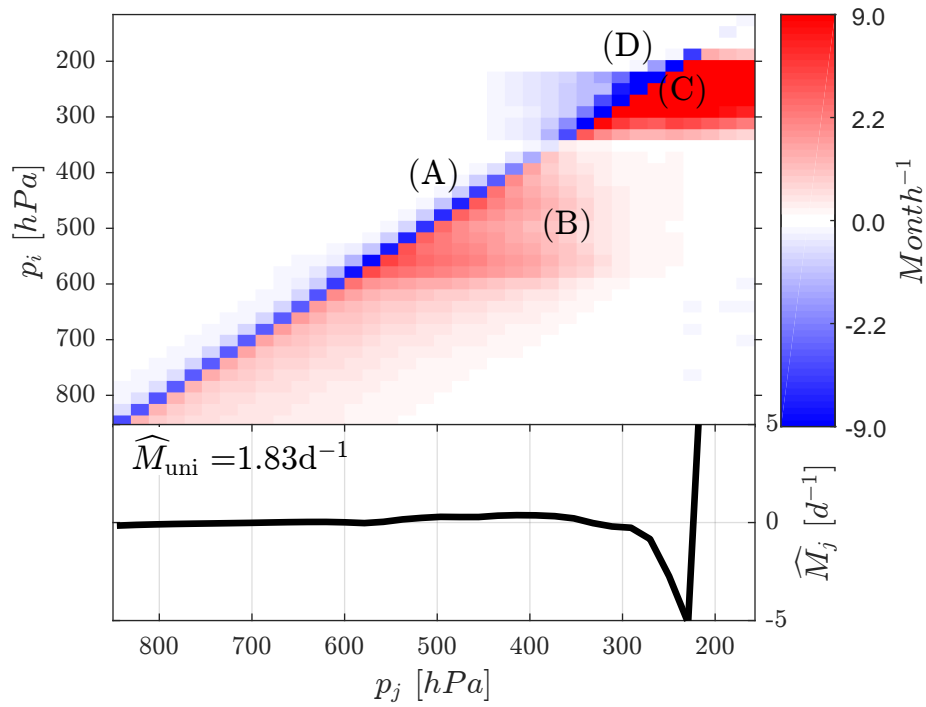


Figure B-4: (Top) Radiative component of the linear response matrix ($M_{\text{LW}} + M_{\text{SW}}$), in units month^{-1} . (Bottom) Column-integrated growth rates (in units day^{-1}) versus perturbation level (in hPa). Letters indicate effects that are described in the text.

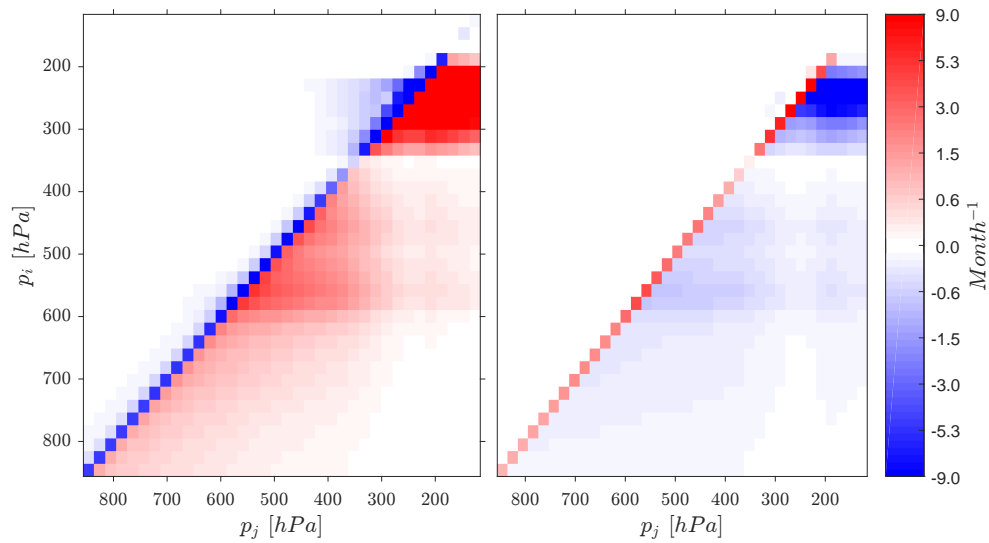


Figure B-5: (a) Longwave (M_{LW}) and (b) Shortwave (M_{SW}) linear response functions, in units month^{-1} .

1, which proportionally increases the radiative growth rates. Furthermore, the RCE specific humidity is so small (smaller than 3g/kg) that even the most absorbing bands of the longwave spectrum are unsaturated. Small moist perturbations will thus increase the optical depth by a greater amount in these dry regions.

(D) The effect of radiative cooling is also amplified in the upper troposphere, including the levels above the moist perturbation, which receive less longwave radiation from the surface.

The shortwave heating acts in the opposite way, which attenuates all of the previous effects (A-D) by a typical factor of 1/3. The column-integrated growth rate is close to zero, except in the upper troposphere, where the remote longwave heating effect can lead to column-integrated growth rates over 1day^{-1} .

B.3.4 Full linear response

The total linear response matrix in the clear-sky case is obtained by summing each of its components. We summarize below the physics of its most important features:

(A) Lower tropospheric perturbations are locally damped through radiative cooling, which dominates over latent heating.

(B) Around 600hPa, the peak in HAM is strong enough for the convective heating to dominate over radiative cooling.

(C) Mid and upper tropospheric perturbations are locally damped through a combination of radiative cooling and convective drying.

(D) Radiative heating effects dominate over the drying effects of downdrafts, and mid to upper tropospheric perturbations moisten the mid-troposphere.

(E) Right below the tropopause, where HAM peaks, strong radiative and convective heating add up and lead to the largest growth rates .

From the appearance of the full linear response and the column-integrated growth rate, we can make several conclusions about the evolution of a small water vapor perturbation for short times. The upper-left part of the matrix is white and blue, corresponding to a damping of the water vapor field above the perturbation level. In contrast, most of the bottom-right part of the matrix is red, corresponding to an am-

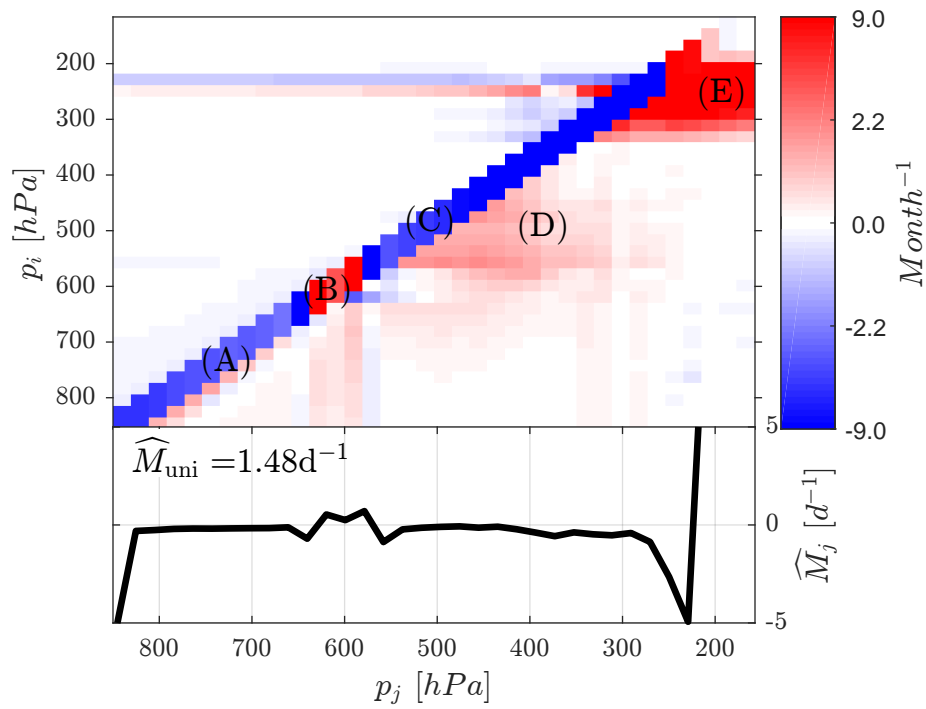


Figure B-6: (Top) Full linear response matrix (M), in units month^{-1} . (Bottom) Column-integrated growth rates (in units day^{-1}) versus perturbation level (in hPa).

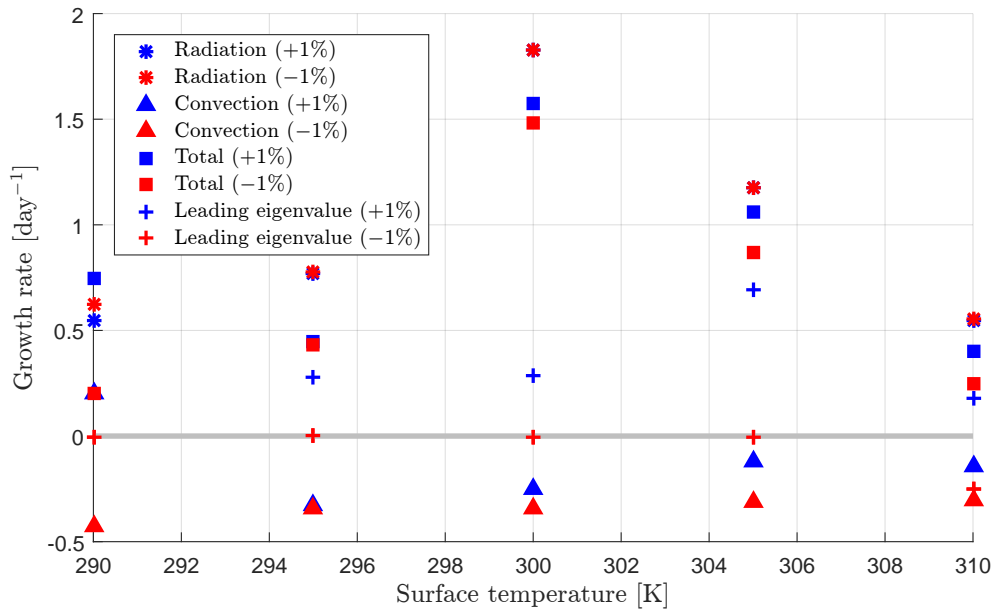


Figure B-7: Growth rate of a uniform water vapor perturbation (in day^{-1}) versus sea surface temperature (in K) for +1% (blue) and -1% (red) perturbations. The total growth rate (square) is decomposed into its radiative (star) and convective (triangle) components.

plification of the water vapor field below the perturbation. Therefore, we expect most perturbations to shift downwards in time as a result of their interaction with clear-sky radiation and convection. There are two regions where water vapor perturbations can potentially grow, with a uniform perturbation growing at the approximate rate $\widehat{M}_{\text{uni}} \approx 1\text{day}^{-1}$: Lower tropospheric perturbations can grow locally through their interaction with convection, while upper tropospheric perturbations can lead to remote growth below the perturbation level, mostly through their interaction with radiation.

Bibliography

- Abbot, D. S. (2014): Resolved snowball earth clouds. *Journal of Climate*, 27, 4391-4402, doi:10.1175/JCLI-D-13-00738.1.
- Adames, A.F. and D. Kim (2016): The MJO as a Dispersive, Convectively Coupled Moisture Wave: Theory and Observations. *Journal of the Atmospheric Sciences*, 73, 913-941, doi:10.1175/JAS-D-15-0170.1.
- Adames, A. F. and Y. Ming. (2018): Moisture and moist static energy budgets of South Asian monsoon low pressure systems in GFDL AM4. *Journal of the Atmospheric Sciences*, 75, 6, 2107–2123, doi:10.1175/JAS-D-17-0309.1.
- Adler, R. F., G. J. Huffman, A. Chang, R. Ferraro, P. Xie, J. Janowiak, B. Rudolf, U. Schneider, S. Curtis, D. Bolvin, A. Gruber, J. Susskind, P. Arkin, and E. Nelkin. (2003): The Version-2 Global Precipitation Climatology Project (GPCP) Monthly Precipitation Analysis (1979-Present). *Journal of Hydrometeorology*, 4(6):0, 1147-1167, doi:10.1175/1525-7541(2003)004<1147:TVGPCP>2.0.CO;2.
- Allan, R. P. and B. Soden (2008): Atmospheric warming and the amplification of precipitation extremes. *Science*, 321(5895), 1481-4, doi:10.1126/science.1160787.
- Arakawa, A. and W. H. Schubert (1974): Interaction of a Cumulus Cloud Ensemble with the Large-Scale Environment, Part I. *Journal of the Atmospheric Sciences*, doi:10.1175/1520-0469(1974)031<0674:IOACCE>2.0.CO;2.
- Aravequia, J. A., V. B. Rao, and J. P. Bonatti. (1995): The role of moist baroclinic instability in the Growth and Structure of Monsoon Depressions. *Journal of the*

Atmospheric Sciences, 52 (24): 4393–4409, doi:10.1175/1520-0469(1995)052<4393:TROMBI>2.0.CO;2.

Armstrong, B. H. (1968): Theory of the diffusivity factor for atmospheric radiation. *Journal of Quantitative Spectroscopy and Radiative Transfer*, 8, 1577-1599, doi: 10.1016/0022-4073(68)90052-6.

Arnold, N. (2015): Convective self-aggregation and the Madden-Julian oscillation, URL: <http://kiwi.atmos.colostate.edu/cmmmap/research/docs/aug15/talknarnold.pdf>.

Arnold, N. and W. Putman (2018): Non-rotating convective self-aggregation in a limited area AGCM. *Journal of Advances in Modeling Earth Systems*, 10.4, 1029-1046.

Arnold, N. P., and D. A. Randall (2015): Global-scale convective aggregation: Implications for the Madden-Julian Oscillation. *Journal of Advances in Modeling Earth Systems*, 7, 1499-1518, doi:10.1002/2015MS000498.

Bauer P. and P. Schluessel: Rainfall, total water, ice water, and water vapor over sea from polarized microwave simulations and Special Sensor Microwave/Imager data. *Journal of Geophysical Research*, 98(D11), 20737, doi:10.1029/93JD01577.

Betts, A. K., and M. J. Miller (1986): A new convective adjustment scheme. Part II: Single column tests using GATE wave, BOMEX, ATEX and arctic air-mass data sets. *Quarterly Journal of the Royal Meteorological Society*, 112(473), 693-709, doi: 10.1002/qj.49711247308.

Betts, A. K., and M. J. Miller (1993): The Betts-Miller Scheme, pp.107–121, *American Meteorological Society*, Boston, MA, doi:10.1007/978-1-935704-13-3_9.

Beucler, T., and T. W. Cronin (2016): Moisture-radiative cooling instability. *Journal of Advances in Modeling Earth Systems*, doi:10.1002/2016MS000763.

- Beucler, T. and T. W. Cronin (2018): A Budget for the Size of Convective Self-aggregation. *Quarterly Journal of the Royal Meteorological Society*, 2018.
- Beucler, T. and Emanuel K. (2016): Instabilities of Radiative Convective Equilibrium with an Interactive Surface. *Extended abstract for the American Meteorological Society 32nd Conference on Hurricanes and Tropical Meteorology*. URL: <https://ams.confex.com/ams/32Hurr/webprogram/Paper293918.html>
- Bevis, M., S. Businger, T. A. Herring, C. Rocken, R. A. Anthes, and R. H. Ware: GPS meteorology: Remote sensing of atmospheric water vapor using the global positioning system. *Journal of Geophysical Research*, 97(D14), 15787, doi:10.1029/92JD01517.
- Bjerknes (1938): Saturated-adiabatic ascent of air. (2), 325-330.
- Bolton, D. (1980): The Computation of Equivalent Potential Temperature. *Monthly Weather Review*, 108(7), 1046-1053, doi:10.1175/1520-0493(1980)108<1046:TCOEPT>2.0.CO;2.
- Bony, S., and Emanuel, K. A. (2001): A Parameterization of the Cloudiness Associated with Cumulus Convection; Evaluation Using TOGA COARE Data. *Journal of the Atmospheric Sciences*, 58(21), 3158-3183, doi:10.1175/1520-0469(2001)058<3158:APOTCA>2.0.CO;2.
- Bony, S., B. Stevens, D. Coppin, T. Becker, K. A. Reed, A. Voigt, and B. Medeiros (2016): Thermodynamic control of anvil cloud amount, *Proceedings of the National Academy of Sciences*, 113(32), 8927-8932, doi:10.1073/pnas.1601472113.
- Bony, S., Stevens, B., Frierson, D. M. W., Jakob, C., Kageyama, M., Pincus, R. and M. J. Webb (2015): Clouds, circulation and climate sensitivity. *Nature Geoscience*, 8(4), 261-268, doi:10.1038/ngeo2398.
- Bretherton, C. S., P. N. Blossey and M. Khairoutdinov (2005): An Energy-Balance Analysis of Deep Convective Self-Aggregation above Uniform SST. *Journal of the Atmospheric Sciences*, 62(12), 4273-4292, doi:10.1175/JAS3614.1.

- Bretherton, C. S. and S. Chen (2000): Self-aggregation and large-scale control of tropical deep convection: A modeling study. *Journal of the Atmospheric Sciences*, 57, 1797-1816, doi:10.1175/1520-0469(2000)057<1797:SAALSC>2.0.CO;2.
- Bretherton, C. S. and M. F. Khairoutdinov (2015): Convective self-aggregation feedbacks in near-global cloud-resolving simulations of an aquaplanet. *Journal of Advances in Modeling Earth Systems*, 07, doi:10.1002/2015MS000499.
- Bretherton, C. S., M.E. Peters, and L. E. Back (2004): Relationships between water vapor path and precipitation over the tropical oceans. *Journal of Climate*, 17(7), 1517-1528, doi:10.1175/1520-0442(2004)017<1517:RBWVPA>2.0.CO;2.
- Bryan, G. H. and J. M. Fritsch (2002): A Benchmark Simulation for Moist Non-hydrostatic Numerical Models. *Monthly Weather Review*, 130(12), 2917-2928, doi:10.1175/1520-0493(2002)130<2917:ABSFMN>2.0.CO;2.
- Charney J. G. and M. E. Stern (1962): On the Stability of Internal Baroclinic Jets in a Rotating Atmosphere. *Journal of the Atmospheric Sciences*, 19(2), 159-172, doi:10.1175/1520-0469(1962)019<0159:OTSOIB>2.0.CO;2.
- Chikira, M. (2014): Eastward-Propagating Intraseasonal Oscillation Represented by Chikira Sugiyama Cumulus Parameterization. Part II: Understanding Moisture Variation under Weak Temperature Gradient Balance. *Journal of the Atmospheric Sciences*, 71(2), 615-639, doi:10.1175/JAS-D-13-038.1.
- Ciesielski, P. E., R. H. Johnson, P. T. Haertel, and J. Wang (2003): Corrected TOGA COARE sounding humidity data: Impact on diagnosed properties of convection and climate over the warm pool, *Journal of Climate*, 16(14), 2370-2384, doi:10.1175/2790.1.
- Cohen, N. Y. and W. R. Boos (2016): Perspectives on Moist Baroclinic Instability: Implications for the Growth of Monsoon Depressions. *Journal of the Atmospheric Sciences*, 73(4), 1767-1788, doi:10.1175/JAS-D-15-0254.1.

- Collins, W.D., C.M. Bitz, M.L. Blackmon, G.B. Bonan, C.S. Bretherton, J.A. Carton, P. Chang, S.C. Doney, J.J. Hack, T.B. Henderson, J.T. Kiehl, W.G. Large, D.S. McKenna, B.D. Santer, and R.D. Smith, (2006): The Community Climate System Model Version 3 (CCSM3), *Journal of Climate*, 19, 2122-2143, doi:10.1175/JCLI3761.1.
- Chandrasekhar, S (1960): *Radiative transfer*. Dover Publications, 1960, 413 pp.
- Coppin, D., and S. Bony (2015): Physical mechanisms controlling the initiation of convective self-aggregation in a general circulation model. *Journal of Advances in Modeling Earth Systems*, doi:10.1002/2015MS000571.
- Coppin, D., and S. Bony (2017): Internal variability in a coupled General Circulation Model in Radiative-Convective Equilibrium. *Geophysical Research Letters*, doi:10.1002/2017GL073658.
- Cormier, J. G., J. T. Hodges and J. R. Drummond (2005): Infrared water vapor continuum absorption at atmospheric temperatures. *The Journal of Chemical Physics*, 122, 114309, doi:10.1063/1.1862623.
- Cronin, T. W. (2014): On the Choice of Average Solar Zenith Angle. *Journal of the Atmospheric Sciences*, 71(8), 2994-3003, doi:10.1175/JAS-D-13-0392.1.
- Cronin, T. W., and K. A. Emanuel (2013): The climate time scale in the approach to radiative-convective equilibrium. *Journal of Advances in Modeling Earth Systems*, 5(4), 843-849, doi:10.1002/jame.20049.
- Cronin, T. W., and A. A. Wing (2017): Clouds, Circulation, and Climate Sensitivity in a Radiative-Convective Equilibrium Channel Model. *Journal of Advances in Modeling Earth Systems*, 9(8), 2883-2905, doi:10.1002/2017MS001111.
- Crueger, T., M. A. Giorgetta, R. Brokopf, M. Esch, S. Fiedler, C. Hohenegger, L. Kornblueh, T. Mauritsen, C. Nam, A. K. Naumann, K. Peters, S. Rast, E. Roeckner, M. Sakradzija, H. Schmidt, J. Vial, R. Vogel, and B. Stevens (2018): ICON-A, the

- atmosphere component of the ICON Earth System Model. Part II: Model evaluation. *Journal of Advances in Modeling Earth Systems*, doi:10.1029/2017MS001233.
- Daniels, T. S., G. Tsoucalas, M. Anderson, W. Moninger, and R. Mamrosh (2002): Tropospheric Airborne Meteorological Data Reporting (TAMDAR) sensor development. URL: <https://ntrs.nasa.gov/search.jsp?R=20040161135>.
- Dee, D. P., S. M. Uppala, A. J. Simmons, P. Berrisford, P. Poli, S. Kobayashi, U. Andrae, M. A. Balmaseda, G. Balsamo, P. Bauer, P. Bechtold, A. C. M. Beljaars, L. van de Berg, J. Bidlot, N. Bormann, C. Delsol, R. Dragani, M. Fuentes, A. J. Geer, L. Haimberger, S. B. Healy, H. Hersbach, E. V. Holm, L. Isaksen, P. Kollberg, M. Kohler, M. Matricardi, A. P. McNally, B. M. Monge-Sanz, J. J. Morcrette, B. K. Park, C. Peubey, P. de Rosnay, C. Tavolato, J. N. Thopaut, and F. Vitart (2011): The ERA-Interim reanalysis: Configuration and performance of the data assimilation system, *Quarterly Journal of the Royal Meteorological Society*, 137(656), 553-597, doi:10.1002/qj.828.
- Divakarla, M. G., C. D. Barnet, M. D. Goldberg, L. M. McMillin, E. Maddy, W. Wolf, L. Zhou, and X. Liu (2006): Validation of Atmospheric Infrared Sounder temperature and water vapor retrievals with matched radiosonde measurements and forecasts. *Journal of Geophysical Research Atmospheres*, 111(9), D09S15, doi:10.1029/2005JD006116.
- Dunn, P. (2005): *Measurement and Data Analysis for Engineering and Science*, CRC Press, Taylor and Francis Group, Boca Raton FL.
- Edelman, A., A. Gelding, E. Konovalov, R. McComiskie, A. Penny, N. Roberts, S. Templeman, D. Trewin, M. Ziemicki, and B. Trewin (2014): *State of the tropics 2014 report*, James Cook University.
- Emanuel, K. A. (1987): An Air-Sea Interaction Model of Intraseasonal Oscillations in the Tropics. *Journal of the Atmospheric Sciences*, doi:10.1175/1520-0469(1987)044<2324:AASIMO>2.0.CO;2.

- Emanuel, K. A. (1991): A Scheme for Representing Cumulus Convection in Large-Scale Models. *Journal of the Atmospheric Sciences*, doi:10.1175/1520-0469(1991)048<2313:ASFRCC>2.0.CO;2.
- Emanuel, K. A. (1994): *Atmospheric convection*. Oxford University Press. 580pp.
- Emanuel, K. A. (1995): The Behavior of a Simple Hurricane Model Using a Convective Scheme Based on Subcloud-Layer Entropy Equilibrium. *Journal of the Atmospheric Sciences*, doi:10.1175/1520-0469(1995)052<3960:TBOASH>2.0.CO;2.
- Emanuel, K. A., A. A. Wing, and E. M. Vincent (2014): Radiative-convective instability. *Journal of Advances in Modeling Earth Systems*, 6, 75-90, doi:10.1002/2013MS000270.
- Emanuel, K. A., and M. Zivkovic-Rothman (1999): Development and Evaluation of a Convection Scheme for Use in Climate Models. *Journal of the Atmospheric Sciences*, 56(11), 1766-1782, doi:10.1175/1520-0469(1999)056<1766:DAEOAC>2.0.CO;2.
- Feldl, N., D. M. W. Frierson, and G. H. Roe (2014): The influence of regional feedbacks on circulation sensitivity. *Geophysical Research Letters*, 41(6), 2212-2220, doi:10.1002/2014GL059336.
- Frigo, M. and Johnson, S. G. (2005): The design and implementation of FFTW3. *Proceedings of the IEEE*, 93, 216-231, URL: <http://www.fftw.org/fftw-paper-ieee.pdf>.
- Folkins, I., and C. Braun (2003): Tropical rainfall and boundary layer moist entropy. *Journal of Climate*, 16(11), 1807-1820, doi:10.1175/1520-0442(2003)016<1807:TRABLM>2.0.CO;2.
- Fouquart, Y., and B. Bonnel (1980): Computations of solar heating of the earth's atmosphere - A new parameterization. *Beitraege zur Physik der Atmosphaere*, 53, 35-62.

- Frierson, D. M. W. (2007): The Dynamics of Idealized Convection Schemes and Their Effect on the Zonally Averaged Tropical Circulation. *Journal of the Atmospheric Sciences*, 64(6), 1959-1976, doi:10.1175/JAS3935.1.
- Fu, L., E. J. Christensen, C. A. Yamarone, M. Lefebvre, Y. Menard, M. Dorrer, and P. Escudier (1994): TOPEX/POSEIDON mission overview. *Journal of Geophysical Research*, 99(C12), 24369, doi:10.1029/94JC01761.
- Gentine, P., M. Pritchard, S. Rasp, G. Reinaudi, and G. Yacalis (2018): Could Machine Learning Break the Convection Parameterization Deadlock? *Geophysical Research Letters*, 45(11), 5742-5751, doi:10.1029/2018GL078202.
- Giorgetta, M. A., R. Brokopf, T. Crueger, M. Esch, S. Fiedler, J. Helmert, C. Hohenegger, L. Kornblueh, M. Kohler, E. Manzini, T. Mauritsen, C. Nam, T. Raddatz, S. Rast, D. Reinert, M. Sakradzija, H. Schmidt, R. Schneck, R. Schnur, L. Silvers, H. Wan, G. Zangl, and B. Stevens (2018): ICON-A, the atmosphere component of the ICON Earth System Model. Part I: Model Description. *Journal of Advances in Modeling Earth Systems*, doi:10.1029/2017MS001242.
- Godbole, R. V. (1977): The composite structure of the monsoon depression. *Tellus A*, 29(1), 25-40, doi:10.3402/tellusa.v29i1.11327.
- Grabowski, W. W., and M. W. Moncrieff (2001): Large-scale organization of tropical convection in two-dimensional explicit numerical simulations. *Quarterly Journal of the Royal Meteorological Society*, 127(585), 445-468, doi:10.1256/qj.01.104.
- Grabowski, W. W., and M. W. Moncrieff (2004): Moisture-convection feedback in the tropics. *Quarterly Journal of the Royal Meteorological Society*, 130(604), 3081-3104, doi:10.1256/qj.03.135.
- Grody, N., J. Zhao, R. Ferraro, F. Weng, and R. Boers (2001): Determination of precipitable water and cloud liquid water over oceans from the NOAA 15 advanced microwave sounding unit. *Journal of Geophysical Research Atmospheres*, 106(D3), 2943-2953, doi:10.1029/2000JD900616.

- Hannah, W. M., and E. D. Maloney (2011): The role of moisture-convection feedbacks in simulating the Madden-Julian oscillation. *Journal of Climate*, 24(11), 2754-2770, doi:10.1175/2011JCLI3803.1.
- Hardinger, S. (2018): Illustrated Glossary of Organic Chemistry, URL: <http://www.chem.ucla.edu/~harding/IGOC/IGOC.html>.
- Harrop, B. E., and D. L. Hartmann (2015): The relationship between atmospheric convective radiative effect and net energy transport in the tropical warm pool. *Journal of Climate*, 28(21), 8620-8633, doi:10.1175/JCLI-D-15-0151.1.
- Hartman, P. (1960): A lemma in the theory of structural stability of differential equations, *Proceedings of the American Mathematical Society*, 11(4), 610-610, doi:10.1090/S0002-9939-1960-0121542-7.
- Hartmann, D. L., and K. Larson (2002): An important constraint on tropical cloud - climate feedback. *Geophysical Research Letters*, 29(20), 12-1-12-4, doi:10.1029/2002GL015835.
- Hastings, W. K. (1970): Monte carlo sampling methods using Markov chains and their applications. *Biometrika*, 57(1), 97-109, doi:10.1093/biomet/57.1.97.
- Held, I. M., R. S. Hemler and V. Ramaswamy (1993): Radiative-Convective Equilibrium with Explicit Two-Dimensional Moist Convection. *Journal of the Atmospheric Sciences*, doi:10.1175/1520-0469(1993)050<3909:RCEWET>2.0.CO;2.
- Held, I. M., M. Zhao and B. Wyman (2007): Dynamic Radiative-Convective Equilibria Using GCM Column Physics. *Journal of the Atmospheric Sciences*, 64, 228-238, URL: <http://journals.ametsoc.org/doi/abs/10.1175/JAS3825.11>.
- Hennermann K. and Guillory A. (2018): *ERA5 data documentation*, URL: <https://www.ecmwf.int/en/forecasts/datasets/archive-datasets/reanalysis-datasets/era5>.

- Herman, M. J., and Z. Kuang (2013): Linear response functions of two convective parameterization schemes. *Journal of Advances in Modeling Earth Systems*, 5(3), 510-541, doi:10.1002/jame.20037.
- Hill, K. A. and G. M. Lackmann: Influence of Environmental Humidity on Tropical Cyclone Size. *Monthly Weather Review*, 137(10), 3294-3315, doi:10.1175/2009MWR2679.1.
- Hohenegger, C. and Stevens, B. (2018): The role of the permanent wilting point in controlling the spatial distribution of precipitation. *Proceedings of the National Academy of Sciences*, 115, 5692-5697.
- Holloway, C. E. and J. D. Neelin (2007): The Convective Cold Top and Quasi Equilibrium. *Journal of the Atmospheric Sciences*, 64, 1467-1487, doi:10.1175/JAS3907.1.
- Holloway, C. E. and J. D. Neelin (2009): Moisture Vertical Structure, Column Water Vapor, and Tropical Deep Convection. *Journal of the Atmospheric Sciences*, 66(6), 1665-1683, doi:10.1175/2008JAS2806.1.
- Holloway, C. E. (2017): Convective aggregation in realistic convective-scale simulations. *Journal of Advances in Modeling Earth Systems*, 9(2), 1450-1472, doi:10.1002/2017MS000980.
- Holloway, C. E., A. A. Wing, S. Bony, C. Muller, H. Masunaga, T. S. L'Ecuyer, D. D. Turner, and P. Zuidema (2017): Observing Convective Aggregation. URL: <http://link.springer.com/10.1007/s10712-017-9419-1>.
- Holloway, C. E., and Woolnough, S. J. (2016): The sensitivity of convective aggregation to diabatic processes in idealized radiative-convective equilibrium simulations. *Journal of Advances in Modeling Earth Systems*, 8(1), 166-195, doi:10.1002/2015MS000511.
- Holton, J. R. (1973): *An Introduction to Dynamic Meteorology*. American Journal of Physics, doi:10.1119/1.1987371.

- Hoskins, B. J. and I. N. James. (2014): *Fluid Dynamics of the Mid-Latitude Atmosphere*, doi:10.1002/9781118526002.
- Houze, R. A. (1989): Observed structure of mesoscale convective systems and implications for large-scale heating. *Quarterly Journal of the Royal Meteorological Society*, 115, 425-461, URL: <http://doi.wiley.com/10.1002/qj.49711548702>.
- Houze, R. A. (2004): Mesoscale convective systems. URL: <http://doi.wiley.com/10.1029/2004RG000150>.
- Hunt, K. M. R., A. G. Turner, P. M. Inness, D. E. Parker, and R. C. Levine: On the Structure and Dynamics of Indian Monsoon Depressions. *Monthly Weather Review*, 144(9), 3391-3416, doi:10.1175/MWR-D-15-0138.1.
- Iacono, M.J., E.J. Mlawer, S.A. Clough and J. J. Morcrette (2000): Impact of an improved longwave radiation model, RRTM. on the energy budget and thermodynamic properties of the NCAR community climate mode, CCM3. *Journal of Geophysical Research*, 105, 14873-14890.
- Iacono, M. J., J. S. Delamere, E. J. Mlawer, M. W. Shephard, S. A. Clough and W. D. Collins (2008): Radiative forcing by long-lived greenhouse gases: Calculations with the AER radiative transfer models. *Journal of Geophysical Research Atmospheres*, 113(13), doi:10.1029/2008JD009944.
- Ingersoll, A. P. (1969): The Runaway Greenhouse: A History of Water on Venus. *Journal of the Atmospheric Sciences*, 26(6), 1191-1198, doi:10.1175/1520-0469(1969)026<1191:TRGAHO>2.0.CO;2.
- Inoue, K., and L. Back (2015): Column-integrated Moist Static Energy Budget Analysis on Various Time Scales during TOGA COARE. *Journal of the Atmospheric Sciences*, 72(5), 1856-1871, doi:10.1175/JAS-D-14-0249.1.
- Inoue, K., and L. Back (2015): Gross Moist Stability Assessment during TOGA COARE: Various Interpretations of Gross Moist Stability. *Journal of the Atmospheric Sciences*, 150904104933002, doi:10.1175/JAS-D-15-0092.1.

- IPCC (2014): *Climate Change 2013 - The Physical Science Basis*. Cambridge, United Kingdom, New York, NY, USA, Cambridge edition, 2014, doi:10.1017/CBO9781107415324.
- Jeevanjee, N., and D. M. Romps (2013): Convective self-aggregation, cold pools, and domain size. *Geophysical Research Letters*, 40(5), 994-998, doi:10.1002/grl.50204.
- Khairoutdinov, M. F., and K. A. Emanuel (2013): Rotating radiative-convective equilibrium simulated by a cloud-resolving model. *Journal of Advances in Earth System Modeling*, 5, 816-825, doi:10.1002/2013MS000253.
- Khairoutdinov, M. F. and K. Emanuel (2018): Intraseasonal Variability in a Cloud-Permitting Near-Global Equatorial Aqua-Planet Model. *Journal of the Atmospheric Sciences*, doi:10.1175/JAS-D-18-0152.1.
- Khairoutdinov, M. F. and D. A. Randall (2003): Cloud Resolving Modeling of the ARM Summer 1997 IOP: Model Formulation, Results, Uncertainties, and Sensitivities. *Journal of the Atmospheric Sciences*, 60, 607-625, doi:10.1175/1520-0469(2003)060<0607:CRMOTA>2.0.CO;2.
- Kuang, Z. (2010): Linear Response Functions of a Cumulus Ensemble to Temperature and Moisture Perturbations and Implications for the Dynamics of Convectively Coupled Waves. *Journal of the Atmospheric Sciences*, 67(4), 941-962, doi:10.1175/2009JAS3260.1.
- Kuang, Z. (2012): Weakly Forced Mock Walker Cells. *Journal of the Atmospheric Sciences*, 69(9), 2759-2786, doi:10.1175/JAS-D-11-0307.1.
- Kuang, Z. (2018): Linear Stability of Moist Convecting Atmospheres. Part I: From Linear Response Functions to a Simple Model and Applications to Convectively Coupled Waves. *Journal of the Atmospheric Sciences*, 75(9), 2889-2907, doi:10.1175/JAS-D-18-0092.1.
- Lee J. M. and M. Khairoutdinov (2015): A Simplified Land Model (SLM) for use

- in cloud-resolving models: Formulation and evaluation. *Journal of Advances in Modeling Earth Systems*, 7(3), 1368-1392, doi:10.1002/2014MS000419.
- LeMone, M. A., E. J. Zipser, and S. B. Trier. (1998): The Role of Environmental Shear and Thermodynamic Conditions in Determining the Structure and Evolution of Mesoscale Convective Systems during TOGA COARE. *Journal of the Atmospheric Sciences*, 55(23), 3493-3518, doi:10.1175/1520-0469(1998)055<3493:TROESA>2.0.CO;2.
- Liou, K. N. (2002): *An Introduction to Atmospheric Radiation.*, Vol. 84, Elsevier.
- Lopez, M. A., D. L. Hartmann, P. N. Blossey, R. Wood, C. S. Bretherton, T. L. Kubar (2009): A Test of the Simulation of Tropical Convective Cloudiness by a Cloud-Resolving Model. *Journal of Climate*, 22(11), 2834-2849, doi:10.1175/2008JCLI2272.1.
- Lutsko, N. J. and T. W. Cronin (2018): Increase in Precipitation Efficiency with Surface Warming in Radiative-Convective Equilibrium. *Journal of Advances in Modeling Earth Systems*, 1-32, doi:10.1029/2018MS001482.
- Madden R. A. and P. R. Julian (1994): Observations of the 40-50-Day Tropical Oscillation-A Review. *Monthly Weather Review*, 122(5), 814-837, doi:10.1175/1520-0493(1994)122<0814:OOTDTP>2.0.CO;2.
- Mahadevan A., G. S. Jaeger, M. Freilich, M. Omand, E. Shroyer and D. Sengupta (2016): Freshwater in the Bay of Bengal: Its Fate and Role in Air-Sea Heat Exchange. *Oceanography*, 29(2), 72-81, doi:10.5670/oceanog.2016.40.
- Malkus, J. S., C. Ronne, and M. Chafee (1961): Cloud Patterns in Hurricane Daisy, 1958, *Tellus*, 13(1), 8-30, doi:10.1111/j.2153-3490.1961.tb00062.x.
- Manabe, S., and R. F. Strickler (1964): Thermal Equilibrium of the Atmosphere with a Convective Adjustment. *Journal of the Atmospheric Sciences.*, doi:10.1175/1520-0469(1964)021<0361:TEOTAW>2.0.CO;2.

- Mapes, B., and R. Neale (2011): Parameterizing convective organization to escape the entrainment dilemma. *Journal of Advances in Modeling Earth Systems*, 3(2), doi:10.1029/2011MS000042.
- Marenco, A., V. Thouret, P. Nedelec, H. Smit, M. Helten, D. Kley, F. Karcher, P. Simon, K. Law, J. Pyle, G. Poschmann, R. Von Wrede, C. Hume, and T. Cook (1998): Measurement of ozone and water vapor by Airbus in-service aircraft: The MOZAIC airborne program, An overview. URL: <http://doi.wiley.com/10.1029/98JD00977>.
- V. Masson-Delmotte, P. Zhai, H. Portner, D. Roberts, J. Skea, P. R. Shukla, A. Pirani, W. Moufouma-Okia, C. Pean, R. Pidcock, S. Connors, J. B. Robin Matthews, Y. Chen, X. Zhou, M. I. Gomis, E. Lonnoy, T. Maycock, M. Tignor, and T. Waterfield (2018): Global warming of 1.5C An IPCC Special Report on the impacts of global warming of 1.5C above pre-industrial levels and related global greenhouse gas emission pathways, in the context of strengthening the global response to the threat of climate change. URL: <http://www.ipcc.ch/pdf/special-reports/sr15/sr15{ }spm{ }final.pdf>.
- C. J. E. Metcalf, K. S. Walter, A. Wesolowski, C. Buckee, E. Shevliakova, A. J. Tatem, W. Boos, D. Weinberger, and V. E. Pitzer (2017): Identifying climate drivers of infectious disease dynamics: Recent advances and challenges ahead, *Proceedings of the Royal Society B*, 284(1860), 20170901.
- Metropolis, N., A. W. Rosenbluth, M. N. Rosenbluth, A. H. Teller, and E. Teller (1953): Equation of State by Fast Computing Machines. *The Journal of Chemical Physics*, 21(1953), 1087-1092, doi:10.1063/1.1699114.
- Mlawer, E. J., S. J. Taubman, P. D. Brown, M. J. Iacono, and S. A. Clough (1997): Radiative transfer for inhomogeneous atmospheres: RRTM, a validated correlated-k model for the longwave, *Journal of Geophysical Research: Atmospheres*. 102(D14), 16,663-16,682, doi:10.1029/97JD00237.

- Molteni, F., R. Buizza, T. N. Palmer, and T. Petroliaigis (1996): The ECMWF ensemble prediction system: Methodology and validation. *Quarterly Journal of the Royal Meteorological Society*, 122(529), 73-119, doi:10.1256/smsqj.52904.
- Morcrette, J.-J. (1991): Radiation and cloud radiative properties in the European Centre for Medium Range Weather Forecasts forecasting system. *Journal of Geophysical Research*, 96(D5), 9121, doi:10.1029/89JD01597.
- Morrison, H., J. A. Curry, V. I. Khvorostyanov, H. Morrison, J. A. Curry, and V. I. Khvorostyanov (2005): A New Double-Moment Microphysics Parameterization for Application in Cloud and Climate Models. Part I: Description. *Journal of the Atmospheric Sciences*, 62(6), 1665-1677, doi:10.1175/JAS3446.1.
- Muller, C., and S. Bony (2015): What favors convective aggregation and why? *Geophysical Research Letters*, 42(13), 5626-5634, doi:10.1002/2015GL064260.
- Muller, C. J., and I. M. Held (2012): Detailed Investigation of the Self-Aggregation of Convection in Cloud-Resolving Simulations. *Journal of the Atmospheric Sciences*, 69, 2551-2565, doi:10.1175/JAS-D-11-0257.1.
- Muller, C. J. and D. M. Romps (2018): Acceleration of tropical cyclogenesis by self-aggregation feedbacks. *Proceedings of the National Academy of Sciences*, 115(12), 2930-2935, doi:10.1073/pnas.1719967115.
- Neelin, J. D. and I. M. Held (1987): Modeling Tropical Convergence Based on the Moist Static Energy Budget. *Monthly Weather Review*, 115, 3-12, doi:10.1175/1520-0493(1987)115<0003:MTCBOT>2.0.CO;2.
- Neelin, J. D., O. Peters, and K. Hales (2009): The Transition to Strong Convection. *Journal of the Atmospheric Sciences*, 66(8), 2367-2384, doi:10.1175/2009JAS2962.1.
- Nicholls, M. E. (2015): An investigation of how radiation may cause accelerated rates of tropical cyclogenesis and diurnal cycles of convective activity. *Atmos. Chem. Phys*, 15, 9003-9029, doi:10.5194/acp-15-9003-2015.

- Nilsson, J., and K. A. Emanuel (1999): Equilibrium atmospheres of a two-column radiative-convective model. *Quarterly Journal of the Royal Meteorological Society*, 125, 2239-2264, doi:10.1002/qj.49712555814.
- Nolan, D. S., E. D. Rappin, and K. A. Emanuel (2007). Tropical cyclogenesis sensitivity to environmental parameters in radiative-convective equilibrium. *Quarterly Journal of the Royal Meteorological Society*, 133, 2085-2107, doi:10.1002/qj.170.
- Pauluis, O. M., and A. A. Mrowiec (2013): Isentropic Analysis of Convective Motions. *Journal of the Atmospheric Sciences*, 70(11), 3673-3688, doi:10.1175/JAS-D-12-0205.1.
- Pierrehumbert, R. T. (2009): *Principles of Planetary Climate*, Earth, 1, 359, Cambridge University Press.
- Pierrehumbert, R. T. (2002): The hydrologic cycle in deep-time climate problems, URL: <http://www.nature.com/doi/finder/10.1038/nature01088>.
- Pierrehumbert, R. T., H. Brogniez, and R. Roca (2007): On the relative humidity of the atmosphere. *The Global Circulation of the Atmosphere*, pp 143-185, URL: <http://citeseerx.ist.psu.edu/viewdoc/download?doi=10.1.1.76.6479&rep=rep1&type=pdf>.
- Plant, R. S. (2009): A review of the theoretical basis for bulk mass flux convective parameterization, *Atmospheric Chemistry and Physics*, pp. 3529-3544, doi:10.5194/acpd-9-24945-2009.
- Posselt, D. J., S. Van Den Heever, G. Stephens, and M. R. Igel (2012): Changes in the interaction between tropical convection, radiation, and the large-scale circulation in a warming environment. *Journal of Climate*, 25, 557-571, URL: <http://journals.ametsoc.org/doi/abs/10.1175/2011JCLI4167.1>.
- Praveen, V., S. Sandeep, and R. S. Ajayamohan (2015): On the relationship between mean monsoon precipitation and low pressure systems in climate model simulations. *Journal of Climate*, 28(13), 5305-5324, doi:10.1175/JCLI-D-14-00415.1.

- Pujol, T., and North, G. R. (2002): Runaway Greenhouse Effect in a Semigray Radiative Convective Model. *Journal of the Atmospheric Sciences*, 59(1967), 2801-2810, doi:10.1175/1520-0469(2002)059<2801:RGEIAS?2.0.CO;2;
- Ramanathan, V., and J. A. Coakley Jr. (1978): Climate modeling through radiative-convective models. *Review of Geophysics*, 16(4), 465-489, doi:10.1029/RG016i004p00465.
- Randall D., M. Khairoutdinov, A. Arakawa, W. Grabowski (2003): Breaking the Cloud Parameterization Deadlock. *Bulletin of the American Meteorological Society*, 84(11), 1547-1564, doi:10.1175/BAMS-84-11-1547.
- Raymond, D. J. (1995): Regulation of Moist Convection over the West Pacific Warm Pool. *Journal of the Atmospheric Sciences.*, doi:10.1175/1520-0469(1995)052<3945:ROMCOT>2.0.CO;2.
- Raymond, D., and A. Blyth (1986): A stochastic mixing model for nonprecipitating cumulus clouds. *Journal of the Atmospheric Sciences.*, doi:10.1175/1520-0469(1986)043<2708:ASMMFN>2.0.CO;2.
- Renno, N. O., K. A. Emanuel and P. H. Stone (1994): Radiative-convective model with an explicit hydrologic cycle. *Journal of Geophysical Research.*, doi:10.1029/94JD00020.
- Renno, N. O. (1997): Multiple equilibria in radiative-convective atmospheres. *Tellus Series A-Dynamic Meteorology And Oceanography*, 49(4), 423-438, doi:10.1034/j.1600-0870.1997.t01-3-00002.
- Robinson, T. D., and D. C. Catling (2012): An analytic radiative-convective model for planetary atmospheres. *The Astrophysical Journal*, 757(1), 104, doi:10.1088/0004-637X/757/1/104.
- Rodgers, C. D. and C. D. Walshaw (1966): The computation of infra-red cooling rate in planetary atmospheres. *Quarterly Journal of the Royal Meteorological Society*, 92, 67-92, doi:10.1002/qj.49709239107.

- Rodell, M., P. R. Houser, U. Jambor, J. Gottschalck, K. Mitchell, C. J. Meng, K. Arsenault, B. Cosgrove, J. Radakovich, M. Bosilovich, J. K. Entin, J. P. Walker, D. Lohmann, and D. Toll (2004): The Global Land Data Assimilation System. *Bulletin of the American Meteorological Society*, 85(3), 381-394, doi:10.1175/BAMS-85-3-381.
- Romps, D. M. (2014): An analytical model for tropical relative humidity. *Journal of Climate*, 27(19), 7432-7449, doi:10.1175/JCLI-D-14-00255.1.
- Rydbeck, A. V., E. D. Maloney, and G. J. Alaka (2016): In Situ Initiation of East Pacific Easterly Waves in a Regional Model. *Journal of the Atmospheric Sciences*, 74JAS-D-1-0124.1, doi:10.1175/JAS-D-16-0124.1.
- Salvekar P. S., L. George, and S. K. Mishra (1986): Low level wind shear and baroclinic growth of monsoon depression scale waves. *Meteorology and Atmospheric Physics*, 35(1-2), 10-18, doi:10.1007/BF01029520.
- Satoh M., K. Aramaki, and M. Sawada (2016): Structure of Tropical Convective Systems in Aqua-Planet Experiments: Radiative-Convective Equilibrium Versus the Earth-Like Experiment. *SOLA*, 12(0), 220-224, doi:10.2151/sola.2016-044.
- Schneider, T., P. A. O’Gorman, and X. Levine (2010): Water vapor and the dynamics of climate changes. *Reviews of Geophysics*, (48), 1-22, doi:10.1029/2009RG000302. 1.INTRODUCTION.
- Seneviratne, S. I., N. Nicholls, D. Easterling, C. M. Goodess, S. Kanae, J. Kossin, Y. Luo, J. Marengo, K. McInnes, and M. Rahimi (2012): Changes in climate extremes and their impacts on the natural physical environment. *Managing the Risks of Extreme Events and Disasters to Advance Climate Change Adaptation: A Special Report of Working Groups I and II of the Intergovernmental Panel on Climate Change (IPCC)*
- Sengupta, D., B. N. Goswami, and R. Senan (2001): Coherent intraseasonal oscillations over the Indian Ocean and the Indian subcontinent. *Journal of Climate*, 14(12), 3322-3332, doi:10.1175/1520-0442(2001)14<3322:COIOAI>2.0.CO;2.

- lations of ocean and atmosphere during the Asian summer monsoon, *Geophysical Research Letters*, 28(21), 4127-4130, doi:10.1029/2001GL013587.
- Serra, Y. L., G. N. Kiladis, and M. F. Cronin (2008): Horizontal and Vertical Structure of Easterly Waves in the Pacific ITCZ. *Journal of the Atmospheric Sciences*, 65(4), 1266-1284, doi:10.1175/2007JAS2341.1.
- Sessions, S. L., M. J. Herman, and S. Sentic (2015): Convective response to changes in the thermodynamic environment in idealized weak temperature gradient simulations. *Journal of Advances in Modeling Earth Systems*, 7(2), 712-738, doi:10.1002/2015MS000446.
- Sessions, S. L., S. Sugaya, D. J. Raymond, and A. H. Sobel (2010): Multiple equilibria in a cloud-resolving model using the weak temperature gradient approximation. *Journal of Geophysical Research: Atmospheres*, 115(12), 1-17. doi:10.1029/2009JD013376.
- Sherwood, S. C., W. Ingram, Y. Tsushima, M. Satoh, M. Roberts, P. L. Vidale, and P. A. O’Gorman (2010): Relative humidity changes in a warmer climate. *Journal of Geophysical Research Atmospheres*, 115(9), D09,104, doi:10.1029/2009JD012585.
- Singh, M. S., and P. A. O’Gorman (2013): Influence of entrainment on the thermal stratification in simulations of radiative-convective equilibrium, *Geophysical Research Letters*, 40(16), 4398-4403, doi:10.1002/grl.50796.
- Sobel A., S. Camargo, M. Previdi and K. A. Emanuel (2018): Aerosol vs. Greenhouse Gas Influences on Tropical Cyclone Potential Intensity. URL: <https://ams.confex.com/ams/33HURRICANE/webprogram/Paper339471.html>.
- Sobel, A. H., G. Bellon and J. Bacmeister (2007): Multiple equilibria in a single-column model of the tropical atmosphere. *Geophysical Research Letters*, 34(22), 1-5, doi:10.1029/2007GL031320.
- Sobel, A. H., and Bretherton, C. S. (2000): Modeling tropical precipitation in a single

- column. *Journal of Climate*, 13, 4378-4392, doi:10.1175/1520-0442(2000)013<4378:MTPIAS>2.0.CO;2.
- Sobel, A. H., J. Nilsson, and L. M. Polvani (2001): The Weak Temperature Gradient Approximation and Balanced Tropical Moisture Waves. *Journal of the Atmospheric Sciences*, 58, 3650-3665. doi:10.1175/1520-0469(2001)058<3650:TWTGAA>2.0.CO;2.
- Sobel, A. H. and H. Gildor (2003): A Simple Time-Dependent Model of SST Hot Spots, *Journal of Climate*, 16,3978-3992, doi:10.1175/1520-0442(2003)016<3978:ASTMOS>2.0.CO;2.
- Stano, G., T. N. Krishnamurti, T. S. Vijaya Kumar, and A. Chakraborty (2002): Hydrometeor structure of a composite monsoon depression using the TRMM radar. *Tellus, Series A: Dynamic Meteorology and Oceanography*, 54(4), 370-381, doi:10.1034/j.1600-0870.2002.01330.x.
- Stein, T. H., C. E. Holloway, I. Tobin, and S. Bony (2017): Observed relationships between cloud vertical structure and convective aggregation over tropical ocean. *Journal of Climate*, 30(6), 2187-2207, doi:10.1175/JCLI-D-16-0125.1.
- Stevens, B. and S. Bony (2013): Water in the atmosphere. *Physics Today*, 66(6), 29-34, doi:10.1063/PT.3.2009.
- Stansifer, E. M., P. A. O'Gorman, and J. I. Holt (2017): Accurate computation of moist available potential energy with the Munkres algorithm. *Quarterly Journal of the Royal Meteorological Society*, 143(702), 288-292, doi:10.1002/qj.2921.
- Takahashi, K. (2009): Radiative Constraints on the Hydrological Cycle in an Idealized Radiative-Convective Equilibrium Model. *Journal of the Atmospheric Sciences*, 66(1), 77-91, doi:10.1175/2008JAS2797.1.
- Tobin, I., S. Bony and R. Roca (2012): Observational Evidence for Relationships between the Degree of Aggregation of Deep Convection, Water Vapor, Sur-

- face Fluxes, and Radiation. *Journal of Climate*, 25(20), 6885-6904, doi:10.1175/JCLI-D-11-00258.1.
- Tompkins, A. M. (2001): Organization of Tropical Convection in Low Vertical Wind Shears: The Role of Water Vapor. *Journal of the Atmospheric Sciences*, 58, 529-545, doi:10.1175/1520-0469(2001)058<0529:OOTCIL>2.0.CO;2.
- Tompkins, A., and G. C. Craig (1998): Radiative-convective equilibrium in a three-dimensional cloud-ensemble model. *Quarterly Journal of the Royal Meteorological Society*, 124, 2073-2097.
- Tompkins, A. M., A. G. Semie (2017): Organization of tropical convection in low vertical wind shears: role of updraft entrainment. *Journal of Advances in Modeling Earth Systems*, doi:10.1002/2016MS000802.
- Trenberth, K. E. and L. Smith (2005): The mass of the atmosphere: A constraint on global analyses. *Journal of Climate*, 18(6), 864-875, doi:10.1175/JCLI-3299.1.
- Trenberth, K. E., D. P. Stepaniak, and J. M. Caron (2002): Interannual variations in the atmospheric heat budget. *Journal of Geophysical Research*, 107(D8), 4066, doi:10.1029/2000JD000297.
- Trepanier, S. (2000): The Structure of Empedocles' Fragment 17. *Essays in Philosophy*, 1(1), 1, 2000.
- Vallis, G. K. (2006): *Atmospheric and oceanic fluid dynamics: Fundamentals and large-scale circulation*. Cambridge.
- Vecchi, G. A., and D. E. Harrison (2002): Monsoon breaks and subseasonal sea surface temperature variability in the Bay of Bengal. *Journal of Climate*, 15(12), 1485-1493, doi:10.1175/1520-0442(2002)015<1485:MBASSS>2.0.CO;2.
- Wang, J. and L. Zhang (2008): Systematic errors in global radiosonde precipitable water data from comparisons with ground-based GPS measurements. *Journal of Climate*, 21(10), 2218-2238, doi:10.1175/2007JCLI1944.1.

Waters, J. W., L. Froidevaux, R. S. Harwood, R. F. Jarnot, H. M. Pickett, W. G. Read, P. H. Siegel, R. E. Cofield, M. J. Filipiak, D. A. Flower, J. R. Holden, G. K. Lau, N. J. Livesey, G. L. Manney, H. C. Pumphrey, M. L. Santee, D. L. Wu, D. T. Cuddy, R. R. Lay, M. S. Loo, V. S. Perun, M. J. Schwartz, P. C. Stek, R. P. T., Mark A. Boyles, K. M. Chandra, M. C. Chavez, G. Chen, B. V. Chudasama, R. Dodge, R. A. Fuller, M. A. Girard, J. H. Jiang, Y. Jiang, B. W. Knosp, R. C. Labelle, J. C. Lam, K. A. Lee, D. Miller, J. E. Oswald, N. C. Patel, D. M. Pukala, O. Quintero, D. M. Scaff, W. Van Snyder, M. C. Tope, P. A. Wagner, and M. J. Walch (2006): The Earth Observing System Microwave Limb Sounder (EOS MLS) on the aura satellite. *IEEE Transactions on Geoscience and Remote Sensing*, 44(5), 1075-1092, doi:10.1109/TGRS.2006.873771.

Weaver, C. P., and V. Ramanathan (1995): Deductions from a simple climate model: Factors governing surface temperature and atmospheric thermal structure. *Journal of Geophysical Research*, doi:10.1029/95JD00770.

Webster, P. J., V. O. Magana, T. N. Palmer, J. Shukla, R. A. Tomas, M. U. Yanai and T. Yasunari (1998): Monsoons: Processes, predictability, and the prospects for prediction. *Journal of Geophysical Research, Oceans*, 103(C7), 14451-14510.

Wheeler, M. C. and H. H. Hendon (2004): An All-Season Real-Time Multivariate MJO Index: Development of an Index for Monitoring and Prediction. *Monthly Weather Review*, 132(8), 1917-1932, doi:10.1175/1520-0493(2004)132<1917:AARMMI>2.0.CO;2.

Whiteman, D. N., S. H. Melfi, and R. A. Ferrare (1992): Raman lidar system for the measurement of water-vapor and aerosols in the Earth's atmosphere. *Applied Optics*, 31(16), 3068-3082, doi:10.1364/AO.31.003068.

Wielicki, B. A., B. R. Barkstrom, E. F. Harrison, R. B. Lee, G. Louis Smith, and J. E. Cooper (1996): Clouds and the Earth's Radiant Energy System (CERES): An Earth Observing System Experiment. *Bulletin of the American Meteorological*

- Society*, 77(5), 853-868, doi:10.1175/1520-0477(1996)077<0853:CATERE>2.0.CO;2.
- Wing, A. A., S. J. Camargo, and A. H. Sobel (2016): Role of radiative-convective feedbacks in spontaneous tropical cyclogenesis in idealized numerical simulations, *Journal of the Atmospheric Sciences*, 73(7), JAS-D-15-0380.1, doi:10.1175/JAS-D-15-0380.1.
- Wing, A. A., and T. W. Cronin (2016): Self-aggregation of convection in long channel geometry, *Quarterly Journal of the Royal Meteorological Society*, 142, 1-15, doi:10.1002/qj.2628.
- Wing, A. A., and K. A. Emanuel (2014): Physical mechanisms controlling self-aggregation of convection in idealized numerical modeling simulations. *Journal of Advances in Modeling Earth Systems*, 6, 59-74, doi:10.1002/2013MS000269..
- Wing, A. A., K. Emanuel, C. E. Holloway, and C. Muller (2017): Convective Self-Aggregation in Numerical Simulations: A Review, *Surveys in Geophysics*, doi:10.1007/s10712-017-9408-4.
- Wolding, B. O., E. D. Maloney, S. Henderson, and M. Branson (2016): Climate Change and the Madden-Julian Oscillation : A Vertically Resolved Weak Temperature Gradient Analysis, *Journal of Advances in Modeling Earth Systems*, doi:10.1002/2016MS000843.
- Yanai, M., S. Esbensen, and J. Chu (1973): Determination of Bulk Properties of Tropical Cloud Clusters from Large-Scale Heat and Moisture Budgets. *Journal of the Atmospheric Sciences*, 30(4), 611-627, doi:10.1175/1520-0469(1973)030<0611:DOBPOT>2.0.CO;2.
- Yang, D. (2017): Boundary layer height and buoyancy determine the horizontal scale of convective self-aggregation. *Journal of the Atmospheric Sciences*, JAS-D-17-0150.1.

- Yano, J.-I., and K. A. Emanuel (1991): An Improved Model of the Equatorial Troposphere and Its Coupling with the Stratosphere. *Journal of the Atmospheric Sciences*, 48(3), 377-389, doi:10.1175/1520-0469(1991)048<0377:AIMOTE>2.0.CO;2.
- Yoon, J. and T. Chen (2005): Water vapor budget of the Indian monsoon depression. *Tellus, Series A: Dynamic Meteorology and Oceanography*, 57(5), 770-782, doi:10.1111/j.1600-0870.2005.00145.x.
- Yu, J., and J. D. Neelin (1997): Analytic Approximations for Moist Convectively Adjusted regions. *Journal of the Atmospheric Sciences*, 54, 1054-1063, doi:10.1175/1520-0469(1997)054<1054:AAFMC>2.0.CO;2.
- Yu J., C. Chou, and J. D. Neelin (1998): Estimating the Gross Moist Stability of the Tropical Atmosphere. *Journal of the Atmospheric Sciences*, 55, 1354-1372, doi:10.1175/1520-0469(1998)055<1354:ETGMSO>2.0.CO;2.
- Zhang, C. (2005): Madden-Julian Oscillation. *Reviews of Geophysics*, 43.2.
- Zhao, M., J.-C. Golaz, I. M. Held, H. Guo, V. Balaji, R. Benson, J.-H. Chen, X. Chen, L. J. Donner, J. P. Dunne, K. Dunne, J. Durachta, S.-M. Fan, S. M. Freidenreich, S. T. Garner, P. Ginoux, L. M. Harris, L. W. Horowitz, J. P. Krasting, A. R. Langenhorst, Z. Liang, P. Lin, S.-J. Lin, S. L. Malyshev, E. Mason, P. C. D. Milly, Y. Ming, V. Naik, F. Paulot, D. Paynter, P. Phillipps, A. Radhakrishnan, V. Ramaswamy, T. Robinson, D. Schwarzkopf, C. J. Seman, E. Shevliakova, Z. Shen, H. Shin, L. G. Silvers, J. R. Wilson, M. Winton, A. T. Wittenberg, B. Wyman, and B. Xiang (2018): The GFDL Global Atmosphere and Land Model AM4.0/LM4.0: 1. Simulation Characteristics With Prescribed SSTs. *Journal of Advances in Modeling Earth Systems*, 10(3), 691-734, doi:10.1002/2017MS001208.
- Zhao, M., J.-C. Golaz, I. M. Held, H. Guo, V. Balaji, R. Benson, J.-H. Chen, X. Chen, L. J. Donner, J. P. Dunne, K. Dunne, J. Durachta, S.-M. Fan, S. M. Freidenreich, S. T. Garner, P. Ginoux, L. M. Harris, L. W. Horowitz, J. P. Krasting, A. R. Langenhorst, Z. Liang, P. Lin, S.-J. Lin, S. L. Malyshev, E. Mason, P. C. D. Milly,

Y. Ming, V. Naik, F. Paulot, D. Paynter, P. Phillipps, A. Radhakrishnan, V. Ramaswamy, T. Robinson, D. Schwarzkopf, C. J. Seman, E. Shevliakova, Z. Shen, H. Shin, L. G. Silvers, J. R. Wilson, M. Winton, A. T. Wittenberg, B. Wyman, and B. Xiang (2018): The GFDL Global Atmosphere and Land Model AM4.0/LM4.0: 2. Model Description, Sensitivity Studies, and Tuning Strategies. *Journal of Advances in Modeling Earth Systems*, 10(3), 735-769, doi:10.1002/2017MS001209.